doi:10.25143/prom-rsu_2024-01_dt

RĪGA STRADIŅŠ UNIVERSITY

Pavels Dimitrijevs

Targeting Cancer Metabolism with Isoselenazolium Salts

Doctoral Thesis for obtaining the scientific degree
"Doctor of Science (*PhD*)"

Sector Group – Medicine and Health Sciences
Sector – Basic Medicine
Sub-Sector – Pharmaceutical Pharmacology

Riga, 2023

RĪGA STRADIŅŠ UNIVERSITY

Pavels Dimitrijevs

ORCID 0000-0002-6332-2395

Targeting Cancer Metabolism with Isoselenazolium Salts

Doctoral Thesis for obtaining the scientific degree
"Doctor of Science (*PhD*)"

Sector Group – Medicine and Health Sciences

Sector – Basic Medicine

Sub-Sector – Pharmaceutical Pharmacology

Supervisor of the Doctoral Thesis:

Dr. chem., LAS full member, **Pavels Arsenjans**,
Latvian Institute of Organic Synthesis

NATIONAL DEVELOPMENT PLAN 2020

EUROPEAN UNION
European Regional Development Fund

INVESTING IN YOUR FUTURE

This work was supported by
ERDF "Development of a novel potent PARP inhibitor" (No. 1.1.1.1/19/A/016)
and BioMedPharm (No. VPP-EM-BIOMEDICINA-2022/1-0001) projects.

Riga, 2023

Abstract

Low therapeutic efficacy and resistance to conventional drugs remain the major obstacles in modern chemotherapy. Scientists around the world are therefore constantly searching for new drugs with different modes of action that, alone or in combination with other drugs, can help cancer patients. In recent years, selenium-containing compounds have been extensively studied as anticancer agents due to the characteristic properties of selenium. The main aim of this study was to evaluate the chemotherapeutic potential of isoselenazolium salts, a novel class of organoselenium compounds, and to explore their mechanism of action.

The first series of isoselenazolium salts exhibited selective cytotoxicity against breast cancer cell lines. These compounds modulated mitochondrial respiration, increased reactive oxygen species production, altered NAD^+ homeostasis, inhibited poly(ADP-ribose) polymerase 1 (PARP1) and possibly interfered with cardiolipin, a signature phospholipid of mitochondria. To test the latter, a new fluorescent cardiolipin-specific probe and a competitive binding assay were developed to quantitatively describe the drugs` affinity for cardiolipin. Using a new method, it was proved that the affinity of isoselenazolium salts for cardiolipin is low, and their interaction is not related to the pharmacological effect.

The second series of isoselenazolium salts with a modified structure was designed to have improved PARP1 inhibitory activity. These compounds displayed high cytotoxicity against T-cell leukaemia, breast, liver, and lung cancer cells. Although the PARP1 inhibitory activity was improved, detailed studies of the mechanism of action showed that isoselenazolium salts are potent and selective inhibitors of pyruvate kinase M2 (PKM2), an enzyme, that is highly expressed in various types of tumours. On the basis of NMR, size-exclusion chromatography, mass photometry, differential scanning fluorimetry, isothermal titration calorimetry, and enzyme kinetic data, isoselenazolium salts were found to be competitive inhibitors and at the same time induce an unstable PKM2 homotetramer formation. Thus, PKM2 translocation to the nucleus is blocked, preventing its nonmetabolic functions.

The discovery of robust PKM2 inhibitors could serve as the basis for new anticancer drug candidates and provide an important insight into the fundamental role of PKM2 in oncogenesis.

Keywords: cancer, cardiolipin, isoselenazolium salts, metabolic reprogramming, PARP1, pyruvate kinase M2, selenium.

Anotācija

Izoselenazolija sāļu ietekme uz vēža metabolismu

Zema terapeitiska efektivitāte un rezistence pret esošām zālēm joprojām ir galvenie šķēršļi mūsdienu ķīmijterapijā. Tāpēc zinātnieki visā pasaulē nemitīgi meklē jaunas zāļvielas ar dažādiem darbības mehānismiem, kas, atsevišķi vai kombinācijā ar citām zālēm, palīdzēs pacientiem ar vēzi. Pēdējos gados selēnu saturošie savienojumi, raksturīgo selēna īpašību dēļ, tiek plaši pētīti kā pretvēža līdzekļi. Šī promocijas darba galvenais mērķis bija novērtēt izoselenazolija sāļu, jaunas organisko selēna savienojumu klases, ķīmijterapijas potenciālu un izpētīt to darbības mehānismu.

Pirmā izoselenazolija sāļu sērija uzrādīja selektīvu citotoksicitāti pret krūts vēža šūnu līnijām. Šie savienojumi modulēja mitohondriālo elpošanu, palielināja reaktīvā skābekļa savienojumu veidošanos, ietekmēja NAD^+ homeostāzi, kavēja poli(ADP-ribozes) polimerāzi 1 (PARP1) un, iespējams, mijiedarbojās ar mitohondrijiem raksturīgo fosfolipīdu – kardiolipīnu. Lai pārbaudītu pēdējo apgalvojumu, tika izstrādāts jauns kardiolipīnam specifiskais fluorescējošais marķieris un uz konkurējošās saistīšanās balstīta metode, lai kvantitatīvi raksturotu zāļu afinitāti pret kardiolipīnu. Izmantojot jaunu metodi, tika pierādīts, ka izoselenazolija sāļu afinitāte pret kardiolipīnu ir zema, un viņu savstarpēja mijiedarbība nav saistīta ar farmakoloģisko efektu.

Otrā izoselenazolija sāļu sērija ar modificētu struktūru tika izstrādāta, lai uzlabotu PARP1 kavējošo aktivitāti. Šiem savienojumiem tika pierādīta augsta citotoksicitāte pret T-šūnu leikēmijas, krūts, aknu un plaušu vēža šūnām. Lai gan PARP1 kavējošā aktivitāte tika uzlabota, detalizēti darbības mehānisma pētījumi parādīja, ka izoselenazolija sāļi spēcīgi un selektīvi kavē piruvāta kināzi M2 (PKM2), enzīmu, kas ir augsti ekspresēta dažādos audzējos. Pamatojoties uz KMR, izmēru izslēgšanas hromatogrāfijas, masas fotometrijas, diferenciālās skenēšanas fluorimetrijas, izotermiskās titrēšanas kalorimetrijas un enzīma kinētikas datiem, tika konstatēts, ka izoselenazolija sāļiem piemīt konkurējošo inhibitoru raksturs, un, tajā pašā laikā tie izraisa nestabilu PKM2 homotetramēru veidošanos. Tādējādi tiek bloķēta PKM2 translokācija uz šūnas kodolu, novēršot tā nemetaboliskās funkcijas.

Spēcīgu PKM2 inhibitoru atklāšana var kalpot par pamatu jauniem pretvēža zāļu kandidātiem un sniegt svarīgu ieskatu par PKM2 lomu onkoģenēzē.

Atslēgvārdi: izoselenazolija sāļi, kardiolipīns, metaboliskā pārprogrammēšana, PARP1, piruvāta kināze M2, selēns, vēzis.

Table of Contents

Abbreviations used in the Thesis

ATP	adenosine triphosphate
ACC	acetyl-CoA carboxylase
ACLY	ATP citrate lyase
ADP	adenosine diphosphate
ANOVA	analysis of variance
AO	acridine orange, 3,6-bis(dimethylamino)acridine
Bcl-2	B-cell lymphoma 2 protein
Bcl2A1	Bcl-2 related protein A1
Bcl2L2	Bcl-2-like protein 2
BclXL	B-cell lymphoma protein extra-large
BINAP	2,2′-bis(diphenylphosphino)-1,1′-binaphthyl
BSA	bovine serum albumin
CCCP	carbonyl cyanide m-chlorophenylhydrazone
cDNA	complementary deoxyribonucleic acid
CI	respiratory complex I, NADH:ubiquinone oxidoreductase
CII	respiratory complex II, succinate dehydrogenase
CIII	respiratory complex III, coenzyme Q – cytochrome c reductase
CL	cardiolipin
CoA	coenzyme A
COX	cyclooxygenase
Cyt c	cytochrome c
DAPI	4′,6-diamidino-2-phenylindole
DCM	dichloromethane
DMF	dimethylformamide
DMSO	dimethyl sulfoxide
DNA	deoxyribonucleic acid
DOPC	1,2-dioleoyl-*sn*-glycero-3- phosphocholine
DSF	differential scanning fluorimetry
EC_{50}	the half-maximal effective concentration
EDC	1-ethyl-3-(3-dimethylaminopropyl) carbodiimide
EGTA	egtazic acid
ESKAPE	*Enterococcus faecium, Staphylococcus aureus, Klebsiella pneumoniae, Acinetobacter baumannii, Pseudomonas aeruginosa, and Enterobacter spp.*
EtOAc	ethyl acetate
EtOH	ethanol

ETS	electron transfer system
FATP	fatty acid transport protein
FBP	fructose 1,6-bisphosphate
FDH	formate dehydrogenase
FI	fluorescence intensity
G	glutamate
G6P	glucose-6-phosphate
GLS1	glutaminase 1
GLUT	glucose transporter
GPx	glutathione peroxidases
HEPES	4-(2-hydroxyethyl)-1-piperazineethanesulfonic acid
HIF-1α	hypoxia-inducible factor 1-alpha
HK	hexokinase
HOBt	1-hydroxybenzotriazole
IC_{50}	the half-maximal inhibitory concentration
IDH	isocitrate dehydrogenase
IDH1(R132H)	isocitrate dehydrogenase 1 with a R132H mutation
IDH2(R140Q)	isocitrate dehydrogenase 2 with a R140Q mutation
IDO1	indoleamine-pyrrole 2,3-dioxygenase 1
IMM	inner mitochondrial membrane
iPrOH	isopropanol
ITC	isothermal titration calorimetry
$K_{App,M}$	apparent Michaelis-Menten constant
LC-MS	liquid chromatography–mass spectrometry
LDH	lactate dehydrogenase
LEAK	non-phosphorylating resting state of mitochondrial respiration
M	malate
MAPK	mitogen-activated protein kinases
MAT2A	methionine adenosyltransferase 2A
Mcl-1	myeloid leukaemia 1 protein
MCT1	monocarboxylate transporter 1
MeOH	methanol
MoA	mechanism of action
mRNA	messenger ribonucleic acid
MTAP	S-methyl-5'-thioadenosine phosphorylase
mtDNA	mitochondrial DNA

MTT	3-(4,5-dimethylthiazol-2-yl)-2,5-diphenyltetrazolinium bromide
N	NADH-generating substrates
NAD^+	nicotinamide adenine dinucleotide
NADH	nicotinamide adenine dinucleotide, reduced
NADPH	nicotinamide adenine dinucleotide phosphate, reduced
NAMPT	nicotinamide phosphoribosyltransferase
NAO	10–*N*–nonyl acridine orange
NMN	nicotinamide mononucleotide
NMR	nuclear magnetic resonance
NOE	nuclear Overhauser effect
NS	NADH and succinate generating substrates
OCR	oxygen consumption rate
OXPHOS	oxidative phosphorylation
P	pyruvate
PA	L-α-phosphatidic acid
PAr	poly(ADP-ribose)
PARP	poly(ADP-ribose) polymerase
PBS	phosphate-buffered saline
PBST	phosphate-buffered saline with Triton X-100 (0.1 %)
PCT	patent cooperation treaty
PE	L-α-phosphatidylethanolamine
PEP	phosphoenolpyruvate
PI	L-α-phosphatidylinositol
PI3K	phosphoinositide 3-kinase
PK	pyruvate kinase
PKL	pyruvate kinase isoform L
PKM1	pyruvate kinase isoform M1
PKM2	pyruvate kinase isoform M2
PKR	pyruvate kinase isoform R
PPP	pentose phosphate pathway
PS	L-α-phosphatidylserine
qPCR	quantitative polymerase chain reaction
RNA	ribonucleic acid
ROS	reactive oxygen species
rot	rotenone
S	succinate

SAR	structure-activity relationship
SD	standard deviation
SEC	Size exclusion chromatography
SLC1A5	solute carrier family 1 member 5A
STAT3	signal transducer and activator of transcription 3
TCA	tricarboxylic acid cycle
TDO	tryptophan 2,3-dioxygenase
TLC	thin layer chromatography
TNKS	tankyrase
TPP	triphenylphosphonium group
Tris	tris(hydroxymethyl)aminomethane
TTAPE-Me	1,1,2,2-tetrakis[4-(2-trimethylammonioethoxy)-phenylethene
UV	ultraviolet
VApp,max	apparent maximum reaction velocity
V_0	initial reaction velocity
Water-LOGSY	Water-ligand observed via gradient spectroscopy
Φ	photoluminescence quantum yield

Introduction

Cancer is a group of diseases caused by the accumulation of genetic mutations and dysregulated gene expression leading to uncontrolled proliferation of cells. To support growth, cancer cells must meet a high energy demand, produce building blocks for biomass generation and maintain a reduction-oxidation balance. This is achieved through so called metabolic reprogramming, which includes upregulation of glucose transport and key glycolytic enzymes, promoting aerobic glycolysis (Upadhyay et al., 2013). In addition, mitochondrial metabolism is equally important for ATP production, regulation of apoptosis and tumorigenesis (Zu and Guppy, 2004; Weinberg et al., 2010; Fan et al., 2013; Weinberg and Chandel, 2015). Cancer cells maintain higher levels of reactive oxygen species (ROS) than normal cells, but despite increased antioxidant capacity, are more vulnerable to the additional ROS induction (Gorrini, Harris and Mak, 2013).

With the discovery of the fundamental roles of selenium and selenoproteins in metabolism and antioxidant systems, as well as the progress in the field of organoselenium chemistry, an intensive development of new organic Se-containing therapeutics has begun (Gandin et al., 2018). Many different classes of organoselenium compounds have been explored as anticancer agents so far, but despite promising preclinical results, none of them has yet found its place on a pharmacy shelf. The clinical application is often limited by the requirement of high doses that lead to the accumulation of toxic selenium-containing metabolites (selenosis) and serious side effects such as drug-induced liver injury, immunosuppression, anaemia and infertility (Johnson et al., 2008; Garbo et al., 2022). Another common problem with selenium-containing agents is an unclear or only superficially studied mechanism of action, which also slows down the development process of a particular class of compounds (Lenardão, Sancineto, and Santi, 2018; Chuai et al., 2021). A solution to these issues requires a deep understanding of the mode of action, finding an objective molecular target and the development of new selenium-containing compounds with higher antiproliferative activity to reduce the effective dose and the risk of selenosis.

Recently, a new group of organoselenium compounds – fused isoselenazolium salts – has been discovered, a heterocyclic system with a Se–N^+ bond (Arsenyan et al., 2015). These compounds have been shown to be highly reactive pro-oxidants that induce DNA double-strand damage and display excellent antibacterial activity against ESKAPE pathogens (Arsenyan and Vasiljeva, 2017; Rendekova et al., 2017; Witek et al., 2017). However, the chemotherapeutic potential of this scaffold has not been explored yet. This Thesis describes the antiproliferative

activity of isoselenazolium salts, structure-activity relationship studies, mechanism of action, challenges faced and solutions found.

Aim of the Thesis

To investigate the antiproliferative activity and establish molecular mechanisms of isoselenazolium salts to increase efficacy through subsequent structural modifications.

Objectives of the Thesis

In order to reach the aim of the Doctoral Thesis, the following objectives have been set:

1. Evaluate cytotoxicity of isoselenazolium salts against different malignant and normal cell lines.
2. Determine the mechanism of action of isoselenazolium salts and identify potential molecular targets.
3. Explore the structure-activity relationship of isoselenazolium derivatives based on *in vitro* pharmacological activity.

Hypothesis of the Thesis

Substituted isoselenazolium chlorides exhibit high antiproliferative activity by targeting cancer metabolism.

Novelty of the Thesis

This study provides the first extensive examination of the antiproliferative activity of isoselenazolium salts and their effect on cancer metabolism. A new fluorescence-based competitive binding assay for the determination of the binding affinity to cardiolipin was developed as part of the study, which should be of great interest to researchers working on the discovery of mitochondria-targeted drugs. The design and synthesis of the second generation of isoselenazolium derivatives led to the discovery of potent PARP1 and PKM2 inhibitors with dual activity. These findings will help in the further fundamental studies of the role of PKM2 in cancer metabolism and provide the basis for a novel class of drug candidates with a unique molecular mechanism. The novelty of the study is underlined by the two international patents for cardiolipin-specific fluorescent probes and the competitive binding assay, as well as a PCT application for the new PKM2 inhibitors.

1 Literature

1.1 Selenium in anticancer agents

Selenium is known for its high chemical activity in oxidation-reduction reactions involving one- or two-electron transfer. In a biological context, selenium is a conductor of the redox system orchestra and exerts most of its functions as an integral component of selenoproteins. Most of these proteins are oxidoreductases, e.g. glutathione peroxidases (GPx), thioredoxin reductases and deiodinases, with a selenocysteine residue in the active centre (Roman, Jitaru, and Barbante, 2014). In recent years, many scientists around the world have sought to benefit from the redox properties of natural and synthetic selenium-containing compounds to use them against a wide variety of diseases including cancer (Shiah et al., 2007; Yang et al., 2011; Hatfield et al., 2014; Vinceti et al., 2014; Fan et al., 2017; Luo et al., 2017; Behroozi et al., 2018; He et al., 2018; Arsenyan et al., 2019; Soares et al., 2019). Among these compounds, various derivatives of selenocysteine, selenides, diselenides and selenophene have been studied, but, unfortunately, with little success. The most studied selenium drug candidate so far is ebselen, which is thought to have several molecular targets due to its abnormal electrophilic properties. The Se–N bond in the ebselen molecule is readily cleaved by thiols to produce the corresponding selenyl sulfides, therefore, it is a potent modulator of proteins that require cysteine for normal function, e.g. lipoxygenases, lactate dehydrogenase, NADPH oxidases, zinc finger containing proteins and others. (Azad and Tomar, 2014) Also, at high concentrations (40 μM), ebselen induces ROS production, DNA damage and apoptosis in a myeloma model (Zhang et al., 2014; Chuai et al., 2021).

A fundamental tool for the evaluation of the electrophilic and nucleophilic properties of selenium is ^{77}Se NMR. Chemical shifts of selenium in compounds with more pronounced nucleophilic properties are located in the high field, while electrophiles exhibit peaks in the low field (Figure 1.1). For instance, naturally occurring aliphatic selenides are apparent nucleophiles, and their selenium shifts are in 100–300 ppm region, e.g., methyl selenocysteine has a signal at 32.0 ppm. Diselenides can act as a nucleophile or an electrophile due to the nonpolar covalent Se–Se bond, and their signals in ^{77}Se NMR spectrum usually occur at 500–300 ppm. Meanwhile, selenium signals of selenophenes are downshifted (600–400 ppm). (Potapov, 2013) For the above-mentioned ebselen, the chemical shift of selenium is observed at 959 ppm, (Roy and Mugesh, 2005) confirming the non-natural electrophilic properties of selenium. It was hypothesised that increasing the electrophilicity of selenium would make a molecule more redox active and, consequently, promote ROS production even more.

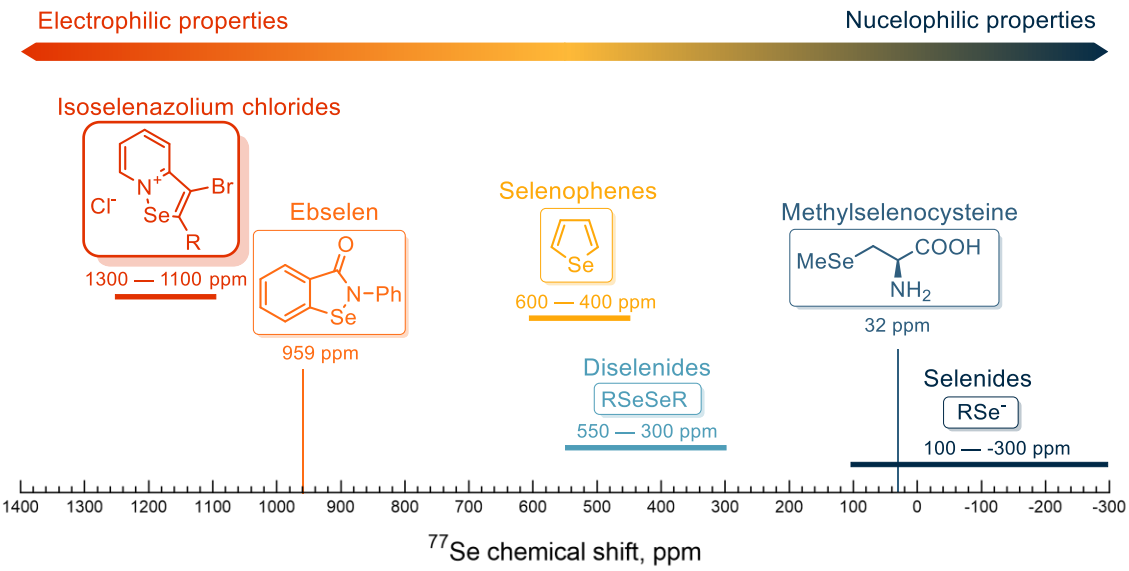

Figure 1.1 **Chemical shifts of selenium in ^{77}Se NMR spectra in different types of compounds**

Recently, a method was developed for the preparation of fused isoselenazolium salts, new heterocyclic system with a Se–N^+ bond (Arsenyan et al., 2015). These compounds have more electrophilic selenium in their structure (1300–1100 ppm in ^{77}Se NMR), and exhibit GPx-like properties similar to those of ebselen, but with a different molecular mechanism (Figure 1.2).

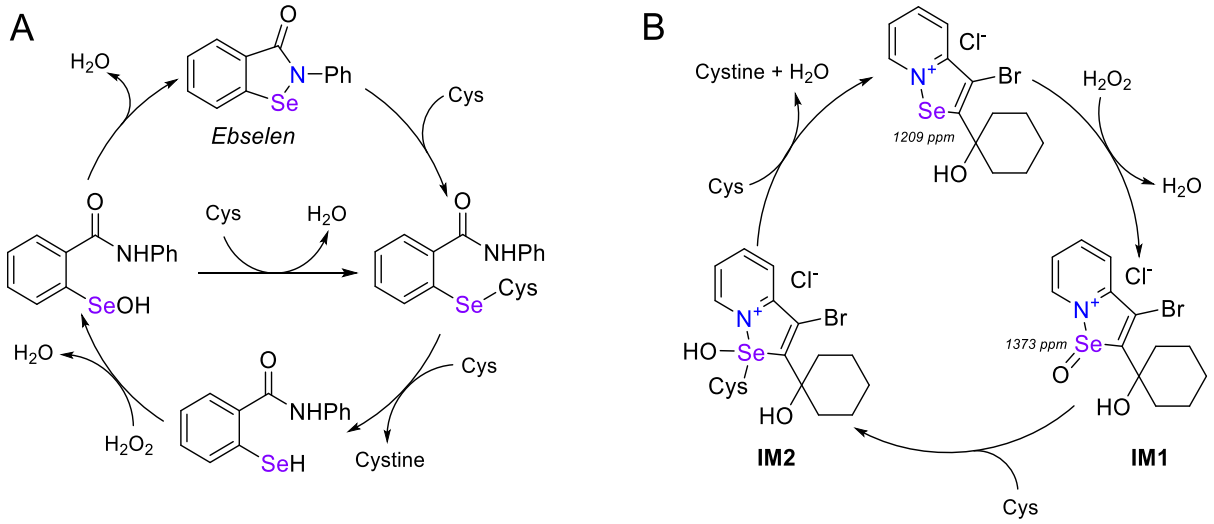

Figure 1.2 **GPx-like mechanisms of A) ebselen; B) isoselenazolium chloride**

Unlike ebselen, the isoselenazolium ring does not open during the oxidation step, as confirmed by ^{1}H, ^{13}C and ^{77}Se NMR data. In the case of isoselenazolium, selenium is oxidised to selenoxide intermediate (IM1), which is accompanied by a downshift of about 160 ppm of the signal in the ^{77}Se spectrum. Exactly this highly reactive compound interacts with L-cysteine (Cys) to form the Cys-Se-OH adduct (IM2). The other cysteine molecule then reduces IM2 and regenerates the parent isoselenazolium salt.

Furthermore, isoselenazolium salts can act as catalysts for the oxidation of aminophenol, Trolox-C and even anthracene by H_2O_2 under mild conditions (Arsenyan and Vasiljeva, 2017). Considering the redox properties of isoselenazolium salts, these compounds can potentially exhibit antiproliferative properties, however, the exact molecular mechanism of action has not been proposed yet.

Revealing the specific molecular target and the mechanism of action (MoA) is of paramount importance for hit-to-lead optimisation. Furthermore, it is impossible to register a new drug in the European Union without a clearly defined MoA, as the European Medicines Agency requires the submission of the MoA in a marketing authorisation application. From an academic point of view, even if a new drug candidate fails to show any efficacy in clinical trials, the MoA should still be pursued in order to broaden the fundamental knowledge.

If there is no preconceived idea of the MoA, the effects of the new agents should first be explored *in vitro*. Observed effects would allow a target list to be narrowed down for a phenotypic screening approach for molecular target identification. (Swinney and Anthony, 2011) As selenium-containing compounds are known for their effects on metabolism and redox systems (Chuai et al., 2021), this is a reasonable starting point for research.

1.2 General metabolic alterations in cancer

Metabolic alterations in cancer cells were first discovered almost a century ago, and their study has emerged as a separate field of research in cancer biology (Warburg, Wind, and Negelein, 1927; Upadhyay et al., 2013). To meet the high demand for proliferation precursors and ATP, tumour cells undergo a coordinated reprogramming of metabolic pathways that control glycolysis, oxidative phosphorylation (OXPHOS), the synthesis of amino acids, nucleotides and lipids, the pentose phosphate pathway (PPP), the tricarboxylic acid cycle (TCA), β-oxidation and glutaminolysis. Another stimulus for the rewiring of the metabolic pathways is the hypoxic and acidic conditions of the tumour environment that require constant adaptation for the survival of the malignant cells (Torresano et al., 2020).

Cancer cells exhibit a high rate of anabolic metabolism and take up increased amounts of glucose and glutamine to use these nutrients to fuel the TCA cycle and OXPHOS, as well as the PPP for the synthesis of nucleotides, amino acids and lipids. Together, these pathways generate sufficient levels of cellular components (both building blocks and ATP) to support cell proliferation. Malignant cells can also take up lactate and free fatty acids, predominantly released by surrounding catabolic cells, which can be used to replenish TCA cycle intermediates and to drive the OXPHOS. Increased generation of ROS in cancer cells requires the production

of appropriate levels of antioxidants, including the reduced form of glutathione, which is generated by glutathione reductase using NADPH derived from the PPP (Figure 1.3) (Martinez-Outschoorn et al., 2017).

Probably the greatest progress in our understanding of the metabolic reprogramming has been made in the area of glucose metabolism and how tumour cells adapt to shift the flux of glycolytic metabolites into pathways branching from glycolysis to yield essential biosynthetic intermediates that fuel tumour progression. This knowledge has enabled the identification of key characteristics and vulnerabilities to exploit for potential therapeutic intervention.

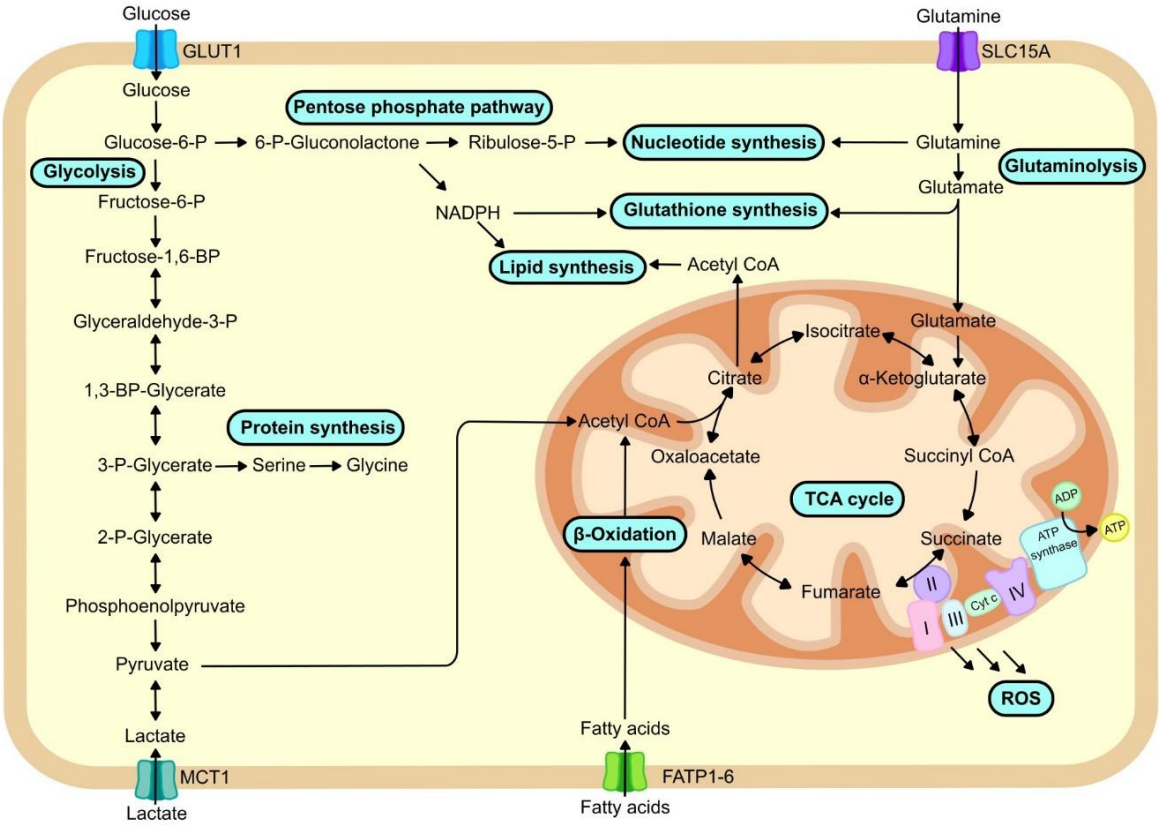

Figure 1.3 **Schematic representation of metabolic reprogramming of cancer cells***

*ADP – adenosine triphosphate, ATP – adenosine triphosphate; CoA – coenzyme A; GLUT1 – glucose transporter 1; MCT1 – monocarboxylate transporter 1; NADH – reduced nicotinamide adenine dinucleotide; NADPH – reduced nicotinamide adenine dinucleotide phosphate; SLC1A5 – solute carrier family 1 member 5A, cyt c – cytochrome c, FATP1-6 – fatty acid transport protein 1-6, ROS – reactive oxygen species.

1.3 Anticancer therapies targeting glycolysis

The dependence of cancer cells on aerobic glycolysis provides a novel perspective and insight for cancer treatment. Since glucose metabolism is a multistep process, it can be inhibited at different levels. Numerous enzymes involved in glucose metabolism have been explored as

potential molecular targets, and new inhibitors are constantly being discovered and developed as anticancer drugs.

The first rate-limiting step in glucose metabolism is its transport through the plasma membrane, which is mediated by glucose transporter (GLUT) proteins. In most cancers under hypoxic conditions hypoxia-inducible factor 1-alpha (HIF-1α) and serine-threonine protein kinases (Akt family proteins) upregulate the GLUT1 subtype, which increases glucose uptake. Many small molecule inhibitors of GLUT1 have been discovered and have shown promising results in preclinical studies; however, GLUT1 is also a prevalent glucose transporter in normal cells, which likely impeded clinical success (Zhang et al., 2022). For example, silibinin, a GLUT1 inhibitor, did not show any efficacy in patients with prostate cancer and hepatocellular patients in two separate phase I clinical trials (Flaig et al., 2010; Siegel et al., 2014).

After entering the cell, glucose is phosphorylated to glucose-6-phosphate (G6P) by hexokinase (HK). There are four mammalian HKs (HK1–4), and tumour cells predominantly express HK2. Two HK2 inhibitors, 2-deoxyglucose and lonidamine, have reached clinical trials, but both of these agents had considerable systemic toxicity and did not show any therapeutic benefit. These failures may arise due to insufficient selectivity for HK2 and/or expression of HK2 in muscle and adipose tissues (Martinez-Outschoorn et al., 2017).

Thus, despite differences in the regulation of glycolysis in cancer cells, certain cancer-characteristic isoforms of enzymes are substantially expressed in normal cells, and their inhibition leads to systemic side effects. However, there is a reaction further downstream that is catalysed by an enzyme that has a more tumour-specific isoform, and that is the conversion of phosphoenolpyruvate to pyruvate by pyruvate kinases.

1.4 Targeting pyruvate kinase M2 for anticancer therapy

Pyruvate kinase (PK) catalyses the final reaction of glycolysis, in which the phosphate group is transferred from phosphoenolpyruvate (PEP) to ADP to form pyruvate, with the production of ATP. There are four types of mammalian PK: PKL, PKR, PKM1, and PKM2, all of which are tissue specific. PKL is expressed in the liver, kidney, and intestine, PKR is expressed in red blood cells, while PKM1 is the most common isoform found in most healthy tissues. Notably, PKM2 is expressed in highly proliferating cells, but especially in tumour and embryonic tissues. As embryogenesis progresses, the PKM2 is replaced by tissue-specific PKM1, PKL, or PKR (Zahra et al., 2020). It has been shown that expression of PKM2 is

upregulated in breast, ovarian, bladder, and non-small-cell lung cancers and is associated with a poor prognosis (Huang et al., 2018).

The last reaction of glycolysis is a crucial point where the flux of glucose-derived carbons is determined, either towards the tricarboxylic acid cycle in mitochondria for ATP production and lactate production by lactate dehydrogenase for the cytosolic oxidation of NADH or pentose phosphate pathway and serine biosynthesis for nucleotide and fatty acid production (Li et al., 2019). PKM2 can be switched between a highly enzymatically active tetramer and a relatively inactive dimer by allosteric activators and inhibitors to adapt to varying environmental conditions (Gui, Lewis, and Vander Heiden, 2013). Moreover, PKM2 is also involved in the regulation of mitochondrial respiration, mitochondrial-dependent apoptosis, and reduces oxidative damage to mitochondria (Gao et al., 2022).

Under hypoxic conditions or upon stimulation, for example, after activation of the epidermal growth factor receptor, the dimeric form of PKM2 can translocate into the nucleus where it acts as a regulator for transcription factors such as HIF-1α and β-catenin, that are essential for tumourigenesis and provoke further cancer-specific metabolic reprogramming (Yang et al., 2011; Azoitei et al., 2016). Additionally, once in the nucleus, PKM2 functions as a protein kinase and phosphorylates signal transducer and activator of transcription 3 (STAT3), histone H3, and the mitotic spindle checkpoint protein Bub3, that promote proliferation and survival of cancer cells (Li et al., 2015; Zhu et al., 2021). As an essential metabolic regulatory node and transcriptional coactivator that is characteristic of cancer cells, PKM2 opens a perfect opportunity for therapeutic intervention.

To date, a few classes of natural and synthetic PKM2 inhibitors have been described, including the amino acids alanine, phenylalanine and tryptophan (Rathod et al., 2021) and flavonoids such as apigenin (Aslan and Adem, 2015); however, the most studied PKM2 inhibitors are naphthoquinones shikonin and its second-generation analogue, compound 3k. Nevertheless, their inhibitory activity is relatively low (*in vitro* $IC_{50} = 8.82 \pm 2.62$ μM and 2.95 ± 0.53 μM for shikonin and 3k, respectively), and the mechanism of inhibition remains to be elucidated (Ning et al., 2018; Arora et al., 2022). Therefore, it is not certain that the antiproliferative effects of shikonin and its derivatives are solely due to PKM2 inhibition, especially considering the pleiotropic effects of this class of compounds (Wiench et al., 2012; Guo et al., 2019).

1.5 Targeting cellular redox circuits

Oncogenic activations and metabolic reprogramming in cancer cells lead to the accumulation of ROS. ROS are intracellular oxygen species, including $O_2^{\bullet-}$, H_2O_2, and $OH^{\cdot}$. The increase in ROS contributes to the activation of signalling pathways associated with tumourigenesis, such as phosphoinositide 3-kinase (PI3K), mitogen-activated protein kinase (MAPK), and HIF-1α. However, ROS levels are strictly controlled because an appropriate balance signal transmission must be maintained while cell damage avoided.

Mitochondria are a major source of ROS, as oxygen radicals and H_2O_2 are produced along the electron transfer system (ETS) and also by the reverse electron transport. There are two mechanisms of increase in ROS production mediated by oncoproteins: (I) intense fuelling of the TCA cycle and development of mitochondrial mass; (II) destabilisation of the ETS used by KRAS, MYC, PI3K-AKT-mTOR, and BCR/ABL (Sainero-Alcolado et al., 2022). Increased mitochondrial ROS production leads to mtDNA damage and peroxidation of the mitochondria-specific lipid – cardiolipin. Both of these events trigger an apoptotic response and lead to cell death. This vulnerability has already been exploited by several chemotherapeutic drugs, such as paclitaxel, vincristine, doxorubicin, cisplatin, 5-fluorouracil, and bleomycin, which exhibit anticancer properties partially due to elevated ROS levels (Wang et al., 2019).

In particular, ROS has been shown to directly oxidise the active cysteine residues of several metabolic enzymes, including PKM2 (Wang et al., 2019). PKM2 has three oxidation-sensitive cysteines (Cys358, Cys423 and Cys424) and their oxidation attenuates PKM2 activity, leading to the diversion of glucose flux into the PPP for ROS detoxification and survival of cancer cells (Irokawa et al., 2021). Furthermore, it has been reported that, after oxidative stress, PKM2 phosphorylates B-cell lymphoma 2 protein (Bcl-2) and prevents its ligase-mediated degradation, thus enhancing tumour cell apoptosis resistance (Liang et al., 2017). Therefore, metabolic reprogramming and cellular redox circuits in cancer cells are tightly interconnected and their elements should be studied together for the investigation of isoselenazolium salts MoA, considering their high oxidative capacity.

2 Materials and methods

2.1 Chemistry

2.1.1 General information

Unless otherwise stated, all reagents were purchased from commercial suppliers and used without further purification. Thin layer chromatography (TLC) was performed using MERCK Silica gel 60 F254 plates and visualised by UV (254 nm) fluorescence. ZEOCHEM silica gel (ZEOprep 60/35–70 microns – SI23501) and aluminium oxide, neutral (Brockmann I, for chromatography, 50–200 μm, 60Å) were used for column chromatography. ^{1}H spectra were recorded on Bruker 300 or Bruker 400 spectrometer at 400 MHz, ^{13}C spectra were recorded on a Bruker 400 spectrometer at 101.3 MHz at 298 K in $CDCl_3$, CD_3OD or CD_3CN. The ^{1}H chemical shifts are given relatively to residual $CHCl_3$ signal (7.26 ppm), CD_3OD (3.31 ppm) or CD_3CN (2.13 ppm), ^{13}C – relatively to $CDCl_3$ (77.16 ppm), CD_3OD (49.0 ppm) or CD_3CN (118.3 ppm). The melting points were determined on "Optimelt", and the results are given without correction. Single crystals were investigated on a Rigaku XtaLAB Synergy, Dualflex, HyPix diffractometer. Compounds **1–7** (Arsenyan et al., 2015), **13** (Grimm et al., 2015), TTAPE-Me (Elmer-Dixon et al., 2019), nonyltriphenylphosphonium bromide (Mostyn et al., 2017) as well as MitoQ (Duveau et al., 2010) were prepared according to the literature procedures.

2.1.2 General procedure for the synthesis of 8–12

Acridine orange was dissolved in hot 1,2-dichlorobenzene followed by the addition of Na_2CO_3 (2 equiv.) and alkyl halide in excess (5 equiv.). The reaction mixture was stirred at 170 °C for 10–40 min and the conversion was assessed by LC-MS every 10 minutes. After the consumption of the starting materials, the reaction mixture was cooled, filtered through a neutral Al_2O_3 pad and washed with DCM, DCM/EtOAc (50:50) and DCM/iPrOH (98:2) mixtures. The last fractions were collected and evaporated. Compounds **8**, **9** and **11** did not require further purification, but compounds **10** and **12** were additionally purified by column chromatography on neutral Al_2O_3 (eluent: DCM/iPrOH 98:2, with a few drops of Et_3N per 100 ml).

2.1.3 General procedure for the synthesis of 14–17

13, $Pd(OAc)_2$ (0.25 equiv.), BINAP (0.3 equiv.), and Cs_2CO_3 (4 equiv.) were added to a vial, dissolved in xylene, sealed, and flushed with argon for 10 min. Then a corresponding cyclic amine (3 equiv.) was added, and the reaction was allowed to stir at 100 °C for 16 h. After that, the reaction mixture was cooled down to room temperature, diluted with DCM and filtered through Al_2O_3 pad. Then, the crude was converted to hydrochloride by evaporating with HCl in methanol. After evaporation, the residue was purified by flash chromatography and the fractions containing a desired product were combined. After that, pH of the aqueous solution was increased to pH=11, followed by extraction with DCM. The organic layer was washed with water and dried over sodium sulphate. The residual solvent was removed by rotary evaporation to yield compounds **14–17**.

2.1.4 General procedure for the synthesis of 18–25

To a preheated suspension of **14–17** in dichlorobenzene at 170 °C (toluene at 110 °C for the synthesis of **18** and **19**) Na_2CO_3 (2 equiv.) was added followed by the addition of a corresponding alkyl halide (5 equiv.). The resulting mixture was stirred at 170 °C for 10–45 min, and the conversion was assessed by LC-MS every 10 min. After the consumption of the starting materials, the reaction mixture was cooled down to room temperature, filtered through an aluminium oxide pad and washed with DCM, EtOAc, and DCM/EtOH (10:1).

2.1.5 General procedure for the synthesis of 27a–k

Copper(I) iodide (0.05 equiv.), $(Ph_3P)_2PdCl_2$ (0.05 equiv.) and α-bromopyridine **26a–k** (1 equiv.) were dissolved in DMF (10 ml for 5 mmol of a bromopyridine) and dry diisopropylamine (4 ml for 5 mmol of a bromopyridine) and flushed with Ar for 10 min. Then, a solution of terminal acetylene (1.4 equiv.) in DMF (5 ml for 6.5 mmol of terminal acetylene) was added in one portion. The reaction mixture was flushed with Ar for additional 10 min and stirred at 50 or 80 °C for 2–5 h. Then, the reaction mixture was cooled, 250 ml of EtOAc was added, and precipitates were filtered off. The organic layer was washed with a 1 % aqueous solution of ammonia (2 × 100 ml), followed by washing with saturated NH_4Cl solution and NaCl solution (both 2 × 100 ml). The organic layer was collected, dried over Na_2SO_4, filtered, and evaporated under reduced pressure.

2.1.6 General procedure for the synthesis of 28a–d

27a–d was dissolved in MeOH and treated with a NaOH (5 equiv.) water solution and stirred at room temperature overnight. The reaction mixture was acidified by 2N HCl at pH 2 and extracted with EtOAc (3 × 50 ml). The organic layers were combined, dried over Na_2SO_4, filtered, and evaporated under reduced pressure to yield pure **28a–d**.

2.1.7 General procedure for the synthesis of 29a–g

5 ml of saturated NH_3 solution in MeOH were added to the solution of ester **27a–g** (1 mmol) in MeOH and stirred at room temperature overnight. The reaction was monitored by LC-MS, and after full conversion, the solvent was removed under reduced pressure. The residue was dissolved several times in MeOH and evaporated under reduced pressure to remove excess of NH_3.

2.1.8 General procedure for the synthesis of 30–32

To a solution of SeO_2 (4 equiv.) in 48 % HBr (16 equiv.), **27**, **28**, or **29** (1 equiv.) in 1,4-dioxane (5 ml for 1 equiv. of **27**, **28**, or **29**) was added and the mixture was stirred at room temperature overnight. After consumption of a substrate (LC-MS), diethyl ether (50 ml) was added and the precipitates were filtered off, dissolved in the mixture of EtOH/water (1:1), eluted through ion exchange resins (IRA-401) pretreated with hydrochloric acid, and evaporated under reduced pressure.

2.2 Cell cultures

MCF-7 (human breast adenocarcinoma, estrogen-positive, ATCC® HTB-22™), 4T1 (mouse mammary carcinoma, ATCC® CRL-2539™), PANC-1 (human pancreatic carcinoma, ATCC® CRL-1469™), MDA-MB-231 (human breast adenocarcinoma, ATCC® HTB-26™), MIA PaCa-2 (human pancreatic carcinoma, ATCC® CRL-1420™), H9C2 (rat cardiomyoblasts, ATCC® CRL-1446™), CHO-K1 (Chinese hamster ovary cells, ATCC® CCL-61™), HT-1080 (human fibrosarcoma, ATCC® CCL-121™), Jurkat (human T cell leukemia, ATCC® TIB-152™), CT26.WT (mouse colon carcinoma, ATCC® CRL-2638™), A2058 (human melanoma, ATCC® CRL-11147™), HCC1937 (human breast carcinoma ATCC® CRL-2336™), NIH/3T3 (mouse embryo fibroblasts, ATCC® CRL-1658™), HEKa (primary human epidermal keratinocytes), MDCK (Madin-Darby Canine Kidney) and A7r5 (rat vascular smooth muscle cells) cell lines were obtained from American Type Culture

Collection (ATCC, Manassas, VA, USA). A suspension of red blood cells: Single Donor Human Red Blood Cells – Washed (Catalogue No.: IPLA-WB3) was obtained from Innovative research™. MCF-7, PANC-1, MDA-MB-231, MIA PaCa-2, H9C2, NIH/3T3, 4T1, HT-1080 cells were cultured in medium containing Dulbecco's Modified Eagle's Medium (DMEM) with 10 % fetal bovine serum. CHO-K1 cells were cultured in medium containing F-12K Medium with 10 % fetal bovine serum. CT26, WT and Jurkat cells were cultured in RPMI-1640 medium with 10 % fetal bovine serum. The cells were cultivated at 37°C and 5 % CO_2.

2.3 Cytotoxicity assay

Cell viability was assessed by the addition of 3-(4.5-dimethylthiazol-2-yl)-2.5-diphenyltetrazolinium bromide (MTT). Briefly, cells were seeded (5×10^3 cells per well) in 96-well plates and allowed to attach for 24 h. The solutions of the test compounds were prepared and serially diluted to obtain the appropriate concentrations. Cells were treated with test compounds at different concentrations (0.041-100 μM) and incubated for 48 h at 37 °C and 5 % CO_2. The culture medium was removed, and the medium containing 1 mg/ml of MTT was added. After 1 h (37 °C, 5 % CO_2), the MTT-containing medium was removed, and 100 μL of isopropanol was immediately added to each sample. The optical density was assessed at 570/650 nm (Hidex Sense microplate reader, Hidex Finland). Jurkat cells were seeded at a density of 10×10^3 cells per well and treated with the test compounds 2 h after seeding. To assess cell viability, Jurkat cells were further incubated with alamarBlue® (Bio-Rad Laboratories, Hercules, California, USA). After 2h, fluorescence (Ex 544 nm/Em 590 nm) was measured using Hidex Sense microplate reader (Hidex, Finland). The half-maximal inhibitory concentration (IC_{50}) of each compound was calculated using GraphPad Prism® 8.0 (GraphPad, Inc., La Jolla, USA).

2.4 High-resolution fluorespirometry

High-resolution fluorespirometry was performed using an Oxygraph-2k system (OROBOROS INSTRUMENTS, Austria). All experiments were carried out at 37 °C in MiR05 medium (110 mM sucrose, 60 mM K-lactobionate, 0.5 mM EGTA, 3 mM $MgCl_2$, 20 mM taurine, 10 mM KH_2PO_4, 20 mM HEPES, pH 7.1 at 30 °C, and 0.1 % BSA (essentially fatty acid free). The medium was reoxygenated when the oxygen concentration dropped to 80 μM. The H_2O_2 flux was measured simultaneously with respirometry in the O2k fluorometer using the H_2O_2-sensitive probe Amplex Red (AmR) as described. (Makrecka-Kuka, Krumschnabel, and Gnaiger, 2015) The H_2O_2/O flux ratio [%] was calculated as the H_2O_2flux/(0.5 O_2 flux).

In permeabilised 4T1 cells, pyruvate + malate (5 and 2 mM) or glutamate + malate (10 and 2 mM) were used to determine complex I (CI)-linked LEAK (L) respiration. ADP was added to a concentration of 5 mM to determine oxidative phosphorylation-dependent respiration (OXPHOS state). Succinate (10 mM, complex II (CII) substrate) was then added to reconstitute convergent CI&II-linked respiration. Rotenone (0.5 μM, an inhibitor of CI) and antimycin A (2.5 μM, an inhibitor of complex III) were added to determine the CII-linked OXPHOS capacity and residual oxygen consumption, respectively. Compound **6** was added to the permeabilised cells after the addition of the respective substrates in the OXPHOS state (titration experiment) or in the LEAK state. Additionally, compounds **3**, **6** and **7** were tested at 1 μM in the OXPHOS coupling protocol in the LEAK state. Compound **30c** (1 μM) was added to permeabilised cells in the LEAK state after the addition of pyruvate and malate. Flux control factors and OXPHOS coupling efficiency were calculated as described by Gnaiger. (Gnaiger, 2020)

2.5 Measurement of NMN, NAD^+ and NADH levels

For fluorometric measurements of NMN, a previously described method was used, with minor modifications (Formentini, Moroni, and Chiarugi, 2009). Briefly, MCF-7 cells (1×10^5 cells per well) were seeded in a 24-well plate. After 24 h, cells were treated with 3 selected compounds (2 μM) for 10 min. Cells were washed with PBS and then lysed by adding 200 μl of 1 M $HClO_4$ to each well and incubating at 4 °C for 20 min. The cells were harvested by scraping and transferred to a tube. The extracts were neutralised with 100 μl of 2 M KOH for 5 min at room temperature and 50 μl of 0.1 M bicine (pH 7.4) was added. The samples were centrifuged at 14 000 × g for 10 min at 4 °C, and the supernatant was collected for further analysis. The protein concentration in each sample was determined using a Bio-Rad protein assay kit. Twenty-five microliters of sample or standard solution (0.3 to 20 μM NMN) was transferred into a flat-bottom 96-well black plate and mixed with 10 μl of 2 M KOH and 10 μl of ice-cold 20 % acetophenone. The reaction mixture was incubated for 2 min at 4 °C, after which 45 μl of 88 % formic acid was added and the samples were incubated for another 10 min at 37 °C on a shaker. The fluorescence was measured using a Tecan multiplate reader Infinite M1000 (Tecan Trading AG, Switzerland) with excitation at 382 nm and emissionat 420 nm.

The concentrations of NAD^+ and NADH, as well as their ratio in MCF-7 cells exposed to compounds **3**, **6**, **7** (2 μM) for 10 min, were measured using an NAD^+/NADH assay kit (Abcam, ab65348) according to the manufacturer's instructions. Analogous measurement was done with 4T1 and H9C2 cells exposed to compound **30c** (1 μM).

2.6 PARP1 activity assay

PARP1 activity was evaluated using PARP1 chemiluminescent assay kit (BPS Bioscience, cat. # 80551) according to the manufacturer`s instructions.

2.7 Liposomes preparation

Cardiolipin (CL) containing liposomes for CL binding studies were prepared by thin film method. Briefly, desired volumes of stock solutions of 1,2-dioleoyl-*sn*-glycero-3-phosphocholine (DOPC, 25 mg/ml solution in $CHCl_3$, Avanti Polar Lipids) and bovine heart CL (5 mg/ml solution in EtOH, Sigma Aldrich) were completely evaporated under reduced pressure, and the resulted lipid film was resuspended in HEPES buffer (20 mM, pH 7.4) to acquire 100:300 μM CL/DOPC. Obtained large multilamellar liposomes were sonicated in a bath-type sonicator (Cole Parmer Ultrasonic Cleaner 8891CPX, USA) at room temperature for 30 min followed by extrusion (LiposoFast-Basic, Avestin) through a 100 nm polycarbonate filter (Nucleopore Corp., CA) for 21 times. The quality of the resulting small unilamellar vesicles was checked by dynamic light scattering technique (Zetasizer Nano ZSP, Malvern Panalytical Ltd., UK). All of the liposomes samples were freshly prepared before use. Liposomes containing other phospholipids – L-α-phosphatidylethanolamine, PE, (Heart, Bovine), L-α-phosphatidylinositol, PI (Liver, Bovine), L-α-phosphatidic acid, PA (Egg, Chicken), L-α-phosphatidylserine, PS (Brain, Porcine), were prepared in the same way and composition, e.g. 100:300 μM PS/DOPC liposomes. In the phospholipid binding assay the concentration of DOPC was 400 μM when DOPC was used alone. Liposomes for modelling of the inner mitochondrial membrane were made from PI, 10 %, CL, 25 %, PE, 30 %, and DOPC 35 % with the total lipid concentration of 400 μM.

Cardiolipin (CL) liposomes for NMR analysis were prepared in the same manner, but more concentrated (total lipid concentration was 2 mM) and the obtained dry lipid films were rehydrated in D18 HEPES buffer (20 mM, pH 7.4, 10 % D_2O).

2.8 Study of interaction with cardiolipin liposomes using NMR

To study the interactions of compound **6** with CL and DOPC liposomes, a stock solution of **6** (2 mM) in D18 HEPES buffer (20 mM, pH 7.4, 10 % D_2O) was added to CL/DOPC or DOPC liposome dispersions to reach 400:1200:400 μM CL/DOPC/**6** solution or 1600:400 μM DOPC/**6** solution followed by gentle vortexing for 30 s. NMR spectra were acquired on a 600-MHz Bruker Avance NEO spectrometer equipped with a 5 mm QCI-F quadruple resonance pulsed-field-gradient cryoprobe. The temperature was calibrated against methanol and set to 25 °C. Chemical shifts were referenced to the water resonance at 4.77 ppm with respect to 4,4-dimethyl- 4-silapentane-1-sulfonic acid. The samples contained 0.8 mM **6** in 90 % H_2O and 10 % D_2O with and without DOPC or CL/DOPC liposomes. The NMR data were processed and analysed using MestReNova software.

2.9 Study of interaction with cardiolipin liposomes using isothermal titration calorimetry

The experiments were carried out using an isothermal titration calorimeter (MicroCal iTC200, Malvern Panalytical Ltd., UK). To carry out the titration, the injection syringe was filled with a solution of compound **6** (100 μM), and the reaction cell was filled with liposome dispersion (200 μM of total lipid). The experiments were performed at 25 °C with a stirring speed of 750 rpm. The titration was conducted with 30 1-μl injections with 180 s intervals between injections to ensure complete equilibration. The data consisted of a series of heat flows as a function of time, which were collected automatically and analysed by Origin 7 software (OriginLab Corporation, Northampton, USA). The changes in enthalpy (ΔH) due to the interactions between **6** and the liposome dispersions were recorded, and then stoichiometry (N), the association constant (K_A), the dissociation constant (K_D), entropy (ΔS) and the Gibbs free energy (ΔG) were calculated. The obtained sigmoidal titration curves were evaluated assuming independent saturable binding sites in the outer vesicle interface. The integration of the enthalpograms was carried out using the one-site binding model (1:1).

2.10 Solubility and stability studies

Stock solutions (50 mg/ml) of NAO (**9**), **12** and **20** were prepared in DMSO and sonicated for 10 in in the ultrasonic bath until full dissolution. Supersaturated solution in buffer was prepared by adding 8 μL of DMSO solution to 1.492 mL of 20 mM HEPES, pH 7.4 (0.5 % DMSO in the final solution) and rigorously stirred for 15 min. After that, the solution was filtered through 0.22 μm filter and aliquot was taken for LC-MS analysis. Concentration

of a respective dye was calculated by comparing peak area with the standard solution in DMSO (λ = 271 nm). After 5 and 24 h the solution was filtered again and analysed in the same manner.

2.11 Luminescence measurements

The luminescence data were collected with a FS5 spectrofluorometer (Edinburgh Instruments Ltd, UK); photoluminescence quantum yield (Φ) was measured using an integrating sphere under an ambient atmosphere. UV-Vis spectra of acridinium salts **2**–**6** were measured in 20 mM HEPES buffer solutions, pH 7.4 at room temperature in an ambient atmosphere at a concentration of 10 μM.

2.12 Binding of acridinium probes to cardiolipin and other phospholipids

To determine the binding ratio of **9**, **12** or **20** with CL, 16 μM probe`s solution in 20 mM HEPES buffer (pH = 7.4) was titrated in a 96-well plate, with increasing concentration of CL/DOPC liposomes and incubated for 15 min at 37 °C. Subsequently, the fluorescence intensity was measured at 529 nm (λ_{exc} = 497 nm) and the saturation ratio was taken at the intersection of 2 best-fit lines. The experiments were carried out in triplicate. Similar experiments were conducted for the assessment of the probes binding with other phospholipids. Relative affinity for a lipid was evaluated by the decrease in fluorescence intensity compared to the intensity of the probe in the absence of liposomes.

2.13 Mitochondria visualisation by confocal microscopy

A2058 cells (1×10^5 cells/mL) were seeded in Ibidi μ-slide 8 wells and cultured overnight at 37 °C and 5 % CO_2 in 250 μL of DMEM medium supplemented with 10 % fetal bovine serum. Live cell mitochondria staining was done with **20** and MitoTracker deep red at final concentrations of 100 nM and 200 nM, respectively. The cells were incubated under normal culture conditions for 30 min, and then visualised by Leica Stellaris 8 confocal microscope (Leica Microsystems, Wetzlar, Germany) using a Leica HC PL APO CS2 86x/1.20 W objective.

2.14 Isolation of mitochondrial and mitoplasts fractions

2.14.1 Mitochondrial fraction isolation from cell cultures

The adherent cells were allowed to grow to 80 % confluence in T75 flask (Sarstedt), then the medium was removed and washed twice with PBS. For suspension cell lines, the medium was separated from the cells in a centrifuge and then washed twice with PBS. Red blood cells were washed three times with PBS and centrifuged at 1000 × *g* for 5 min. Mitochondrial fractions were isolated as described elsewhere. In summary, cells were scraped off the plate and transferred to a tube. Cells were collected by centrifugation at 370 × *g* for 10 min. The supernatant was decanted, and cells were resuspended in buffer consisting of 1 mM Tris, pH 7.4, 130 mM NaCl, 5 mM KCl, 7.5 mM $MgCl_2$ and washed twice. After that, cells were resuspended in homogenisation buffer: 10 mM Tris-HCl, pH 6.7, 10 mM KCl, 0.15 = mM $MgCl_2$, incubated for 10 min and homogenised using a homogeniser (LabGEN 7, Cole-Parmer). The homogenate was transferred to a centrifuge tube containing 2 M sucrose solution and gently mixed. Unbroken cells, nuclei, and large debris were pelleted at 1200 × *g* for 5 min at 4 °C, after that supernatant was separated and centrifuged at 7000 × *g* for 10 min at 4 °C. The mitochondrial pellet was washed once (10 min at 7000 × *g*) and resuspended in buffer containing 10 mM KCl and 10 mM Tris, pH 6.7. The protein concentration was measured by the bicinchoninic acid method using BSA as the standard, and the mitochondria were frozen at −20 °C and stored until analysis.

2.14.2 Mitochondrial fraction isolation from tissues

Cardiac, kidney and brain tissue samples from healthy C57Bl/6J mice were homogenised on ice in 1:10 (w/v) medium containing 180 mM KCl, 10 mM Tris/HCl and 1 mM EGTA (pH 7.7 at 4 °C) using a Teflon glass homogeniser. The homogenate was centrifuged at 750 × g for 5 min at 4 °C, after that supernatant was separated and centrifuged at 6800 × g for 10 min at 4 °C. The mitochondrial pellet was washed once (10 min at 6800 × g) and resuspended in buffer containing 10 mM KCl and 10 mM Tris/HCl (pH 6.7 at 4 °C). Mitochondria were used immediately after isolation or were frozen at −20 °C and stored until analysis. Protein concentration was measured by the Lowry method using BSA as the standard.

2.14.3 Mitoplasts isolation from rat tissue

Cardiac or liver tissue from healthy Sprague-Dawley rats was homogenised on ice in 1:10 (w/v) medium containing 180 mM KCl, 10 mM Tris/HCl and 1 mM EGTA (pH 7.7 at 4 °C) using Teflon glass homogeniser. Mitochondria were isolated as described above, then the outer membranes of fresh mitochondria were removed by 20 min incubation on ice in hypotonic solution (5 mM sucrose, 5 mM HEPES, 1 mM EGTA, pH 7.2, v/v 1:4). To remove electrostatically bound cytochrome c, a 1 M KCl solution was added (the final concentration of KCl was 300 mM) and the mixture was centrifuged for 30 min at 14500 × g at 4 °C. The supernatant was discarded, and the pellet was washed with 300 mM KCl and centrifuged twice. The final pellet was redissolved in the buffer containing 20 mM HEPES, pH 6.8, centrifuged again for 5 min at 14500 × g at 4 °C to completely remove excess of KCl, then resuspended in 20 mM HEPES buffer, pH 6.8 and stored at −20 °C until analysis.

2.15 Cardiolipin quantitative analysis

A 10 mM stock solution of **20** in ethanol was made and diluted to 40 μM with buffer containing 10 mM KCl and 10 mM Tris, pH 6.7. TTAPE-Me stock solution (500 μM) was prepared using buffer. Before measuring the CL concentration in the mitochondrial fraction, liposomes titration with **20** and TTAPE-Me was performed in triplicate to obtain a calibration curve. In a 96-well plate, a solution of **20** (10 μM) or TTAPE-Me (125 μM) in buffer containing 10 mM KCl and 10 mM Tris, pH 6.7, was titrated with diluted mitochondrial fraction and incubated for 15 min at 37 °C. The fluorescence intensity was measured at 529 nm (λ_{exc} = 497 nm). The CL concentration in the sample well was calculated by interpolation of the calibration curve, and the total mitochondrial CL concentration was calculated using Eq. 1:

$$C_{CL} = \frac{n \times D \times 1000}{V \times P}; nmol/mg\ prot \quad (1)$$

where:

n – the amount of CL in the sample well, nmol

D – the sample dilution factor

V – the sample volume added into the reaction well, μL

P – the mitochondrial protein concentration of the sample, mg/ml

2.16 Fluorescence-based competitive binding assay

A 10 mM stock solution of **20** in ethanol was made and diluted to 50 μM with 20 mM HEPES buffer, pH 6.8, 7.4 or 7.8. A 20 μM stock solution of CL containing lipid vesicles and a stock solution of a ligand were prepared in the same buffer. In a 96-well microplate, a solution of lipid vesicles containing CL (CL final concentration 2.5 μM) was titrated in triplicate with a ligand and gently mixed with a micropipette. Additionally, CLs containing lipid vesicles without a ligand were prepared in triplicate (vehicle). Next, a 96-well plate was incubated in a plate shaker with a thermostat for 10/30/60 min (500 rpm, 25 or 37 °C). Then an appropriate amount of **20** stock solution was added to the wells (the final concentration of **20** was 5 μM) and gently mixed with a micropipette. The 96-well plate was incubated for 15 min in a plate shaker with a thermostat (500 rpm, 37 °C), and the fluorescence intensity was measured using a Tecan Infinite M1000 microplate reader (Tecan Trading AG, Switzerland) at excitation and emission wavelengths of 497 and 529 nm, respectively. The data obtained were analysed with GraphPad Prism® 8.0 (GraphPad, Inc., La Jolla, USA). The fluorescence intensity was normalised by setting CL vesicles with **20** without a ligand (vehicle) as 0 % and the maximal effect of the ligand as 100 %. Normalised fluorescence intensity was plotted against ligand concentration on a logarithmic scale and fitted with a suitable fitting model (4PL, 5PL or biphasic) to calculate EC_{50} values. Before conducting a competitive binding experiment on isolated mitoplasts, **20** mitoplasts from each batch to determine the optimal volume of mitoplast solution to saturate a 5 μM probe solution. In other aspects, competitive binding assay was performed similarly to that in CL vesicles.

2.17 Screening on metabolic enzyme panel and Bcl family proteins

Screening was performed by BPS Bioscience (San Diego, USA) according to the standard biochemical assay procedures with relevant reference controls.

2.18 Pyruvate kinase activity assay

Pyruvate kinase (PK) activity was measured by a coupled enzyme system with lactate dehydrogenase (LDH) in which the pyruvate produced by PK was reduced to lactate with the concomitant oxidation of NADH to NAD^+. The test was conducted at room temperature in a solution containing 50 mM Tris (pH 7.4), 10 mM $MgCl_2$, 100 mM KCl, 2 mM ADP, 5 U/ml lactate dehydrogenase (LDH from rabbit muscle, Sigma-Aldrich, cat. # 427217-M), 0.4 mM NADH, 1.75 nM PK (PKM2, BPS Bioscience, cat. #50295, PKM1, BPS Bioscience, cat. #40502, PKR, BPS Bioscience, cat. #40500) and the test compounds at different concentrations

(0–10 μM). After 10 min incubation, the reaction was initiated with 1 mM PEP (the final reaction volume was 200 μl). The reaction progress was monitored by the decrease in the absorbance at 340 nm at 37 °C for 20 min (Hidex Sense microplate reader, Hidex Finland, Finland). Negative control experiments contained no PK. For additional experiments, where PKM2 activation was desired, 250 μM FBP (Sigma-Aldrich, cat. #F0752) was added. The half-maximal inhibitory concentration (IC_{50}) of each compound was calculated by plotting inhibition % against the concentration of the ligand on a logarithmic scale and fitting with a 4PL model using GraphPad Prism® 8.0 (GraphPad, Inc., La Jolla, USA).

2.19 LDH activity assay

LDH activity assay was performed in a solution containing 50 mM Tris (pH 7.4), 100 mM KCl, 10 mM $MgCl_2$, 0.5 mM NADH, 5 U/ml of LDH and 1 μM of the tested compounds. After 10 min incubation at room temperature, the reaction was initiated by the addition of pyruvate (5 mM final concentration) and the reaction progress was monitored by the decrease in the absorbance at 340 nm at 37 °C for 10 min (Hidex Sense microplate reader, Hidex Finland, Finland).

2.20 Measurement of PKM2 steady-state kinetics

Steady-state kinetic measurements of PKM2 were performed using a Hidex Sense microplate reader (Hidex Finland, Finland). Initial velocities for the forward reaction were measured using a coupled reaction with LDH as described above. First, calibration curve for NADH (0–0.5 mM) was obtained in the reaction buffer in the absence of PKM2. Initial reaction velocity versus substrate concentrations were measured by the decrease in absorbance at 340 nm at 37 °C in the absence or in the presence of **30c**, in a reaction buffer containing 50 mM Tris (pH 7.4), 10 mM $MgCl_2$, 100 mM KCl, 1.75 nM PKM2, 0.4 mM NADH, 2 mM ADP and 5 units of LDH. Reactions were initiated by adding PEP at a desired concentration (0–3 mM) in a total reaction volume of 200 μL per well. Analogues experiment was carried out with respect to ADP, when PEP concentration was kept constant (1 mM), and ADP concentration was varied from 0 to 3 mM. The experiments were carried out in triplicate. Kinetic constants were determined by fitting initial velocity curves to Michaelis-Menten steady-state kinetic model using GraphPad Prism® 8.0 (GraphPad, Inc., La Jolla, USA).

2.21 Protein expression and purification

The PKM2 synthetic gene fragment was prepared by Twist Bioscience (California, US) using the canonical PKM2 protein sequence (Uniprot P14618-1) as template for DNA codon-optimisation for expression in *E. coli*. The synthetic gene was cloned into a pEXP-GB1 expression vector (Addgene #112565) containing an N-terminal His 8-tag fused to a GB1 solubility enhancing tag, followed by a TEV protease cleavage site. The expression plasmid was transformed into chemi-competent *E. coli* strain T7Express (New England Biolabs, #C2566H) and the cells were used to inoculate 4 L of 2xYT medium supplemented with 100 µg/ml ampicillin. Cells were grown at 37 °C with shaking at 200 rpm until an OD600 = 0.7–1.0, after which they were cooled down to 18 °C and overnight expression was induced with 500 µM IPTG. Next day, cells were collected by centrifugation, resuspended in lysis buffer (50 mM Tris pH 8.0, 500 mM NaCl, 10 % glycerol, 20 mM imidazole) and lysed by sonication. The lysate was applied on a HisTrap HP 5 ml column (Cytiva) pre-equilibrated with IMAC buffer A (50 mM Tris pH 8.0, 500 mM NaCl, 10 % glycerol, 20 mM imidazole). The column was then washed with 8 CV IMAC buffer A, and the protein was eluted with IMAC buffer B (50 mM Tris pH 8.0, 500 mM NaCl, 200 mM imidazole). Protein-containing fractions were pooled and concentrated on an Amicon 10 kDa MWCO spin concentrator (Merck Millipore), after which the protein was applied on a Superdex 200 16/600 size exclusion column (Cytiva) pre-equilibrated with SEC buffer (20 mM HEPES pH 7.5, 300 mM NaCl). PKM2 eluted at 60–70 ml volume and peak fractions were collected, concentrated to ~20 mg/ml and flash-frozen for long-term storage.

2.22 WaterLOGSY experiment

NMR samples were prepared in 18 mM Tris pH 8.0, 90 mM KCl, 9 mM $MgCl_2$, 10 % D_2O, 0.25 % DMSO-d6. **32c** was analysed either alone at 250 µM or pre-incubated with 10 µM PKM2. NMR experiments were performed at 298 K on a 600 MHz Bruker Avance Neo 600 spectrometer equipped with an HCN triple-resonance pulsed-field-gradient cryoprobe. Water-LOGSY experiments were collected in 256 scans using a mixing time of 2 s, a 20 ms trim pulse to suppress protein signals, and water suppression using excitation sculpting with gradients.

2.23 Analytical size-exclusion chromatography

PKM2 was buffer-exchanged into analytical size-exclusion chromatography (SEC) buffer (50 mM Tris pH 8.0, 150 mM KCl, 10 mM $MgCl_2$) on a NAP-5 desalting column (Cytiva). A Superdex 200 10/300 SEC column was equilibrated with the same buffer. PKM2

was diluted to the desired final concentration and incubated with **30c**, **32c** or DMSO control. Final DMSO concentration was 1 % in all measurements. 300 μL of each sample was applied on the SEC column and eluted at 0.7 ml/min flow rate. The absorbance values (mAU) at 280 nm were normalised against the early-eluting, highest peak corresponding to the tetrameric species.

2.24 Single-molecule mass photometry

The mass photometry experiments were carried out on TwoMP instrument (Refeyn, UK) at room temperature, i.e. approx. 21 °C. Microscope coverslips (High Precision 24 × 50 mm, Marienfeld Superior) were prepared by rinsing them successively with isopropanol and Milli-Q water and drying under a stream of clean nitrogen. The high concentration protein stocks were buffer exchanged on PD Sephadex SpinTrap G-25 column (Sigma) to fresh and degassed PBS buffer.

Standard protein solutions of BSA, Immunoglobulin G, and triglobulin protein were used to generate the mass calibration of the contrast intensity to mass values. Mass photometry data was acquired with 10.9 μm × 4.3 μm instrument field of view and collected for 60 s at a 50 Hz frame rate on a 46.3 μm^2 detection area. At least 5×10^3 particles were detected in each acquisition. A series of solutions containing PKM2 and **32c** (0.1, 1, and 5 μM) in the absence or presence of 100 μM FBP were incubated for approximately 10 min before being loaded into the well on the coverslip. PKM2 and **32c** solution was mixed with the PBS buffer in 1:1 drop ratio to obtain samples of 50 nM total protein concentration. The PBS buffer was supplemented with appropriate concentration of **32c** and FBP to prevent additives dilution during the measurement.

The resulting video data was analysed using DiscoverMP software provided by the instrument manufacturer (Refeyn, UK). Raw contrast values were converted to molecular mass using the standard mass calibration, and binding events combined in 5.8 kDa bin width. Quantification of oligomer populations was achieved by integrating the peaks around the assumed size of the respective oligomer species and by calculation according to the total binding events or PKM2 population. The experiment was carried out in triplicate.

2.25 Differential scanning fluorimetry

Differential scanning fluorimetry (DSF) reactions were set up in DSF buffer (50 mM Tris pH 8.0, 150 mM KCl, 10 mM $MgCl_2$), containing 10 μM protein and 10x SYPRO orange dye (ThermoFisher). 25 μL reactions were set up in in triplicates, in a 96-well PCR plate (Sarstedt #72.1979.202). Additionally, FBP and/or **32c** were included in the reactions. Thermal

denaturation was measured over a 15–95.3 °C temperature range, with a 2 % per min gradient, on a Prism 7500 real-time PCR system (Applied Biosystems) using the ROX filter set. Melt curves were fitted with a web implementation of the MTSA software, using a Sigmoid-5 model with Tm value at the mid-point. Normalised fluorescence values were plotted with GraphPad Prism 8.0 (GraphPad, Inc., La Jolla, USA).

2.26 Competitive isothermal titration calorimetry

Purified PKM2 was buffer-exchanged into ITC buffer (20 mM HEPES pH 7.4, 150 mM KCl, 10 mM $MgCl_2$) on a NAP-5 desalting column (Cytiva) and diluted in the same buffer to 40 μM. 32c was diluted in DMSO to a concentration of 10 mM and then further diluted in ITC buffer to 80 μM. For preparing cell solution, equal volumes of PKM2 and **32c** solutions were then mixed, resulting in final concentrations of 40 μM and 20 μM for **32c** and PKM2, respectively. Alternatively, ligand-free cell solution was prepared by mixing PKM2 solution with ITC buffer supplemented with 0.8 % DMSO. Syringe solution was prepared by diluting FBP to 200 μM in ITC buffer supplemented with 0.4 % DMSO. All solutions were degassed by applying low vacuum and then kept on ice prior measurement. The same syringe solution was used for both measurements to minimise stoichiometry differences due to pipetting error. Titrations were performed on a PEAQ ITC instrument (Malvern Pananalytical, UK) using the following settings: 25 °C, DP = 5 μcal/s, 750 rpm stirring, 18 2-μl injections. Thermograms were integrated and isotherms fitted using the ITC analysis software provided by the manufacturer (Malvern Pananalytical, UK).

2.27 Quantitative polymerase chain reaction

The effect of compound **30c** on PKM1 and PKM2 mRNA expression in 4T1 and HCC1937 cells was determined using quantitative polymerase chain reaction (qPCR) analysis. 4T1 and HCC1937 cells were seeded in a 24-well plate at a density of 1×10^5 cells per well and incubated with compound 3k (BLDpharm, cat. #94164-88-2) or compound **30c** (0.25 μM and 0.5 μM final concentration) for 24 h. Total RNA from cells was isolated using Ambion PureLink RNA Mini Kit according to the manufacturer's protocol. First-strand cDNA synthesis was performed using the High-Capacity cDNA Reverse Transcription Kit (Applied BiosystemsTM, Foster City, CA, USA) following the manufacturer's instructions. The qPCR analysis of gene expression was performed using SYBR Green Master Mix (Applied BiosystemsTM) on a Bio-Molecular Systems MIC qPCR Cycler according to the manufacturer's protocol and using the following conditions: 95.0 °C for 10 min, [95.0 °C for

15 sec, 60 °C for 60 sec] (60 cycles), 95.0 °C for 60 sec, followed by melt curve analysis from 72.0 to 95.0 °C, 0.3 °C/s. The relative expression levels for PKM1 and PKM2 genes were calculated using ΔΔCt method and normalised to the expression of the β-actin gene. Primers were designed using Primer-BLAST tool. The primers are listed in the Table 2.1.

Table 2.1

Primers used for qPCR

Gene	Forward primer sequence	Reverse primer sequence
h-PKM1	CGAGCCTCAAGTCACTCCAC	GTGAGCAGACCTGCCAGACT
h-PKM2	ATTATTTGAGGAACTCCGCCGCCT	ATTCCGGGTCACAGCAATGATGG
h-β-actin	GCCGTTCCGAAAGTTGCC	ATCATCATCCATGGTGAGCTGG
m-PKM1	CGAGCCTCCAGTCACTCCAC	GTGAGCACTCCTGCCAGACT
m-PKM2	GCTATTCGAGGAACTCCGCCGCCT	ATTTCGAGTCACGGCAATGATAG
m-β-actin	CCTCTATGCCAACACAGTGC	CATCGTACTCCTGCTTGCTG

2.28 Immunostaining and confocal microscopy

4T1 cells were seeded (2×10^4 cells per well) in 8 chamber slides (Ibidi) and allowed to attach overnight. Cells were treated with **32c**, olaparib or vehicle at a concentration of 2 μM and incubated for 24 h at 37 °C and 5 % CO_2. Subsequently, $CoCl_2$ dissolved in culture medium was added (100 μM final concentration) to stimulate PKM2 translocation to the nucleus. After 24 h, the medium was removed, cells were fixed and permeabilised with ice-cold methanol for 20 min on ice. The methanol was removed, and the cells were washed with PBS 3 times. Cells were covered with blocking solution (10 % goat serum in PBST) and incubated at room temperature for 30 min. After removing the blocking solution, 100 μL of primary antibody solution were added, and the cells were incubated overnight at 4 °C. The next day, cells were washed with PBST 3 times, followed by the addition of 120 μL of secondary antibody solution. After 2 h of incubation, cells were washed 3 times with PBST and stained with DAPI solution (1 μM) in PBS. The following primary antibodies were used: rabbit anti-PKM2 antibody (1:100, #04053, Cell signal technology, Danvers, MA, USA), mouse antiPAR/pADPr antibody (1:100, #4335-MC-100, R&D Systems, Inc. Minneapolis, MN, Canada). The following secondary antibodies were used: goat anti-rabbit IgG (H+L) highly cross-adsorbed secondary antibody, Alexa Fluor™ 488 (1:1000, #A-11034, Thermo Fisher Scientific, Waltham, MA, USA); and goat anti-mouse IgG (H+L) cross-adsorbed secondary antibody, Alexa Fluor™ 647 (1:1000, #A-21235, Thermo Fisher Scientific, Waltham, MA, USA). Negative controls without primary antibodies were prepared to evaluate the background staining. The imaging was performed with a Leica Stellaris 8 confocal microscope (Leica Microsystems, Wetzlar, Germany) using Leica HC PL APO CS2 86x/1.20 W objective. The experiment was carried out in duplicate, and three fields of view were randomly chosen in each sample to capture

the 3D image for quantitative analysis. Quantitative analysis was done using LAS X analysis tool (Leica Microsystems, Wetzlar, Germany). Nuclear localisation of PKM2 and PAr was measured as a volume percent or signal counts inside the region of interest set based on DAPI.

3 Statistical Analysis

The results are expressed as the mean ± standard deviation (SD). Due to the small sample size in most of the experiments, the distribution of the variables was assessed by carrying out Shapiro-Wilk normality test. The sample size for the quantitative analysis of confocal images was greater than 50, so the Kolmogorov-Smirnov test was used. Based on the results of the normality tests, parametric (normal distribution, p-value > 0.05) or non-parametric (non-normal distribution, p-value < 0.05) tests with appropriate post-hoc tests were used as stated below.

One-way ANOVA was used to analyse the effects of isoselenazolium salts **3**, **6** and **7** on mitochondrial respiration, flux control factors, H_2O_2 production rate, H_2O_2/O ratio in permeabilised 4T1 cells, as well as on the levels of NMN, NAD^+ and NADH and NAMPT activity in MCF-7 cells. Additionally, one-way ANOVA was used to compare differences in the percentage of oligomeric species of PKM2 after treatment with different concentrations of compound **32c** with or without FBP, and to analyse the data obtained from PKM2 qPCR. When ANOVA test provided $p < 0.05$, the Dunnett's test was performed.

Independent samples *t*-test was used to compare the mean concentrations of CL in mitochondrial fractions obtained by TTAPE-Me or compound **20**. Also, independent samples *t*-test was used to analyse the effects of compound **30c** on mitochondrial respiration, flux control factors, H_2O_2 production rate, H_2O_2/O ratio in permeabilised MCF-7, 4T1, HCC1937 and Jurkat cells, NAD^+ and NADH concentrations as well as their ratio in 4T1 and H9C2 cells.

Kruskal-Wallis test followed by Dunn`s multiple comparison test was used to analyse the signal counts inside the nuclei obtained by confocal microscopy and the relative volume occupied by PKM2 and PAr after the treatment with vehicle, compound **32c** or olaparib.

The data were analysed using Graph Pad Prism software (Graph Pad Inc., La Jolla, USA), and differences were considered significant when $p < 0.05$.

4 Results

4.1 Effects of isoselenazolium salts on cancer metabolism

4.1.1 Isoselenazolium salts cytotoxicity

First, cytotoxicity of fused isoselenazolium salts **1**–**7** (Figure 4.1) was examined against breast cancer and normal cells by MTT assay, and the results are summarised in the Table 4.1. All the compounds demonstrated higher cytotoxic activities (IC_{50} values ranging from 0.044 to 3.23 μM) than the reference compound, Na_2SeO_3, in breast tumour cell lines. The IC_{50} of the studied isoselenazolium salts **1–7** were similar to that of doxorubicin; however, mammary carcinoma (4T1) cells were more susceptible to derivative **3**. Compound **1** was cytotoxic against the tumour cell lines, however, was not selective. The replacement of the methyl group with a phenyl substituent (**2**) potentiated the cytotoxic effect in the MCF-7 breast adenocarcinoma cell line. Notably, compound **3** showed the lowest cytotoxicity IC_{50} values against breast tumour cells. The introduction of a methyl substituent on the pyridine ring (**4**) led to a slight decrease in the cytotoxicity. Cyclohexyl ring (**4**) expansion to cycloheptyl (**5**) resulted in approx. 3-fold increase in cytotoxicity against MCF-7 cells. To study the influence of the fused heterocycle on the activity, the pyridine fragment was replaced with thiazole and imidazole rings obtaining thiazolo- and imidazoloisoselenazolium heterocyclic systems. The introduction of the thiazole (**6**) or imidazole (**7**) rings decreased the cytotoxicity to tumour cells, however, compound **7** showed higher toxicity than compound **6** against normal cell lines. It is worth noting that 3-bromo-2-(1-hydroxycyclohexyl)-[1,2]selenazolo[2,3-*a*]pyridinium chloride (**3**) had the most pronounced selectivity towards tumour cell lines (> 42-fold). For the further research, derivatives **3**, **6** and **7** were chosen to study the possible mechanisms of action of fused isoselenazolium salts.

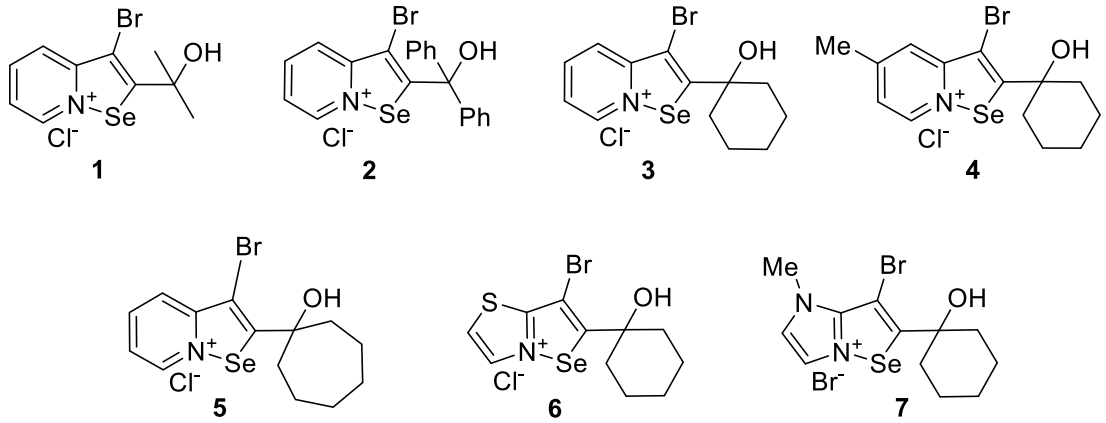

Figure 4.1 **Molecular structures of fused isoselenazolium salts 1–7**

Table 4.1

Cytotoxic activity of compounds 1–7 against breast tumour and normal cell lines

Compound	Cytotoxicity, IC_{50}, μM						
	Breast cancer cell lines		Normal cell lines				
	MCF-7	4T1	H9C2	3T3	HEKa	MDCK	A7R5
Na_2SeO_3	17.10 ± 2.40	4.90 ± 0.60	1.50 ± 0.30	22.30 ± 3.60	13.30 ± 1.10	6.30 ± 0.40	39.40 ± 8.20
Doxorubicin	1.00 ± 0.30	0.16 ± 0.06	11.00 ± 1.00	0.75 ± 0.09	n.t.	57.00 ± 6.10	1.82 ± 0.35
1	3.10 ± 0.03	0.30 ± 0.03	1.80 ± 0.10	0.13 ± 0.02	2.31 ± 0.02	3.26 ± 0.40	2.89 ± 0.42
2	0.39 ± 0.03	1.10 ± 0.08	4.20 ± 0.30	1.60 ± 0.30	2.78 ± 0.08	6.27 ± 0.29	1.87 ± 0.26
3	0.50 ± 0.02	0.044 ± 0.005	2.20 ± 0.10	0.39 ± 0.05	2.21 ± 0.02	2.91 ± 0.13	1.85 ± 0.22
4	1.48 ± 0.04	0.45 ± 0.02	2.90 ± 0.10	0.79 ± 0.02	2.05 ± 0.05	2.54 ± 0.57	1.93 ± 0.16
5	0.29 ± 0.01	0.41 ± 0.05	9.30 ± 0.20	0.98 ± 0.03	2.01 ± 0.08	1.51 ± 0.37	1.92 ± 0.44
6	3.23 ± 0.03	1.70 ± 0.20	3.70 ± 0.20	7.40 ± 0.80	2.84 ± 0.08	6.58 ± 0.33	1.97 ± 0.27
7	1.48 ± 0.02	0.94 ± 0.06	0.67 ± 0.02	2.20 ± 0.30	2.19 ± 0.09	4.28 ± 0.34	1.66 ± 0.25

*Values are shown as the means ± SD from 3 independent experiments.
n.t. – not tested.

4.1.2 Modulation of mitochondrial respiration and ROS production

One of the most important oxidation-reduction processes in the cell are carried out in the ETS in mitochondria, which is also the main site of the intracellular ROS production. Taking in mind that isoselenazolium salts in the presence of H_2O_2 act as a strong oxidant, it was of special interest to study their impact on mitochondrial function. First, the concentration-dependent effects of compounds **3** and **6** on the complex I (NADH-linked) and complex II (succinate-linked) pathways were determined. Both compounds inhibited the mitochondrial respiration rate in a concentration-dependent manner and increased H_2O_2 production with complex I (CI, NADH-linked) substrates (both pyruvate + malate and glutamate + malate) (Figure 4.2 A and B). In addition, there were no significant changes in mitochondrial function in the CII-linked OXPHOS state. Despite the difference in the compounds` potency, the most pronounced increase in the H_2O_2/O ratio in the presence of isoselenazolium salts **3** and **6** was observed when pyruvate and malate were used as substrates (Figure 4.2 C). These results indicated that isoselenazolium salts most likely affected pyruvate-dependent mitochondrial metabolism.

To determine whether the observed effects of the fused isoselenazolium salts were related to the inhibition of the pyruvate-dependent pathway but not to the direct inhibition of CI, the mitochondrial function in permeabilised breast cancer cells was evaluated in the presence of compounds **3**, **6** and **7** at 1 μM. Although only compound **6** decreased the respiration rate in the OXPHOS state with pyruvate and malate (Figure 4.3 A and E), both compounds **3** and **6** induced a significant decrease in the OXPHOS coupling efficiency (corresponds to 1-Respiratory Control Ratio^{-1}) (Figure 4.3 B). The addition of another NADH-dependent complex I substrate, glutamate, compensated for the decrease in respiration with pyruvate and malate, as shown by the increased flux control factor (characterises individual substrate/pathway input to the ET system performance) for glutamate. Together with the unchanged flux control factor for rotenone, these results indicated that fused isoselenazolium salts did not inhibit CI.

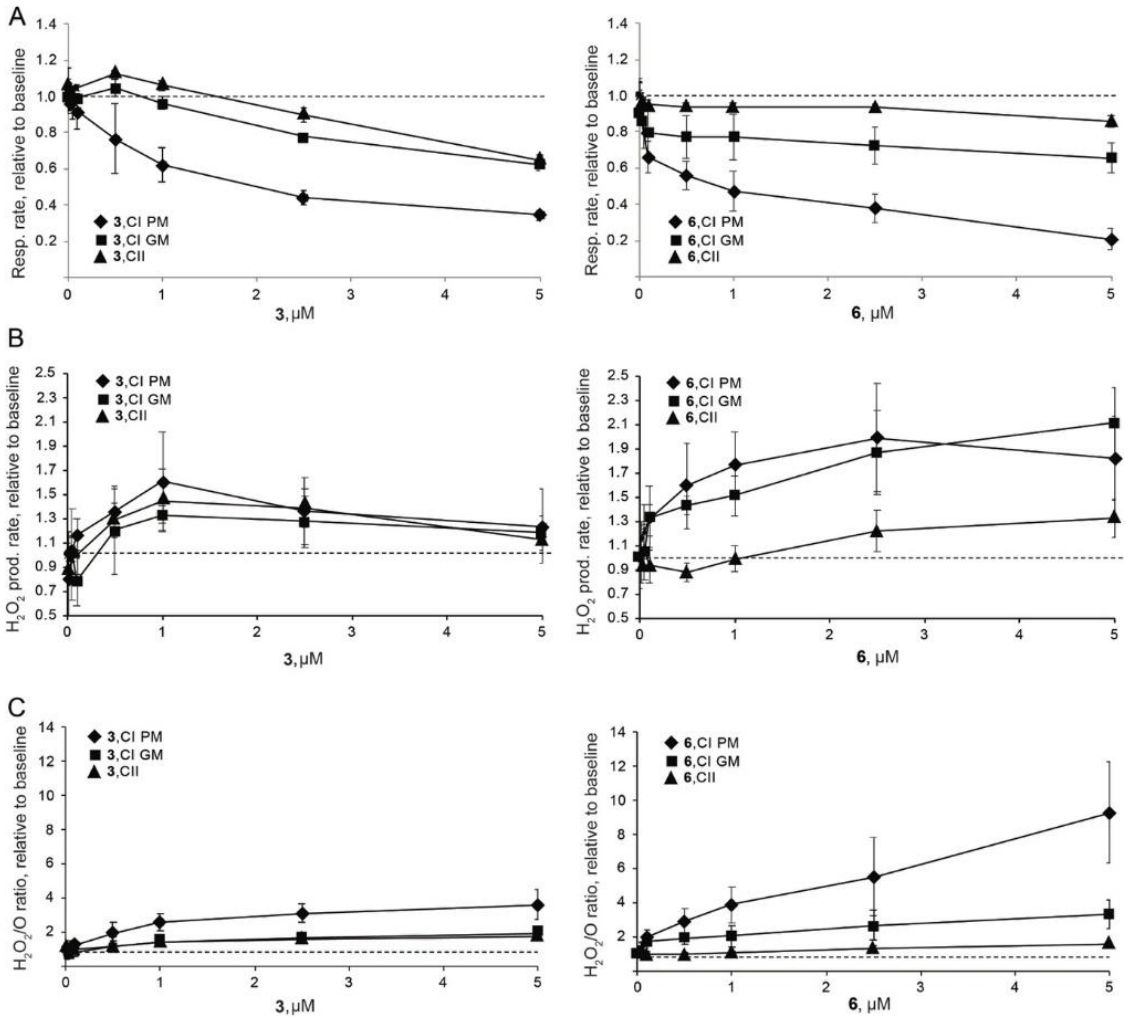

Figure 4.2. **The concentration-dependent effects of compounds 3 and 6 on mitochondrial function in permeabilised 4T1 cells. A) Concentration dependent changes in mitochondrial respiration rate; B) H_2O_2 production rate; C) H_2O_2/O ratio at Complex I or II linked OXPHOS***

*P – pyruvate; M- malate; G – glutamate. Values are shown as mean ± SD (n = 3–5 experiments) relative to baseline (dashed line) – before addition of the compound.

All three tested isoselenazolium derivatives **3, 6** and **7** induced immediate and significant increases in H_2O_2 production and the H_2O_2/O ratio in the pyruvate-dependent OXPHOS state (Figure 4.3 C, D and F). The effects of compound **6** on H_2O_2 production and the H_2O_2/O ratio were the most pronounced (2.3- and 2.8-fold increases, respectively). Taken together, the results obtained indicate that fused isoselenazolium salts inhibit pyruvate-dependent mitochondrial respiration and facilitate ROS production.

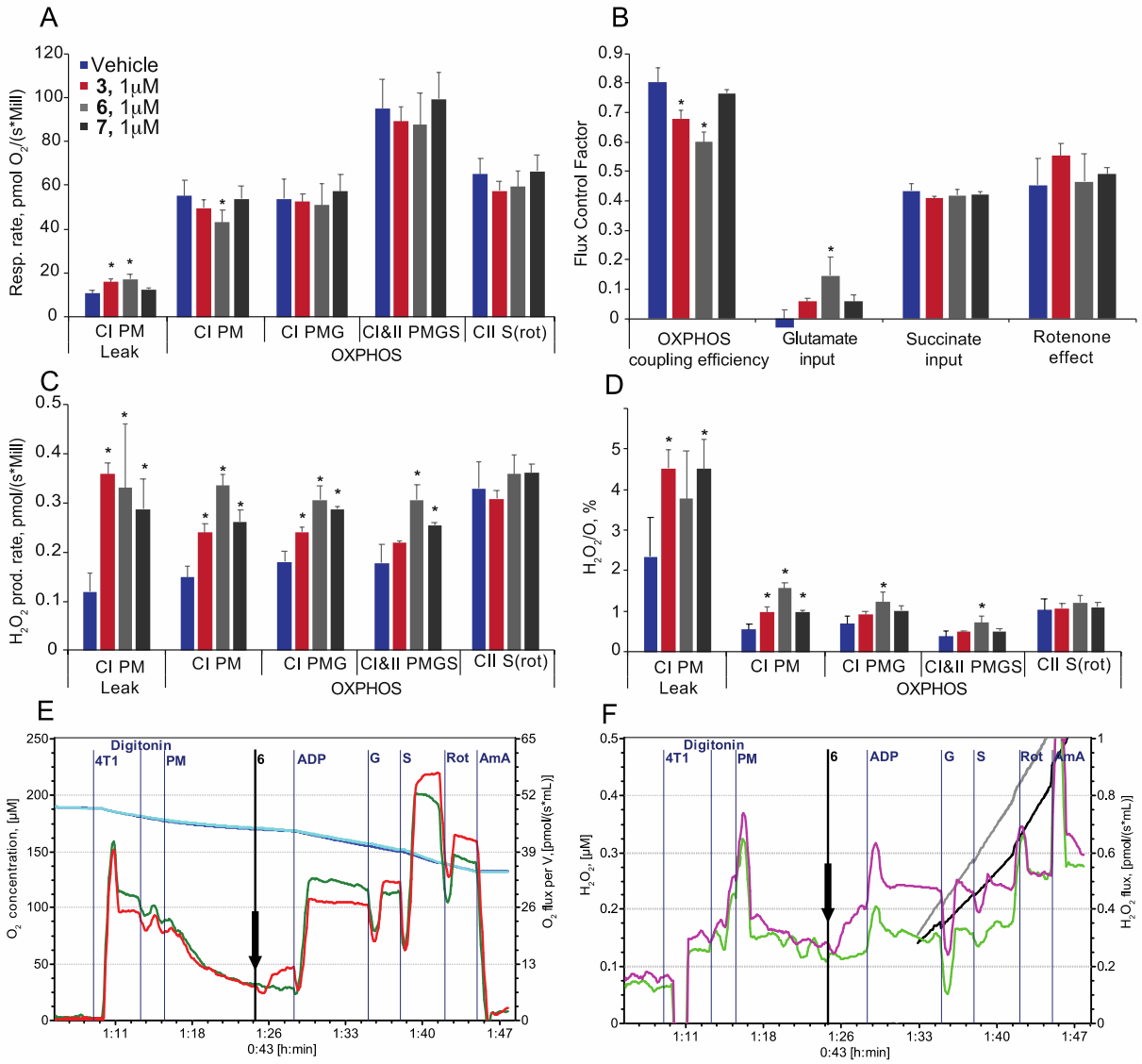

Figure 4.3 **The effect of fused isoselenazolium salts 3, 6 and 7 at 1 μM concentration on mitochondrial respiration in permeabilised 4T1 cells. A) Respiration rate; B) flux control factors; C) H_2O_2 production rate; D) H_2O_2/O ratio. E) Representative traces of respiration (green – vehicle, DMSO, red – comp. 6); F) H_2O_2 production rate measurement (light green – vehicle, DMSO, purple – comp. 6)***

*CI – complex, I; CII – complex II; LEAK – substrate dependent respiration rate; OXPHOS – oxidative phosphorylation dependent state; P – pyruvate; M – malate; G – glutamate; S – succinate; Rot – rotenone, AmA – antimycin A. OXPHOS coupling efficiency corresponds to 1-Respiratory control ratio^{-1}. Flux control factor indicates on the input of each substrate and/or pathway to the ETS performance. Values are shown as mean ± SD (n = 3–4 experiments). Statistically significant difference (*) was considered when $p < 0.05$ (one-way ANOVA) compared to the control group (vehicle-DMSO).

4.1.3 Impact on NAD^+ homeostasis

NAD^+ and its metabolites are used in many cellular processes and their levels are critical for tumour cell proliferation (Houtkooper et al., 2010; Poljsak, 2016; Zhu et al., 2019; Katsyuba et al., 2020); therefore, the effects of the fused isoselenazolium salts on the NMN, NAD^+ and NADH levels as well as nicotinamide phosphoribosyltransferase (NAMPT) activity were tested.

Compounds **3** and **6**, but not compound **7**, induced a decrease in NMN levels by 33 % and 26 %, respectively. In addition, compound **3** significantly decreased the levels of NAD^+ and NADH by 59 % and 33 %, respectively, and as a result, the NAD^+/NADH ratio was decreased by 38 % (Figure 4.4 A and B). Compound **6** induced a 25 % decrease in the NAD^+ level without affecting the NADH content or the NAD^+/NADH ratio in the cells. In contrast to compound **6**, compound **7** induced a decrease in NADH level without affecting the NAD^+ concentration, and as a result, the NAD^+/NADH ratio was 1.65-times higher than that in untreated cells. Notably, only imidazoloisoselenazolium salt **7** induced a moderate reduction (by 31 %) in NAMPT activity at 2 μM concentration (Figure 4.4 C).

Together, these results indicate that fused isoselenazolium salts altered NAD^+ homeostasis in breast tumour cells, but this impact was not exerted through the NAD^+ salvage pathway.

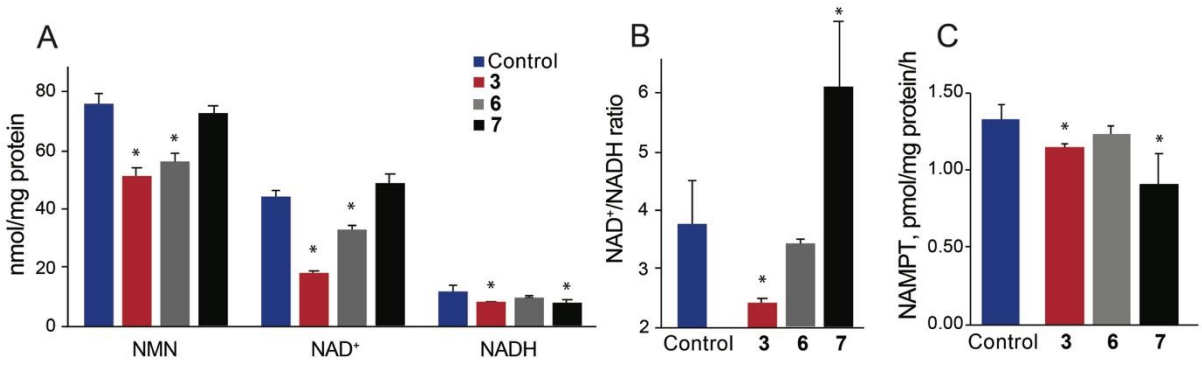

Figure 4.4 **The effects of isoselenazolium salts 3, 6 and 7 on the levels of NMN, NAD^+, NADH and NAMPT activity in MCF-7 cells. A) NMN, NAD^+ and NADH concentrations; B) NAD^+/NADH ratio; C) NAMPT inhibition by compounds 3, 6 and 7***

*Values are shown as the mean ± SD (n = 6). Statistically significant difference (*) was considered when $p < 0.05$ (one-way ANOVA) compared to the control group (vehicle).

4.1.4 Poly(ADP-ribose) polymerase 1 inhibitory activity

The poly(ADP-ribose) polymerases (PARP) are enzymes that cleave NAD^+ to nicotinamide and ADP-ribose and couple one or more ADP-ribose units to proteins involved in the regulation of multiple cellular processes including DNA repair, chromatin regulation, transcription, and the stress response. (Gupte, Liu, and Kraus, 2017) Upon excessive DNA damage PARP becomes activated and dramatically reduces NAD^+ levels even down to 20–30 % of their normal levels (Houtkooper et al., 2010). Since isoselenazolium salts disturbed NAD^+ homeostasis, an important question was whether they modulate PARP activity. There are 17 different proteins in PARP enzyme family, although PARP1 accounts for the vast majority of PARP activity in the cell. (Cantó, Sauve, and Bai, 2013) Surprisingly, it was found that compounds **3** and **7** inhibited PARP1 with IC_{50} of 0.970 ± 0.030 and 0.880 ± 0.010 μM,

respectively, while compound **6** was the most active with IC_{50} 0.140 ± 0.010 μM. Consequently, a reduction in NAD^+ concentration cannot be attributed to the overactivation of PARP1.

4.1.5 Interaction with cardiolipin

Phospholipids are the main building blocks of all the membranes, and every organelle`s membrane bears its own phospholipid composition. Cardiolipin (CL) is a unique phospholipid which is localised and synthesized in the inner mitochondrial membrane (IMM) where it makes up approximately 20 % of the total IMM phospholipids. It is now widely accepted that CL plays an important role in mitochondrial membrane morphology, stability, dynamics and is required for optimal activity of several mitochondrial membrane proteins, e.g., ETS complexes and cytochrome c (cyt c) (Paradies et al., 2019). Cardiolipin peroxidation due to increased ROS production leads to decreased activity of ETS complex I, III and IV and promotes cyt c release from mitochondria which, in turn, induces apoptosis by caspase cascade activation (McMillin and Dowhan, 2002).

To evaluate whether fused isoselenazolium salts directly interact with CL, the interactions of derivative **6** with CL/1,2-dioleoyl-*sn*-glycero-3-phosphocholinediole (DOPC) liposomes were studied. In the absence of DOPC and CL, compound **6** showed sharp resonances with clearly distinguishable spin coupling patterns. (Figure 4.5 A) In the presence of DOPC liposomes, the aromatic resonances of compound **6** were noticeably broadened such that the coupling pattern was not resolved. This could indicate a weak interaction between compound **6** and DOPC liposomes or, alternatively, the changes in resonance could be due to altered molecular surroundings (liposomal dispersion). However, in the presence of CL-containing liposomes, these resonances were significantly broadened. These results were also confirmed by the isothermal titration calorimetry (ITC) experiments (Figure 4.5 B and C). DOPC liposomes titration with compound **6** did not result in any heat release, and no signs of binding were observed. In contrast, the negative heat flow observed after each injection of compound **6** indicated that the isoselenazolium cation–CL interaction was accompanied by a decrease in enthalpy. These results indicated that compound **6** was clearly bound to the simplified mitochondrial membrane model. However, large energy release as well as broad and asymmetric peaks did not allow to estimate the precise binding affinity of compound **6**.

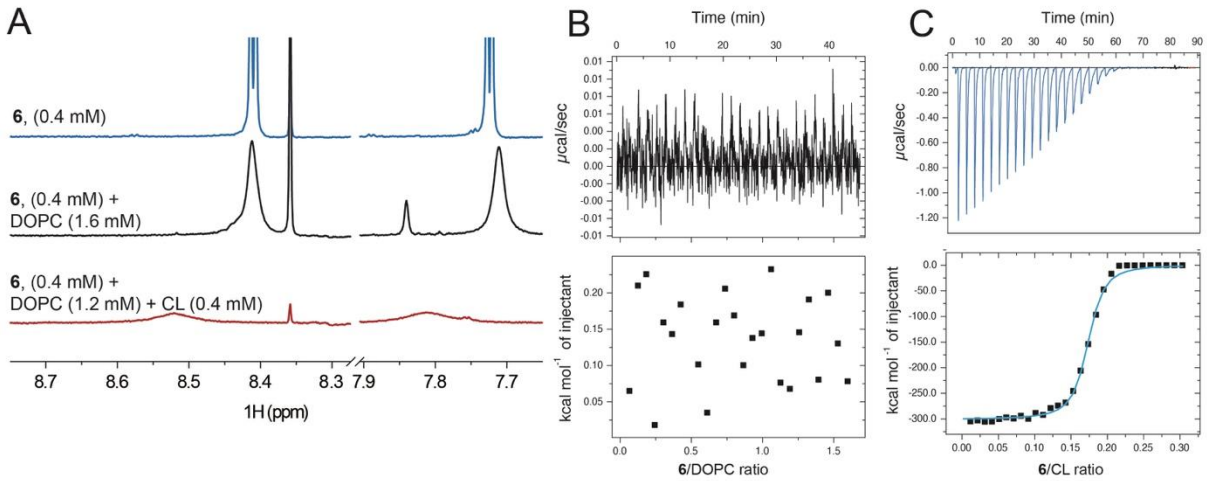

Figure 4.5 **Interaction of compound 6 with CL. A) 600 MHz ^{1}H NMR spectra of 6 (top), 6 and DOPC (middle) and 6 and DOPC with CL (bottom) in 90 % H_2O/10 % D_2O, D18 HEPES, pH 7.4 (the zoomed aromatic region is shown); B) and C) Binding isotherms and calorimetric titration curves for DOPC (B) and CL/DOPC (1:3) vesicles (C) titrations with the compound 6**

At that stage of the research, PARP1 and CL were identified as the most promising molecular targets for isoselenazolium salts. Screening of a larger set of compounds for PARP1 inhibitory activity can be readily done with a commercially available assay kit, however, there were no convenient and precise methods for estimating the affinity for CL. Therefore, to advance the studies of the mechanism of action, the research continued with the development of a new method for CL-targeted compound screening.

4.2. Development of the new cardiolipin-specific fluorescent probe

The depletion of CL is a major indicator of aging, Barth syndrome, and a number of diseases associated with mitochondrial respiratory function such as heart ischemia, cardiac failure, diabetes and neurodegenerative disorders (Valianpour et al., 2003; Han et al., 2007; Paradies et al., 2014; Pointer and Klegeris, 2017). Therefore, it is highly important to develop an effective method for the detection and quantification of CL. Besides mitochondrial membrane, CL is the characteristic lipid of bacterial membranes with CL content varying between different bacterial strain (Epand and Epand, 2009). Owing to its certain localisation (either mitochondrial inner membrane or bacterial membrane) and peculiar functions, CL has driven scientists' attention as a target molecule for mitochondria function protecting drugs as well as a target for antibacterial agents (Szeto, 2014; El Khoury et al., 2017). In addition, some drugs side effects might be attributed to their interaction with CL, for example, vancomycin`s nephrotoxicity or cardiotoxicity of chemotherapy drugs (Sakamoto et al., 2017; Gorini et al., 2018). Consequently, exploring binding with CL is crucial for screening new, CL-targeted

modulators of mitochondrial functions and antibiotics, as well as for evaluating drugs` potential to cause mitochondrial toxicity by interacting with CL.

Previously, compounds binding with CL was detected by ^{1}H and ^{13}C NMR (Soussi et al., 1990; Parker, King, and Howard, 2001) or ITC, but these methods are time-consuming, semi-quantitative and require large amount of both compound of interest and CL. Also, Ca^{2+} can be used as a probe for evaluating compounds binding with anionic lipids (Mather and Rottenberg, 2001), but this protocol also has significant disadvantages: non-specific Ca^{2+} binding to other lipids, no hydrophobic interaction with CL and the requirement of Ca^{2+} electrode. Other methods are based on a compound`s intrinsic properties and include circular dichroism measurements (Sinibaldi et al., 2008) or separation and quantification of unbound ligand. (Nicolay et al., 1984).

In the early 1980s a fluorescent dye, 10–*N*–nonyl acridine orange (NAO), was introduced for selective CL detection and mitochondria staining (Mileykovskaya et al., 2001). In the presence of CL the green fluorescence of NAO is decreased allowing to quantitively analyse CL content ranging from 0.2 to 10 μM (Kaewsuya, Danielson, and Ekhterae, 2007). NAO also has been used as a fluorescent probe for the evaluation of 3′,6-dinonyl neamine binding to anionic phospholipids (Sautrey et al., 2016). However, NAO has significant drawbacks and, therefore, a limited use as a probe for both quantitative analysis and competition assays – fluorescence intensity of NAO is relatively low and unstable due to low solubility in aqueous medium, low photoluminescence quantum yield (Φ) and small intensity differences between CL-bound and unbound states. Another commercially available CL-specific fluorescent probe, TTAPE-Me, forms a fluorescent complex with CL, but its fluorescence intensity is also very low (Chen et al., 2015); hence, a large amount of both sample and probe is necessary for obtaining qualitative results. Another major disadvantage of TTAPE-Me is its binding mode - it binds with CL only electrostatically and sodium ions compete with the probe, making it unusable for competitive binding studies.

Therefore, there is a great demand for a more stable and sensitive CL-specific probe for CL concentration measurements as well as for a robust method for rapid biologically active compound screening for CL targeting and quantitative binding affinity characterisation. For this reason, improvements should be made in a fluorescent probe`s solubility, stability, photoluminescence quantum yield and fluorescence intensity.

4.2.1 Synthesis of the new cardiolipin-specific fluorescent probes

To overcome the issues mentioned above, the research was focused on improving the physicochemical properties of NAO. Firstly, solubility and stability issues were addressed. It was known that N^+ cation is crucial for the probe`s interaction with phosphate groups of CL, at the same time, alkyl chain should retain lipophilicity to form hydrophobic bonds with CL`s fatty acid chains (Rodriguez et al., 2008). Obviously, the hydrophobic alkyl chain of NAO negatively impacts its solubility and for this reason was chosen for modification.

At first glance, the synthesis of 10-*N*-alkylated derivatives of acridine orange seems like a simple quaternisation of the commercially available 3,6-bis(dimethylamino)acridine (AO) with a corresponding alkyl halide in toluene, benzene, or chloroform under reflux (Yamaglshi et al., 1981; Kaewsuya et al., 2008; Rodriguez et al., 2008). However, the reaction proceeds slowly (24–72 h) with low conversion and is accompanied by the formation of many side products, that can be explained by 3,6-dimethylamino acridinium salts demethylation under prolonged heating. To produce more active alkylating agents for the reduction of the reaction time and heat exposure of the starting materials, *in situ* formed dialkyl carbonates, sulphates and trialkyl phosphates were tested in toluene, xylene and dichlorobenzene under reflux. Surprisingly, it was found that AO quaternisation with 1-bromononane or 1-iodononane in dichlorobenzene at 170 °C in the presence of 2 equiv. Na_2CO_3 resulted in 91 and 98 % conversion, respectively, without a significant amount of demethylated by-products (Figure 4.6). This method allowed to obtain quaternised acridinium salts in good yields and with high purity (≥ 96.5 %, HPLC).

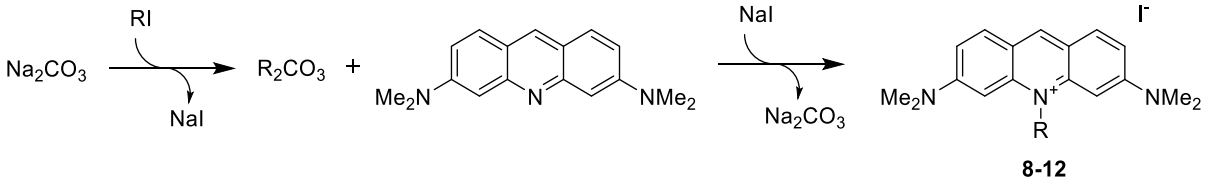

8-12

Figure 4.6 **Synthesis of compounds 8–12***

*Reaction conditions: alkyl iodide, dichlorobenzene, 170˚ C, Na_2CO_3 (2 equiv.). **8**, R=methyl, 98 %; **9**, NAO, R=nonyl, 77 %; **10**, R=dodecyl, 76 %; **11**, R= 3-(trimethylsilyl) propyl, 97 %); **12**, R= 3-silatranylpropyl, 14 %.

To increase the solubility of a probe in aqueous medium without losing lipophilicity, (3-iodopropyl) trimethylsilane was used. The obtained 3-(trimethylsilyl) propyl substituted acridinium iodide **12** had 5-fold higher solubility in 20 mM HEPES (pH = 7.4) compared to NAO and better stability after 24 h. The change of the alkyl chain did not affect the excitation and emission maxima of the new probe. Furthermore, the introduction of the 3-(trimethylsilyl) propyl substituent led to a slight increase in Φ compared to NAO (18.7 % and

15.5 %, respectively); however, this small increase in Φ resulted in ~30 % increase in fluorescence intensity (FI). The new probe interacted with CL in the same manner as NAO, reaching saturation with CL in a 2:1 ratio (Figure 4.7 A). For this study, it was of interest to investigate whether compound **12** can be used for quantitative analysis of CL. For this reason, liposomes representing inner mitochondrial membrane (IMM) were prepared from its major composing phospholipids – 10 % phosphatidylinositol (PI), 30 % phosphatidylethanolamine (PE), 35 % DOPC and 25 % CL (Horvath and Daum, 2013), and NAO was used as a control. CL could be quantified ($R^2 > 0.99$) with both probes in the 0.5–8 μM range, but compound **12** provided stronger response compared to NAO (Figure 4.7 B). Moreover, these results confirmed the selectivity of compound **12** toward CL in the presence of other IMM phospholipids.

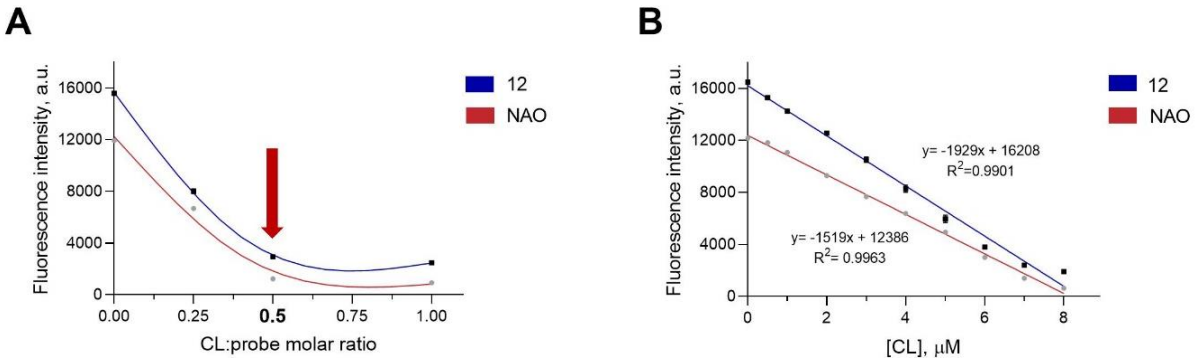

Figure 4.7 **A) CL binding ratio of compound 12 and NAO; B) Titration of compound 12 and NAO, 20 μM, with the IMM model**

*Titration values are shown as means of at least 6 independent experiments.

It has been shown in similar heterocyclic systems that an azetidinyl group significantly improves Φ, presumably by hindering twisting of the C_{aryl}–N bond and disfavouring the formation of a twisted internal charge transfer state (Grimm et al., 2015). To confirm this, replacement of dimethylamino groups with cyclic amino substituents in positions 3 and 6 of the acridinium salt structure was performed. First, compounds **14–17** were synthesised using palladium-catalysed cross-coupling of compound **13** with cyclic amines and then alkylated using the previously developed method with the corresponding alkyl iodide in the presence of sodium carbonate to obtain acridinium iodides **18–25** (Figure 4.8).

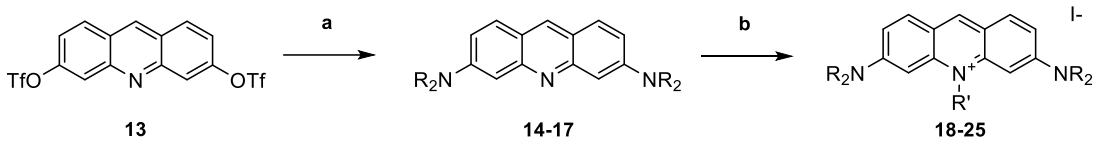

Figure 4.8 **Synthesis of acridinium salts 6–15***

*Reaction conditions: a) cyclic amine (3 equiv.), $Pd(OAc)_2$ (25 mol- %), BINAP (30 mol-%), Cs_2CO_3 (4 equiv.), xylene, reflux, 16h; b) R`-I, $Na_2CO_3$, dichlorobenzene or toluene, reflux, 10–40 min. **14**, $NR_2$ = azetidinyl, 69 %; **15**, $NR_2$ = pyrrolidyl, 54 %; **16**, $NR_2$ = piperidyl, 65 %; **17**, $NR_2$ = morpholyl, 67 %; **18**, $NR_2$ = azetidinyl, R` = CH_3, 75 %; **19**, NR_2 = azetidinyl, R` = $CD_3$, 89 %; **20**, $NR_2$ = azetidinyl, R` = $Me_3Si(CH_2)_3$, 61 %; **21**, NR_2 = azetidinyl, R` = $C_9H_{19}$, 76 %; **22**, $NR_2$ = azetidinyl, R` = $C_{12}H_{25}$, 54 %; **23**, NR_2 = pyrrolidyl, R` = $Me_3Si(CH_2)_3$, 98 %; **24**, $NR_2$ = piperidyl, R` = $Me_3Si(CH_2)_3$, 59 %; **25**, NR_2 = morpholyl, R` = $Me_3Si(CH_2)_3$, 63 %.

As expected, azetidinyl AO analogues **18–20** exhibited a 4-fold higher Φ (≈60 %) than NAO (Table 4.2). Pyrrolidyl-substituted acridinium salt **23** displayed moderate Φ (40 %), but piperidyl and morpholyl analogues **24** and **25** had very low Φ, 2.7 % and 6.8 %, respectively. Azetidinyl-substituted analogues with methyl and 3-(trimethylsilyl) propyl group displayed the highest Φ, and the elongation of the alkyl chain at position 10 led to the decrease of Φ. Deuterium atoms in the *N*-methyl group did not make any impact on the fluorescent properties, therefore, azetidinyl-substituted acridinium iodides **18** and **20** were selected for further studies.

Table 4.2

Photoluminescence properties of NAO analogues (20 mM HEPES buffer, pH = 7.4)

Compound	R	R'	Φ, %	$\lambda_{abs}/\lambda_{em}$, nm
9 (NAO)	Me_2N	C_9H_{19}	15.5	497/529
12	Me_2N	$Me_3Si(CH_2)_3$	18.7	491/529
18		CH_3	59.9	498/529
19		CD_3	61.5	498/529
20		$Me_3Si(CH_2)_3$	60.7	497/529
21		C_9H_{19}	47.9	498/529
22		$C_{12}H_{25}$	16.1	496/529
23		$Me_3Si(CH_2)_3$	40.0	511/529
24		$Me_3Si(CH_2)_3$	2.7	484/547
25		$Me_3Si(CH_2)_3$	6.8	488/547

As was supposed, in the absence of a hydrophobic alkyl chain, *N*-methyl-substituted diazetidinyl acridinium **18** did not form a stable complex with CL, which was confirmed by a 13 % increase in FI in 10 min after the addition of the compound to CL. In turn, 3-(trimethylsilyl) propyl substituted derivative **20** interacted with CL similarly to NAO with a 2 to 1 saturating ratio but with a substantially larger intensity difference between CL-bound and unbound states. Notably, the FI of compound **20** and its complex with CL was stable in buffer for at least 30 min, in contrast to NAO. This fact could be explained by approx. 5-fold higher

solubility of compound **20** (0.188 mg/ml versus 0.041 mg/ml for NAO) in the buffer. It is important to note that compound **20** retained the same specificity toward CL as NAO (Figure 4.9). It is worth to point out that in this experiment, phospholipids – phosphatidylethanolamine, phosphatidylinositol, phosphatidic acid and phosphatidylserine – were taken at equal concentrations (8 μM the lipid of interest, 24 μM DOPC), but in the IMM, the total amount of negatively charged phospholipids is significantly lower than the amount of CL, therefore, their impact on the decrease in the FI is much lower in the actual IMM (Horvath and Daum, 2013). This was confirmed by showing that the decrease in FI in the simple CL/DOPC liposomal model was similar to the more complex IMM model (10 PI, 25 % CL, 30 % PE, 35 % DOPC).

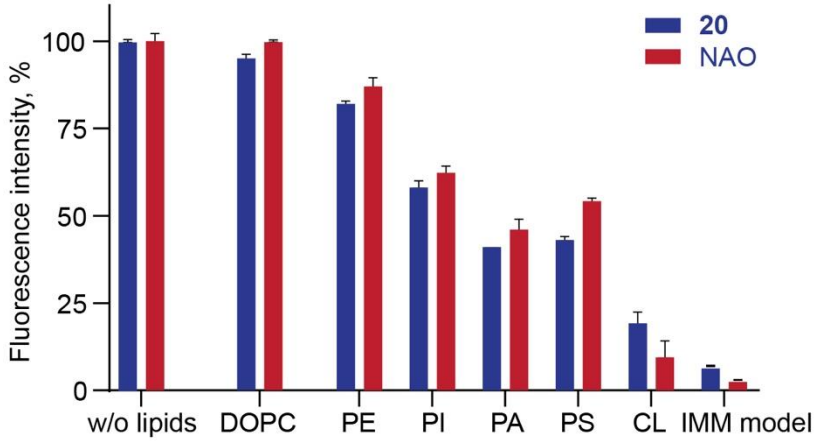

Figure 4.9 **Interaction of compound 20 and NAO with phospholipids***

*Columns represent relative fluorescence intensity – the lower intensity indicates higher specificity toward a particular phospholipid.

Moreover, compound **20** was successfully implemented in live cell imaging of mitochondria (Figure 4.10). For comparison, MitoTracker deep red, a commercially available dye for mitochondria staining, was applied to confirm mitochondrial localisation of compound **20**. The fluorescent signal of compound **20** precisely overlapped with MitoTracker deep red and did not significantly spread to other organelles.

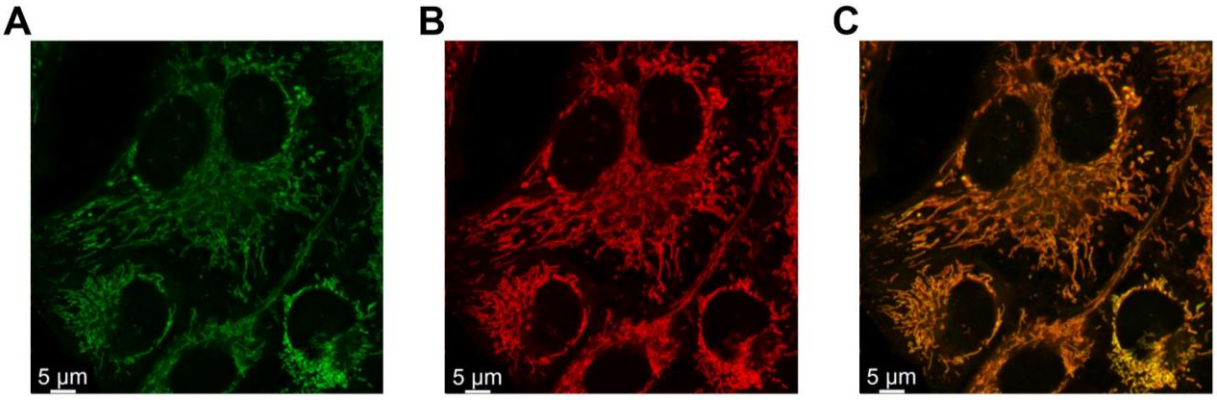

Figure 4.10 **A) Subcellular localisation of compound 20 (100 nM) in human melanoma cells (A2058); B) Mitochondria in A2058 cells stained with MitoTracker deep red (200 nM); C) Representative colocalisation of 20 and MitoTracker deep red**

Thus, the introduction of the 3-(trimethylsilyl)propyl group improved solubility and stability in aqueous medium; in turn, azetidynil groups significantly enhanced the fluorescent properties without the loss of specificity toward CL. Consequently, compound **20** was chosen as a fluorescent probe for the quantitative analysis of CL and for the development of an assay to measure the binding affinity of biologically active substances for CL.

4.2.2 Cardiolipin quantitative analysis

First, a quantitative analysis of CL was performed in a CL/DOPC liposomal model: compound **20** was titrated with CL in the 0.05–8 μM range, and a linear regression curve ($R^2 = 0.9930$) was obtained (Figure 4.11 A) with a greater linear slope of the titration curve (-6403 ± 135) than that of NAO (-1223 ± 27). As compound **20** binds with CL at a 2:1 ratio, the maximal CL concentration that can be measured is half the concentration of the probe.

Next, since CL is almost exclusively located in mitochondria, the amount of CL was measured in mitochondrial fractions isolated from different cell lines using calibration curves obtained with liposomal CL solutions. Human erythrocyte lysate was taken as a negative control because human erythrocytes do not have no mitochondria and, therefore, do not have CL. In parallel, CL concentration was measured with TTAPE-Me and compared with the results obtained with compound **20** using Student`s *t*-test (Figure 4.11 B).

In all cell lines studied, no statistically significant difference ($p > 0.37$, Student`s t-test) in the determined CL concentration was found using compound **20** or TTAPE-Me. Moreover, in erythrocytes, no CL was detected, thus confirming the selectivity of compound **20** for CL. Cardiomyoblasts are considered rich in mitochondria and contain a relatively large amount of CL. For example, 26.6 ± 3.7 nmol of CL per mg of mitochondrial protein was found in rat cardiomyoblasts (H9C2). Strikingly, cancer cell lines and cell lines with high proliferation rates

(NIH/3T3, mouse Swiss albino embryo fibroblasts, and CHO-K1, Chinese hamster ovary cells) contain comparable or even higher amounts of CL. The highest concentration of CL among the studied cell lines, 108.5 ± 16.0 nmol/mg prot., was found in the mitochondria of mouse colon carcinoma cells (CT-26), which is consistent with published data on elevated CL levels in colon cancer. (Zichri et al., 2021) To check the reproducibility of the results obtained, the CL concentration was measured in mitochondrial fractions from 3 different subcultures of H9C2, Jurkat, 4T1 and MCF-7 cells, and no significant deviations were found between subcultures.

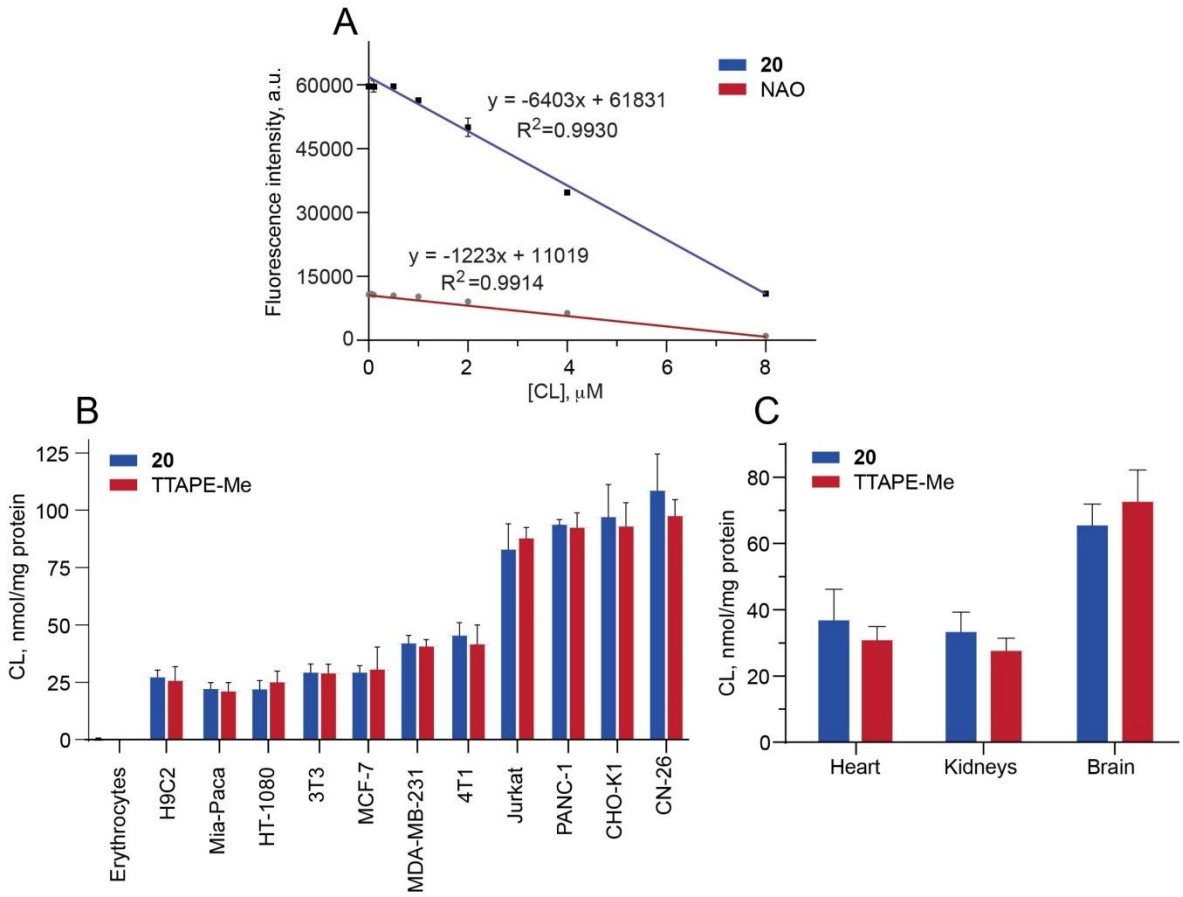

Figure 4.11 **A) Compound`s 20 and NAO (16 μM) titration with CL/DOPC liposomes in 20 mM HEPES, pH 7.4; B) CL amount in mitochondrial fractions from cell lysates, measured using 20 and TTAPE-Me; C) CL amount in mitochondrial fractions from C57Bl/6J mice tissue homogenates, measured using 20 and TTAPE-Me***

*n = 3–5. In all cases $p > 0.05$ (Student`s t-test).

The next step was to confirm whether it is possible to measure CL concentration in mitochondrial fractions isolated from animal tissue. For example, this would allow the study of CL levels under different pathological conditions or exploration of the influence of drug treatment on CL levels by analysing samples from *in vivo* experiments. Mitochondrial fractions were isolated from healthy C57Bl/6J mouse heart, kidney and brain tissue homogenates, and CL content was analysed by the same method as previously described (Figure 4.11 C). No statistically significant differences were found between CL concentrations obtained by

compound **20** or TTAPE-Me ($p > 0.44$, Student`s *t*-test). The mouse heart and kidney mitochondria contained similar amounts of CL, 37.49 ± 8.69 and 33.95 ± 5.32 nmol/mg prot., respectively. Previously reported CL concentrations of 15–20 nmol/mg prot. for mouse heart mitochondria (Grevengoed et al., 2015; Pennington et al., 2019) could be underestimated due to the possible loss of CL during lipid extraction and separation procedures. Remarkably, CL concentration in mouse brain mitochondria (66.11 ± 5.78 nmol/mg prot.) was almost twice that of the heart and kidneys. The obtained value was slightly higher than the previously reported value (52.7 ± 4.5 nmol/mg prot.) (Kiebish et al., 2009), which could also be explained by the lipid extraction step before CL quantification or CL level fluctuations between different mouse strains.

In summary, the developed fluorescent dye **20** is suitable for the fast and straightforward measurement of CL concentrations in mitochondrial fractions isolated from cultured cells and animal tissues. The greatest advantages are the simplicity of the procedure (lipid extraction and separation are not necessary), only 15 min incubation and a single-point emission measurement, that produces a clear and stable response. Considering that loss of CL content is a characteristic attribute of mitochondrial dysfunctions, e.g., Barth syndrome (Valianpour et al., 2003), coronary heart disease (Paradies et al., 2014), neurodegenerative diseases (Pointer and Klegeris, 2017) and ageing (Chicco and Sparagna, 2007), this practical tool will be indispensable in studying the role of CL levels in these pathological conditions. Although the developed assay allows quantification of the total amount of CL, its limitation is the inability to distinguish between CL species with different alkyl chain compositions.

4.2.3 Fluorescence-based competitive binding assay

Cytochrome c (cyt c), an endogenous CL ligand (Vladimirov, Proskurnina, and Alekseev, 2013), and CL/DOPC liposomes (25:75 mol %) were selected for the development and optimisation of the experimental procedure. Based on the data obtained, 10 min incubation at 37 °C was sufficient for complete saturation of CL with cyt c. The most pronounced response was when compound **20** and CL were used in a saturating ratio of 2:1 at 5 and 2.5 μM concentrations, respectively. Nonlinear regression analysis of the normalised fluorescence intensity versus decimal logarithm of ligand`s concentration plot allowed the determination of EC_{50} values. Cyt c showed high affinity for CL, and at pH 7.4 had EC_{50} value of 0.32 ± 0.06 μM (Figure 4.12 A). A similar EC_{50} value (0.44 ± 0.02 μM) was obtained in experiments in a more complex model of the IMM (PI, CL, PE and DOPC, 10:25:30:35 mol %). Therefore, simple CL/DOPC liposomes were suitable for competitive binding studies as an artificial membrane

model. Mitoplasts isolated from a rat heart, representing a natural lipid membrane, were also successfully applied. In this case, cyt c had an approx. twofold higher EC_{50} value (0.78 ± 0.15 μM, value obtained from 3 separately isolated mitochondrial fractions, n = 9), probably because of the interaction with other IMM components such as intermembrane proteins or other lipids. Next, the ability of cyt c to bind to CL was evaluated at different pH values representing the mitochondrial intermembrane space (6.8), cytosol (7.4), and mitochondrial matrix (7.8) (Santo-Domingo and Demaurex, 2012). The results confirmed that the affinity of cyt c for CL is independent of pH.

The developed method allowed fast and convenient determination of cyt c binding affinity for CL in both artificial and natural membrane models at different pH values. Considering the strong and pH-independent binding of cyt c as well as its commercial availability, cyt c can be proposed as a reference compound. To validate the method, different ligands were studied (Table 4.3).

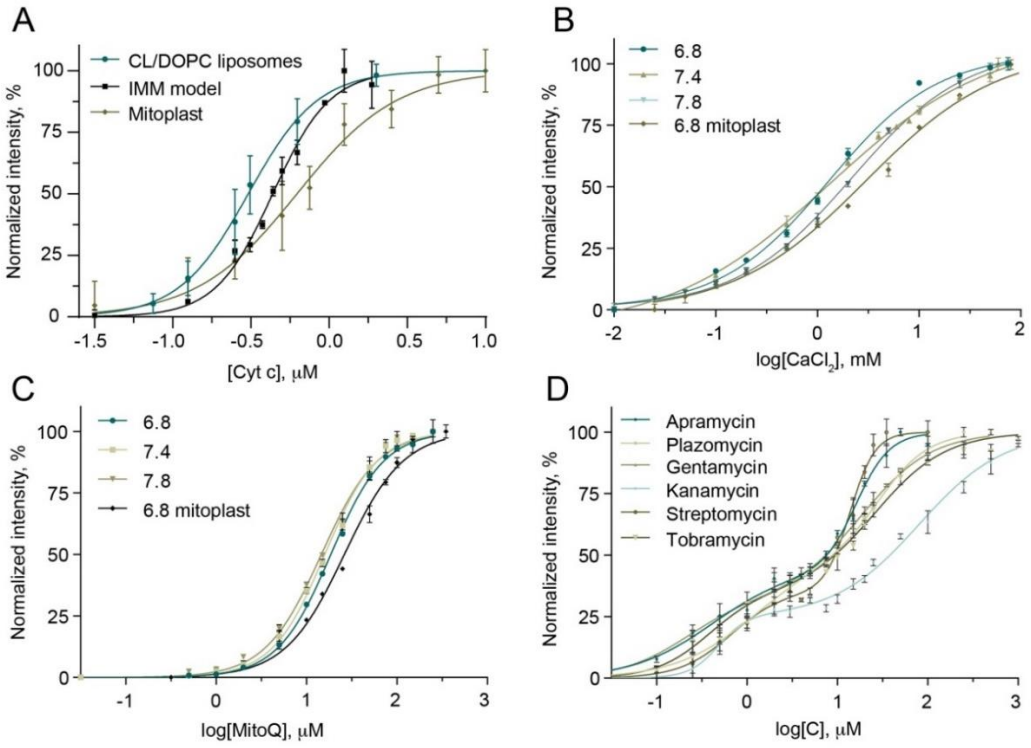

Figure 4.12 **A) Cyt c binding with CL in CL/DOPC liposomes, IMM model (10 PI, 25 % CL, 30 % PE, 35 % DOPC) and mitoplasts. B) Representative curves of $CaCl_2$ and mitoQ (C) binding with CL in CL/DOPC liposomes in 20 mM HEPES at pH 6.8, 7.4 and 7.8 and isolated mitoplasts in 20 mM HEPES, pH 6.8. D) Aminoglycosides` binding with CL in CL/DOPC liposomes in 20 mM HEPES, pH 7.4***

*PE – phosphatidylethanolamine, PI – phosphatidylinositol, PA – phosphatidic acid, PS – phosphatidylserine.

Due to two negative charges in the molecule of CL, inorganic salts were chosen as the first compound group, and interaction of Ca^{2+} (Huang et al., 2006), Mg^{2+} and monovalent cations (Merchant and Glonek, 1992) with CL have been already reported. In this assay, Ca^{2+}

(Figure 4.12 B), Mg^{2+} and Zn^{2+} competed with the probe to bind with CL, but in contrast to cyt c, their EC_{50} values were in the millimolar range. NH_4^+ cations had lower affinity for CL and showed a two-site binding pattern; in turn, Na^+ cations failed to reach saturation even at 300 mM concentration. Notably, Hg^{2+} ions quenched the fluorescence of the probe, probably due to the formation of a complex with compound **20**.

Table 4.3

Compounds relative affinity toward CL

	EC_{50}, μM			
Model / **pH**	**CL/DOPC 6.8**	**CL/DOPC 7.4**	**CL/DOPC 7.8**	**Mitoplasts 6.8**
Inorganic salts				
$MgCl_2$	1141 ± 122	1102 ± 66	1300 ± 94	1576 ± 190
Zn gluconate	683 ± 111	736 ± 37	344 ± 32	792 ± 125
$CaCl_2$	1285 ± 129	1334 ± 101	1701 ± 154	2703 ± 246
NH_4Cl	14849 ± 2002: 88827 ± 3392	14270 ± 165; 45130 ± 153	9170 ± 149; 82020 ± 130	4930 ± 107; 68290 ± 810
NaCl	> 100000	> 100000	> 100000	> 100000
$HgCl_2$	q	q	q	q
Compounds that affect mitochondrial function				
Cytochrome c	0.26 ± 0.02	0.32 ± 0.06	0.33 ± 0.06	0.78 ± 0.15
Nonyl TPP	36.65 ± 2.93	19.76 ± 0.75	28.82 ± 1.02	43.31 ± 3.87
MitoQ	19.55 ± 1.67	15.92 ± 0.87	17.06 ± 0.17	30.67 ± 5.14
Metformin	> 500	> 500	> 500	n.t.
Thimerosal	> 500	> 500	> 500	n.t.
Acyclovir	> 500	> 500	> 500	n.t.
Abacavir	> 500	> 500	> 500	n.t.
Antimycin A	q	q	q	n.t.
CCCP	q	q	q	n.t.
Antibiotics				
Vancomycin	796 ± 47	434 ± 62	346 ± 21	1732 ± 29
Rifampicin	q	q	q	n.t.
Ampicillin Na	> 500	> 500	> 500	n.t.
Dodecyl trimethyl-ammonium chloride	74.41 ± 8.47	30.71 ± 2.75	23.16 ± 2.74	69.20 ± 3.67
Apramycin	0.85 ± 0.04; 102.5 ± 1.5	0.63 ± 0.21; 14.54 ± 0.59	0.58 ± 0.04; 27.87 ± 2.70	2.79 ± 0.31; 593 ± 76
Gentamycin	1.04 ± 0.09; 384 ± 18	0.22 ± 0.03; 19.19 ± 1.44	0.38 ± 0.05; 24.15 ± 3.90	1.83 ± 0.69; 298 ± 55
Streptomycin	1.22 ± 0.20; 87.5 ± 6.2	0.60 ± 0.15; 14.15 ± 2.17	0.89 ± 0.12; 16.28 ± 2.83	2.33 ± 0.05; 155 ± 69
Tobramycin	n.t.	0.40 ± 0.16; 26.16 ± 2.79	n.t.	n.t.
Kanamycin	n.t.	0.44 ± 0.10; 80.1 ± 13.5	n.t.	n.t.
Plazomicin	n.t.	1.13 ± 0.46; 29.4 ± 4.2	n.t.	n.t.

All experiments were done at least in triplicate, n ≥ 9 for cyt c.
n.t. – not tested, q- fluorescence of the compound **20** is quenched by a studied compound.

The second group included compounds that affect mitochondrial functions: triphenylphosphonium (TPP) salts that are used for drug delivery to mitochondria – nonyl TPP and MitoQ, the TPP cation conjugated to ubiquinone (Zielonka et al., 2017); metformin, which inhibits mitochondrial respiratory complex I; acyclovir and abacavir, which inhibit mitochondrial DNA polymerase γ; antimycin A, which inhibits mitochondrial respiratory complex III (Chan et al., 2005); thimerosal, which causes depolarisation of mitochondrial membrane potential (Yel et al., 2005); and carbonyl cyanide m-chlorophenylhydrazone (CCCP), a protonophore used to uncouple mitochondrial respiration (Ganote, 2003). The obtained results showed that compounds containing TPP cations readily bind to CL with EC_{50} values in the range of 15–37 μM (Figure 4.12 C). In turn, metformin, thimerosal, acyclovir and abacavir did not displace the probe at the concentrations tested. It was not possible to assess the binding of antimycin A and CCCP to CL due to quenching of the fluorescent probe.

The third group of compounds included antibiotics, represented by vancomycin, which inhibits mitochondrial respiratory complex I (Arimura et al., 2012); dodecyl trimethylammonium chloride, a membrane permeabilizing agent (Wessels and Ingmer, 2013); rifampicin and ampicillin, that induce overproduction of ROS and mitochondrial dysfunction (Chowdhury et al., 2006; Kalghatgi et al., 2013) and various aminoglycosides that not only cause mitochondrial damage (Esterberg et al., 2016), but could include CL as one of the molecular targets responsible for their antimicrobial activity (El Khoury et al., 2017). Considering CL as a potential target for antibiotics, experiments conducted at pH 7.4 are more relevant because this value is close to the pH in the periplasm of Gram-negative bacteria, e.g., *E. coli* (Wilks and Slonczewski, 2007). Vancomycin affinity for CL was low, with EC_{50} values the in sub-millimolar range in the artificial membrane and reached ≈1.7 mM when mitoplasts were used as the membrane model. These results were in a good agreement with data published by Domenech (Domenech et al., 2009), who showed that a high concentration (600 nM) of vancomycin was required to induce only a slight permeabilisation of CL-containing lipid vesicles. Rifampicin quenched the fluorescence of the compound **20**, which could be explained by the fact that the tetrahydroxynaphthalene moiety in rifampicin molecule exhibits a pKa of 1.7 related to the 4-hydroxy group (O'Neil, 2001). Under physiological conditions at pH 6.8–7.8, rifampicin can interact with the compound **20** electrostatically and by π-π stacking, depleting the photoluminescence of the compound **20**. Ampicillin did not interact with CL at the concentrations tested, supporting the observation that the bactericidal effect of ampicillin is not influenced by the reduced amount of anionic lipids in *E. coli* (Rodionov and Ishiguro, 1997). The affinity of dodecyl trimethylammonium chloride for CL was close to that of the lipophilic

phosphonium cation and was pH-dependent: a 3-fold decrease in the EC_{50} values was observed when the pH was raised from 6.8 to 7.8.

Aminoglycosides showed a two-site binding pattern and exhibit a high affinity for CL with EC_{50H} values ≤ 1 μM (Figure 4.12 D) and EC_{50L} in the range of 14–80 μM. Aminoglycosides at high concentrations cause destabilisation and disruption of the negatively charged membranes (Brasseur et al., 1984; Forge et al., 1989; Joshi et al., 2015). Therefore, a logical explanation for the two-site binding pattern is that the first part of the binding curve with low EC_{50} value describes electrostatic binding of positively charged aminoglycosides with negatively charged phosphate groups of CL in the external surface of a bilayer membrane, and the second part of the binding curve with high EC_{50} value is a consequence of the apparent destabilisation or disruption of the membrane that renders more free phosphate groups that can bind with aminoglycosides from otherwise inaccessible inside of the lipid bilayer. Gentamycin had the highest affinity for CL among all the drugs studied, and its EC_{50H} values were almost equal to those of cyt *c* at pH 7.4–7.8.

In total, the assay was validated by testing 25 substances of different nature – inorganic salts, peptide (cyt c), glycopeptide (vancomycin), polycationic sugars (aminoglycosides), lipophilic phosphonium and ammonium salts, drugs containing guanine (abacavir, acyclovir) and guanidine (metformin) moieties, and other substances. The developed assay does not require special equipment other than a fluorimeter and is time-efficient, which makes it suitable for screening a large number of compounds. In general, positively charged substances bind to CL, but their affinity varies markedly; the EC_{50} values lie in the sub-micromolar to millimolar range. The interaction of the fluorescent probe with the studied compounds, e.g., heavy metal ions, is a limitation of the assay; therefore, a blank titration without CL must always be performed to avoid misinterpretation of the results.

The new screening technique allows to evaluate CL as a potential molecular target for therapies designed to protect or damage the mitochondrial membrane, for selective drug delivery into mitochondria or for antimicrobial therapy. Additionally, this method might help predict drugs interactions with the mitochondrial membrane and, perhaps, to warn about possible side effects related to mitochondrial dysfunction.

4.2.4 Isoselenazolium salts affinity for cardiolipin

After the development of the new method, it was finally possible to measure the affinity of isoselenazolium salts for CL. Despite the previous data obtained by ITC showing a clear exothermic interaction between compound **6** and CL containing liposomes, both compounds **6**

and **3** tested in the CL/DOPC model had EC_{50} > 500 μM, which means that their affinity for CL is low, and it is unlikely that their impact on mitochondrial respiration and overall cytotoxic effect is exerted through interaction with CL. Therefore, it was decided to modify isoselenazolium salt's structure, and focus studies on pyruvate-dependent mitochondrial respiration, NAD^+ metabolism and PARP1 inhibitory activity.

4.3 Second generation of isoselenazolium salts and their mechanism of action

4.3.1 Synthesis of new isoselenazolium derivatives

The original plan was to introduce the nicotinamide moiety in the isoselenazolopyridinium core to resemble to some extent a part of the NAD^+ structure, which is a substrate for PARP1, and study the impact of the amide group and its position on cytotoxicity. Additionally, similar functional groups – carboxyl or methyl ester groups were introduced in the pyridine ring (Figure 4.13).

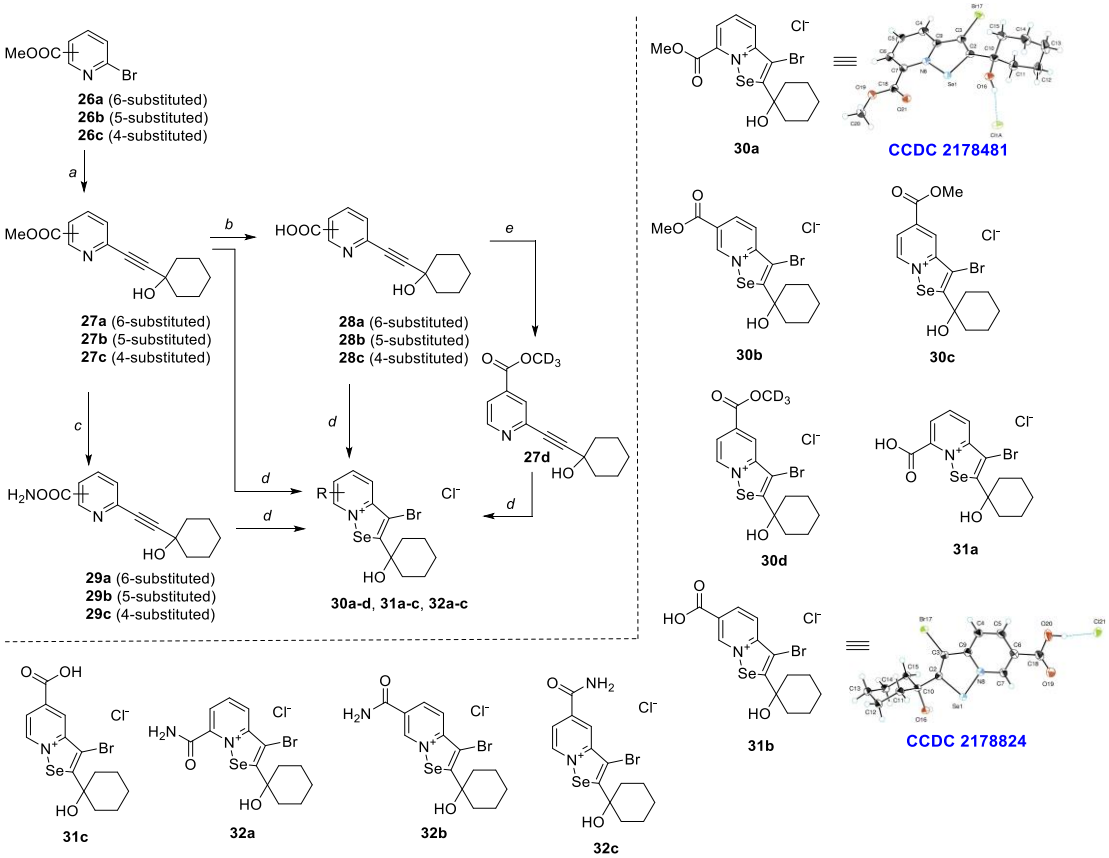

Figure 4.13 **Synthesis of isoselenazolopyridinium chlorides 30a–e, 31a–c and 32a–c***

*Reaction conditions: a) terminal acetylene (1.4 equiv.), CuI (0.01–0.05 equiv.), $(Ph_3P)_2PdCl_2$ (0.01–0.05 equiv.), DMF/iPr_2NH or Et_3N, 50 or 80 ˚C, 2–5 h; b) 1. NaOH (5 equiv.), 2. HCl, MeOH/H_2O, rt, overnight; c) NH_3, MeOH, rt, overnight; d) $SeBr_4$, dioxane/water, rt; e) CD_3OD, EDC·HCl, HOBt·H_2O, DMF, rt, 2 h.

The synthetic route started from α-bromopyridines **26a–c**, that were treated with ethynyl cyclohexanol in the presence of palladium catalyst to produce ethynyl-substituted derivatives **27a–c** in high yields. The corresponding carboxylic acids were obtained by hydrolysis of the ester group of compounds **28a–c** with NaOH, and amides **29a–c** were synthesised in reaction of compounds **27a–c** with saturated methanolic solution of NH_3. Methyl-d3 2-((1-hydroxycyclohexyl) ethynyl) isonicotinate (**27d**) was prepared by treating a suspension of the compound **28c** and CD_3OD with HOBt hydrate and EDC·HCl in DMF.

After obtaining all derivatives of ethynyl pyridines, the corresponding isoselenazolium salts were synthesised based on a previously established procedure (Arsenyan et al., 2015). Ethynyl pyridines **27a–d**, **28a–c** and **29a–c** were treated with *in situ* prepared $SeBr_4$ by dissolving selenium(IV) oxide in the concentrated hydrobromic acid in dioxane/water. After consumption of a substrate, the crude material was dissolved in the EtOH/water mixture and eluted through ion-exchange resins (IRA-401) pretreated with hydrochloric acid to produce isoselenazolopyridinium chlorides **30a–d**, **31a–c** and **32a–c**. However, the treatment of 2-((1-hydroxycyclohexyl) ethynyl) nicotinic acid as well as its amide and methyl ester derivatives with $SeBr_4$ was unsuccessful and resulted in only traces of the desired products.

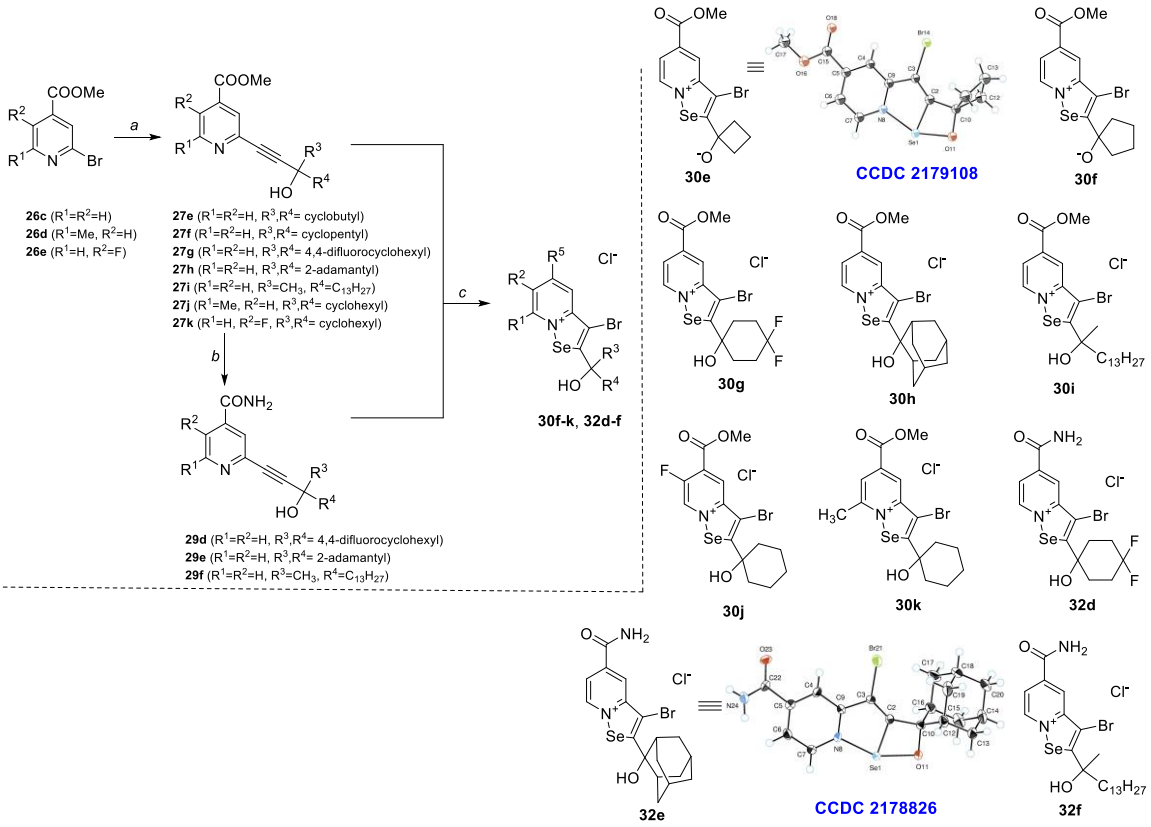

Figure 4.14 **Synthesis of isoselenazolopyridinium chlorides 30f–k and 32d–f***

*Reaction conditions: a) terminal acetylene (1.4 equiv.), CuI (0.01–0.05 equiv.), $(Ph_3P)_2PdCl_2$ (0.01–0.05 equiv.), DMF/iPr_2NH or Et_3N, 50 or 80 ˚C, 2–5 h; b) NH_3, MeOH, rt, overnight; c) $SeBr_4$, dioxane/water, rt.

Based on preliminary structure-activity relationship (SAR) data, cyclohexyl substituent at position 2 was replaced by cyclobutyl, cyclopentyl, adamantlyl, tridecyl and difluorocyclohexyl groups. Isoselenazolopyridinium chlorides **30f–k**, **32d–f** were synthesised similarly to the previous set of compounds (Figure 4.14). Compounds **30j** and **30k** were synthesised using methyl- and fluoro- substituted pyridine bromides as a starting material. The molecular structures of the compounds **30a** (CCDC 2178481), **30e** (CCDC 2179108), **31b** (CCDC 2178824), and **32e** (CCDC 2178826) were confirmed by X-ray diffraction. Depending on the pH of the medium, isoselenazolium chlorides can exist in chloride and zwitterion forms (Arsenyan et al., 2015). The exact form can be detected by X-ray and ^{77}Se NMR spectra. The selenium signal was found in the region of 1200 to 1300 ppm for isoselenazolium chlorides and around 1100 ppm for zwitterions such as compounds **30e** and **30f**.

Also, it should be noted that the distance between selenium and oxygen of the hydroxy group is shorter in zwitterions forming an additional bond (Se–O = 2.006 Å; Se–N^+ = 2.131 Å in the crystal structure of the compound **30e**).

4.3.2 Cytotoxicity of the new isoselenazolium derivatives

The cytotoxicity of new isoselenazolium salts was studied in human and mouse breast cancer (MCF-7, MDA-MB-231, 4T1), T cell leukaemia (Jurkat), human hepatocellular carcinoma (HCC1937) and human lung adenocarcinoma (A549) cells, and the data are summarised in Table 4.4. As the new compounds were likely to modulate mitochondrial function, rat cardiomyoblasts (H9C2) were selected as a control normal cell line because they contain a large number of mitochondria (Kuznetsov et al., 2015) and are widely used to assess mitochondrial toxicity *in vitro* (Kim and Choi, 2021).

First, the influence of the position of the carboxyl, methoxy carbonyl, and amide group of the pyridinium ring was studied. The carboxyl group in the isoselenazolopyridinium ring (compounds **31c** and **31b**) reduced cytotoxicity and selectivity toward cancer cells, probably, because of the poor solubility and low cell permeability. Compounds **30a** and **31a** were excluded from the study due to low solubility in aqueous medium. In turn, derivatives with the methoxy carbonyl or amide group in positions 5 or 6 exhibited high cytotoxicity toward a wide range of malignant cell lines. In particular, compound **30c** with the methoxy carbonyl group at position 5 stood out with a favourable cytotoxicity profile. In turn, the introduction of fluorine atom in position 6 or methyl group in position 7 reduced selectivity toward cancer cells. Then, substituents at position 2 were modified, and it was concluded that bulky (adamantyl) or lipophilic (2-hydroxypentadecan-2-yl) substituents reduce cytotoxicity and/or selectivity

toward cancer cells. However, it was found that the optimal substituent is 1-hydroxycyclohexanyl group, and cytotoxicity for most of the cell lines decreased with a smaller number of carbon atoms in the hydroxycycloalkane ring.

Table 4.4

Cytotoxic activity of 30b-32f against cancer cell lines and cardiomyoblasts

	Cytotoxicity, IC_{50}, µM						
Compound	**H9C2**	**Jurkat**	**MCF7**	**HCC1937**	**A549**	**MDA-MB-231**	**4T1**
Doxorubicin	3.90 ± 0.60	0.32 ± 0.08	0.47 ± 0.14	1.08 ± 0.10	0.23 ± 0.07	0.41 ± 0.08	0.065 ± 0.008
30b	0.89 ± 0.27	0.25 ± 0.06	0.87 ± 0.29	0.31 ± 0.11	1.31 ± 0.20	0.43 ± 0.14	0.70 ± 0.18
30c	2.46 ± 0.60	0.44 ± 0.25	1.16 ± 0.09	0.33 ± 0.03	1.30 ± 0.23	0.51 ± 0.15	0.32 ± 0.03
30d	0.64 ± 0.28	0.49 ± 0.06	0.38 ± 0.09	0.54 ± 0.02	1.20 ± 0.46	0.40 ± 0.11	1.11 ± 0.04
30e	2.97 ± 0.22	3.24 ± 0.49	2.80 ± 0.75	3.03 ± 0.40	9.12 ± 1.42	6.51 ± 0.67	>10
30f	0.77 ± 0.14	0.48 ± 0.22	0.36 ± 0.13	0.41 ± 0.13	8.70 ± 1.43	1.66 ± 0.35	2.04 ± 0.60
30g	1.06 ± 0.03	0.48 ± 0.27	0.28 ± 0.13	0.24 ± 0.10	1.16 ± 0.25	0.48 ± 0.13	1.48 ± 0.44
30h	4.76 ± 0.18	6.18 ± 0.16	6.87 ± 0.75	2.89 ± 0.37	n.t.	n.t.	n.t.
30i	3.63 ± 0.38	3.38 ± 0.30	3.79 ± 0.57	2.45 ± 0.43	n.t.	n.t.	n.t.
30j	1.68 ± 0.36	1.16 ± 0.19	1.08 ± 0.02	1.19 ± 0.27	2.93 ± 0.47	1.38 ± 0.40	2.34 ± 0.51
30k	0.90 ± 0.24	0.45 ± 0.11	0.30 ± 0.18	0.34 ± 0.05	1.12 ± 0.26	0.37 ± 0.14	0.96 ± 0.14
31b	3.55 ± 0.18	3.26 ± 0.54	> 10	3.85 ± 0.61	n.t.	n.t.	n.t.
31c	7.82 ± 0.19	6.61 ± 2.15	> 10	5.82 ± 0.72	7.03 ± 0.10	6.12 ± 0.47	6.81 ± 0.33
32a	2.63 ± 0.44	1.88 ± 0.42	3.85 ± 0.41	1.33 ± 0.30	n.t.	n.t.	n.t.
32b	1.27 ± 0.13	0.60 ± 0.25	2.30 ± 0.87	1.50 ± 0.34	n.t.	n.t.	n.t.
32c	1.41 ± 0.17	1.00 ± 0.15	2.22 ± 0.57	0.60 ± 0.25	2.81 ± 0.58	1.15 ± 0.20	1.41 ± 0.28
32d	1.41 ± 0.26	1.43 ± 0.36	1.00 ± 0.08	0.60 ± 0.25	3.17 ± 0.23	1.36 ± 0.18	1.25 ± 0.08
32e	0.91 ± 0.25	0.91 ± 0.29	0.61 ± 0.04	0.74 ± 0.26	2.21 ± 0.36	0.65 ± 0.21	0.56 ± 0.02
32f	1.91 ± 0.55	2.00 ± 0.25	1.01 ± 0.08	0.91 ± 0.10	3.72 ± 0.40	2.42 ± 0.18	4.32 ± 0.73

*Values are shown as the means ± S.D. from 3-5 independent experiments. n.t. = not tested.

While some analogues, such as **30g** and **30f**, were worth mentioning, compound **30c** was the most selective and exhibited the highest cytotoxic activity in a wider spectrum of cancer cell lines. Hence, compound **30c** was selected to study the mechanism of action.

4.3.3 Influence on mitochondrial respiration, ROS production and coupling state of the electron transfer system

The impact of compound **30c** on mitochondrial respiration was studied in HCC1937, MCF-7, 4T1 and Jurkat cells by high-resolution fluorespirometry. These cell lines showed significant differences in mitochondrial metabolic activity, and their maximal oxygen consumption rate (OCR) was in the following descending order: MCF-7 > 4T1 > HCC1937 > Jurkat (Figure 4.15 A–D).

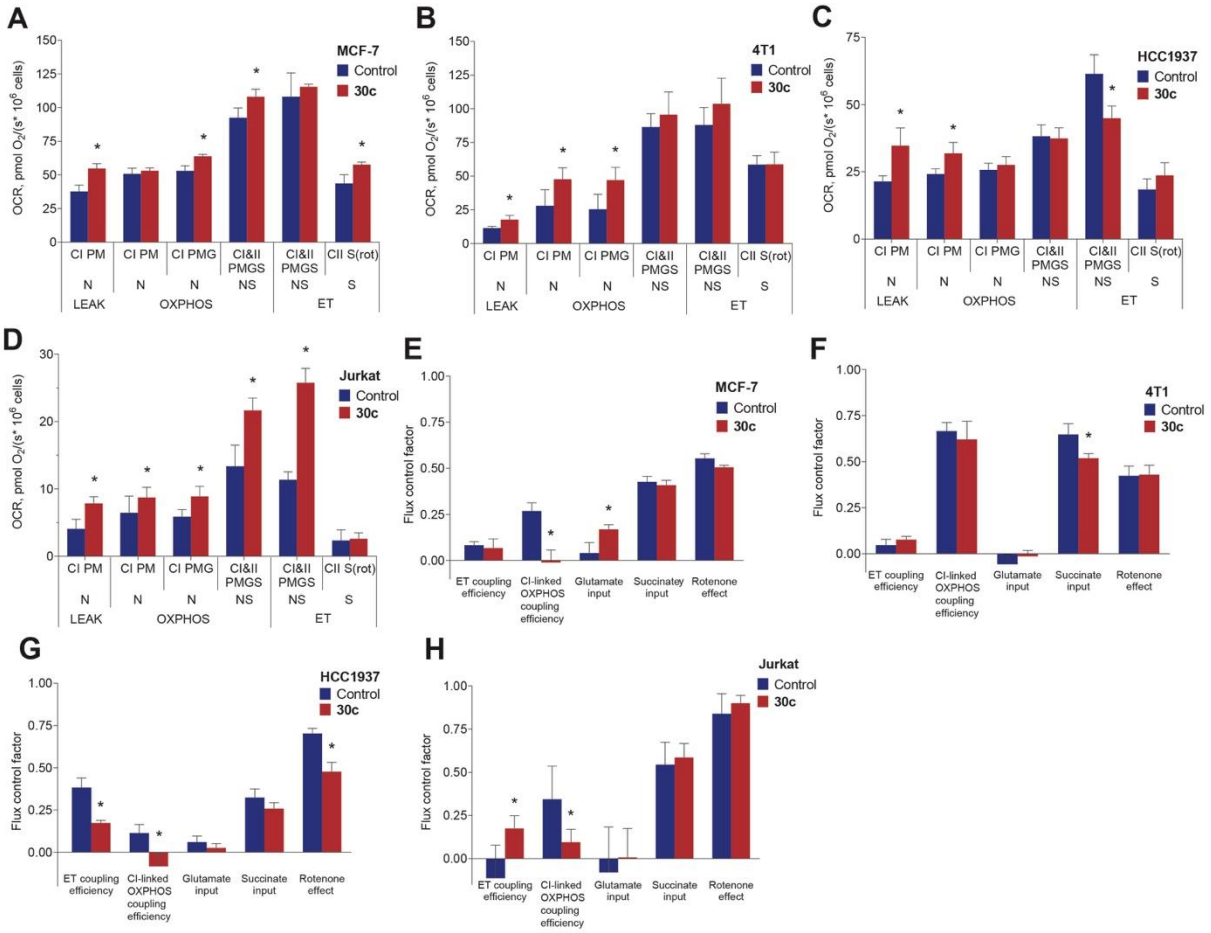

Figure 4.15 **The effect of compound 30c at 1 μM concentration on mitochondrial respiration. Respiratory parameters in permeabilised (A) MCF-7, (B) 4T1, (C) HCC1937, (D) Jurkat cells. Flux control factors in permeabilised (E) MCF-7, (F) 4T1, (G) HCC1937, (H) Jurkat cells***

*OCR2 – oxygen consumption rate, CI – complex I; CII – complex II; LEAK – substrate dependent respiration rate; OXPHOS – oxidative phosphorylation dependent state; ET – electron transfer, uncoupled state; P – pyruvate; M – malate; G – glutamate; S – succinate; N – NADHgenerating substrates; NS – NADH and succinate generating substrates; rot – rotenone. Flux control factors indicate the input of each substrate and/or pathway to the ETS performance. Rotenone effect corresponds to 1-OCR after the addition of rot/OCR before the addition of rot. Values are shown as mean ± SD (n = 3–5 experiments). Statistically significant difference (*) was considered when $p < 0.05$ (Students *t*-test) compared to the control group (vehicle-DMSO).

Surprisingly, compound **30c** significantly increased OCR in all cell lines in the presence of pyruvate and malate in LEAK, OXPHOS or both states. However, **30c** abruptly interrupted OXPHOS coupling in the presence of CI substrates (pyruvate and malate) in MCF-7 (Figure 4.15 E), HCC1937 (Figure 4.15 G) and Jurkat (Figure 4.15 H), but not in 4T1 cells (Figure 4.15 F). Compound **30c** does not appear to have a direct impact on CI because the effect of rotenone (CI inhibitor) was almost identical in the treatment and control groups, except for HCC1937, where the effect of rotenone was reduced. In addition, there were no substantial changes in mitochondrial function in the CII-linked OXPHOS state.

Elevated OCR can be explained by the increase in ROS production. Immediately after addition of compound **30c** there was a massive increase in the rate of H_2O_2 production in all cell lines. (Figure 4.16 A–D).

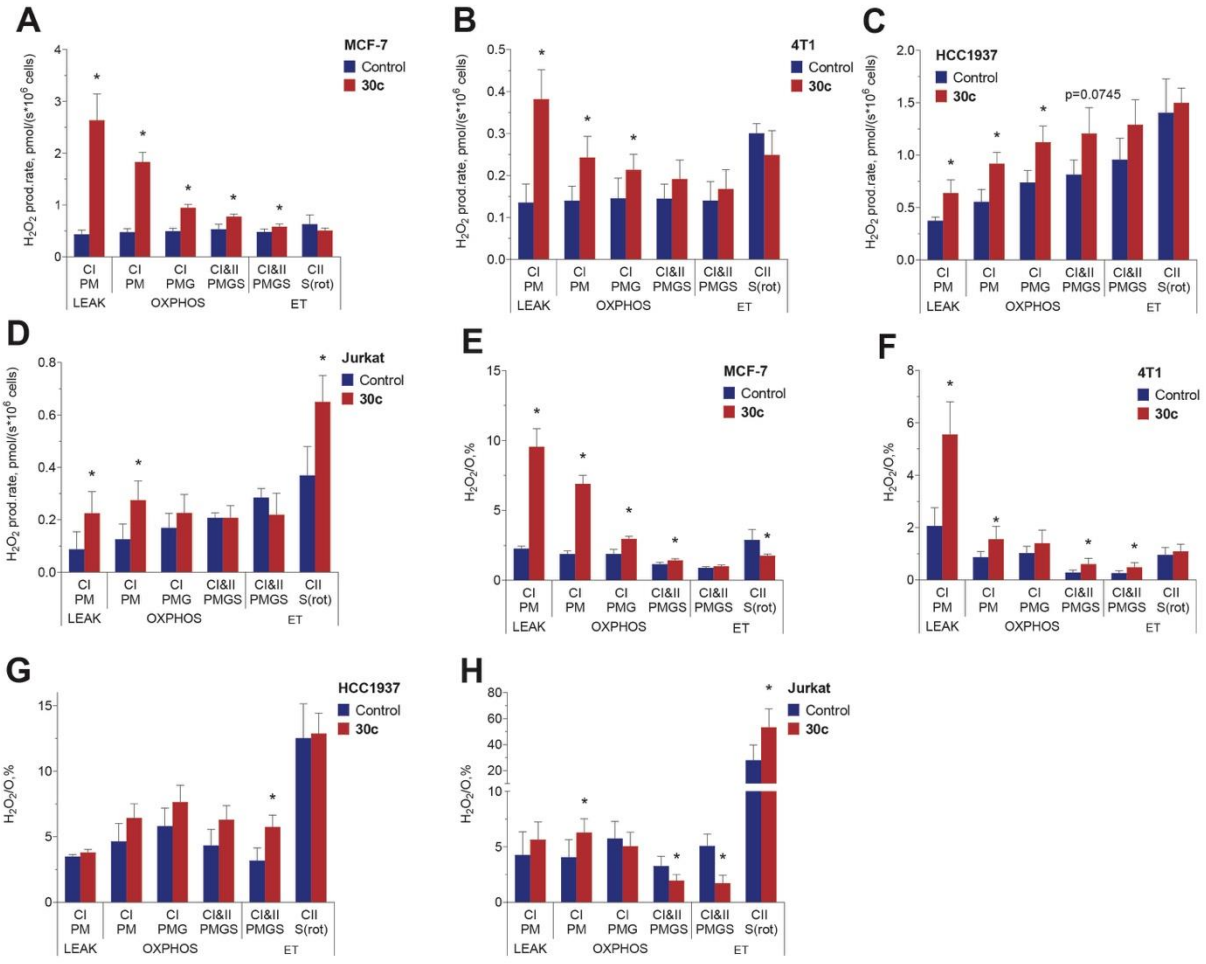

Figure 4.16 **Effect of 1 µM compound 30c on H_2O_2 production rate in permeabilised (A) MCF-7, (B) 4T1, (C) HCC1937 and (D) Jurkat cells. H_2O_2/O ratio in in permeabilised (E) MCF-7, (F) 4T1, (G) HCC1937 and (H) Jurkat cells***

*CI – complex I; CII – complex II; LEAK – substrate dependent respiration rate; OXPHOS – oxidative phosphorylation dependent state; ET – electron transfer, uncoupled state; P – pyruvate; M – malate; G – glutamate; S – succinate; rot–rotenone. Values are shown as mean ± SD (n = 3–5 experiments). Statistically significant difference (*) was considered when $p < 0.05$ (Students *t*-test) compared to the control group (vehicle-DMSO).

The most pronounced H_2O_2 production spikes were in the presence of CI substrates. Higher H_2O_2/O ratios (Figure 4.16 E–H) indicate that more oxygen was shifting toward ROS production rather than participating in ETS. Some studies also report that an increase in ROS level causes an increase in proton leak, (Echtay et al., 2002; Brookes, 2005) and this phenomenon might explain the observed reduction in coupling efficiency.

The increase in mitochondrial ROS production may arise from CI or complex III (CIII) produced superoxide anion. However, the production of $O_2^{\bullet-}$ by CIII is generally low and it is unlikely to be associated with such significant effects (Forman and Azzi, 1997). In turn, CI can produce a large amount of $O_2^{\bullet-}$ and H_2O_2 during both forward (NADH-oxidizing) and reverse (NAD^+-reducing) electron transport. The latter can be ruled out, because the upsurge of H_2O_2 production is not levelled out by rotenone, confirming that electrons do not enter into CI through the coenzyme Q-binding site(s) in the opposite direction (Murphy, 2009).

Another way to induce mitochondrial ROS production is by decreasing NAD^+/NADH ratio (Murphy, 2009). Compound **30c** significantly reduced the intracellular pools of NAD^+ and NADH by 42.8 % and 57.4 %, respectively (Figure 4.17 A) in 4T1 cells. In contrast, no effect on NAD^+ and NADH pools or NAD^+/NADH ratio was found in a parallel experiment with H9C2 cells (Figure 17 B). Surprisingly, compound **30c** did not decrease NAD^+/NADH ratio in 4T1 cells but increased it (Figure 4.17 C). Thus, changes in the NAD^+/NADH ratio are not the ones that induce ROS overproduction.

To determine whether the interaction of the modified isoselenazolium salt **30c** with CL could potentially lead to the observed proton leak and ROS formation, the fluorescence-based competitive binding assay was carried out using mitoplasts isolated from rat liver (Figure 4.17 D).

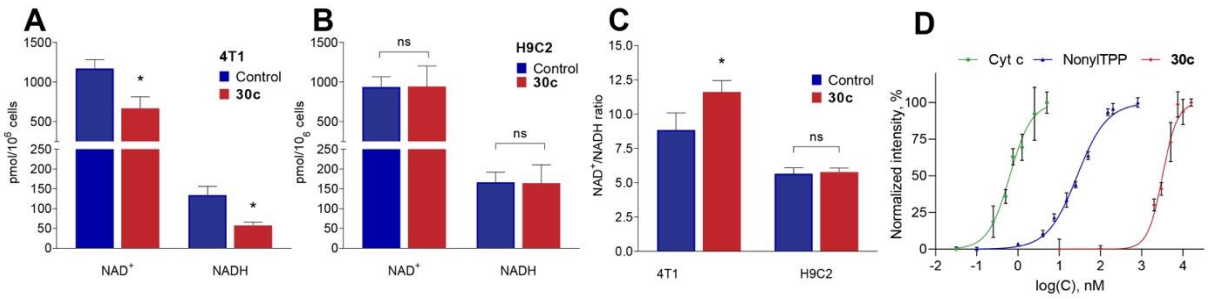

Figure 4.17 **NAD^+ and NADH concentrations in (A) 4T1 and (B) H9C2 cells after treatment with 1 µM compound 30c. (C) NAD^+/NADH ratio in 4T1 and H9C2 cells after treatment with 1 µM 30c. (D) Cardiolipin binding curves of cytochrome c (cyt c), nonyltriphenyphosphonium bromide (Nonyl TPP) and 30c in mitoplasts isolated from rat liver***

*Values are shown as mean ± SD (n = 3–5 experiments). Statistically significant difference (*) was considered when $p < 0.05$ (Students *t*-test) compared to the control group.

Although compound **30c** apparently interacted with CL (EC_{50} = 3490 ± 298 μM), the affinity was approximately 100-fold lower compared to the classic mitotargeting moiety nonyl-TPP bromide (EC_{50} = 32.22 ± 2.64 μM) and approx. 5000-fold lower compared to cyt c (EC_{50} = 0.70 ± 0.14 μM). Therefore, it is unlikely that the interaction of the compound **30c** with CL induces proton leak and decreases the coupling efficiency, especially, considering that the majority of the basal proton conductance is regulated through the proteins of the inner mitochondrial membrane, and the lipid bilayer of the inner membrane accounts for only 5 % of the proton leak (Brand et al., 2005; Cheng et al., 2017). Hence, other molecular targets were examined that could be associated with mitochondrial metabolism.

4.3.4 Enzymatic screening of isoselenazolium salts

First, PARP inhibitory activity of compound **30c** (0.25 μM) was examined on 13 PARP family proteins (Table 4.5), and it was found that **30c** selectively inhibits PARP1 isoform.

Table 4.5

Inhibitory effects of the compound 30c on different PARP isoforms

Enzyme	Inhibition, %	
	30c, 0.25 μM	**Reference (~1×C_{50})**
PARP1	100	50
PARP2	11	27
PARP3	2	84
TNKS1	24	45
TNKS2	9	27
PARP6	1	70
PARP7	36	18
PARP8	23	69
PAPR10	25	45
PARP11	51	64
PARP12	0	48
PARP14	0	51
PARP15	29	57

*PARP1-15 – poly(ADP-ribose) polymerase isoforms, TNKS1-2 – tankyrase 1 and 2

Looking for other possible molecular targets, compound **30c** (in 1 μM concentration) was tested on a metabolic enzyme panel, as well as on several members of the Bcl-2 family proteins (Table 4.6), which, among other processes, regulate apoptosis, as well as mitochondrial fission and fusion (Hardwick and Soane, 2013). Surprisingly, compound **30c** was found to selectively inhibit pyruvate kinase M2 (PKM2), one of the four isoforms of pyruvate kinase that is predominantly expressed in cancer tissues (Israelsen et al., 2013; Liu et al., 2015).

Table 4.6

Inhibitory effects of the compound 30c on metabolic enzymes activity

Enzyme	Inhibition, %	
	30c, 1 μM	**Reference (~1×C_{50})**
ACC1	6	60
ACC2	2	43
ACLY	2	94
COX1	10	33
COX2	4	94
FDH	0	–
GLS1	0	67
IDH1	4	–
IDH1(R132H)	0	64
IDH2	7	–
IDH2(R140Q)	5	11
IDO1	4	49
MAT2A	2	60
MTAP	1	–
PKL	1	–
PKR	21	–
PKM1	8	–
PKM2	96	–
Bcl-2	11	42
BclXL	8	29
Bcl2A1	24	66
Bcl2L2	10	40
Mcl-1	6	35

*ACC1 – acetyl-CoA carboxylase 1, ACC2 – acetyl-CoA carboxylase 2, ACLY – ATP citrate lyase, COX1 – cyclooxygenase 1, COX2 – cyclooxygenase 2, FDH – formate dehydrogenase, GLS1 – glutaminase 1, IDH1 – isocitrate dehydrogenase 1, IDH1(R132H) – isocitrate dehydrogenase 1 with a R132H mutation, IDH2 – isocitrate dehydrogenase 2, IDH2(R140Q) – isocitrate dehydrogenase 2 with a R140Q mutation, IDO1 – indoleamine-pyrrole 2,3-dioxygenase 1, MAT2A – methionine adenosyltransferase 2A, MTAP – S-methyl-5'-thioadenosine phosphorylase, PKL – pyruvate kinase L, PKR – pyruvate kinase R, PKM1 – pyruvate kinase M1, PKM2 – pyruvate kinase M2, TDO – tryptophan 2,3-dioxygenase, Bcl-2 – B-cell lymphoma 2 protein, BclXL – B-cell lymphoma protein extra-large, Bcl2A1 – Bcl-2 related protein A1, Bcl2L2 – Bcl-2-like protein 2, Mcl-1 – myeloid leukemia 1 protein.

After these intriguing findings, PARP1 and PKM2 inhibitory properties of other isoselenazolium salts were determined (Table 4.7). It turned out that compound **30c** had the highest PARP1 inhibitory activity among studied compounds with IC_{50} of 0.250 ± 0.08 μM, that is approx. 4 times lower than that of the compound **3**. It was clearly observed that the carboxyl groups in the pyridinium ring and lipophilic substituents in position 2 reduced the inhibitory activity.

PKM2 IC_{50} values for the isoselenazolium series were determined by a LDH-coupled assay. Isoselenazolium salts did not inhibit LDH and, therefore, were suitable for the chosen assay. Compounds **30b–32f** were found to selectively inhibit PKM2, and compound **30c** and its amide analogue **32c** stood out with 0.350 ± 0.068 and 0.420 ± 0.097 μM IC_{50} values, respectively. Surprisingly, the previously described PKM2 inhibitors apigenin and compound

3k did not inhibit PKM2 at concentrations up to 20 μM in used conditions. The studied isoselenazolium salts were more selective toward PKM2, as no compound reached a 50 % inhibition of either PKM1 or PKR at a concentration of 1 μM. In particular, the addition of fructose-1,6-bisphosphate (FBP), the natural allosteric activator of PKM2, did not significantly affect the inhibitory activity of the compounds studied.

Importantly, the ester or amide group in the isoselenazolopyridinium ring was essential for PKM2 inhibition, since the previously described unsubstituted isoselenazolopyridinium chloride **3** was approximately 8 times less active than compounds **30c** and **32c**.

Table 4.7

IC_{50} values of isoselenazolium chlorides for PKM2 and PARP1 inhibition and their inhibitory activity on PKM1, PKR and LDH at 1 μM concentration

Compound	IC_{50}, μM			Inhibition at 1 μM, %		
	PARP1	PKM2	PKM2 with FBP (250 μM)	PKM1	PKR	LDH
Apigenin	n.t.	> 20	> 20	n.t.	n.t.	n.t.
Comp. 3k (Ning et al., 2017)	n.t.	> 20	> 20	n.t.	n.t.	n.t.
Olaparib	0.0035 ± 0.0005	> 10	> 10	n.t.	n.t.	n.t.
3	0.970 ± 0.030	2.924 ± 0.356	2.731 ± 0.277	n.t.	n.t.	n.t.
30b	0.359 ± 0.070	0.545 ± 0.059	0.303 ± 0.081	16 ± 4	39 ± 6	10 ± 3
30c	0.250 ± 0.080	0.350 ± 0.068	0.477 ± 0.104	13 ± 1	21 ± 11	10 ± 7
30d	0.769 ± 0.021	0.478 ± 0.143	0.610 ± 0.022	10 ± 2	16 ± 14	13 ± 4
30e	0.307 ± 0.010	0.854 ± 0.263	0.603 ± 0.023	26 ± 4	20 ± 2	7 ± 2
30f	0.322 ± 0.012	0.380 ± 0.138	0.517 ± 0.036	20 ± 10	42 ± 3	6 ± 2
30g	0.438 ± 0.090	0.637 ± 0.137	0.572 ± 0.021	11 ± 4	29 ± 13	2 ± 1
30h	> 1	> 1	n.t.	n.t.	n.t.	n.t.
30i	> 1	> 1	n.t.	n.t.	n.t.	n.t.
30j	0.378 ± 0.020	0.897 ± 0.385	n.t.	29 ± 1	15 ± 6	7 ± 3
30k	> 1	1.355 ± 0.295	n.t.	10 ± 6	28 ± 14	7 ± 2
31b	1.370 ± 0.070	> 1	n.t.	n.t.	n.t.	n.t.
31c	1.620 ± 0.130	1.064 ± 0.266	n.t.	4 ± 3	5 ± 3	9 ± 4
32a	0.275 ± 0.014	> 1	n.t.	n.t.	n.t.	n.t.
32b	0.315 ± 0.080	> 1	n.t.	n.t.	n.t.	n.t.
32c	0.355 ± 0.090	0.420 ± 0.097	0.572±0.103	15 ± 8	37 ± 1	6 ± 2
32d	0.303 ± 0.080	0.362 ± 0.038	0.542±0.030	26 ± 4	40 ± 17	13 ± 5
32e	> 1	1.010 ± 0.264	n.t.	21 ± 3	11 ± 4	6 ± 1
32f	> 1	0.901 ± 0.173	n.t.	23 ± 3	29 ± 10	9 ± 2

*Values are shown as the means ± SD from at least 3 independent experiments. PKM2, pyruvate kinase M2 isoform; PKM1, pyruvate kinase M1 isoform; PKR, pyruvate kinase R isoform; LDH, L-lactate dehydrogenase from rabbit muscle; FBP, fructose-1,6-bisphosphate; n.t. – not tested.

4.3.5 Pyruvate kinase M2 inhibition mechanisms

The structure-activity relationship (SAR) pattern of the newly discovered PKM2 inhibitors (Figure 4.18 A) corresponded well to that of cytotoxicity. To elucidate the binding and inhibition mechanisms of isoselenazolium salts, the most potent inhibitors **30c** and **32c** were selected for the further biochemical and biophysical studies. To characterise the inhibition mechanism steady-state kinetic parameters for PKM2 for both PEP and ADP were determined in the presence of **30c** at different concentrations. It was established that in the presence of the compound **30c** the value of $V_{App,max}$ was constant, while the $K_{App,M}$ increased at higher inhibitor concentrations for both enzyme substrates. Additionally, a classic competitive inhibitor pattern was revealed in Lineweaver-Burk plots for both substrates (Figure 4.18 B and C).

The selenium atom in the isoselenazolium moiety has an electrophilic nature and may potentially react covalently with the nucleophilic cysteine side chains on the surface of PKM2. The reversibility of compound`s **32c** binding was tested using water ligand-observed gradient spectroscopy (WaterLOGSY). WaterLOGSY experiments detect the transfer of magnetisation from water protons to the ligand or, in the case of ligand association and dissociation occurring at the timescale of the NMR measurement, the transfer of magnetisation from water to the protein and then to the ligand.

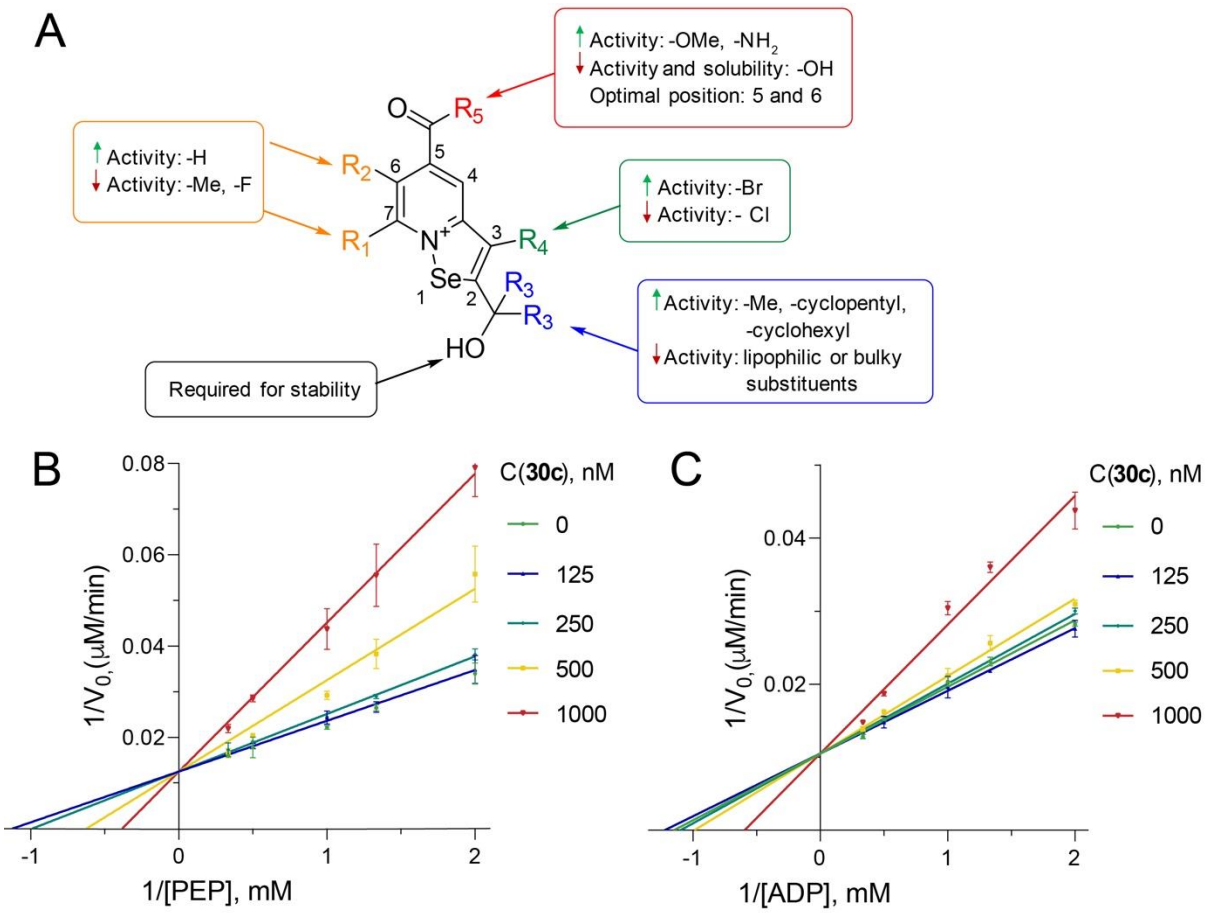

Figure 4.18 **A) Structure-activity relationship for PKM2 inhibitory activity of soselenazolopyridinium salts; B) PKM2 initial reaction rate (V_0) with respect to PEP oncentration at constant ADP concentration (2 mM) in the absence or in the presence of 30c at different concentrations; C) PKM2 initial reaction rate (V_0) with respect to ADP concentration at constant PEP concentration (2 mM) in the absence or in the presence of 30c at different concentrations**

Protons of free compound **32c** were observed with negative peak intensities, resulting from the cross relaxation via the nuclear Overhauser effect (NOE) (Figure 4.19 A, bottom). The addition of PKM2 to the compound **32c** caused an inversion of the peak intensity, i.e., negative NOE, suggesting that a reversible, noncovalent binding of the ligand to PKM2 has occurred, and the molecule has dissociated during the mixing time of the WaterLOGSY sequence (Figure 4.19 A, top).

PKM2 activity is regulated by a variety of metabolites that affect its quaternary assembly by promoting or inhibiting the more active tetrameric state, or by inducing interprotomer movements that result in altered activity (Wang et al., 2015; Macpherson et al., 2019; Srivastava, Nandi, and Dey, 2019; Nandi and Dey, 2020). To evaluate the effect of isoselenazolium salts on the oligomeric assembly of PKM2, analytical size-exclusion chromatography (SEC) measurements were performed. Under the experimental conditions tested, PKM2 eluted from the column primarily as tetrameric species, corresponding to the first peak in the chromatogram, followed by a dimer/monomer peak of a smaller magnitude

(Figure 4.19 B). As expected, the ratio of tetramer to dimer/monomer increased at higher protein concentrations. Incubation of 5 μM PKM2 with compounds **30c** or **32c** resulted in a dose-dependent increase in the tetramer ratio, with a concurrent reduction in the dimer/monomer peak (Figure 4.19 C).

However, SEC required a micromolar concentration of a protein, and the observed PKM2 dimer/tetramer ratio could not be physiologically relevant, considering its strong dependence on the concentration. Therefore, it was decided to apply single-molecule mass photometry to explore the oligomeric state of PKM2 at 100 times lower concentration. At a concentration of 50 nM (Figure 4.19 D) PKM2 was mostly in the dimeric state (69.1 ± 1.9 % of total oligomers), while monomers and tetramers were less prevalent (11.1 ± 3.0 % and 19.8 ± 4.3 %, respectively). As in the SEC experiment, the addition of compound **32c** led to a decrease in the dimer population in a dose-dependent manner, and at 5 μM two-fold reduction was observed (69.1 ± 1.9 % vs 35.8 ± 4,0 %, $p < 0.0001$). At the same time, the percentage of monomers was increased only at 5 μM (up to 38.0 ± 3.8 %, $p = 0.0002$). Interestingly, formation of trimeric species with molecular mass of approx. 180 kDa, that could not be distinguished by the SEC, could be clearly observed in mass photometry histograms. As expected, the addition of FBP (100 μM) increased the amount of tetramer and trimer at the expense of the dimer (Figure 4.19 E). When both FBP and compound **32c** were added, the changes in the populations became more complex, however, at 5 μM concentration, there was also an almost two-fold reduction in the amount of dimer (43.2 ± 2.5 % vs 23.7 ± 1.8 %, $p < 0.0001$), but in this case there was an increase in the proportion of tetrameric species (36.6 ± 1.5 % vs 52.6 ± 3.7 %, $p = 0.0004$). The results of both SEC and mass photometry are in stark contrast to previously published observations that natural activators of PKM2, such as FBP and serine, promote the formation of tetramers, while PKM2 inhibitors increase the proportion of dimeric/monomeric species (Nandi and Dey, 2020).

The melting temperature of PKM2 was examined using a SYPRO Orange-based differential scanning fluorimetry (DSF) assay. The PKM2 melting curves displayed a multimodal character (Figure 4.19 F). The decrease in PKM2 concentration from 5 to 2.5 μM led to an increase in low-stability species. For 2.5 μM PKM2, three distinct transitions were observed: the first in 20–40 °C range, followed by 40–50 °C, and finally a dominant transition at 60 °C. These data suggest that a mixture of species of different stabilities exist that, presumably, represent distinct oligomeric states. Alternatively, the observed species may represent different conformational states in the oligomeric assembly, such as the previously reported T- or R-states (Wang et al., 2015).

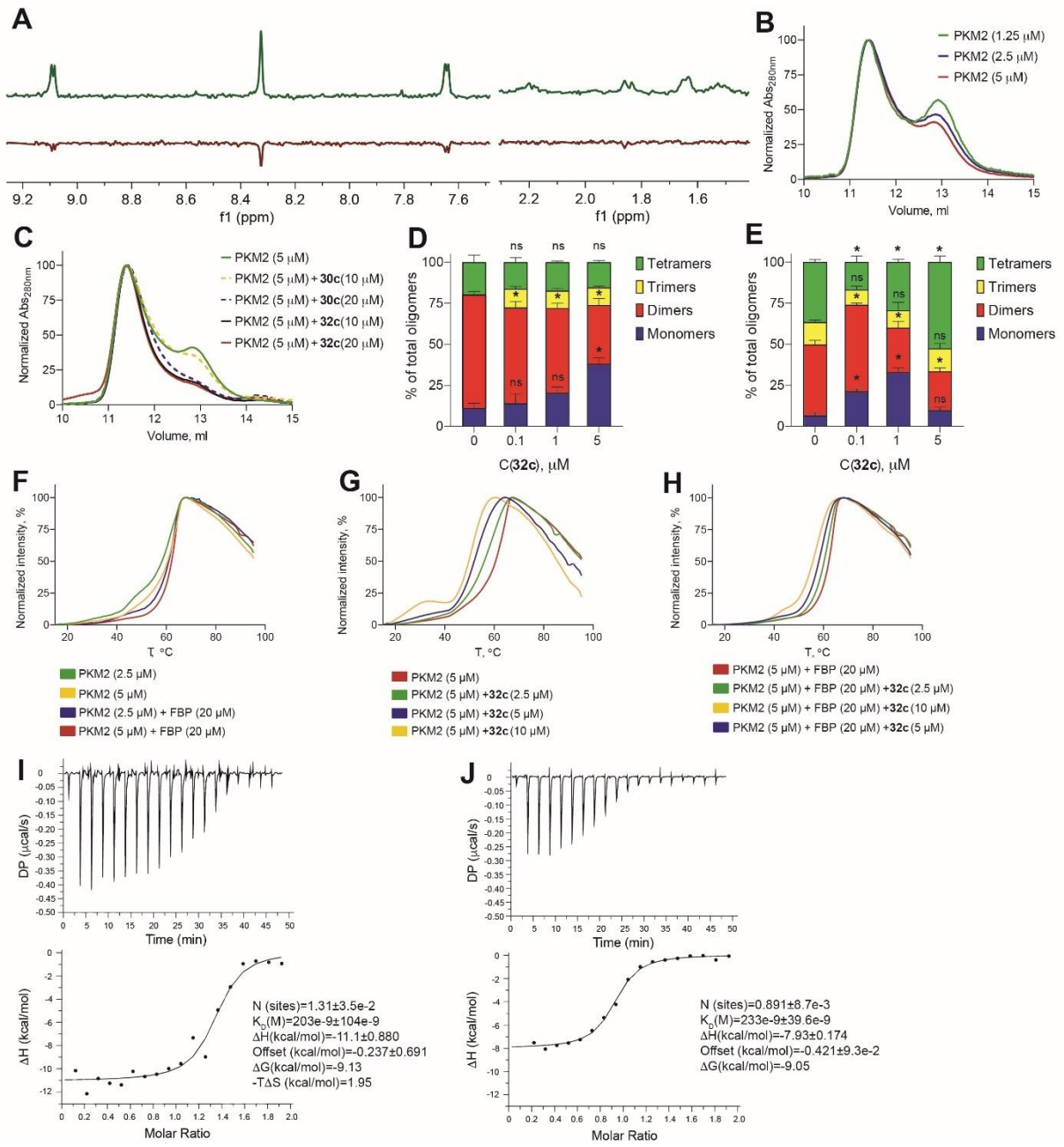

Figure 4.19 **A) WaterLOGSY spectra of 250 μM compound 32c alone (bottom, red) or in the presence of 12.5 μM PKM2 (top, green); B) SEC of PKM2 at various concentrations; C) SEC of 5 μM PKM2 preincubated with 30c or 32c at either 10 μM or 20 μM concentration; D) Oligomeric state of PKM2 (50 nM) in the presence of 32c at different concentrations revealed by mass photometry (n=3); E) Oligomeric state of PKM2 (50 nM) in the presence of FBP (100 μM) and 32c at different concentrations revealed by mass photometry (n=3); F) DSF thermal melt data for PKM2 alone or in the presence of FBP; G) DSF thermal melt data for PKM2 (5 μM) in the presence of 32c at various concentrations; H) DSF thermal melt data for PKM2 (5 μM) in the presence of FBP (20 μM) and 32c at various concentrations; I) Isotherm of PKM2 (20 μM) titration with FBP (200 μM); J) Isotherm of PKM2 (20 μM) titration with FBP (200 μM) after preincubation with 32c (40 μM); ***

*The results are presented as a mean value of at least 3 independent experiments. Statistically significant difference (*) was considered when $p<0.05$ (one-way ANOVA) compared to the control group.

FBP has been shown to stabilise PKM2 against thermal denaturation, and the data obtained was in a good agreement with previously published report and consistent with the mass photometry measurements (Wang et al., 2015). FBP decreased the population of low-stability species but did not change the temperature at which maximum fluorescence is obtained, suggesting that FBP induced the formation of high-stability species but did not significantly stabilise the tertiary fold.

Compound **32c** destabilised PKM2 in a dose-dependent manner (Figure 4.19 G). Destabilisation may arise as a result of a change in the oligomeric assembly or as a result of changes in the tertiary fold. At high concentration (10 μM), compound **32c** induced the formation of a significantly destabilised population which melts at 2040 °C, that is only marginally present for PKM2 alone. In turn, FBP decreased the magnitude of destabilisation induced by the compound **32c** (Figure 4.19 H). Because FBP does not appear to stabilise the tertiary, but rather the quaternary structure, it is possible that the compound **32c** and FBP induce competing conformational changes in the PKM2 oligomer. This suggestion is in line with the ITC data, which showed that FBP had a high affinity for PKM2 in the absence (Figure 4.19 I) and in the presence of the compound **32c** (Figure 4.19 J) but had a substantially lower binding enthalpy in the latter case, suggesting that the local interactions of FBP with the enzyme are maintained, while its effect on the quaternary structure is perturbed.

4.3.6 Alterations in mRNA expression of pyruvate kinases M2 and M1

Another way to modulate enzyme activity is to reduce its expression. The expression of PKM1 and PKM2 mRNA was evaluated by qPCR, and compound 3k was used as a positive control (Park et al., 2021). Treatment of 4T1 cells with the compound **30c** (0.25 and 0.5 μM) for 24 h resulted in an approximately three-fold decrease in the expression of PKM2 mRNA compared to untreated cells ($p < 0.001$), while the expression of PKM1 was not significantly altered (Figure 4.20 A and B, respectively). Although compound 3k was not active in the enzymatic assay, it was able to reduce the expression of PKM2 mRNA in 4T1 cells at 0.5 μM. In case of HCC1937, treatment with 0.25 and 0.5 μM compound **30c** caused a 4-fold and 20-fold decrease in the expression of PKM2, respectively (Figure 4.20 C), while 3k was effective only at 0.5 μM. At the same time, PKM1 expression was not statistically significantly reduced by the compound **30c** (Figure 4.20 D); however, compound 3k induced a three-fold decrease in PKM1 mRNA levels ($p = 0.0021$). Therefore, compound **30c** modulated the expression of PKM2 mRNA more effectively and selectively than compound 3k in both studied cell lines.

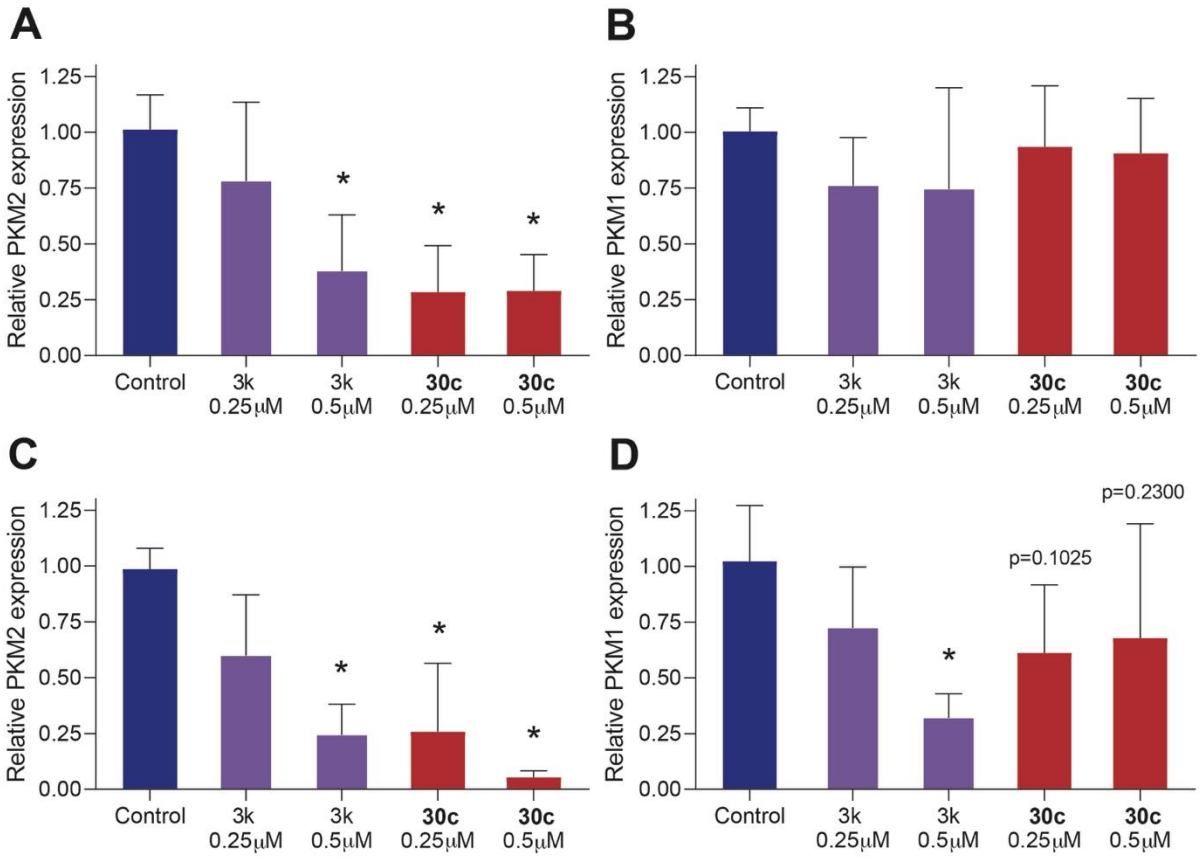

Figure 4.20 **Relative PKM2 mRNA expression in 4T1(A) and HCC1937 (C) cells and relative PKM1 mRNA expression in 4T1(B) and HCC1937 (D) cells obtained by qPCR after 24h treatment with compound 3k or 30c at 0.25 and 0.5 µM concentrations***

* The results are presented as mean ± SD of 5–7 independent experiments. Statistically significant difference (*) was considered when $p < 0.05$ (one-way ANOVA) compared to the control group (vehicle).

4.3.7 Prevention of pyruvate kinase M2 nuclear translocation

Apart from its role in glycolysis, dimeric form of PKM2 can translocate into the nucleus where it functions as protein kinase and a transcriptional coactivator of many genes associated with carcinogenesis (Zahra et al., 2020). Furthermore, it has been reported that among numerous post-translational modifications PKM2 can undergo PArylation (modification with poly(ADP-ribose), PAr) in a nucleus catalysed by PARP1. PArylation enhances nuclear retention of PKM2 and is required for proto-oncogene c-Myc and glycolysis-related GLUT and LDH genes induction (Li et al., 2016). Also, synergy between the PKM2 inhibitor shikonin and PARP1 inhibitor olaparib has been recently shown in ovarian cancer models both *in vitro* and *in vivo* (Zhou et al., 2022). Considering isoselenazolium salts PARP1 inhibitory activity and ability to reduce dimer amount of PKM2, it was of special interest to investigate whether they can impede nuclear translocation of PKM2.

Intracellular localisation of PKM2 and PAr in 4T1 cells was examined by double immunofluorescence labelling with subsequent analysis by confocal microscopy. While PAr was clearly and almost exclusively located in the nuclei in 4T1 cells, PKM2 was all around the

cytoplasm after stimulation with $CoCl_2$, and it was difficult to assess nuclear localisation in regular 2D confocal images. Therefore, only 3D confocal imaging with the inspection of orthogonal projections could help to define the true location inside nuclei (Figure 4.21).

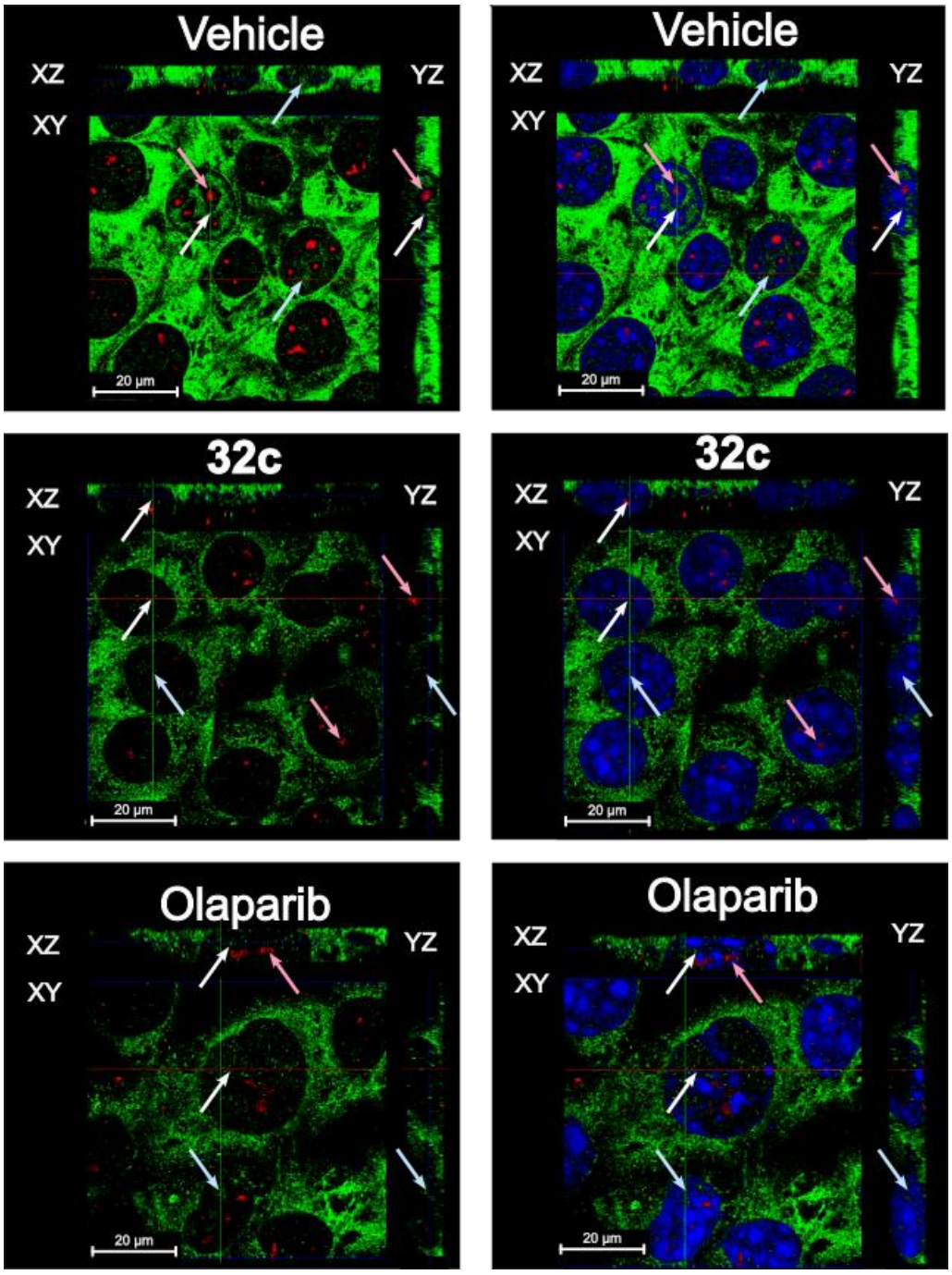

Figure 4.21 **Representative confocal images of PKM2 (green) and PAr (red) localisation in 4T1 cells in orthogonal projections after treatment with vehicle (control, upper section), compound 32c (2 µM, middle section) or olaparib (2 µM, lower section) followed by stimulation with $CoCl_2$ (100 µM). Nuclei were counterstained with DAPI (blue)**

In the control group (vehicle), the PKM2 signal was high all across the cytoplasm, however nuclear location of PKM2 was indisputably confirmed in the XZ and YZ sections by counterstaining the nuclei with DAPI. After treatment of the cells with compound **32c**, as

anticipated from the qPCR data, PKM2 signal throughout the cells was lower, and, surprisingly, treatment with olaparib gave similar results.

To quantitatively assess nuclear translocation of PKM2 and the amount of PAr, signal counts inside the nuclei and relative volume occupied were analysed. The analysis revealed that both compound **32c** and olaparib significantly decreased the PKM2 signal count (Figure 4.22 A) and the relative volume (Figure 4.22 B) compared to the control cells, and a pairwise comparison using Dunn's test showed that compound **32c** was superior to olaparib ($p < 0.001$) in both aspects.

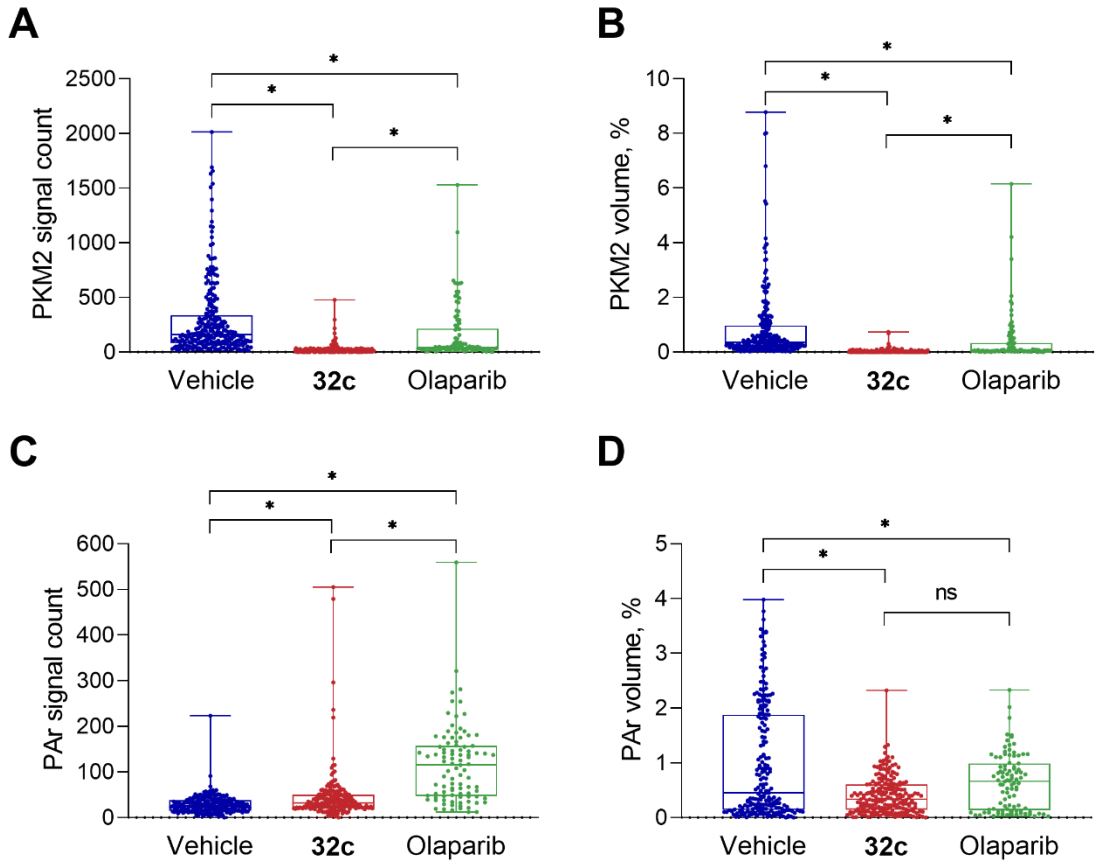

Figure 4.22 **A) PKM2 signal count inside the nuclei; B) Relative volume of nuclei taken by PKM2; C) PAr signal count inside the nuclei; D) Relative volume of nuclei taken by PAR after 24 h treatment of 4T1 cells with vehicle, compound 32c or olaparib (2 µM) with subsequent stimulation with $CoCl_2$ (100 µM) for 24h***

*Each point represents a single cell. Data was analysed with Kruskal-Wallis test followed by Dunn`s multiple comparisons test. Statistically significant difference (*) was considered when $p < 0.05$.

Unlike PKM2, which mainly generates a point signal, PAr forms long polymer chains that are seen on image as large aggregates. PAr count inside the nuclei after the treatment with compound **32c** or olaparib (Figure 4.22 C) was higher than in the control group ($p < 0.001$), but the relative volume taken by these aggregates (Figure 4.22 D) was smaller ($p < 0.001$). Thus, shorter PAr chains were formed that confirmed inhibition of PARP activity. The effects of

compound **32c** and olaparib were similar, although PAr count after **32c** treatment was slightly lower than after olaparib, while no difference between reduction in relative volume was observed between the two. Therefore, isoselenazolium salts reduce PKM2 amount in the nuclei, presumably, by decreasing the amount of PKM2 dimers and preventing its nuclear retention by inhibition of PARP1.

From the results, it is clear that isoselenazolium chlorides bearing a carbonyl-[1,2]isoselenazolo[2,3-a]pyridinium moiety are prospective cytotoxic agents with potent and isoform-selective PARP1 and PKM2 inhibitory properties. Unlike other PKM2 inhibitors, isoselenazolium derivatives reduce the proportion of dimeric PKM2 species and induce an unstable PKM2 conformation that results in impaired enzymatic function and reduced nuclear translocation. Furthermore, PKM2 is inhibited at both the protein and transcript levels, as was shown by the reduction in PKM2 mRNA. This inhibitory activity leads to intracellular redox imbalance and, consequently, to a cell death.

5 Discussion

The discovery of a mechanism of action is a corner stone in the development of new drug candidates for anticancer therapy. The first generation of isoselenazolium salts had high cytotoxicity against breast cancer *in vitro* and was much less cytotoxic to normal cells. As expected, these selenium-containing compounds affected cellular metabolism: reduced NAD^+ and NADH levels, inhibited PARP1, pyruvate-dependent mitochondrial respiration, and induced ROS production. It was clear, that isoselenazolium salts compromise mitochondrial CI output, but do not directly inhibit CI, however, the precise mechanism of action was not identified first. As CI is stabilised by CL, its activity can be affected by ROS-induced peroxidation of CL or by destabilisation of lipid bilayer through a direct interaction (Paradies et al., 2002; Petrosillo et al., 2007). NMR and ITC data suggested that isoselenazolium salts interacted with CL and it was initially proposed as a potential molecular target.

Traditional drug targets, e.g. enzymes, receptors and ion channels usually have robust screening assays that are suitable for high throughput screening. Historically, particular phospholipids, such as CL, were recognised as a prospective drug target much later and until now there were no available drug screening methods. Therefore, a new CL-specific fluorescent probe was developed for a competitive binding assay. The new screening assay allows to assess CL as a potential molecular target and would be highly appreciated by scientists working on therapies designed to protect or damage the inner mitochondrial membrane, targeted drug delivery into mitochondria, or antimicrobial therapy. Additionally, this method might help predict drugs interactions with the mitochondrial membrane and, perhaps, warn about possible side effects related to mitochondrial dysfunction in the early stage of a research. However, the isoselenazolium salts in this assay showed a low affinity for CL; therefore, their cytotoxic effect can hardly be attributed to the direct interaction with CL. These results underscore the importance of using various methods based on different principles to validate a molecular target.

The second generation of isoselenazolium derivatives exhibited high cytotoxic effect not only against breast cancer, but also against hepatocellular carcinoma, lung cancer and T cell leukaemia models *in vitro*. These compounds were more potent PARP1 inhibitors, however, showed similar effect on mitochondrial respiration as the first-generation compounds. Consequently, it was found that compound **30c** is a potent and selective PKM2 inhibitor.

Understanding the precise molecular mechanism of the interaction of a ligand with a target protein is crucial for hit-to-lead optimisation. Atomic-level structural methods, such as protein X-ray crystallography, provide the most detailed insight for target-based drug design,

however, attempts to obtain PKM2 and isoselenazolium salts co-crystals were unsuccessful. Apparently, co-crystallisation was obstructed by the destabilisation of the quaternary structure by the compounds. Therefore, other biochemical and biophysical methods had to be used to explore the binding mechanism. Although isoselenazolium salts have a kinetic signature of a competitive inhibitor, it does not necessarily mean that they unequivocally bind to the active site of the enzyme. An inhibitor and a substrate could bind to different sites that negatively interfere with one another, that is, through allosteric interactions driven by inhibitor-induced conformational changes. (Robert A. Copeland, 2013) This is a rare occasion, but such competitive allosteric inhibition mechanism has been reported a few times. (Luo et al., 2007; Alphey et al., 2013; Feldman et al., 2016) DSF, SEC and mass photometry data indicate that isoselenazolium salts inhibit PKM2 in a noncanonical fashion, inducing an unstable, functionally deficient tetrameric conformation. Notably, a natural PKM2 allosteric activator FBP does not compete with isoselenazolium salts binding site nor restore enzymatic function and quaternary structure at physiologically relevant concentration (Macpherson et al., 2019).

The proposed isoselenazolium`s mechanism of action is schematically shown in Figure 5.1. As PKM2 is the only enzyme producing ATP in the energy payoff phase of glycolysis, inhibition of PKM2 enzymatic function makes the main ATP production pathway in cancer cells unprofitable. At the same time, CI and OXPHOS coupling are disrupted, presumably by a drastic increase in ROS production, that should furthermore exacerbate the cellular energy crisis. Although it has been shown that PKM2 in its inactive dimeric state stimulates ROS detoxification by increasing glucose-6-phosphate flux into the pentose phosphate pathway, which provides NADPH for glutathione reductase (Anastasiou et al., 2011), and inhibits ROS-induced apoptosis by phosphorylating and stabilizing Bcl-2 (Liang et al., 2017), it does not cope with isoselenazolium induced oxidative burst. Concurrently, overall PKM2 expression is also substantially reduced. Additionally, it was found that **30c** significantly decreased NAD^+ and NADH pools in breast cancer cells and had no effect in cardiomyoblasts. Whether it is a consequence of inhibition of PKM2 or an off-target effect remains to be discovered.

As previously reported, the dimeric form of PKM2 translocates to the nucleus, where it acts as a protein kinase and a transcriptional coactivator, while the tetrameric form does not (Dong et al., 2016). Therefore, a decrease in the amount of dimeric species is crucial for the suppression of PKM2 nonmetabolic function and the suppression of the tumour growth.

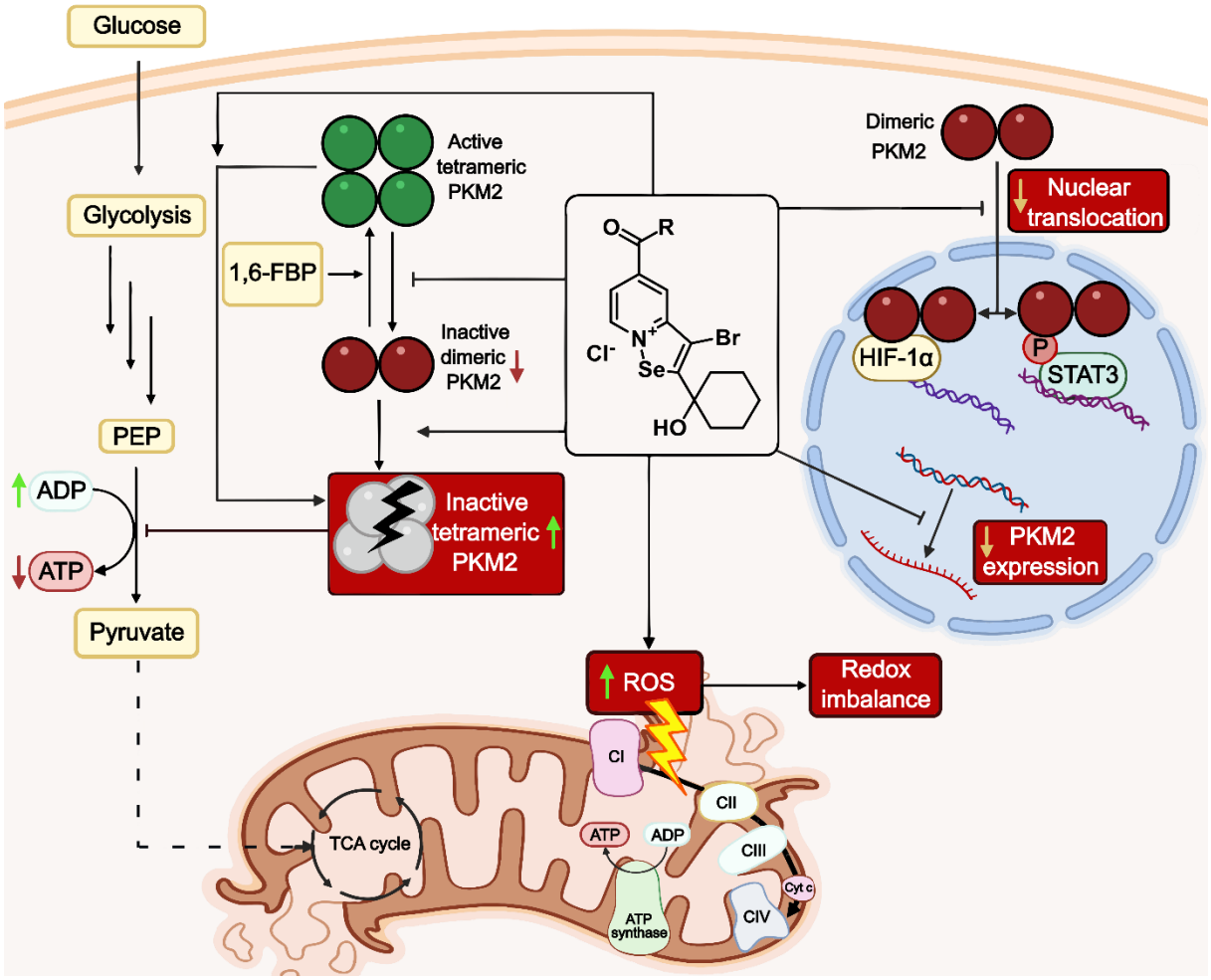

Figure 5.1 **Proposed mechanism of action of isoselenazolium salts***

*Isoselenazolium salts reduce dimer/tetramer ratio of PKM2 and induce inactive conformation of both dimeric and tetrameric PKM2, thus inhibiting the production of pyruvate and ATP. Increased ROS production causes uncoupling of complex I and OXPHOS, leading to redox imbalance. In parallel, PKM2 nuclear translocation is blocked and PKM2 gene expression reduced.

For example, Gao and colleagues has shown that a mutant PKM2 (R399E), which does not form a tetramer, promotes STAT3 phosphorylation and increases tumour growth rate *in vivo* compared to the wild-type PKM2-expressing tumour in a colon adenocarcinoma model (Gao et al., 2012). In this work it was found that compound **32c** decreases the presence of PKM2 in the nuclei and there are two mechanisms involved. Firstly, the dimer amount of PKM2 that can move into the nuclei is lowered, and secondly, PArylation of PKM2 by PARP1 is inhibited and nuclear retention is impaired.

Thereby, isoselenazolium salts restrain PKM2 functions at three levels: decrease protein expression, reduce metabolic enzymatic function, and prevent nuclear non-metabolic functions by the restriction of translocation. It is yet unknown which of these effects contributes the most to the antiproliferative activity, but it can be speculated that the decrease in the dimer/tetramer ratio is the most important. Such assumption has been supported by the similar antiproliferative

activity of small molecule PKM2 activators that promote active tetramer formation, reduce dimer amount, and block nuclear translocation (Warner, Carpenter, and Bearss, 2014; Giannoni et al., 2015; Li et al., 2018).

An open question is how isoselenazolium salts cause such an increase in mitochondrial ROS production. The results demonstrated that ROS overproduction is not caused by the decrease of the NAD^+/NADH ratio nor the reverse electron transport. What is noticeable is that PKM2 has also been reported to be involved in mitochondrial ROS generation, although the precise mechanism is unknown (Gao et al., 2022). Inversely, PKM2 activators TEPP-46 and DASA-58 were shown to reduce ROS production. Thus, these results suggest the possible relationship between PKM2 inhibition and ROS overproduction. However, it is possible that isoselenazolium salts affect reduced glutathione levels or its metabolism, but further studies are needed to verify this.

Taken together, these findings establish a ground for the novel class of drug candidates with a unique molecular mechanism and reveal specific structural features of PKM2. Furthermore, a potent and stable inhibitor would be an integral part of future studies focusing on the metabolic role of PKM2 in cancer.

Conclusions

1. The hypothesis was confirmed: isoselenazolium derivatives exhibit high cytotoxicity in breast, liver, lung, and T-cell leukaemia cell models. These compounds have a wide impact on energy metabolism in cancer cells, including modulation of pyruvate-dependent mitochondrial respiration, induction of H_2O_2 production, dyscoupling of the electron transport system, decrease in NAD^+ concentration, inhibition of PARP1 and PKM2.
2. The competitive binding assay based on the cardiolipin-specific fluorescent probe **20** offers a robust way to determine relative affinity for cardiolipin. However, isoselenazolium salts affinity is low and is unlikely to be associated with its pharmacological activity.
3. An ester or amide group in the position 5 or 6 of the isoselenazolopyridinium ring is essential for both PARP1 and PKM2 inhibitory activity.
4. The major molecular target for isoselenazolium salts is PKM2. Isoselenazolium chlorides have an unusual mechanism of PKM2 inhibition, inducing a functionally deficient tetrameric assembly that leads to impaired enzymatic function and decreased nuclear transfer.

Publications and reports on topics of Doctoral Thesis

Publications

1. **Dimitrijevs, P.,** Domracheva, I., Arsenyan, P. 2020. Improved method for the preparation of nonyl acridine orange analogues and utilization in detection of cardiolipin. *New Journal of Chemistry*. 44(23), 9626–9633. doi:10.1039/D0NJ02116D
2. Makrecka-Kuka, M., **Dimitrijevs, P.,** Domracheva, I., Jaudzems, K., Dambrova, M., Arsenyan, P. 2020. Fused isoselenazolium salts suppress breast cancer cell growth by dramatic increase in pyruvate-dependent mitochondrial ROS production. *Scientific Reports*. 10(1), 21595. doi:10.1038/s41598-020-78620-8
3. **Dimitrijevs, P.,** Arsenyan, P. 2021. Cardiolipin in the spotlight: Quantitative analysis and fluorescence-based competitive binding assay. *Sensors and Actuators B: Chemical*. 346, 130537. doi:10.1016/j.snb.2021.130537
4. **Dimitrijevs, P.,** Makrecka-Kuka, M., Bogucka, A., Hyvönen, M., Pantelejevs, T., Arsenyan, P. 2023. Development of isoselenazolium chlorides as selective pyruvate kinase isoform M2 inhibitors. *European Journal of Medicinal Chemistry*. 257, 115504. doi:10.1016/ j.ejmech.2023.115504

Reports and theses at international congresses and conferences

1. **Dimitrijevs, P.** Novel method for evaluating cardiolipin as a potential molecular drug target and its quantitative analysis, 12th World Congress on Targeting Mitochondria, October 27-29, 2021, online.

Patent applications

1. Arsenjans, P., **Dimitrijevs, P.** Fluorescent acridinium salts, synthesis thereof and use for detection of cardiolipin. WO2021105780A1, 2021.
2. Arsenjans, P., **Dimitrijevs, P.** An assay for measuring binding affinity for cardiolipin of biologically active compounds. WO2022038424A1, 2022.
3. Arsenjans, P., **Dimitrijevs, P.**, Makrecka-Kuka, M. Novel pyruvate kinase isoform M2 inhibitors. Filed: 20.04.2022, (LVP2022000034).

References

1. Alphey, M. S., Pirrie, L., Torrie, L. S., Boulkeroua, W. A., Gardiner, M., Sarkar, A., Maringer, M., Oehlmann, W., Brenk, R., Scherman, M. S., Mcneil, M., Rejzek, M., Field, R. A., Singh, M., Gray, D., Westwood, N. J., Naismith, J. H. 2013. Allosteric Competitive Inhibitors of the Glucose-1-phosphate Thymidylyltransferase (RmlA) from Pseudomonas aeruginosa. *ACS Chemical Biology*. 8, 387–397.

2. Anastasiou, D., Poulogiannis, G., Asara, J. M., Boxer, M. B., Jiang, J. kang, Shen, M., Bellinger, G., Sasaki, A. T., Locasale, J. W., Auld, D. S., Thomas, C. J., Heiden, M. G. Vander, Lewis, C. 2011. Inhibition of pyruvate kinase M2 by reactive oxygen species contributes to cellular antioxidant responses. *Science*. 334(6060), 1278–1283. doi:10.1126/science.1211485.Inhibition

3. Arimura, Y., Yano, T., Hirano, M., Sakamoto, Y., Egashira, N., Oishi, R. 2012. Mitochondrial superoxide production contributes to vancomycin-induced renal tubular cell apoptosis. *Free Radical Biology and Medicine*. 52(9), 1865–1873. doi:10.1016/j.freeradbiomed.2012.02.038

4. Arora, S., Joshi, G., Chaturvedi, A., Heuser, M., Patil, S., Kumar, R. 2022. A Perspective on Medicinal Chemistry Approaches for Targeting Pyruvate Kinase M2. *Journal of Medicinal Chemistry*. 65(2), 1171–1205. doi:10.1021/acs.jmedchem.1c00981

5. Arsenyan, P., Vasiljeva, J., Belyakov, S., Liepinsh, E., Petrova, M. 2015. Fused Selenazolinium Salt Derivatives with a Se-N^+ Bond: Preparation and Properties. *European Journal of Organic Chemistry*. 2015(26), 5842–5855. doi:10.1002/ejoc.201500582

6. Arsenyan, P., Vasiljeva, J., Domracheva, I., Kenepe-Lapsa, I., Gulbe, A. 2019. Selenopheno[2,3-f]coumarins: a novel scaffold with antimetastatic activity against melanoma and breast cancer. *New Journal of Chemistry*. 43, 11851–11864. doi:10.1039/c9nj01682a

7. Arsenyan, P., Vasiljeva, J. 2017. Selenazolium salts as catalysts in oxidation reactions. *Mendeleev Communications*. 27(6), 621–622. doi:10.1016/j.mencom.2017.11.028

8. Aslan, E., Adem, S. 2015. In Vitro Effects of Some Flavones on Human Pyruvate Kinase Isoenzyme M2: THE EFFECTS OF FLAVONES ON PKM2. *Journal of Biochemical and Molecular Toxicology*. 29(3), 109–113. doi:10.1002/jbt.21673

9. Azad, G. K., Tomar, R. S. 2014. Ebselen, a promising antioxidant drug: mechanisms of action and targets of biological pathways. *Molecular Biology Reports*. 41(8), 4865–4879. doi:10.1007/s11033-014-3417-x

10. Azoitei, N., Becher, A., Steinestel, K., Rouhi, A., Diepold, K., Genze, F., Simmet, T., Seufferlein, T. 2016. PKM2 promotes tumor angiogenesis by regulating HIF-1α through NF-κB activation. *Molecular Cancer*. 15(1), 3. doi:10.1186/s12943-015-0490-2

11. Behroozi, F., Abdkhodaie, M. J., Abandansari, H. S., Satarian, L., Molazem, M., Al-Jamal, K. T., Baharvand, H. 2018. Engineering folate-targeting diselenide-containing triblock copolymer as a redox-responsive shell-sheddable micelle for antitumor therapy in vivo. *Acta Biomaterialia*. 76, 239–256. doi:10.1016/j.actbio.2018.05.031

12. Brand, M. D., Pakay, J. L., Ocloo, A., Kokoszka, J., Wallace, D. C., Brookes, P. S., Cornwall, E. J. 2005. The basal proton conductance of mitochondria depends on adenine nucleotide translocase content. *Biochemical Journal*. 392(2), 353–362. doi:10.1042/BJ20050890

13. Brasseur, R., Laurent, G., Ruysschaert, J. M., Tulkens, P. 1984. Interactions of aminoglycoside antibiotics with negatively charged lipid layers. *Biochemical Pharmacology*. 33(4), 629–637. doi:10.1016/0006-2952(84)90319-8

14. Brookes, P. S. 2005. Mitochondrial H+ leak and ROS generation: An odd couple. *Free Radical Biology and Medicine*. 38(1), 12–23. doi:10.1016/j.freeradbiomed.2004.10.016

15. Cantó, C., Sauve, A. A., Bai, P. 2013. Crosstalk between poly(ADP-ribose) polymerase and sirtuin enzymes. *Molecular Aspects of Medicine*. 34(6), 1168–1201. doi:10.1016/j.mam.2013.01.004

16. Chan, K., Truong, D., Shangari, N., O'Brien, P. J. 2005. Drug-induced mitochondrial toxicity. *Expert Opinion on Drug Metabolism & Toxicology*. 1(4), 655–669. doi:10.1517/17425255.1.4.655

17. Chen, Z., Tan, L., Hu, L., Luan, Y. 2015. Superior fluorescent probe for detection of potassium ion. *Talanta*. 144, 247–251. doi:10.1016/j.talanta.2015.06.015

18. Cheng, J., Nanayakkara, G., Shao, Y., Cueto, R., Wang, L., Yang, W. Y., Tian, Y., Wang, H., Yang, X. 2017. Mitochondrial Proton Leak Plays a Critical Role in Pathogenesis of Cardiovascular Diseases. *Adv Exp Med Biol*. 982, 359–370. doi:10.1007/978-3-319-55330-6_20

19. Chicco, A. J., Sparagna, G. C. 2007. Role of cardiolipin alterations in mitochondrial dysfunction and disease. *American Journal of Physiology-Cell Physiology*. 292(1), C33–C44. doi:10.1152/ajpcell.00243.2006

20. Chowdhury, A., Santra, A., Bhattacharjee, K., Ghatak, S., Saha, D. R., Dhali, G. K. 2006. Mitochondrial oxidative stress and permeability transition in Isoniazid and Rifampicin induced liver injury in mice. *Journal of Hepatology*. 45(1), 117–126. doi:10.1016/j.jhep.2006.01.027

21. Chuai, H., Zhang, S. Q., Bai, H., Li, J., Wang, Y., Sun, J., Wen, E., Zhang, J., Xin, M. 2021. Small molecule selenium-containing compounds: Recent development and therapeutic applications. *European Journal of Medicinal Chemistry*. 223, 113621. doi:10.1016/j.ejmech.2021.113621

22. Domenech, O., Francius, G., Tulkens, P. M., Van Bambeke, F., Dufrêne, Y., Mingeot-Leclercq, M. P. 2009. Interactions of oritavancin, a new lipoglycopeptide derived from vancomycin, with phospholipid bilayers: Effect on membrane permeability and nanoscale lipid membrane organization. *Biochimica et Biophysica Acta - Biomembranes*. 1788(9), 1832–1840. doi:10.1016/j.bbamem.2009.05.003

23. Dong, G., Mao, Q., Xia, W., Xu, Y., Wang, J., Xu, L., Jiang, F. 2016. PKM2 and cancer: The function of PKM2 beyond glycolysis. *Oncology Letters*. 11(3), 1980–1986. doi:10.3892/ol.2016.4168

24. Duveau, D. Y., Arce, P. M., Schoenfeld, R. A., Raghav, N., Cortopassi, G. A., Hecht, S. M. 2010. Synthesis and characterization of mitoQ and idebenone analogues as mediators of oxygen consumption in mitochondria. *Bioorganic & Medicinal Chemistry*. 18(17), 6429–6441. doi:10.1016/j.bmc.2010.06.104

25. Echtay, K. S., Roussel, D., St-Plerre, J., Jekabsons, M. B., Cadenas, S., Stuart, J. A., Harper, J. A., Roebuck, S. J., Morrison, A., Pickering, S., Clapham, J. C., Brand, M. D. 2002. Superoxide activates mitochondrial uncoupling proteins. *Nature*. 415(6867), 96–99. doi:10.1038/415096a

26. El Khoury, M., Swain, J., Sautrey, G., Zimmermann, L., Van Der Smissen, P., Décout, J. L., Mingeot-Leclercq, M. P. 2017. Targeting Bacterial Cardiolipin Enriched Microdomains: An Antimicrobial Strategy Used by Amphiphilic Aminoglycoside Antibiotics. *Scientific Reports*. 7(1), 1–12. doi:10.1038/s41598-017-10543-3

27. Elmer-Dixon, M. M., Hoody, J., Steele, H. B. B., Becht, D. C., Bowler, B. E. 2019. Cardiolipin Preferentially Partitions to the Inner Leaflet of Mixed Lipid Large Unilamellar Vesicles. *The Journal of Physical Chemistry B*. 123(43), 9111–9122. doi:10.1021/acs.jpcb.9b07690

28. Epand, R. M., Epand, R. F. 2009. Hormonal, metabolic and cardiovascular responses to hypoglycaemia in type 1 diabetes. Madsbad. 1982.pdf. *BBA - Biomembranes*. 1788(1), 289–294. doi:10.1016/j.bbamem.2008.08.023

29. Esterberg, R., Linbo, T., Pickett, S. B., Wu, P., Ou, H. C., Rubel, E. W., Raible, D. W. 2016. Mitochondrial calcium uptake underlies ROS generation during aminoglycoside-induced hair cell death. *Journal of Clinical Investigation*. 126(9), 3556–3566. doi:10.1172/JCI84939

30. Fan, C. D., Fu, X. Y., Zhang, Z. Y., Cao, M. Z., Sun, J. Y., Yang, M. F., Fu, X. T., Zhao, S. J., Shao, L. R., Zhang, H. F., Yang, X. Y., Sun, B. L. 2017. Selenocysteine induces apoptosis in human glioma cells: Evidence for TrxR1-targeted inhibition and signaling crosstalk. *Scientific Reports*. 7(1), 1–11. doi:10.1038/s41598-017-06979-2

31. Fan, J., Kamphorst, J. J., Mathew, R., Chung, M. K., White, E., Shlomi, T., Rabinowitz, J. D. 2013. Glutamine-driven oxidative phosphorylation is a major ATP source in transformed mammalian cells in both normoxia and hypoxia. *Molecular Systems Biology*. 9(712), 1–11. doi:10.1038/msb.2013.65

32. Feldman, H. C., Tong, M., Wang, L., Meza-acevedo, R., Gobillot, T., Lebedev, I., Hari, S. B., Gliedt, M. J., Arinjay, K., Backes, B. J., Papa, F. R., Seeliger, M. A., Maly, D. J. 2016. Structural and Functional Analysis of the Allosteric Inhibition of IRE1α with ATP-Competitive Kinase Ligands Structural and Functional Analysis of the Allosteric Inhibition of IRE1α with ATP-Competitive Ligands. *ACS Chemical Biology*. 11(8), 2195–2205. doi:10.1021/acschembio.5b00940

33. Flaig, T. W., Glodé, M., Gustafson, D., Van Bokhoven, A., Tao, Y., Wilson, S., Su, L. J., Li, Y., Harrison, G., Agarwal, R., Crawford, E. D., Lucia, M. S., Pollak, M. 2010. A study of high-dose oral silybin-phytosome followed by prostatectomy in patients with localized prostate cancer: Silybin-Phytosome in Prostate Cancer. *The Prostate*. 70(8), 848–855. doi:10.1002/pros.21118

34. Forge, A., Zajic, G., Davies, S., Weiner, N., Schacht, J. 1989. Gentamicin alters membrane structure as shown by freeze-fracture of liposomes. *Hearing Research*. 37(2), 129–139. doi:10.1016/0378-5955(89)90035-X

35. Forman, H. J., Azzi, A. 1997. On the virtual existence of superoxide anions in mitochondria: thoughts regarding its role in pathophysiology. *The FASEB Journal*. 11(5), 374–375. doi:10.1096/fasebj.11.5.9141504

36. Formentini, L., Moroni, F., Chiarugi, A. 2009. Detection and pharmacological modulation of nicotinamide mononucleotide (NMN) in vitro and in vivo. *Biochemical Pharmacology*. 77(10), 1612–1620. doi:10.1016/j.bcp.2009.02.017

37. Gandin, V., Khalkar, P., Braude, J., Fernandes, A. P. 2018. Organic selenium compounds as potential chemotherapeutic agents for improved cancer treatment. *Free Radical Biology and Medicine*. 127, 80–97. doi:10.1016/j.freeradbiomed.2018.05.001

38. Ganote, C. 2003. Effects of CCCP-induced mitochondrial uncoupling and cyclosporin A on cell volume, cell injury and preconditioning protection of isolated rabbit cardiomyocytes. *Journal of Molecular and Cellular Cardiology*. 35(7), 749–759. doi:10.1016/S0022-2828(03)00114-7

39. Gao, J., Zhao, Y., Li, T., Gan, X., Yu, H. 2022. The Role of PKM2 in the Regulation of Mitochondrial Function: Focus on Mitochondrial Metabolism, Oxidative Stress, Dynamic, and Apoptosis. *Oxidative Medicine and Cellular Longevity*. 2022.

40. Gao, X., Wang, H., Yang, J. J., Liu, X., Liu, Z. R. 2012. Pyruvate Kinase M2 Regulates Gene Transcription by Acting as a Protein Kinase. *Molecular Cell*. 45(5), 598–609. doi:10.1016/j.molcel.2012.01.001

41. Garbo, S., Di Giacomo, S., Łażewska, D., Honkisz-Orzechowska, E., Di Sotto, A., Fioravanti, R., Zwergel, C., Battistelli, C. 2022. Selenium-Containing Agents Acting on Cancer – A New Hope? *Pharmaceutics*. 15(1), 104. doi:10.3390/pharmaceutics15010104

42. Giannoni, E., Taddei, M. L., Morandi, A., Comito, G., Calvani, M., Bianchini, F., Richichi, B., Raugei, G., Wong, N., Tang, D., Chiarugi, P. 2015. Targeting stromal-induced pyruvate kinase M2 nuclear translocation impairs OXPHOS and prostate cancer metastatic spread. *Oncotarget*. 6(27), 24061–24074. doi:10.18632/oncotarget.4448

43. Gnaiger, E. 2020. Mitochondrial Pathways and Respiratory Control: An Introduction to OXPHOS Analysis. 5th ed. doi:10.26124/BEC:2020-0002

44. Gorini, S., De Angelis, A., Berrino, L., Malara, N., Rosano, G., Ferraro, E. 2018. Chemotherapeutic drugs and mitochondrial dysfunction: Focus on doxorubicin, trastuzumab, and sunitinib. *Oxidative Medicine and Cellular Longevity*. 2018. doi:10.1155/2018/7582730

45. Gorrini, C., Harris, I. S., Mak, T. W. 2013. Modulation of oxidative stress as an anticancer strategy. *Nature Reviews Drug Discovery*. 12(12), 931–947. doi:10.1038/nrd4002

46. Grevengoed, T. J., Martin, S. A., Katunga, L., Cooper, D. E., Anderson, E. J., Murphy, R. C., Coleman, R. A. 2015. Acyl-CoA synthetase 1 deficiency alters cardiolipin species and impairs mitochondrial function. *Journal of Lipid Research*. 56(8), 1572–1582. doi:10.1194/jlr.M059717

47. Grimm, J. B., English, B. P., Chen, J., Slaughter, J. P., Zhang, Z., Revyakin, A., Patel, R., Macklin, J. J., Normanno, D., Singer, R. H., Lionnet, T., Lavis, L. D. 2015. A general method to improve fluorophores for live-cell and single-molecule microscopy. *Nature Methods*. 12(3), 244–250. doi:10.1038/nmeth.3256

48. Gui, D. Y., Lewis, C. A., Vander Heiden, M. G. 2013. Allosteric regulation of PKM2 allows cellular adaptation to different physiological states. *Science Signaling*. 6(263), 1–5. doi:10.1126/scisignal.2003925]

49. Guo, C., He, J., Song, X., Tan, L., Wang, M., Jiang, P., Li, Y., Cao, Z., Peng, C. 2019. Pharmacological properties and derivatives of shikonin – A review in recent years. *Pharmacological Research*. 149, 104463. doi:10.1016/j.phrs.2019.104463

50. Gupte, R., Liu, Z., Kraus, W. L. 2017. PARPs and ADP-ribosylation: recent advances linking molecular functions to biological outcomes. *Genes & Development*. 31(2), 101–126. doi:10.1101/gad.291518.116

51. Han, X., Yang, J., Yang, K., Zhongdan, Z., Abendschein, D. R., Gross, R. W. 2007. Alterations in myocardial cardiolipin content and composition occur at the very earliest stages of diabetes: A shotgun lipidomics study. *Biochemistry*. 46(21), 6417–6428. doi:10.1021/bi7004015

52. Hardwick, J. M., Soane, L. 2013. Multiple Functions of BCL-2 Family Proteins. *Cold Spring Harbor Perspectives in Biology*. 5(2), a008722–a008722. doi:10.1101/cshperspect.a008722

53. Hatfield, D. L., Tsuji, P. A., Carlson, B. A., Gladyshev, V. N. 2014. Selenium and selenocysteine: roles in cancer, health and development. *Trends Biochem Sci*. 39(3), 112–120. doi:10.1016/j.tibs.2013.12.007

54. He, X., Zhang, J., Li, C., Zhang, Y., Lu, Y., Zhang, Y., Liu, L., Ruan, C., Chen, Q., Chen, X., Guo, Q., Sun, T., Cheng, J., Jiang, C. 2018. Enhanced bioreduction-responsive diselenide-based dimeric prodrug nanoparticles for triple negative breast cancer therapy. *Theranostics*. 8(18), 4884–4897. doi:10.7150/thno.27581

55. Horvath, S. E., Daum, G. 2013. Lipids of mitochondria. *Progress in Lipid Research*. 52(4), 590–614. doi:10.1016/j.plipres.2013.07.002

56. Houtkooper, R. H., Cantó, C., Wanders, R. J., Auwerx, J. 2010. The secret life of NAD^+: An old metabolite controlling new metabolic signaling pathways. *Endocrine Reviews*. 31(2), 194–223. doi:10.1210/er.2009-0026

57. Huang, C., Huang, Z., Bai, P., Luo, G., Zhao, X., Wang, X. 2018. Expression of pyruvate kinase M2 in human bladder cancer and its correlation with clinical parameters and prognosis. *OncoTargets and Therapy*. Volume 11, 2075–2082. doi:10.2147/OTT.S152999

58. Huang, Y., Liu, L., Shi, C., Huang, J., Li, G. 2006. Electrochemical analysis of the effect of Ca^{2+} on cardiolipin–cytochrome c interaction. *Biochimica et Biophysica Acta (BBA) - General Subjects*. 1760(12), 1827–1830. doi:10.1016/j.bbagen.2006.08.013

59. Irokawa, H., Numasaki, S., Kato, S., Iwai, K., Inose-Maruyama, A., Ohdate, T., Hwang, G. W., Toyama, T., Watanabe, T., Kuge, S. 2021. Comprehensive analyses of the cysteine thiol oxidation of PKM2 reveal the effects of multiple oxidation on cellular oxidative stress response. *Biochemical Journal*. 478(7), 1453–1470. doi:10.1042/BCJ20200897

60. Israelsen, W. J., Dayton, T. L., Davidson, S. M., Fiske, B. P., Hosios, A. M., Bellinger, G., Li, J., Yu, Y., Sasaki, M., Horner, J. W., Burga, L. N., Xie, J., Jurczak, M. J., Depinho, R. A., Clish, C. B., Jacks, T., Kibbey, R. G., Wulf, G. M., Di Vizio, D., Mills, G. B., Cantley, L. C., Vander Heiden, M. G. 2013. PKM2 isoform-specific deletion reveals a differential requirement for pyruvate kinase in tumor cells. *Cell*. 155(2), 397. doi:10.1016/j.cell.2013.09.025

61. Johnson, W. D., Morrissey, R. L., Kapetanovic, I., Crowell, J. A., McCormick, D. L. 2008. Subchronic oral toxicity studies of Se-methylselenocysteine, an organoselenium compound for breast cancer prevention. *Food and Chemical Toxicology*. 46(3), 1068–1078. doi:10.1016/j.fct.2007.11.001

62. Joshi, T., Voo, Z. X., Graham, B., Spiccia, L., Martin, L. L. 2015. Real-time examination of aminoglycoside activity towards bacterial mimetic membranes using Quartz Crystal Microbalance with Dissipation monitoring (QCM-D). *Biochimica et Biophysica Acta (BBA) - Biomembranes*. 1848(2), 385–391. doi:10.1016/j.bbamem.2014.10.019

63. Kaewsuya, P., Danielson, N. D., Ekhterae, D. 2007. Fluorescent determination of cardiolipin using 10-N-nonyl acridine orange. *Analytical and Bioanalytical Chemistry*. 387(8), 2775–2782. doi:10.1007/s00216-007-1135-0

64. Kaewsuya, P., Miller, J. D., Danielson, N. D., Sanjeevi, J., James, P. F. 2008. Comparison of N-alkyl acridine orange dyes as fluorescence probes for the determination of cardiolipin. *Analytica Chimica Acta*. 626(2), 111–118. doi:10.1016/j.aca.2008.08.002

65. Kalghatgi, S., Spina, C. S., Costello, J. C., Liesa, M., Morones-Ramirez, J. R., Slomovic, S., Molina, A., Shirihai, O. S., Collins, J. J. 2013. Bactericidal antibiotics induce mitochondrial dysfunction and oxidative damage in mammalian cells. *Science Translational Medicine*. 5(192). doi:10.1126/scitranslmed.3006055

66. Katsyuba, E., Romani, M., Hofer, D., Auwerx, J. 2020. NAD+ homeostasis in health and disease. *Nature Metabolism*. 2(1), 9–31. doi:10.1038/s42255-019-0161-5

67. Kiebish, M. A., Han, X., Cheng, H., Seyfried, T. N. 2009. In Vitro Growth Environment Produces Lipidomic and Electron Transport Chain Abnormalities in Mitochondria from Non-Tumorigenic Astrocytes and Brain Tumours. *ASN Neuro*. 1(3), AN20090011. doi:10.1042/AN20090011

68. Kim, C. W., Choi, K. C. 2021. Effects of anticancer drugs on the cardiac mitochondrial toxicity and their underlying mechanisms for novel cardiac protective strategies. *Life Sciences*. 277(February), 119607. doi:10.1016/j.lfs.2021.119607

69. Kuznetsov, A. V., Javadov, S., Sickinger, S., Frotschnig, S., Grimm, M. 2015. H9C2 and HL-1 cells demonstrate distinct features of energy metabolism, mitochondrial function and sensitivity to hypoxia-reoxygenation. *Biochimica et Biophysica Acta - Molecular Cell Research*. 1853(2), 276–284. doi:10.1016/j.bbamcr.2014.11.015

70. Lenardão, E. J., Sancineto, L., Santi, C. 2018. *New Frontiers in Organoselenium Compounds* 1st ed. 2018. Cham : Springer International Publishing : Imprint: Springer. doi:10.1007/978-3-319-92405-2

71. Li, J., Li, S., Guo, J., Li, Q., Long, J., Ma, C., Ding, Y., Yan, C., Li, L., Wu, Z., Zhu, H., Li, K. K., Wen, L., Zhang, Q., Xue, Q., Zhao, C., Liu, N., Ivanov, I., Luo, M., Xi, R., Long, H., Wang, P. G., Chen, Y. 2018. Natural Product Micheliolide Irreversibly Activates Pyruvate Kinase M2 and Suppresses Leukemia. *Journal of Medicinal Chemistry*. 61(9), 4155–4164. doi:10.1021/acs.jmedchem.8b00241

72. Li, N., Feng, L., Liu, H., Wang, J., Kasembeli, M., Tran, M. K., Tweardy, D. J., Lin, S. H., Chen, J. 2016. PARP Inhibition Suppresses Growth of EGFR-Mutant Cancers by Targeting Nuclear PKM2. *Cell Reports*. 15(4), 843–856. doi:10.1016/j.celrep.2016.03.070

73. Li, Q., Zhang, D., Chen, X., He, L., Li, T., Xu, X., Li, M. 2015. Nuclear PKM2 contributes to gefitinib resistance via upregulation of STAT3 activation in colorectal cancer. *Scientific Reports*. 5(1), 16082. doi:10.1038/srep16082

74. Li, T., Han, J., Jia, L., Hu, X., Chen, L., Wang, Y. 2019. PKM2 coordinates glycolysis with mitochondrial fusion and oxidative phosphorylation. *Protein and Cell*. 10(8), 583–594. doi:10.1007/s13238-019-0618-z

75. Liang, J., Cao, R., Wang, X., Zhang, Y., Wang, P., Gao, H., Li, C., Yang, F., Zeng, R., Wei, P., Li, D., Li, W., Yang, W. 2017. Mitochondrial PKM2 regulates oxidative stress-induced apoptosis by stabilizing Bcl2. *Cell Research*. 27(3), 329–351. doi:10.1038/cr.2016.159

76. Liu, W. R., Tian, M. X., Yang, L. X., Lin, Y. L., Jin, L., Ding, Z. Bin, Shen, Y. H., Peng, Y. F., Gao, D. M., Zhou, J., Qiu, S. J., Dai, Z., He, R., Fan, J., Shi, Y. H. 2015. PKM2 promotes metastasis by recruiting myeloid-derived suppressor cells and indicates poor prognosis for hepatocellular carcinoma. *Oncotarget*. 6(2), 846–861. doi:10.18632/oncotarget.2749

77. Luo, J., Hu, Z., Xiao, Y., Yang, T., Dong, C., Huang, J., Zhou, H. B. 2017. Rational design and optimization of selenophenes with basic side chains as novel potent selective estrogen receptor modulators (SERMs) for breast cancer therapy. *MedChemComm*. 8(7), 1485–1497. doi:10.1039/c7md00163k

78. Luo, L., Parrish, C. A., Nevins, N., McNulty, D. E., Chaudhari, A. M., Carson, J. D., Sudakin, V., Shaw, A. N., Lehr, R., Zhao, H., Sweitzer, S., Lad, L., Wood, K. W., Sakowicz, R., Annan, R. S., Huang, P. S., Jackson, J. R., Dhanak, D., Copeland, R. A., Auger, K. R. 2007. ATP-competitive inhibitors of the mitotic kinesin KSP that function via an allosteric mechanism. *Nature Chemical Biology*. 3(11), 722–726. doi:10.1038/nchembio.2007.34

79. Macpherson, J. A., Theisen, A., Masino, L., Fets, L., Driscoll, P. C., Encheva, V., Snijders, A. P., Martin, S. R., Kleinjung, J., Barran, P. E., Fraternali, F., Anastasiou, D. 2019. Functional cross-talk between allosteric effects of activating and inhibiting ligands underlies PKM2 regulation. *eLife*. 8, 1–36. doi:10.7554/eLife.45068

80. Makrecka-Kuka, M., Krumschnabel, G., Gnaiger, E. 2015. High-Resolution Respirometry for Simultaneous Measurement of Oxygen and Hydrogen Peroxide Fluxes in Permeabilized Cells, Tissue Homogenate and Isolated Mitochondria. *Biomolecules*. 5(3), 1319–1338. doi:10.3390/biom5031319

81. Martinez-Outschoorn, U. E., Peiris-Pagés, M., Pestell, R. G., Sotgia, F., Lisanti, M. P. 2017. Cancer metabolism: a therapeutic perspective. *Nature Reviews Clinical Oncology*. 14(1), 11–31. doi:10.1038/nrclinonc.2016.60

82. Mather, M., Rottenberg, H. 2001. Polycations induce the release of soluble intermembrane mitochondrial proteins. *Biochimica et Biophysica Acta (BBA) - Bioenergetics*. 1503(3), 357–368. doi:10.1016/S0005-2728(00)00231-0

83. McMillin, J. B., Dowhan, W. 2002. Cardiolipin and apoptosis. *Biochimica et Biophysica Acta – Molecular and Cell Biology of Lipids*. 1585(2–3), 97–107. doi:10.1016/S1388-1981(02)00329-3

84. Merchant, T. E., Glonek, T. 1992. 31P NMR of tissue phospholipids: Competition for Mg^{2+}, Ca^{2+}, Na^{+} and K^{+} cations. *Lipids*. 27(7), 551–559. doi:10.1007/BF02536139

85. Mileykovskaya, E., Dowhan, W., Birke, R. L., Zheng, D., Lutterodt, L., Haines, T. H. 2001. Cardiolipin binds nonyl acridine orange by aggregating the dye at exposed hydrophobic domains on bilayer surfaces. *FEBS Letters*. 507(2), 187–190. doi:10.1016/S0014-5793(01)02948-9

86. Mostyn, S. N., Carland, J. E., Shimmon, S., Ryan, R. M., Rawling, T., Vandenberg, R. J. 2017. Synthesis and Characterization of Novel Acyl-Glycine Inhibitors of GlyT2. *ACS Chemical Neuroscience*. 8(9), 1949–1959. doi:10.1021/acschemneuro.7b00105

87. Murphy, M. P. 2009. How mitochondria produce reactive oxygen species. *Biochemical Journal*. 417(1), 1–13. doi:10.1042/BJ20081386

88. Nandi, S., Dey, M. 2020. Biochemical and structural insights into how amino acids regulate pyruvate kinase muscle isoform 2. *Journal of Biological Chemistry*. 295(16), 5390–5403. doi:10.1074/jbc.RA120.013030

89. Nicolay, K., Timmers, R. J. M., Spoelstra, E., Neut, R. V. D., Fok, J. J., Huigen, Y. M., Verkleij, A. J., Kruijff, B. D. 1984. The interaction of adriamycin with cardiolipin in model and rat liver mitochondrial membranes. *Biochimica et Biophysica Acta (BBA) - Biomembranes*. 778(2), 359–371. doi:10.1016/0005-2736(84)90380-8

90. Ning, X., Qi, H., Li, R., Jin, Y., McNutt, M. A., Yin, Y. 2018. Synthesis and antitumor activity of novel 2, 3-didithiocarbamate substituted naphthoquinones as inhibitors of pyruvate kinase M2 isoform. *Journal of Enzyme Inhibition and Medicinal Chemistry*. 33(1), 126–129. doi:10.1080/14756366.2017.1404591

91. Ning, X., Qi, H., Li, R., Li, Y., Jin, Y. 2017. Discovery of novel naphthoquinone derivatives as inhibitors of the tumor cell specific M2 isoform of pyruvate kinase. *European Journal of Medicinal Chemistry*. 138, 343–352. doi:10.1016/j.ejmech.2017.06.064

92. O'Neil, M. J. 2001. *The Merck Index - An Encyclopedia of Chemicals, Drugs, and Biologicals. 13th Edition*. Whitehouse Station, NJ: Merck and Co., Inc.

93. Paradies, G., Paradies, V., Ruggiero, F. M., Petrosillo, G. 2019. Role of Cardiolipin in Mitochondrial Function and Dynamics in Health and Disease: Molecular and Pharmacological Aspects. *Cells*. 8(7), 728. doi:10.3390/cells8070728

94. Paradies, G., Paradies, V., Ruggiero, F. M., Petrosillo, G. 2014. Cardiolipin and mitochondrial function in health and disease. *Antioxidants and Redox Signaling*. 20(12), 1925–1953. doi:10.1089/ars.2013.5280

95. Paradies, G., Petrosillo, G., Pistolese, M., Ruggiero, F. M. 2002. Reactive oxygen species affect mitochondrial electron transport complex I activity through oxidative cardiolipin damage. *Gene*. 286(1), 135–141. doi:10.1016/S0378-1119(01)00814-9

96. Park, J. H., Kundu, A., Lee, S. H., Jiang, C., Lee, S. H., Kim, Y. S., Kyung, S. Y., Park, S. H., Kim, H. S. 2021. Specific pyruvate kinase m2 inhibitor, compound 3k, induces autophagic cell death through disruption of the glycolysis pathway in ovarian cancer cells. *International Journal of Biological Sciences*. 17(8), 1895–1908. doi:10.7150/ijbs.59855

97. Parker, M. A., King, V., Howard, K. P. 2001. Nuclear magnetic resonance study of doxorubicin binding to cardiolipin containing magnetically oriented phospholipid bilayers. *Biochimica et Biophysica Acta (BBA) - Biomembranes*. 1514(2), 206–216. doi:10.1016/S0005-2736(01)00371-6

98. Pennington, E. R., Funai, K., Brown, D. A., Shaikh, S. R. 2019. The role of cardiolipin concentration and acyl chain composition on mitochondrial inner membrane molecular organization and function. *Biochimica et Biophysica Acta (BBA) - Molecular and Cell Biology of Lipids*. 1864(7), 1039–1052. doi:10.1016/j.bbalip.2019.03.012

99. Petrosillo, G., Portincasa, P., Grattagliano, I., Casanova, G., Matera, M., Ruggiero, F. M., Ferri, D., Paradies, G. 2007. Mitochondrial dysfunction in rat with nonalcoholic fatty liver. *Biochimica et Biophysica Acta (BBA) - Bioenergetics*. 1767(10), 1260–1267. doi:10.1016/j.bbabio.2007.07.011

100. Pointer, C. B., Klegeris, A. 2017. Cardiolipin in Central Nervous System Physiology and Pathology. *Cellular and Molecular Neurobiology*. 37(7), 1161–1172. doi:10.1007/s10571-016-0458-9

101. Poljsak, B. 2016. NAD+ in Cancer Prevention and Treatment: Pros and Cons. *Journal of Clinical & Experimental Oncology*. 5(4), 1–15. doi:10.4172/2324-9110.1000165

102. Potapov, V. A. 2013. Organic Diselenides, Ditellurides, Polyselenides and Polytellurides. Synthesis and Reactions. In: Rappoport, Z. (ed.), *PATAI'S Chemistry of Functional Groups*. Chichester, UK: John Wiley & Sons, Ltd, p. pat0716. doi:10.1002/9780470682531.pat0716

103. Rathod, B., Chak, S., Patel, S., Shard, A. 2021. Tumor pyruvate kinase M2 modulators: a comprehensive account of activators and inhibitors as anticancer agents. *RSC Medicinal Chemistry*. 12(7), 1121–1141. doi:10.1039/D1MD00045D

104. Rendekova, J., Vlasakova, D., Arsenyan, P., Vasiljeva, J., Nasim, M. J., Witek, K., Dominguez-Alvarez, E., Zeslawska, E., Manikova, D., Tejchman, W., Zaib Saleem, R. S., Rory, K., Handzlik, J., Chovanec, M. 2018. The Selenium-Nitrogen Bond as Basis for Reactive Selenium Species with Pronounced Antimicrobial Activity. Current Organic Synthesis. 14(8). doi:10.2174/1570179414666170525104735

105. Robert A. Copeland 2013. *Evaluation of Enzyme Inhibitors in Drug Discovery: A Guide for Medicinal Chemists and Pharmacologists* 2nd edn. John Wiley & Sons, Inc. doi:10.1002/9781118540398

106. Rodionov, D. G., Ishiguro, E. E. 1997. Ampicillin-induced bacteriolysis of Escherichia coli is not affected by reduction in levels of anionic phospholipids. *FEMS Microbiology Letters*. 156(1), 85–89. doi:10.1016/S0378-1097(97)00406-0

107. Rodriguez, M. E., Azizuddin, K., Zhang, P., Chiu, S. mao, Lam, M., Kenney, M. E., Burda, C., Oleinick, N. L. 2008. Targeting of mitochondria by 10-N-alkyl acridine orange analogues: Role of alkyl chain length in determining cellular uptake and localization. *Mitochondrion*. 8(3), 237–246. doi:10.1016/j.mito.2008.04.003

108. Roman, M., Jitaru, P., Barbante, C. 2014. Selenium biochemistry and its role for human health. *Metallomics*. 6(1), 25–54. doi:10.1039/C3MT00185G

109. Roy, G., Mugesh, G. 2005. Anti-Thyroid Drugs and Thyroid Hormone Synthesis: Effect of Methimazole Derivatives on Peroxidase-Catalyzed Reactions. *Journal of the American Chemical Society*. 127(43), 15207–15217. doi:10.1021/ja054497u

110. Sainero-Alcolado, L., Liaño-Pons, J., Ruiz-Pérez, M. V., Arsenian-Henriksson, M. 2022. Targeting mitochondrial metabolism for precision medicine in cancer. *Cell Death & Differentiation*. 29(7), 1304–1317. doi:10.1038/s41418-022-01022-y

111. Sakamoto, Y., Yano, T., Hanada, Y., Takeshita, A., Inagaki, F., Masuda, S., Matsunaga, N., Koyanagi, S., Ohdo, S. 2017. Vancomycin induces reactive oxygen species-dependent apoptosis via mitochondrial cardiolipin peroxidation in renal tubular epithelial cells. *European Journal of Pharmacology*. 800(December 2016), 48–56. doi:10.1016/j.ejphar.2017.02.025

112. Santo-Domingo, J., Demaurex, N. 2012. The renaissance of mitochondrial pH. *Journal of General Physiology*. 139(6), 415–423. doi:10.1085/jgp.201110767

113. Sautrey, G., El Khoury, M., Dos Santos, A. G., Zimmermann, L., Deleu, M., Lins, L., Décout, J. L., Mingeot-Leclercq, M. P. 2016. Negatively Charged Lipids as a Potential Target for New Amphiphilic Aminoglycoside Antibiotics. *Journal of Biological Chemistry*. 291(26), 13864–13874. doi:10.1074/jbc.M115.665364

114. Shiah, H. S., Lee, W. S., Juang, S. H., Hong, P. C., Lung, C. C., Chang, C. J., Chou, K. M., Chang, J. Y. 2007. Mitochondria-mediated and p53-associated apoptosis induced in human cancer cells by a novel selenophene derivative, D-501036. *Biochemical Pharmacology*. 73(5), 610–619. doi:10.1016/j.bcp.2006.10.019

115. Siegel, A. B., Narayan, R., Rodriguez, R., Goyal, A., Jacobson, DrPH, J. S., Kelly, K., Ladas, E., Lunghofer, P. J., Hansen, R. J., Gustafson, D. L., Flaig, T. W., Yann Tsai, W., Wu, D. P. H., Lee, V., Greenlee, H. 2014. A Phase I Dose-Finding Study of Silybin Phosphatidylcholine (Milk Thistle) in Patients With Advanced Hepatocellular Carcinoma. *Integrative Cancer Therapies*. 13(1), 46–53. doi:10.1177/1534735413490798

116. Sinibaldi, F., Fiorucci, L., Patriarca, A., Lauceri, R., Ferri, T., Coletta, M., Santucci, R. 2008. Insights into Cytochrome *c* −Cardiolipin Interaction. Role Played by Ionic Strength. *Biochemistry*. 47(26), 6928–6935. doi:10.1021/bi800048v

117. Soares, A. T. G., Rodrigues, L. B. L., Salgueiro, W. G., Dal Forno, A. H. de C., Rodrigues, C. F., Sacramento, M., Franco, J., Alves, D., Oliveira, R. de P., Pinton, S., Ávila, D. S. 2019. Organoselenotriazoles attenuate oxidative damage induced by mitochondrial dysfunction in mev-1 Caenorhabditis elegans mutants. *Journal of Trace Elements in Medicine and Biology*. 53, 34–40. doi:10.1016/j.jtemb.2019.01.017

118. Soussi, B., Bylund-Fellenius, A. C., Scherstén, T., Ångström, J. 1990. 1H-n.m.r. evaluation of the ferricytochrome *c* -cardiolipin interaction. Effect of superoxide radicals. *Biochemical Journal*. 265(1), 227–232. doi:10.1042/bj2650227

119. Srivastava, D., Nandi, S., Dey, M. 2019. Mechanistic and Structural Insights into Cysteine-Mediated Inhibition of Pyruvate Kinase Muscle Isoform 2. *Biochemistry*. 58(35), 3669–3682. doi:10.1021/acs.biochem.9b00349

120. Swinney, D. C., Anthony, J. 2011. How were new medicines discovered? *Nature Reviews Drug Discovery*. 10(7), 507–519. doi:10.1038/nrd3480

121. Szeto, H. H. 2014. First-in-class cardiolipin-protective compound as a therapeutic agent to restore mitochondrial bioenergetics. *British Journal of Pharmacology*. 171(8), 2029–2050. doi:10.1111/bph.12461

122. Torresano, L., Nuevo-Tapioles, C., Santacatterina, F., Cuezva, J. M. 2020. Metabolic reprogramming and disease progression in cancer patients. *Biochimica et Biophysica Acta (BBA) – Molecular Basis of Disease*. 1866(5), 165721. doi:10.1016/j.bbadis.2020.165721

123. Upadhyay, M., Samal, J., Kandpal, M., Singh, O. V., Vivekanandan, P. 2013. The Warburg effect: Insights from the past decade. *Pharmacology and Therapeutics*. 137(3), 318–330. doi:10.1016/j.pharmthera.2012.11.003

124. Valianpour, F., Wanders, R. J. A., Overmars, H., Vaz, F. M., Barth, P. G., Van Gennip, A. H. 2003. Linoleic acid supplemention of Barth syndrome fibroblasts restores cardiolipin levels: Implications for treatment. *Journal of Lipid Research*. 44(3), 560–566. doi:10.1194/jlr.M200217-JLR200

125. Vinceti, M., Dennert, G., Crespi, C. M., Zwahlen, M., Brinkman, M., Zeegers, M. P., Horneber, M., D'Amico, R., Del Giovane, C. 2014. Selenium for preventing cancer. (Cochrane Gynaecological, Neuro-oncology and Orphan Cancer Group, Ed.)*Cochrane Database of Systematic Reviews*. . doi:10.1002/14651858.CD005195.pub3

126. Vladimirov, Yu. A., Proskurnina, E. V., Alekseev, A. V. 2013. Molecular mechanisms of apoptosis. Structure of cytochrome c-cardiolipin complex. *Biochemistry (Moscow)*. 78(10), 1086–1097. doi:10.1134/S0006297913100027

127. Wang, K., Jiang, J., Lei, Y., Zhou, S., Wei, Y., Huang, C. 2019. Targeting Metabolic–Redox Circuits for Cancer Therapy. *Trends in Biochemical Sciences*. 44(5), 401–414. doi:10.1016/j.tibs.2019.01.001

128. Wang, P., Sun, C., Zhu, T., Xu, Y. 2015. Structural insight into mechanisms for dynamic regulation of PKM2. *Protein and Cell*. 6(4), 275–287. doi:10.1007/s13238-015-0132-x

129. Warburg, O., Wind, F., Negelein, E. 1927. THE METABOLISM OF TUMORS IN THE BODY. *Journal of General Physiology*. 8(6), 519–530. doi:10.1085/jgp.8.6.519

130. Warner, S. L., Carpenter, K. J., Bearss, D. J. 2014. Activators of PKM2 in cancer metabolism. *Future Medicinal Chemistry*. 6(10), 1167–1178. doi:10.4155/fmc.14.70

131. Weinberg, F., Hamanaka, R., Wheaton, W. W., Weinberg, S., Joseph, J., Lopez, M., Kalyanaraman, B., Mutlu, G. M., Budinger, G. R. S., Chandel, N. S. 2010. Mitochondrial metabolism and ROS generation are essential for Kras-mediated tumorigenicity. *Proceedings of the National Academy of Sciences of the United States of America*. 107(19), 8788–8793. doi:10.1073/pnas.1003428107

132. Weinberg, S. E., Chandel, N. S. 2015. Targeting mitochondria metabolism for cancer therapy. *Nature Chemical Biology*. 11(1), 9–15. doi:10.1038/nchembio.1712

133. Wessels, S., Ingmer, H. 2013. Modes of action of three disinfectant active substances: A review. *Regulatory Toxicology and Pharmacology*. 67(3), 456–467. doi:10.1016/j.yrtph.2013.09.006

134. Wiench, B., Eichhorn, T., Paulsen, M., Efferth, T. 2012. Shikonin Directly Targets Mitochondria and Causes Mitochondrial Dysfunction in Cancer Cells. *Evidence-Based Complementary and Alternative Medicine*. 2012, 1–15. doi:10.1155/2012/726025

135. Wilks, J. C., Slonczewski, J. L. 2007. pH of the cytoplasm and periplasm of Escherichia coli: Rapid measurement by green fluorescent protein fluorimetry. *Journal of Bacteriology*. 189(15), 5601–5607. doi:10.1128/JB.00615-07

136. Witek, K., Nasim, M., Bischoff, M., Gaupp, R., Arsenyan, P., Vasiljeva, J., Marć, M., Olejarz, A., Latacz, G., Kieć-Kononowicz, K., Handzlik, J., Jacob, C. 2017. Selenazolinium Salts as "Small Molecule Catalysts" with High Potency against ESKAPE Bacterial Pathogens. Molecules. 22(12), 2174. doi:10.3390/molecules22122174

137. Yamaglshi, A., Masui, T., Fumlyukl, W. 1981. Selective Activation of Reactant Molecules by Reversed Micelles Akihlko. *Journal of Physical Chemistry*. 85, 281–285. doi:doi:10.1021/j150603a013

138. Yang, W., Xia, Y., Ji, H., Zheng, Y., Liang, J., Huang, W., Gao, X., Aldape, K., Lu, Z. 2011. Nuclear PKM2 regulates β-catenin transactivation upon EGFR activation. *Nature*. 480(7375), 118–122. doi:10.1038/nature10598

139. Yang, Y. N., Chou, K. ming, Pan, W. Y., Chen, Y. wen, Tsou, T. C., Yeh, S. C., Cheung, C. H. A., Chen, L. T., Chang, J. Y. 2011. Enhancement of non-homologous end joining DNA repair capacity confers cancer cells resistance to the novel selenophene compound, D-501036. *Cancer Letters*. 309(1), 110–118. doi:10.1016/j.canlet.2011.05.023

140. Yel, L., Brown, L., Su, K., Gollapudi, S., Gupta, S. 2005. Thimerosal induces neuronal cell apoptosis by causing cytochrome c and apoptosis-inducing factor release from mitochondria. *International Journal of Molecular Medicine*. . doi:10.3892/ijmm.16.6.971

141. Zahra, K., Dey, T., Ashish, Mishra, S. P., Pandey, U. 2020. Pyruvate Kinase M2 and Cancer: The Role of PKM2 in Promoting Tumorigenesis. *Frontiers in Oncology*. 10, 159. doi:10.3389/fonc.2020.00159

142. Zhang, L., Zhou, L., Du, J., Li, M., Qian, C., Cheng, Y., Peng, Y., Xie, J., Wang, D. 2014. Induction of Apoptosis in Human Multiple Myeloma Cell Lines by Ebselen via Enhancing the Endogenous Reactive Oxygen Species Production. *BioMed Research International*. 2014, 1–10. doi:10.1155/2014/696107

143. Zhang, Y., Li, Q., Huang, Z., Li, B., Nice, E. C., Huang, C., Wei, L., Zou, B. 2022. Targeting Glucose Metabolism Enzymes in Cancer Treatment: Current and Emerging Strategies. *Cancers*. 14(19), 4568. doi:10.3390/cancers14194568

144. Zhou, S., Li, D., Xiao, D., Wu, T., Hu, X., Zhang, Y., Deng, J., Long, J., Xu, S., Wu, J., Li, G., Peng, M., Yang, X. 2022. Inhibition of PKM2 Enhances Sensitivity of Olaparib to Ovarian Cancer Cells and Induces DNA Damage. *International Journal of Biological Sciences*. 18(4), 1555–1568. doi:10.7150/ijbs.62947

145. Zhu, S., Guo, Y., Zhang, X., Liu, H., Yin, M., Chen, X., Peng, C. 2021. Pyruvate kinase M2 (PKM2) in cancer and cancer therapeutics. *Cancer Letters*. 503, 240–248. doi:10.1016/j.canlet.2020.11.018

146. Zhu, Y., Liu, J., Park, J., Rai, P., Zhai, R. G. 2019. Subcellular compartmentalization of NAD+ and its role in cancer: A sereNADe of metabolic melodies. *Pharmacology and Therapeutics*. 200, 27–41. doi:10.1016/j.pharmthera.2019.04.002

147. Zichri, S. B., Kolusheva, S., Shames, A. I., Schneiderman, E. A., Poggio, J. L., Stein, D. E., Doubijensky, E., Levy, D., Orynbayeva, Z., Jelinek, R. 2021. Mitochondria membrane transformations in colon and prostate cancer and their biological implications. *Biochimica et Biophysica Acta (BBA) - Biomembranes*. 1863(1), 183471. doi:10.1016/j.bbamem.2020.183471

148. Zielonka, J., Joseph, J., Sikora, A., Hardy, M., Ouari, O., Vasquez-Vivar, J., Cheng, G., Lopez, M., Kalyanaraman, B. 2017. Mitochondria-Targeted Triphenylphosphonium-Based Compounds: Syntheses, Mechanisms of Action, and Therapeutic and Diagnostic Applications. *Chemical Reviews*. 117(15), 10043–10120. doi:10.1021/acs.chemrev.7b00042

149. Zu, X. L., Guppy, M. 2004. Cancer metabolism: Facts, fantasy, and fiction. *Biochemical and Biophysical Research Communications*. 313(3), 459–465. doi:10.1016/j.bbrc.2003.11.136

Acknowledgments

I would like to express my sincerest gratitude to my scientific supervisor and teacher, Dr. Pavels Arsenjans, for his patience and time, literally standing behind me, sharing his knowledge and giving me lots of advice. Thanks to him, I had the best learning and training experience I could have ever imagined. I will never forget his fantastic master classes and "classical" methods.

I would like to thank my colleagues Alla Petrenko and Dr. Sindija Lapcinska for their helpful contributions and sharing of useful chemical insights. Special thanks to Prof. Maija Dambrova, Dr. Marina Makrecka-Kuka, Dr. Edijs Vavers, Dr. Baiba Svalbe, Dr. Ilona Domracheva, Ludmila Jackevica, Stanislava Korzh, and the upcoming PhD Melita Ozola for valuable lessons and practical assistance in numerous experiments.

A warm thank you to Dr. Sergey Belyakov for carrying out X-ray analysis and Dr. Kaspars Leduskrasts for the help in characterising the luminescence properties.

I am also grateful to Dr. Teodors Pantelejevs for PKM2 expression and help with biophysical experiments, Dr. Marko Hyvonen and Dr. Agnieszka Bogucka for the mass photometry measurements and kind feedback.

I am deeply indebted to my beautiful wife Anna, who listened to my presentations countless times and helped to make them understandable to a normal human being.

The completion of my thesis would not have been possible without the love and unwavering support of my family and friends, and I truly appreciate the care.

I would like to acknowledge the financial support from Latvian Institute of Organic Synthesis (student internal grant IG-2020-01), ERDF "Development of a novel potent PARP inhibitor" (Nr. 1.1.1.1/19/A/016) and BioMedPharm (Nr. VPP-EM-BIOMEDICINA-2022/1-0001) projects.

Annexes

First Publication

NJC

ROYAL SOCIETY OF CHEMISTRY

PAPER

Check for updates

Cite this: *New J. Chem.*, 2020, **44**, 9626

Improved method for the preparation of nonyl acridine orange analogues and utilization in detection of cardiolipin†

Pavels Dimitrijevs,[ab] Ilona Domracheva[a] and Pavel Arsenyan*[a]

Received 27th April 2020,
Accepted 21st May 2020

DOI: 10.1039/d0nj02116d

rsc.li/njc

This study was designed to develop a fast and convenient methodology for the preparation of 10-nonyl acridine orange (NAO) and its silyl analogues to improve their photo-physical properties for the detection and quantification of cardiolipin (CL). Optimized conditions allow the effective synthesis of NAO analogues with good yield and excellent purity. The introduction of a 3-(trimethylsilyl)propyl moiety improves the dye's solubility and stability in buffer solution and increases its emission intensity by ≈30%. The novel dye can be used for the selective quantification of CL in a liposomal inner mitochondrial membrane model with greater fluorescence intensity and linear slope compared to NAO. The novel silicon-containing NAO analogue has lower cytotoxicity, and is a convenient fluorescent dye for cell staining.

Introduction

Although different acridines have served as antibiotics and antiprotozoan drugs since World War I[1,2] and even now are still being studied as therapeutics, *e.g.* for cancer treatment,[3] this class of compounds became especially appreciated, due to their photo-physical properties, after the rise of fluorescence microscopy in the 1930s.[2] For example, 3,6-bis(dimethylamino)acridine (Acridine orange, AO) binds with DNA and RNA and has been widely used for cell staining. Acriflavin (trypaflavin), which is a 50 : 50 mixture of AO and 10-methyl AO (MAO), is selective towards DNA and can be used for its quantitative analysis in animal nuclei.[4] However one unique fluorescent probe stands out from many acridine derivatives – 10-nonyl AO (NAO), which is a mitochondria-specific fluorescent probe[5–9] that allows visualization of phospholipid domains[10–12] due to its ability to bind with cardiolipin (CL), an anionic phospholipid that is almost exclusively located in the inner mitochondrial membrane.[13] CL plays an important role in mitochondrial membrane morphology and stability and is required for the optimal activity of several mitochondrial membrane proteins (*e.g.* electron transport chain (ETC) complexes, cytochrome *C*).[14] The level of CL is a significant clinical marker,[14–16] and the abnormally high abundance and chemical diversity of CL were identified as novel molecular signatures of oncocytic and prostate tumors.[17–19] Therefore, there is a high demand for a fluorescent probe that would be effective and convenient for the detection and quantification of CL.

Unfortunately, NAO does not meet these requirements because of its poor solubility in aqueous media, relatively low photoluminescence quantum yield (Φ) and the small differences in intensity between CL-bound and unbound states.[20] Moreover, the synthesis and purification of quaternized AO analogues is also sophisticated[20,21] which only makes matters worse, and even commercially available NAO is often sold with low purity.

Herein, we would like to report our findings on the improvement of the synthetic method for the quaternization of AO. Novel CL-specific silicon containing AO derivatives exhibit higher solubility in physiological media than NAO. Advanced photo-physical properties allow the detection of CL and measurement of its concentration. The cytotoxicity of the newly acquired dyes was evaluated and preliminary cell staining was performed.

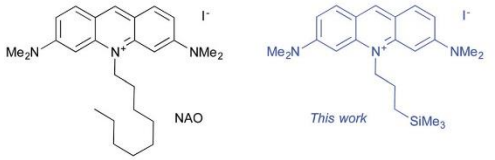

[a] *Latvian Institute of Organic Synthesis, Aizkraukles 21, LV-1006, Riga, Latvia. E-mail: pavel@osi.lv*
[b] *Riga Stradins University, Dzirciema 16, Riga, LV-1007, Latvia*

† Electronic supplementary information (ESI) available: Copies of ^{1}H, ^{13}C, ^{29}Si, HRMS, IR, HPLC, absorption, emission spectra, and DLS data, as well as a stereo view of **5**. CCDC 1975762. For ESI and crystallographic data in CIF or other electronic format see DOI: 10.1039/d0nj02116d

Results and discussion

At first glance the synthesis of 10-*N*-alkylated derivatives of acridine orange looks like a straightforward one-step synthesis from commercially available 3,6-bis(dimethylamino)acridine (AO), comprising its quaternization with a corresponding alkyl halide in chloroform, benzene or toluene under reflux. But looking more closely at the described methods of AO quaternization,[20–22] one may notice that these reactions are very time consuming, lasting up to 72 h, and the products are obtained in low yield. In our hands, the quaternization of AO in the presence of 1-iodononane (xylene, reflux, 48 h) ended up in 26% conversion. However, the tricky part is the purification of the product because of the many similar by-products that are formed in the reaction. This explains why commercially available 10-*N*-nonyl acridine orange (NAO) is often offered only with ≥90% purity, and difficult purification may possibly explain the low yields, since a considerable amount of the product is lost during complicated chromatography on neutral Al_2O_3.[21]

So far, we have faced three issues to be solved: the long duration of the reaction, low yield and complicated purification. To overcome these complications, we looked for other possible quaternization methods. There is a described method of acridine *N*-methylation with dimethyl sulfate;[23] dialkyl carbonates,[24] and trialkyl phosphates[25] can also be used for the alkylation of N-heterocycles. Methyl carbonates, sulfates and phosphates are common reagents, although such alkylating agents with longer alkyl chains (*e.g.* $\geq C_9H_{19}$), are not commercially available. However, various alkyl halides as well as inorganic carbonates, sulfates and phosphates are cheap and can be easily found in every synthetic lab. So, we tested the possibility of forming alkyl substituted salts *in situ* and their ability to improve the outcome of AO quaternization. At first, 1-iodononane was used for the quaternization of AO to test our hypothesis. Since acceleration of the reaction is desired, the conversion after 10 and 25 min was checked. Treatment of AO with 1-iodononane in toluene at 110 °C in 25 minutes led to very low conversion, which was not altered by the presence of 2 equiv. of either Na_2CO_3 or K_3PO_4 (Table 1, entries 1, 4 and 5). Heating to 140 °C (using xylene as the solvent) without salts did not improve the yield (entry 2). However, in this case *in situ* formed dialkyl carbonate (R_2CO_3) and trialkyl phosphate (R_3PO_4) in the reaction of alkyl halide with sodium carbonate or potassium phosphate came in handy, increasing the conversion to 70% and 71%, respectively, after 25 min (entries 6 and 7). Then we decided to raise the temperature even higher – up to 170 °C and used dichlorobenzene as the solvent. Strikingly, in the presence of K_3PO_4 conversion increased to 94% after only 10 min (entry 10); in turn Na_2CO_3 increased the conversion to 98% without any noticeable number of by-products (entry 11). This can be explained by the instability of 3,6-dimethyl amino acridinium salts under prolonged heating. Thus acceleration of the reaction by the *in situ* formation of highly reactive alkyl carbonate or phosphate allows us to avoid extended heating of the reaction mixture and

Table 1 Optimization of reaction conditions for the preparation of nonyl acridine orange (NAO)

Entry	R-Hal	Additive	Solvent	Δ, °C	Time, min	Conversion, %
1	Nonyl-I	—	Toluene	110	25	<10
2	Nonyl-I	—	Xylene	140	25	<10
3	Nonyl-I	—	Dichlorobenzene	170	10	67
4	Nonyl-I	Na_2CO_3	Toluene	110	25	<10
5	Nonyl-I	K_3PO_4	Toluene	110	25	<10
6	Nonyl-I	Na_2CO_3	Xylene	140	25	70
7	Nonyl-I	K_3PO_4	Xylene	140	25	71
8	Nonyl-I	K_2CO_3	Dichlorobenzene	170	10	73
9	Nonyl-I	Na_2SO_4	Dichlorobenzene	170	10	74
10	Nonyl-I	K_3PO_4	Dichlorobenzene	170	10	94
11	**Nonyl-I**	**Na_2CO_3**	**Dichlorobenzene**	**170**	**10**	**98**
12	Nonyl-Br	—	Xylene	140	25	<10
13	Nonyl-Br	—	Dichlorobenzene	170	10	40
14	Nonyl-Br	Na_2CO_3	Xylene	140	25	15
15	Nonyl-Br	K_3PO_4	Xylene	140	25	25
16	Nonyl-Br	K_2CO_3	Dichlorobenzene	170	10	38
17	Nonyl-Br	Na_2SO_4	Dichlorobenzene	170	10	43
18	Nonyl-Br	K_3PO_4	Dichlorobenzene	170	10	88
19	Nonyl-Br	Na_2CO_3	Dichlorobenzene	170	10	91

demethylation of the desired product. Neither K_2CO_3 nor Na_2SO_4 significantly improved the reaction outcome after 10 min. Additionally, 1-bromononane was tested under the same reaction conditions and the same trend was discovered – a higher conversion rate is observed at the elevated temperature using dichlorobenzene as a solvent (entry 13), while the presence of Na_2CO_3 gave a two-fold increase in the conversion (entry 19). The optimal amount of Na_2CO_3 is 2 equiv., because a lower amount of sodium carbonate resulted in decreased conversion (94%, 1-iodononane). In order to test the applicability of the optimized reaction conditions and to obtain desired AO derivatives for further studies, different alkyl iodides were used to obtain compounds **2–6** (Scheme 1) in good yields (except for compound **6**) with purity ≥96.5% (HPLC data found in ESI†). Notably, isolation of **2**, **3** and **5** did not even require further purification by means of chromatography. *N*-Methyl **2** and 3-(trimethylsilyl)propyl **5** acridinium iodides were isolated in almost quantitative yields, which can be explained by the high reactivity of active alkyl halides. Nevertheless, the developed reaction conditions allow us to obtain desired products with inactive long-chain alkyl halides as well such as 1-iodononane and 1-iodododecane (**3**, **4**).

Even very polar, silatranylpropyl substituted derivative **6** can be obtained, although in low yield. This might be due to the low stability of the silatranyl group in the presence of basic agents; thus a better yield was acquired using K_3PO_4 because of its lower basicity compared to Na_2CO_3. In ^{29}Si NMR spectra a chemical shift (CS) of Me_3Si in **5** was detected at 2.1 ppm; in addition, the silatranyl moiety showed CS at −71.06 ppm (see ESI†). CSs in ^{29}Si NMR spectra are in agreement with previously published data.[26–28] Moreover, the molecular structure of **5** was unambiguously confirmed with X-ray analysis (Fig. 1, CCDC 1975762).†

To evaluate the impact of the silicon-containing group in the dye's structure, *N*-3-(trimethylsilyl)propyl and 3-(silatranyl)-propyl substituted bis(dimethylamino)acridines **5** and **6** were

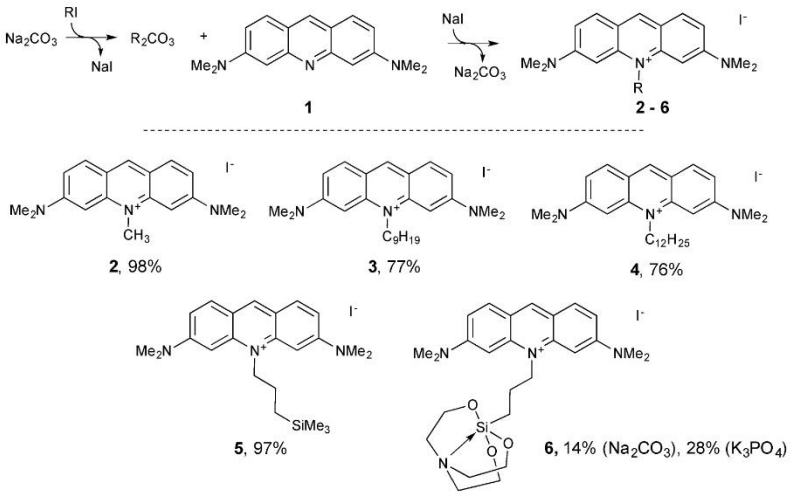

Scheme 1 Synthesis of **2–6**. Reaction conditions: alkyl halide, dichlorobenzene, 170 °C, Na_2CO_3 (2 equiv.).

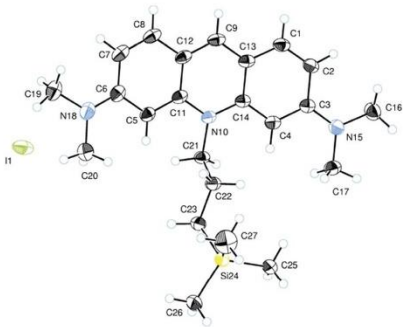

Fig. 1 Molecular structure of **5** with anisotropic displacement ellipsoids drawn at 50% probability.

Table 2 Photo-physical properties of **2–6** in 20 mM HEPES

Compound	2	3	4	5	6
Ex_{max}, nm	497	498	496	491	498
Em_{max}, nm	527	528	527	529	529
Φ, %	14.0	15.5	9.5	18.7	10.8
Solubility, mM	n.d	0.0795	n.d	$\geq$0.466	$\geq$0.08
Stability (5 h), %	n.d	96%	n.d	98%	97%
Stability (24 h), %	n.d	81%	n.d	87%	83%

n.d. – not detected.

used for in-depth studies. Nonyl acridine orange (**3**), a well-known CL-sensitive fluorescent dye, was used as a reference compound. Experiments were performed in 20 mM HEPES (4-(2-hydroxyethyl)piperazine-1-ethanesulfonic acid) at pH 7.4. Incorporation of silyl groups did not significantly change the absorption and emission profiles (Table 2, ESI†). Introduction of the lipophilic trimethylsilylpropyl substituent led to a slight increase in quantum yield (Φ). In addition, the presence of hydrophilic silatrane in the acridinium salt structure decreased Φ to 10.8% compared with **3** (15.5%). Interestingly, this negligible increase in Φ was accompanied by an ~30% increase in fluorescence intensity at the concentrations used in further experiments (Fig. 2A). This more pronounced emission intensity of **5** might be attributed to its better solubility ($\geq$0.466 mM) in buffer solution compared to **3** (0.0795 mM), since 3-(trimethylsilyl)propyl is shorter than the nonyl moiety. It is worth noting that owing to the presence of the silicon atom, this shorter alkyl chain is still sufficiently lipophilic, which is crucial for binding to cardiolipin.[20] The quantum yield (Φ = 14.0%) of *N*-methyl analogue **2** is close to that of **3**; however, elongation of the lipophilic chain to C_{12} (**4**) decreased Φ to 9.5%. Considering the low efficiency of binding of **2** to CL[20] and the low quantum yield of **4**, further studies focused on **3**, **5** and **6**. The silatranyl moiety is more polar and its solubility in aqueous media is slightly better compared to **3** (Table 2). Compounds **3**, **5** and **6** are stable at relatively high concentrations in 20 mM HEPES at pH 7.4, for at least 5 h (Table 2).

A fluorescent dye's self-quenching determines the maximal concentration that can be used. According to data in the literature, NAO's self-quenching concentration is 25 μM in a 50 : 50 H_2O/MeOH solution.[29] In our hands, NAO (**3**), **5** and **6** have similar properties – for all three compounds self-quenching is observed at 50 μM in 20 mM HEPES, pH 7.4. (Fig. 2A)

Introducing a 3-(trimethylsilyl)propyl group increased the fluorescence intensity by 30% compared with NAO, so the next step was to confirm that new Si-containing acridine derivatives bind to cardiolipin (CL) in a liposome model and can be used for CL detection. Liposomes made of CL in aqueous solutions

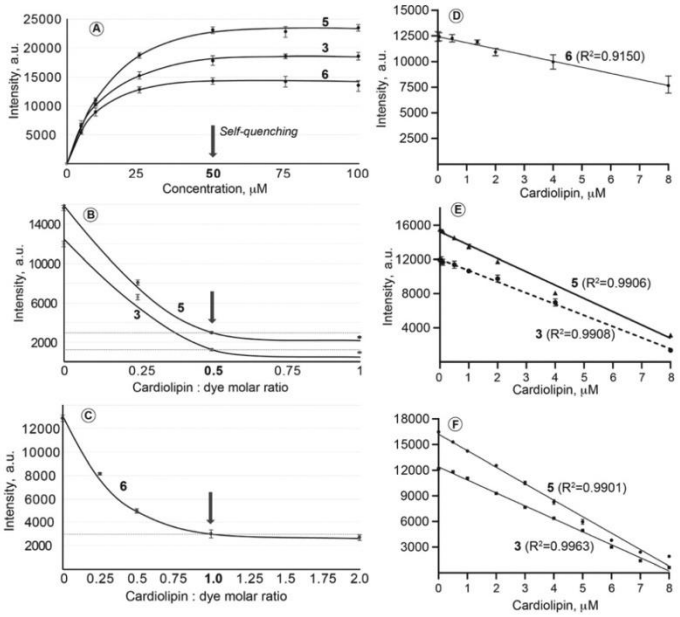

Fig. 2 (A) Emission intensities and self-quenching concentrations of **3**, **5** and **6**; (B) CL binding ratio with **3** and **5**; (C) CL binding ratio with **6**; (D) titration of **3** (●) and **5** (▲), 16 μM, with CL/DOPC liposomes (CL conc. 0.05–8 μM); (E) titration of **6**, 16 μM, with CL/DOPC liposomes (CL conc. 0.05–8 μM); (F) titration of **3** (●) and **5** (■), 20 μM, with the IMM model (CL conc. 0.05–8 μM). Titration values are shown as means of at least 6 independent experiments. CL – cardiolipin, DOPC – dioleoyl phosphatidylcholine, IMM – inner mitochondrial membrane.

tend to aggregate and are not stable enough (data not shown); thus CL liposomes are stabilized with the addition of 1,2-dioleoyl-*sn*-glycero-3-phosphocholine (DOPC) so that the CL content in the liposomes is similar to the inner mitochondrial membrane (IMM) content – 25%. NAO binds to CL in a 2 to 1 molar ratio, and binding is accompanied by a decrease in fluorescence intensity at 529 nm (CIE coordinates: *X*: 0.050031497, *Y*: 0.274001803, pure emerald green).[30] Derivative **5** interacted with CL in a similar manner to NAO, with a 2 to 1 saturating **5** : CL ratio (Fig. 2B) and an approximately five-fold decrease in fluorescence intensity. In contrast, the silatranyl moiety shifted the binding ratio to 1 : 1, probably because of its polar nature (Fig. 2C).

Nonetheless, both **5** and **6** can be used for the detection of CL. Next, the feasibility of using **5** and **6** for the quantitative analysis of CL was assessed by comparison with **3** as a standard. Derivative **6** cannot be used for the quantification of CL (linear regression curve, $R^2 < 0.99$), apparently because of its instability in aqueous medium at pH 7.4 and different binding profile as a result of the absence of a hydrophobic alkyl chain (Fig. 2D). In turn, **5** was titrated with CL in the 0.05–8 μM range, and a reliable linear regression curve ($R^2 = 0.9908$) was obtained (Fig. 2E). Consequently, **5** can be successfully used for qualitative and quantitative cardiolipin assay with superior fluorescence intensity and greater linear slope (-1557 ± 20) compared to commercially available NAO (-1311 ± 20).

Next, we tested whether compounds **3** and **5** can be used to quantify CL in a more complex liposomal model of IMM. Liposomes representing IMM were made of its major composing phospholipids – 10% phosphatidyl inositol (PI), 30% phosphatidyl ethanolamine (PE), 35% DOPC and 25% CL.[31] In both cases CL can be quantified ($R^2 > 0.99$) in the 0.5–8 μM range, and again **5** had ~30% greater fluorescence intensity and ~30% greater slope compared to **3** (Fig. 2F). More importantly, these results confirm the selectivity of **5** towards CL in the presence of other phospholipids that are characteristic for IMM.

Cytotoxicity data were collected to determine the maximal allowed dye concentrations for cell staining. Cancer and normal cells were treated with acridinium iodides **2**, **3**, **5**

Table 3 Cytotoxic activity of **2**, **3**, **5**, and **6** on breast carcinoma (MDA-MB-231), uterus sarcoma (MES-SA) and cardiomyocyte (H9C2) cell lines (48 h, MTT)

	IC_{50}, μM		
Compound	MDA-MB-231	MES-SA	H9C2
2	0.25 ± 0.03	0.38 ± 0.10	1.56 ± 0.35
3	0.31 ± 0.06	0.15 ± 0.06	1.33 ± 0.23
5	0.21 ± 0.06	0.17 ± 0.09	1.52 ± 0.32
6	2.68 ± 0.09	1.73 ± 0.17	11.87 ± 1.50

Values are shown as the means ± S.D. from 3 independent experiments.

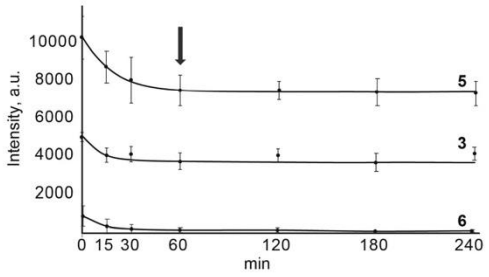

Fig. 3 Fluorescence stability in rat cardiomyocyte (H9C2) cell medium (excitation at 490 nm, emission at 520 nm).

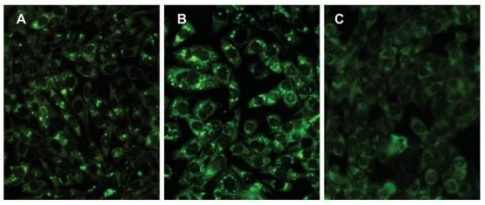

Fig. 4 Rat cardiomyocyte (H9C2) cells stained with acridinium salts in 200 nM concentration: (A) **3**; (B) **5**; (C) **6** (excitation at 490 nm, emission at 520 nm).

and **6**, and cell viability is summarized in Table 3. All the compounds demonstrated high cytotoxic activities (IC_{50} values ranging from 0.17 to 2.68 μM) in tumour cell lines. Besides, IC_{50} values on cardiomyocytes H9C2 were lower. Bearing in mind that the self-quenching of an acridinium salt is higher than its IC_{50}, the concentration of NAO and silicon-containing analogues should not exceed 1 μM for cell staining. To prevent cell apoptosis/necrosis during experiments, a concentration of 200 nM was chosen for cell staining studies. Fluorescence stability in cell media was monitored on cardiomyocytes for 4 h (Fig. 3). Based on the obtained results it can be concluded that trimethylsilyl analogue **5** exhibits double the emission intensity of **3** (NAO). Moreover, the fluorescence of **5** remains stable in a period from 1 to 4 h. As expected from previous studies, silatranyl derivative **6** is not suitable for cell imaging. Notably, the impact in intensity can be seen even with the naked eye (Fig. 4). This discovery opens a way for the improvement of photo-physical properties of fluorescent dyes by the introduction of silyl substituents into their structures.

Experimental

Unless otherwise stated, all reagents were purchased from commercial suppliers and used without further purification. Thin layer chromatography (TLC) was performed using MERCK Silica gel 60 F254 plates and visualized by UV (254 nm) fluorescence. ZEOCHEM silica gel (ZEOprep 60/35-70 microns – SI23501) was used for column chromatography. ^{1}H, ^{13}C, ^{29}Si NMR spectra were recorded on a Bruker 400 spectrometer at 400, 101, and 79 MHz, respectively, at 298 K in $CDCl_3$. The ^{1}H chemical shifts are given relative to the residual $CHCl_3$ signal (7.26 ppm), ^{13}C – relative to $CDCl_3$ (77.0 ppm), and ^{29}Si – relative to Me_4Si (0.0 ppm). The melting points were determined on an "Optimelt", and the results are given without correction. A suitable single crystal of 5 of size 0.17 × 0.09 × 0.06 mm^3 was selected and mounted on a Rigaku, XtaLAB Synergy, Dualflex, HyPix diffractometer. Diffraction data were collected at 150 K using monochromated Mo-K_α radiation (λ = 0.71073 Å). Absorption correction was performed by the empirical multi-scan method using functions of spherical harmonics, implemented in the SCALE3 ABSPACK scaling algorithm. The crystal structure of 5 was solved by direct methods with the *ShelXT*[32] structure solution program using Intrinsic Phasing and refined with the *olex2.refine* refinement package[33] using Gauss – Newton minimization. All calculations were performed with the help of *Olex2* software.[34] Crystal data for 5: monoclinic, space group *I*2/*a* (no. 15), a = 19.4926(7) Å, b = 9.8565(4) Å, c = 25.494(1) Å, β = 102.680(4)°, V = 4778.7(3) $Å^3$, Z = 8, μ(MoKα) = 1.404 mm^{-1}, D_{calc} = 1.411 g cm^{-3}, 27 563 reflections measured ($2\Theta \leq 60.0°$), 7979 unique (R_{int} = 0.0544, R_{sigma} = 0.0434) which were used in all calculations. The final R factor was 0.0345 ($I > 2\sigma(I)$) and the wR^2 index was 0.1050 (all data). For further details, see crystallographic data for **5** deposited at the Cambridge Crystallographic Data Centre as Supplementary Publication Number CCDC 1975762.†

Purification of 1

Pure acridine orange **1** was obtained from commercially available acridine orange × 0.5$ZnCl_2$ × HCl (CAS 10127-02-3) as follows: **1** was dissolved in ethyl acetate, then aqueous 1 M HCl solution was added and the mixture stirred for 10 minutes. Next, NH_3 × H_2O was added, increasing the pH to 10–11. The organic phase was separated, and the aqueous phase was extracted with ethyl acetate (3 times). The combined organic phases were washed with brine (200 ml), and then dried with anhydrous sodium sulfate. Evaporation of the solvent left the crude product, which was purified by reversed phase column chromatography previously converting 1 to hydrochloride (H_2O + 0.1% HCl/MeCN from 7% to 50%, the product came out at 15%). Next, pure fractions were combined, and the pH of the solution was increased to pH = 11. Pure acridine orange **1** was extracted with dichloromethane, washed with water and dried over sodium sulfate. After solvent evaporation a dark orange solid was obtained.

Quaternization of 1

A 100 ml round-bottom flask was charged with **1** (100 mg, 0.377 mmol) and 1 ml of a solvent (toluene, xylene or dichlorobenzene) was added and stirred at the appropriate temperature (see Table 1) until full dissolution. Then 2 equiv. (0.754 mmol) of a salt (Na_2SO_4, Na_2CO_3, K_2CO_3 or K_3PO_4) and alkyl halide in excess were added. Conversion was assessed after 10 and 25 min by LC-MS. Then the reaction mixture was filtered through a neutral Al_2O_3 pad and washed with DCM,

DCM/EtOAc (50 : 50), and DCM/iPrOH (98 : 2) mixtures. The last fractions were collected and evaporated. Compounds **2**, **3**, **5**, did not require further purification; however, **4** and **6** were additionally purified by column chromatography on neutral Al_2O_3 (eluent: DCM/iPrOH 98 : 2, with a few drops of Et_3N per 100 ml).

10-Methyl-3,6-bis(dimethylamino)acridin-10-ium iodide (2)[20]. Dark red solid. M.p. = 304–307 °C (petroleum ether/CH_2Cl_2). ^{1}H NMR (400 MHz, DMSO-d_6) δ 8.81 (s, 1H, H-9), 7.94 (d, J = 9.3 Hz, 2H, H-1 and H-8), 7.28 (dd, J = 9.3, 2.2 Hz, 2H, H-2 and H-7), 6.73 (d, J = 2.2 Hz, 2H, H-4 and H-5), 4.13 (s, 3H, N^+-CH_3), 3.28 (s, 12H, 3- and 6-N$(CH_3)_2$). ^{13}C NMR (101 MHz, chloroform-d) δ 155.5 (C-9), 143.2 (C_{Ar}), 142.6 (C_{Ar}), 133.0 (C-1 and C-8), 116.6 (C-2 and C-7), 114.5 (C-4 and C-5), 93.0 (C-3 and C-6), 40.6 (N^+-CH_3), 35.8 (3- and 6-N$(CH_3)_2$). HRMS (ESI/Q-TOF) m/z: $[M]^+$ calcd for $[C_{18}H_{22}N_3]^+$ 280.1814; found 280.1821. HPLC: 98.0% (λ = 270 nm, RT = 4.03 min, Apollo C18-9 (4.6 mm × 150 mm), mobile phase 40–95% acetonitrile + 0.1% H_3PO_4, 1 mL min^{-1}, 40 °C).

10-Nonyl-3,6-bis(dimethylamino)acridin-10-ium iodide (3)[20]. Dark red solid. M.p. = 244–247 °C (from EtOH/CH_2Cl_2). ^{1}H NMR (400 MHz, chloroform-d) δ 8.72 (s, 1H, H-9), 7.95 (d, J = 9.3 Hz, 2H, H-1 and H-8), 7.12 (dd, J = 9.3, 2.1 Hz, 2H, H-2 and H-7), 6.68 (d, J = 2.1 Hz, 2H, H-4 and H-5), 4.85 (t, J = 7.8 Hz, 2H, N^+-CH_2–), 3.35 (s, 12H, 3- and 6-N$(CH_3)_2$), 2.02 (p, J = 7.8 Hz, 2H, N^+-CH_2-CH_2–), 1.73–1.62 (m, 2H, alkyl CH_2), 1.51–1.40 (m, 2H, alkyl CH_2), 1.39–1.20 (m, 8H, alkyl CH_2), 0.87 (t, J = 6.0 Hz, 3H, –CH_3). ^{13}C NMR (101 MHz, chloroform-d) δ 155.6 (C-9), 143.2 (C_{Ar}), 142.7 (C_{Ar}), 133.5 (C-1 and C-8), 117.2 (C-2 and C-7), 114.2 (C-4 and C-5), 92.8 (C-3 and C-6), 48.5 (N^+-CH_2), 41.3 (3- and 6-N$(CH_3)_2$), 31.9 (C_{alkyl}), 29.6 (C_{alkyl}), 29.5 (C_{alkyl}), 29.3 (C_{alkyl}), 27.3 (C_{alkyl}), 26.3 (C_{alkyl}), 22.7 (C_{alkyl}), 14.2 (CH_3). HRMS (ESI/Q-TOF) m/z: $[M]^+$ calcd for $[C_{26}H_{38}N_3]^+$ 392.3066.; found 392.3072. HPLC: 97.9% (λ = 270 nm, RT = 11.35 min, Inertsil CN-3 (4.6 mm × 150 mm), mobile phase 5–50% acetonitrile + 0.1% H_3PO_4, 1 mL min^{-1}, 40 °C).

10-Dodecyl-3,6-bis(dimethylamino)acridin-10-ium iodide (4). Dark red solid. M.p. = 197–199 °C (from EtOH/CH_2Cl_2). ^{1}H NMR (400 MHz, chloroform-d) δ 8.77 (s, 1H, H-9), 7.95 (d, J = 9.3 Hz, 2H, H-1 and H-8), 7.07 (dd, J = 9.3, 2.1 Hz, 2H, H-2 and H-7), 6.61 (s, 2H, H-4 and H-5), 4.81 (t, J = 7.9 Hz, 2H, N^+-CH_2–), 3.33 (s, 12H, 3- and 6-N$(CH_3)_2$), 1.98 (p, J = 7.9 Hz, 2H, N^+-CH_2-CH_2–), 1.71–1.60 (m, 3H, alkyl CH_2), 1.49–1.38 (m, 3H, alkyl CH_2), 1.36–1.20 (m, 12H, alkyl CH_2), 0.86 (t, J = 6.0 Hz, 3H, -CH_3). ^{13}C NMR (101 MHz, chloroform-d) δ 155.7 (C-9), 143.3 (C_{Ar}), 142.9 (C_{Ar}), 133.6 (C-1 and C-8), 117.4 (C-2 and C-7), 114.3 (C-4 and C-5), 93.0 (C-3 and C-6), 48.6 (N^+-CH_2–), 41.3 (3- and 6-N$(CH_3)_2$), 32.0 (C_{alkyl}), 29.76 (C_{alkyl}), 29.74 (C_{alkyl}), 29.69 (C_{alkyl}), 29.6 (C_{alkyl}), 29.5 (C_{alkyl}), 27.4 (C_{alkyl}), 26.4 (C_{alkyl}), 22.8 (C_{alkyl}), 14.3 (CH_3). HRMS (ESI/Q-TOF) m/z: $[M]^+$ calcd for $[C_{29}H_{44}N_3]^+$ 434.3535; found 434.3543 HPLC: 97.0% (λ = 270 nm, RT = 12.79 min, Inertsil CN-3 (4.6 mm × 150 mm), mobile phase 5–50% acetonitrile + 0.1% H_3PO_4, 1 mL min^{-1}, 40 °C).

10-(3-(trimethylsilyl)propyl)-3,6-bis(dimethylamino)acridin-10-ium iodide (5). Dark red solid. M.p. = 272–275 °C (from EtOH). IR (film, ν_{max}, cm^{-1}) 3463, 3222, 2919, 2810, 1606, 1600, 1522, 1503, 1439, 1364, 1333, 1279, 1247, 1190, 1171, 918. ^{1}H NMR (400 MHz, chloroform-d) δ 8.78 (s, 1H, H-9), 7.94 (d, J = 9.3 Hz, 2H, H-1 and H-8), 7.05 (dd, J = 9.3, 2.1 Hz, 2H, H-2 and H-7), 6.52 (d, J = 2.1 Hz, 2H, H-4 and H-5), 4.79–4.71 (m, 2H, N^+-CH_2–), 3.31 (s, 12H, 3- and 6-N$(CH_3)_2$), 1.95–1.84 (m, 2H, N^+-CH_2-CH_2–), 0.91–0.83 (m, 2H, –CH_2-Si), 0.00 (s, 9H, Si-$(CH_3)_3$). ^{13}C NMR (101 MHz, chloroform-d) δ 155.6 (C-9), 143.3 (C_{Ar}), 142.6 (C_{Ar}), 133.5 (C-1 and C-8), 117.2 (C-2 and C-7), 114.2 (C-4 and C-5), 92.7 (C-3 and C-6), 51.3 (N^+-CH_2), 41.3 (3- and 6-N$(CH_3)_2$), 20.9 (N^+-CH_2-CH_2–), 14.4 (-CH_2-Si), −1.7 (Si-$(CH_3)_3$). ^{29}Si NMR (79 MHz, chloroform-d) δ 2.11. HRMS (ESI/Q-TOF) m/z: $[M]^+$ calcd for $[C_{23}H_{34}N_3Si]^+$ 380.2522; found 380.2530. HPLC: 96.5% (λ = 270 nm, RT = 10.29 min, Inertsil CN-3 (4.6 mm × 150 mm), mobile phase 5–50% acetonitrile + 0.1% H_3PO_4, 1 mL min^{-1}, 40 °C).

10-(3-(Silatranyl)propyl)-3,6-bis(dimethylamino)acridin-10-ium iodide (6). Dark red solid. M.p. = 296–299 °C. IR (film, ν_{max}, cm^{-1}) 3403, 2929, 2876, 1607, 1600, 1523, 1503, 1437, 1276, 1170, 1121, 1089, 918. ^{1}H NMR (400 MHz, chloroform-d) δ 8.63 (s, 1H, H-9), 7.89 (d, J = 9.3 Hz, 2H, H-1 and H-8), 7.09 (dd, J = 9.3, 2.1 Hz, 2H, H-2 and H-7), 6.52 (d, J = 2.1 Hz, 2H, H-4 and H-5), 4.48–4.39 (m, 2H, N^+-CH_2–), 3.76 (t, J = 5.9 Hz, 6H, O-CH_2-CH_2-N), 3.29 (s, 12H, 3- and 6-N$(CH_3)_2$), 2.92 (t, J = 5.9 Hz, 6H, O-CH_2-CH_2-N), 2.08–2.00 (m, 2H, N^+-CH_2-CH_2–), 0.61 (t, J = 7.7 Hz, 2H, -CH_2-Si). ^{13}C NMR (101 MHz, chloroform-d) δ 155.6 (C-9), 142.9 (C_{Ar}), 142.8 (C_{Ar}), 133.3 (C-1 and C-8), 117.2 (C-2 and C-7), 114.4 (C-4 and C-5), 92.7 (C-3 and C-6), 57.6 (O-CH_2-CH_2-N), 51.5 (N^+-CH_2-), 51.0 (O-CH_2-CH_2-N), 40.9 (3- and 6-N$(CH_3)_2$), 22.0 (N^+-CH_2-CH_2–), 14.2 (–CH_2-Si). ^{29}Si NMR (79 MHz, chloroform-d) δ −71.06. HRMS (ESI/Q-TOF) m/z: $[M]^+$ calcd for $[C_{26}H_{37}N_4O_3Si]^+$ 481.2635; found 481.2643. HPLC: 97.4% (λ = 270 nm, RT = 4.80 min, Apollo C18-11 (4.6 mm × 150 mm), mobile phase 40–95% acetonitrile + 0.1% H_3PO_4, 1 mL min^{-1}, 40 °C).

Luminescence measurements

The luminescence data was collected with an Edinburgh Instruments FS5 Spectrofluorometer; photoluminescence quantum yields (Φ) were measured using an integrating sphere under an ambient atmosphere. UV-Vis spectra of acridinium salts 2–6 were measured in 20 mM HEPES buffer solutions, pH 7.4 at room temperature under an ambient atmosphere at *ca.* 10^{-5} M concentration (see ESI†).

Preparation of liposomes

Cardiolipin (CL) containing liposomes for CL binding studies were prepared by a thin film method. Briefly, the desired volume of stock solutions of 1,2-dioleoyl-*sn-glycero*-3-phosphocholine – DOPC (25 mg mL^{-1}, $CHCl_3$, Avanti Polar Lipids) and bovine heart CL (5 mg mL^{-1}, EtOH, Avanti Polar Lipids) was completely evaporated under reduced pressure, and the acquired lipid film was resuspended in HEPES buffer (20 mM, pH 7.4) to acquire 100 : 300 μM CL/DOPC. Liposomes for modelling the inner mitochondrial membrane were made from L-α-phosphatidylinositol (PI, 10%), cardiolipin (CL, 25%), L-α-phosphatidylethanolamine (PE, 30%) and 1,2-dioleoyl-*sn-glycero*-3-phosphocholine (DOPC, 35%) with a total lipid concentration of 400 μM. The obtained large multilamellar liposomes were sonicated in a bath-type

sonicator (Cole Parmer Ultrasonic Cleaner 8891CPX (USA)) at room temperature for 30 min followed by extrusion (LiposoFast-Basic, Avestin) through a 100 nm polycarbonate filter (Nucleopore Corp., CA) 21 times. The quality of the resulting small unilamellar vesicles was checked by a dynamic light scattering technique (Zetasizer Nano ZSP, Malvern Panalytical Ltd, UK). All of the liposome samples used were freshly prepared before each set of measurements. A representative DLS data confirming liposome size and low polydispersity can be found in ESI.†

Fluorescence measurements

The first liposome stock solution (100 : 300 μM CL/DOPC) was diluted 5 times with HEPES buffer (20 mM, pH = 7.4) to acquire the final stock solution (20 : 60 μM CL/DOPC). 10 mM of stock solutions of 3 and 5 were prepared in ethanol, and a 50/50 mixture of ethanol and acetonitrile was used for 6. These stock solutions were diluted with HEPES buffer down to 40 μM to obtain the working solutions. Self-quenching concentrations of 3, 5 and 6 were determined by measuring the fluorescence intensity of the dye solutions (20 mM HEPES, pH = 7.4) at 529 nm (λ_{ex} = 497 nm) using a Tecan Infinite 1000 microplate reader. In order to determine the optimal CL:dye ratio and perform CL quantitative analysis, different amounts of CL containing liposomes were added to a constant amount of 3, 5 or 6 (the final concentration was 16 μM). The final volume (100 μL) was adjusted with HEPES buffer. The fluorescence intensity was measured after 15 minutes at 529 nm (λ_{ex} = 497 nm) at 37 °C using a Tecan Infinite 1000 microplate reader. To obtain calibration curves the data was analysed using GraphPad Prism® 7.0.

Cytotoxicity assay[35]

Cell viability was assessed by the addition of 3-(4,5-dimethylthiazol-2-yl)-2,5-diphenyltetrazolinium bromide (MTT). Briefly, cells were seeded (2–6 × 10^4 cells per ml) in 96-well plates and allowed to attach for 24 h. Solutions of test compounds were prepared and serially diluted to obtain the appropriate concentrations. The cells were treated with the test compounds at different concentrations (0.016–100 μM) and incubated for 48 h at 37 °C and 5% CO_2. Then, the culture medium was removed, and medium containing 0.2 mg mL^{-1} of MTT was added. After 3 h (37 °C, 5% CO_2), the MTT-containing medium was removed, and 200 μl of dimethyl sulfoxide (DMSO) was immediately added to each sample. The absorbance was assessed at 540 nm using a Tecan multiplate reader Infinite 1000 (Austria). The half-maximal inhibitory concentration (IC_{50}) of each compound was calculated using Graph Pad Prism® 3.0.

Cell staining and fluorescence stability assay

Rat embryo myoblast cells lines H9C2 (2-1) were purchased from ATCC (ATCC® CRL-1446™, Rockville, MD) and maintained in DMEM supplemented with 10% FBS at 37 °C in humidified air containing 5% CO_2. Cells were seeded (15 000 cells per well) in 96-well plates and allowed to grow for 48 h (80% confluence in each well). Then the cells were treated with the test compounds at 200 nM concentration. Cell media were photographed after 15 min, 30 min, 1 h, 2 h, 3 h, and 4 h of incubation using a Nikon Eclipse TE300 inverted fluorescence microscope with a Nikon B-2A Filter (EX 450-490, DM 505, BA 520). Magnification: 100×.

Conclusions

A simple, fast and convenient procedure has been developed by adding Na_2CO_3 or K_3PO_4 to the reaction mixture as a quaternization mediator. This accelerates the rate of the reaction from 72 h to 10 min., significantly increases the yield and almost completely eradicates by-products, so that in some cases the product does not even require additional purification. Moreover, the reagents needed to form *in situ* alkyl carbonates with various alkyl chain lengths are easily commercially available and cheap. The introduction of a 3-(trimethylsilyl)propyl moiety increases solubility and stability in buffer solution. Improvement in the fluorescence intensity by ≈30% resulted in more favourable selective quantification of CL in a liposomal inner mitochondrial membrane model compared to NAO. This novel AO analogue has the potential to serve as a fluorescent dye for cell staining. Our future efforts will be focused on the further modification of a dye structure with the aim of gaining quantum yield in order to further increase the sensitivity of CL detection.

Conflicts of interest

There are no conflicts to declare.

Acknowledgements

This work was supported by Latvian Institute of Organic Synthesis internal grant (IG-2020-01 for Pavels Dimitrijevs) Authors would like to sincerely thank Dr S. Belyakov for X-ray analysis and K. Leduskrasts for photo-physical experiments.

Notes and references

1 M. Wainwright, *J. Antimicrob. Chemother.*, 2001, **47**, 1–13.
2 F. H. Kasten, *Fluorescent and Luminescent Probes for Biological Activity*, 1999, pp. 17–39.
3 S. Hassan, D. Laryea, H. Mahteme, J. Felth, M. Fryknäs, W. Fayad, S. Linder, L. Rickardson, J. Gullbo, W. Graf, L. Påhlman, B. Glimelius, R. Larsson and P. Nygren, *Cancer Sci.*, 2011, **102**, 2206–2213.
4 U. S. Singh and R. P. Singh, *Molecular Methods in Plant Pathology*, CRC Press, Inc., 1st edn, 1995.
5 K. G. Lyamzaev, N. V. Sumbatyan, A. M. Nesterenko, E. G. Kholina, N. Voskoboynikova, H. J. Steinhoff, A. Y. Mulkidjanian and B. V. Chernyak, *Oxid. Med. Cell. Longev.*, 2019, **2019**, 9710208.
6 C. W. T. Leung, Y. Hong, J. Hanske, E. Zhao, S. Chen, E. V. Pletneva and B. Z. Tang, *Anal. Chem.*, 2014, **86**, 1263–1268.
7 Y. Wang, X. Han, X. Zhang, L. Zhang and L. Chen, *Analyst*, 2020, **145**, 1389–1395.

8 K. N. Wang, Y. Zhu, M. Xing, D. Cao, R. Guan, S. Zhao, Z. Liu and Z. W. Mao, *Sens. Actuators, B*, 2019, **295**, 215–222.
9 M. Gao, F. Yu, H. Chen and L. Chen, *Anal. Chem.*, 2015, **87**, 3631–3638.
10 M. H. Ratinaud, P. Leprat and R. Julien, *Cytometry*, 1988, **9**, 206–212.
11 L. D. Renner and D. B. Weibel, *Proc. Natl. Acad. Sci. U. S. A.*, 2011, **108**, 6264–6269.
12 M. Kicia, N. Janeczko, J. Lewicka and A. B. Hendrich, *J. Med. Microbiol.*, 2012, **61**, 520–524.
13 E. Mileykovskaya and W. Dowhan, *J. Bacteriol.*, 2000, **182**, 1172–1175.
14 G. Paradies, V. Paradies, F. M. Ruggiero and G. Petrosillo, *Cells*, 2019, **8**, 728.
15 C. B. Pointer and A. Klegeris, *Cell. Mol. Neurobiol.*, 2017, **37**, 1161–1172.
16 F. Valianpour, R. J. A. Wanders, H. Overmars, F. M. Vaz, P. G. Barth and A. H. Van Gennip, *J. Lipid Res.*, 2003, **44**, 560–566.
17 J. Zhang, W. Yu, S. W. Ryu, J. Lin, G. Buentello, R. Tibshirani, J. Suliburk and L. S. Eberlin, *Cancer Res.*, 2016, **76**, 6588–6597.
18 A. Sapandowski, M. Stope, K. Evert, M. Evert, U. Zimmermann, D. Peter, I. Päge, M. Burchardt and L. Schild, *Mol. Cell. Biochem.*, 2015, **410**, 175–185.
19 G. Larrouy-Maumus, *Curr. Med. Chem.*, 2018, **26**, 1924–1932.
20 M. E. Rodriguez, K. Azizuddin, P. Zhang, S. mao Chiu, M. Lam, M. E. Kenney, C. Burda and N. L. Oleinick, *Mitochondrion*, 2008, **8**, 237–246.
21 P. Kaewsuya, J. D. Miller, N. D. Danielson, J. Sanjeevi and P. F. James, *Anal. Chim. Acta*, 2008, **626**, 111–118.
22 A. Yamaglshi, T. Masui and W. Fumlyukl, *J. Phys. Chem.*, 1981, **85**, 281–285.
23 D. Sabolová, M. Vilková, J. Imrich and I. Potočňák, *Tetrahedron Lett.*, 2016, **57**, 5592–5595.
24 P. Tundo, M. Musolino and F. Aricò, *Green Chem.*, 2018, **20**, 28–85.
25 A. M. Modro and T. A. Modro, *J. Phys. Org. Chem.*, 1989, **2**, 263–270.
26 V. F. Sidorkin, V. A. Pestunovieh and M. G. Voronkov, *Magn. Reson. Chem.*, 1985, **23**, 491–493.
27 J. H. Iwamiya and G. E. Maciel, *J. Am. Chem. Soc.*, 1993, **115**, 6835–6842.
28 E. Kupče and B. Wrackmeyer, *Appl. Organomet. Chem.*, 2010, **24**, 837–841.
29 P. Kaewsuya, N. D. Danielson and D. Ekhterae, *Anal. Bioanal. Chem.*, 2007, **387**, 2775–2782.
30 J.-M. Petit, A. Maftah, M.-H. Ratinaud and R. Julien, *Eur. J. Biochem.*, 1992, **209**, 267–273.
31 S. E. Horvath and G. Daum, *Prog. Lipid Res.*, 2013, **52**, 590–614.
32 G. M. Sheldrick, *Acta Crystallogr., Sect. A: Found. Crystallogr.*, 2015, **71**, 3–8.
33 L. J. Bourhis, O. V. Dolomanov, R. J. Gildea, J. A. K. Howard and H. Puschmann, *Acta Crystallogr., Sect. A: Found. Crystallogr.*, 2015, **71**, 59–75.
34 O. V. Dolomanov, L. J. Bourhis, R. J. Gildea, J. A. K. Howard and H. Puschmann, *J. Appl. Crystallogr.*, 2009, **42**, 339–341.
35 T. Mosmann, *J. Immunol. Methods*, 1983, **65**, 55–63.

Second Publication

www.nature.com/scientificreports

scientific reports

Check for updates

OPEN

Fused isoselenazolium salts suppress breast cancer cell growth by dramatic increase in pyruvate-dependent mitochondrial ROS production

Marina Makrecka-Kuka[1], Pavels Dimitrijevs[1,2], Ilona Domracheva[1], Kristaps Jaudzems[1], Maija Dambrova[1,2] & Pavel Arsenyan[1]✉

The development of targeted drugs for the treatment of cancer remains an unmet medical need. This study was designed to investigate the mechanism underlying breast cancer cell growth suppression caused by fused isoselenazolium salts. The ability to suppress the proliferation of malignant and normal cells in vitro as well as the effect on NAD homeostasis (NAD^+, NADH, and NMN levels), NAMPT inhibition and mitochondrial functionality were studied. The interactions of positively charged isoselenazolium salts with the negatively charged mitochondrial membrane model were assessed. Depending on the molecular structure, fused isoselenazolium salts display nanomolar to high micromolar cytotoxicities against MCF-7 and 4T1 breast tumor cell lines. The studied compounds altered NMN, NAD^+, and NADH levels and the NAD^+/NADH ratio. Mitochondrial functionality experiments showed that fused isoselenazolium salts inhibit pyruvate-dependent respiration but do not directly affect complex I of the electron transfer system. Moreover, the tested compounds induce an immediate dramatic increase in the production of reactive oxygen species. In addition, the isoselenazolothiazolium derivative selectively binds to cardiolipin in a liposomal model. Isoselenazolium salts may be a promising platform for the development of potent drug candidates for anticancer therapy that impact mitochondrial pyruvate-dependent metabolism in breast cancer cells.

Breast cancer is the most common cancer in women and is the second leading cause of cancer-related deaths worldwide[1,2]. In clinical practice, a wide range of chemotherapeutic agents are used for treating cancer, but most of these agents are also toxic to nonmalignant cells and therefore cause serious side effects, which further worsen the patients' well-being. Chemotherapeutic agents frequently lack selectivity, and their use may result in tumors becoming resistant to the drug[3]. Due to key role of mitochondria in cellular proliferation and death[4], targeting mitochondria is a perspective anticancer strategy, that has reached clinical trial stage and received FDA approval. For example, venetoclax, an inhibitor of mitochondrial antiapoptotic protein Bcl-2, and enasidenib, an inhibitor of mitochondrial metabolic enzyme IDH2, were approved by the FDA for the treatment of chronic lymphocytic leukemia and acute myeloid leukemia, respectively[5]. Classic approaches targeting the mitochondria of cancer cells are usually aimed at directly affecting the functions of mitochondrial antiapoptotic proteins or inducing changes in energy metabolism (causing a shift from glycolysis to oxidative phosphorylation). Despite the well-known Warburg effect, cancer cells can also develop a hybrid metabolic phenotype (both glycolysis and oxidative phosphorylation to support ATP production), which ensures the plasticity of cancer cells in metastasis and therapy resistance[6]. Moreover, mitochondria participate in metabolic crosstalk with the tumor microenvironment, which plays a key role in the progression of breast cancer[7]. Thus, approaches targeting cancer mitochondrial bioenergetics (affecting metabolism and/or apoptotic pathways) are promising for the development of novel and effective anticancer therapeutics[8].

Since selenium is involved in many signaling pathways in the human body and is vital for proper physiological performance and the prevention of cell mutations leading to oncological diseases[9], the introduction of selenium into the structures of these molecules has attracted the attention of researchers[10,11]. Various research groups have

[1]Latvian Institute of Organic Synthesis, Aizkraukles 21, Riga 1006, Latvia. [2]Riga Stradins University, Dzirciema 16, Riga 1007, Latvia. ✉email: pavel@osi.lv

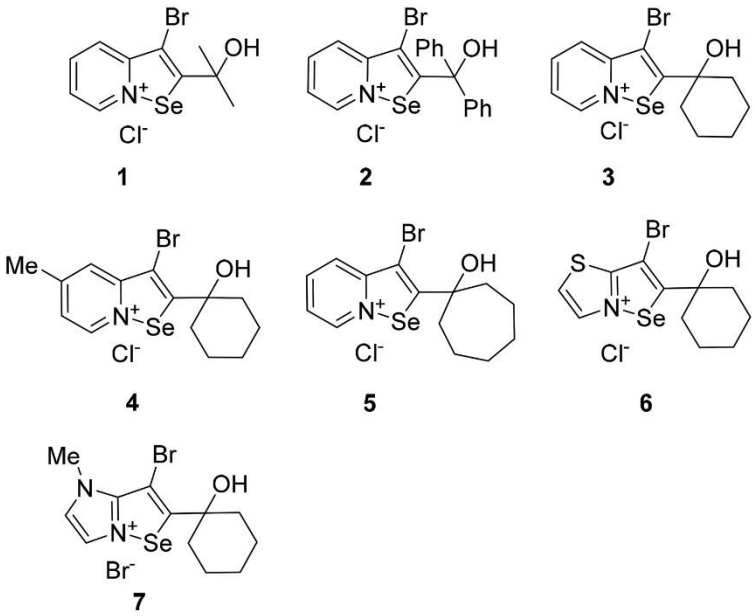

Figure 1. Tested fused isoselenazolium salts **1**–7.

focused on developing prospective drug candidates[11–20]; however, the most famous selenium drug candidate so far is ebselen, which contains Se–N bonds. It is a multifunctional compound that catalyzes several essential reactions (e.g., reduces reactive oxygen species (ROS) in a manner similar to glutathione peroxidase (GPx), and highly efficiently oxidizes reduced thioredoxin and catalyzes hydrogen peroxide reduction by thioredoxin reductase (TrxR), which acts as a dehydroascorbic acid (DHA) reductase mimetic) for the protection of cellular components from oxidative and free radical damage[21]. Recently, we elaborated methods for the preparation of novel, stable fused isoselenazolium salts, namely, systems with a Se–N^+ bond[22]. These compounds, which possess electrophilic selenium in their structure, exhibit glutathione peroxidase-like properties, are toxic to *S. feltiae*, induce DNA double-strand damage at moderate doses, and display excellent antibacterial activity[23–25]. Interestingly, bacteria and mitochondria share a unique phospholipid in their membrane structures, cardiolipin (CL), which is a prospective therapeutic target[26–28]. CL was identified as a novel molecular signature of oncocytic and prostate tumors characterized by abnormally high abundance and chemical diversity[29–31]. Thus far, interactions of selenium-containing compounds with CL and the corresponding effects on mitochondrial function have not been studied.

In this report, we evaluated the ability of isoselenazolium salts to inhibit human breast adenocarcinoma MCF-7 and mouse carcinoma 4T1 proliferation. Their effects on rat cardiomyoblasts (H9C2), mouse fibroblasts (NIH 3T3), primary human epidermal keratinocytes (HEKa), Madin-Darby Canine Kidney (MDCK) cells, and rat vascular smooth muscle cells (A7r5) are included in this study to demonstrate whether these compounds are harmless to normal cells. The effects of these compounds on NAD^+ homeostasis and mitochondrial function were studied. The ability of isoselenazolium salts to interact with CL-containing mitochondrial model membranes was evaluated by NMR spectroscopy and isothermal titration calorimetry (ITC).

Results

Fused isoselenazolium salts display up to nanomolar cytotoxic activity. The cytotoxicities of fused isoselenazolium salts **1**–**7** (Fig. 1) are summarized in Table 1. All the compounds demonstrated higher cytotoxic activities (IC_{50} values ranging from 0.044 to 3.23 μM) than the reference compound, Na_2SeO_3, in breast tumor cell lines. IC_{50} values of the studied isoselenazolium salts **1**–**7** were in the same range as for doxorubicin, however, mammary carcinoma (4T1) cells were more susceptible to derivative **3** than to doxorubicin. The IC_{50} values of compound **1** for the tumor cell lines were comparable to its IC_{50} values for normal cell lines. The replacement of the methyl group with a phenyl group (**2**) potentiated the cytotoxic effect on the MCF-7 breast tumor cell line. Notably, compound **3** showed the lowest cytotoxicity IC_{50} values (nanomolar range) against breast tumor cells. The introduction of a methyl substituent on the pyridine ring (**4**) led to a slight decrease in the cytotoxicity. Cyclohexyl ring (**4**) expansion to cycloheptyl (**5**) increased the cytotoxicity by approximately 3

	Cytotoxicity, IC_{50}, μM						
	Breast cancer cell lines		Normal cell lines				
Compound	MCF-7	4T1	H9C2	3T3	HEKa	MDCK	A7r5
Na_2SeO_3	17.1 ± 2.4	4.9 ± 0.6	1.5 ± 0.3	22.3 ± 3.6	13.3 ± 1.1	6.3 ± 0.4	39.4 ± 8.2
Doxorubicin	1.0 ± 0.3	0.16 ± 0.06	11.0 ± 1.0	0.75 ± 0.09	n.t	57.0 ± 6.1	1.82 ± 0.35
1	3.10 ± 0.03	0.30 ± 0.03	1.8 ± 0.1	0.13 ± 0.02	2.31 ± 0.02	3.26 ± 0.40	2.89 ± 0.42
2	0.39 ± 0.03	1.1 ± 0.08	4.2 ± 0.3	1.6 ± 0.3	2.78 ± 0.08	6.27 ± 0.29	1.87 ± 0.26
3	0.50 ± 0.02	0.044 ± 0.005	2.2 ± 0.1	0.39 ± 0.05	2.21 ± 0.02	2.91 ± 0.13	1.85 ± 0.22
4	1.48 ± 0.04	0.45 ± 0.02	2.9 ± 0.1	0.79 ± 0.02	2.05 ± 0.05	2.54 ± 0.57	1.93 ± 0.16
5	0.29 ± 0.01	0.41 ± 0.05	9.3 ± 0.2	0.98 ± 0.03	2.01 ± 0.08	1.51 ± 0.37	1.92 ± 0.44
6	3.23 ± 0.03	1.7 ± 0.2	3.7 ± 0.2	7.4 ± 0.8	2.84 ± 0.08	6.58 ± 0.33	1.97 ± 0.27
7	1.48 ± 0.02	0.94 ± 0.06	0.67 ± 0.02	2.2 ± 0.3	2.19 ± 0.09	4.28 ± 0.34	1.66 ± 0.25

Table 1. Cytotoxic activity of **1**–**7** against breast tumor and normal cell lines. Values are shown as the means ± S.D. from 3 independent experiments. nt, not tested.

times against MCF-7 cells. To study the influence of the heterocycle on the activity of the fused isoselenazolium salt, we replaced the pyridine with thiazole and imidazole rings. The introduction of a thiazole ring (**6**) decreased the cytotoxicity to tumor cells and to normal cell lines. However, [1,2]selenazolo[2,3-*b*]imidazolinium bromide (**7**) exhibited a slightly higher ability than compound **6** to suppress tumor cell growth. However, **7** showed higher toxicity than compound **6** against cardiomyocytes H9C2 and fibroblasts 3T3.

In addition, IC_{50} values of **1**–**7** on HEKa and A7r5 were around 2 μM and did not depend on particular structure of isoselenazolium. Derivatives **2** and **6** were less toxic to MDCK cells than the other compounds. It is worth noting that 3-bromo-2-(1-hydroxycyclohexyl)-[1,2]selenazolo[2,3-*a*]pyridinium chloride (**3**) had the most pronounced selectivity towards tumor cell lines (> 42 fold, comparing 4T1 to A7r5). Derivatives **3**, **6** and **7** were chosen to study the possible mechanisms of action of fused isoselenazolium salts, taking into consideration the difference in cytotoxic effects on carcinoma and normal cell lines.

Fused isoselenazolium salts affect on NAD⁺ homeostasis. The levels of NAD^+ and its metabolites are critical for tumor cell proliferation[32–35]; therefore, the effects of the fused isoselenazolium salts on the NMN, NAD^+ and NADH levels as well as NAMPT activity were tested. As shown in Fig. 2A, compounds **3** and **6**, but not compound **7**, induced a decrease in NMN levels by 33% and 26%, respectively. In addition, compound **3** significantly decreased the levels of NAD^+ and NADH by 59% and 33%, respectively, and as a result, the NAD^+/NADH ratio was decreased by 38% (Fig. 2A,B). Compound **6** induced a 25% decrease in the NAD^+ level without affecting the NADH content or the NAD^+/NADH ratio in the cells (Fig. 3A,B). In contrast to compound **6**, compound **7** induced a decrease in NADH level without affecting the NAD^+ concentration, and as a result, the NAD^+/NADH ratio was 1.65-times higher than that in untreated cells (Fig. 2A,B). Notably, only isoselenazoloimidazolium salt **7** induced a notable reduction in NAMPT activity (by 31%, Fig. 2C). Taken together, these results indicate that fused isoselenazolium salts alter NAD^+ homeostasis in breast tumor cells.

Fused isoselenazolium salts inhibit pyruvate-dependent mitochondrial respiration and facilitate ROS production. Since mitochondria play a significant role in ROS production and NAD^+ metabolism and experiments showed that fused isoselenazolium salts affect NAD^+ homeostasis, the next step was to test whether the compounds alter mitochondrial function. First, the concentration-dependent effects of compounds **3** and **6** on the complex I (NADH-linked) and complex II (succinate-linked) pathways were determined. Both compounds, **3** and **6**, inhibited the mitochondrial respiration rate in a concentration-dependent manner and increased H_2O_2 production with complex I (CI, NADH-linked) substrates (both pyruvate + malate and glutamate + malate) (Fig. 3A,B). In addition, there were no significant changes in mitochondrial function in the CII-linked OXPHOS state (Fig. 3). Despite difference in compound potency, the most pronounced increase in the H_2O_2/O ratio in the presence of isoselenazolium salts **3** and **6** was observed when pyruvate and malate were used as substrates (Fig. 3C). These results indicate that isoselenazolium salts most likely affects pyruvate-dependent mitochondrial metabolism.

To determine whether the observed effects of the fused isoselenazolium salt are related to the inhibition of the pyruvate-dependent pathway but not to the direct inhibition of complex I, the mitochondrial function in permeabilized breast cancer cells was evaluated in the presence of 1 μM **3, 6** and **7**. Although only compound **6** decreased the respiration rate in the OXPHOS state with pyruvate and malate (Fig. 4A,E), both compounds **3** and **6** induced a significant decrease in the OXPHOS coupling efficiency (corresponds to 1-Respiratory Control Ratio^{-1}) (Fig. 4B; ESI Fig S1). The addition of another NADH-dependent complex I substrate, glutamate, compensated for the decrease in respiration with pyruvate + malate, as shown by the increased flux control factor (characterizes individual substrate/pathway input to the electron transfer system performance) for glutamate (Fig. 5B). Together with the unchanged flux control factor for rotenone (Fig. 4B), these results indicate that fused isoselenazolium salts do not inhibit complex I. All three tested isoselenazolium derivatives (**3, 6** and **7**) induced immediate significant increases in H_2O_2 production and the H_2O_2/O ratio in the pyruvate-dependent OXPHOS state (Fig. 4C,D,F). The effects of compound **6** on H_2O_2 production and the H_2O_2/O ratio were the most

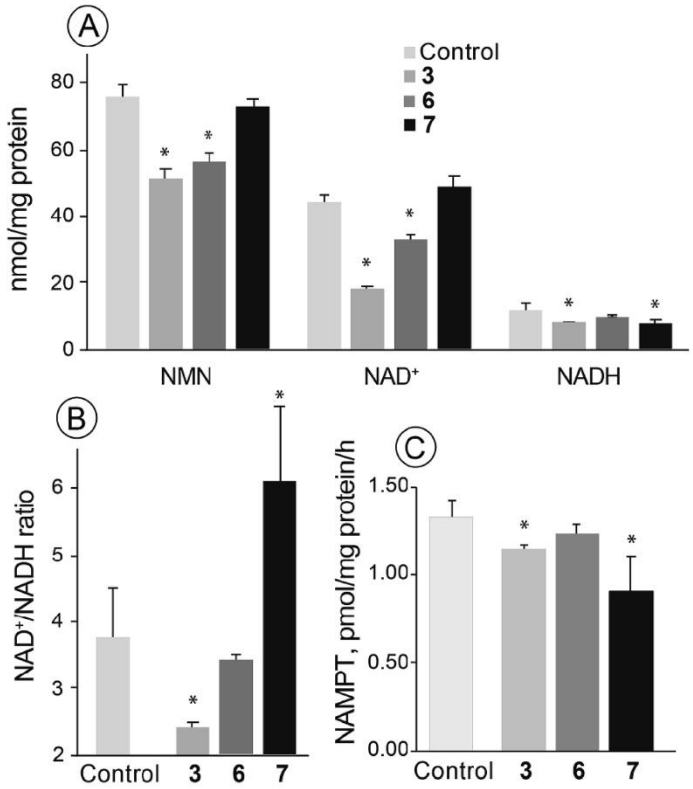

Figure 2. The effects of fused isoselenazolium salts on the levels of NMN, NAD^+ and NADH and NAMPT activity in MCF-7 cells (**A**); NAD^+/NADH ratio (**B**); NAMPT inhibition by **3**, **6** and **7**. Values are shown as the mean ± S.D. ($n = 6$). Significant difference (*- $p < 0.05$) compared with control.

pronounced (2.3- and 2.8-fold increases, respectively). In addition, significant increases in H_2O_2 production and the H_2O_2/O ratio in the CI&II-linked OXPHOS state were observed in cells treated with **6** (Fig. 4C,D). Taken together, the obtained results indicate that fused isoselenazolium salts inhibit pyruvate-dependent mitochondrial respiration and facilitate ROS production.

Fused isoselenazolium salts selectively interact with cardiolipin. To evaluate whether fused isoselenazolium salts can act directly on mitochondria, the interactions of derivative **6** with mitochondrial membrane components, DOPC/CL liposomes, were tested. As seen in Fig. 5A, in the absence of DOPC and CL, compound **6** shows sharp resonances with clearly distinguishable spin coupling patterns. In the presence of DOPC liposomes, the aromatic resonances of compound **6** are noticeably broadened such that the coupling pattern is not resolved. This could indicate a weak interaction between compound **6** and DOPC liposomes or, alternatively, the changes in resonance could be due to altered molecular surroundings (liposomal dispersion). However, in the presence of CL-containing liposomes, these resonances are broadened. These results were also confirmed by the ITC experiments (Fig. 5B,C). DOPC liposome titration with compound **6** did not result in any heat release, and no signs of binding were observed (Fig. 5B). In contrast, the negative heat flow observed after each injection of compound **6** (in µcal/s) indicates that the isoselenazolium cation–CL interaction is accompanied by a decrease in enthalpy (Fig. 5C). These results indicate that compound **6** binds to the mitochondrial model membrane.

Discussion

The discovery of a mechanism of action is a corner stone in the development of new drug candidates for anticancer therapy. In the study presented in herein, we sought to "lift the veil" and determine the nature of cancer cell growth suppression by isoselenazolium salts.

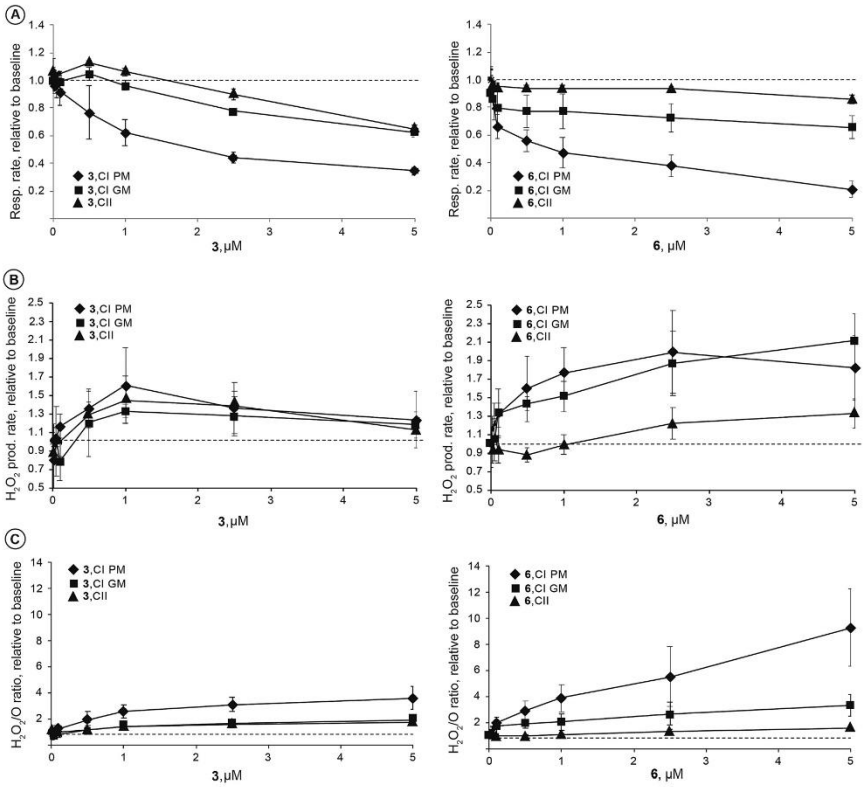

Figure 3. The concentration-dependent effects of compounds **3** and **6** on mitochondrial function in permeabilized 4T1 cells. Concentration dependent changes in mitochondrial respiration rate (**A**) and H_2O_2 production rate (**B**) and H_2O_2/O ratio (**C**) at Complex I or II linked OXPHOS. P—pyruvate; M—malate; G—glutamate. Values are shown as mean ± S.D. (n = 3–5 experiments) relative to baseline (dashed line)—before addition of the compound.

Here, we show for the first time that isoselenazolium salts exhibit in vitro cytotoxic effects against breast cancer cells at nanomolar to low micromolar concentrations. These compounds are more cytotoxic on studied cancer cell lines than widely known doxorubicin (up to 3.6 fold on 4T1 cell line), moreover, some derivatives are equally or less harmful to normal cells. The IC_{50} values of doxorubicin in tumor cells versus cardiomyocytes are 10–100-fold lower, alongside some of studied isoselenazolium salts showed similar tendency. Thus, we can expect that therapeutic potential of presented compounds could be comparable to doxorubicin, however, to maximize it, improvement of isoselenazolium salts selectivity towards tumor cells is required. Furthermore, our study shows the potential mechanisms responsible for the anticancer activities of fused isoselenazolium salts. The compounds inhibit pyruvate metabolism and simultaneously increase ROS production, resulting in altered NAD^+ homeostasis in breast cancer cells. Based on differences in cytotoxic effects against malignant and normal cells, isoselenazolium salts could be a powerful platform for further optimization to develop agents that target cancer cell mitochondrial energy metabolism. The studied derivatives significantly increased mitochondrial ROS production and inhibited pyruvate-dependent metabolism (Fig. 6), thus showing cancer cell-specific cytotoxic activity.

Targeting mitochondrial metabolic pathways and the redox homeostasis of tumor cells is an attractive approach for anticancer therapy[36–38]. Isoselenazolium salts have intriguing effects on the main metabolic pathways in tumor cells and are associated with cell bioenergetics, affecting mitochondrial NAD^+/NADH-dependent metabolism. The NAD^+/NADH ratio plays an important role in the regulation of the intracellular redox state and proliferation, impaired cell death signaling, and deregulated metabolism[32,39]. The induction of excess NAD^+ over NADH is an attractive approach for the prevention of tumor metastasis in vivo[33]. Although NAMPT inhibition has been proposed as an effective strategy for disturbing NAD^+ homeostasis in cancer cells[34], only slight decreases in NAMPT activity were observed with **3** and **7**, and this result could not explain the changes in NAD^+

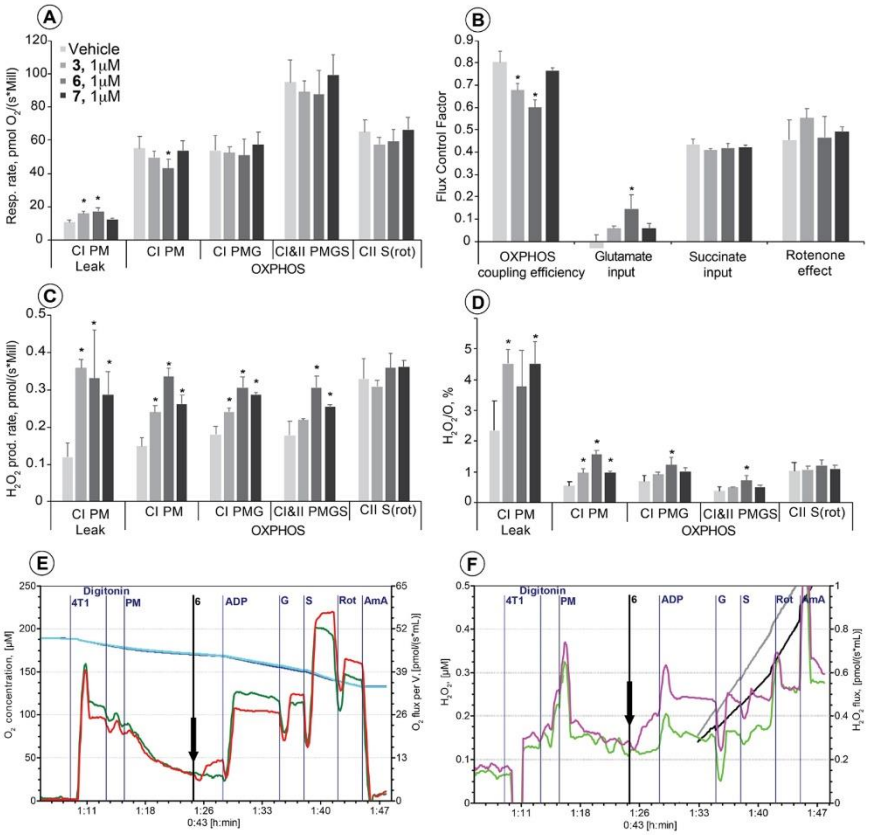

Figure 4. The effect of fused isoselenazolium salts at 1 μM concentration on mitochondrial respiration (**A**), flux control factors (**B**), H_2O_2 production rate (**C**) and H_2O_2/O ratio (**D**) in permeabilized 4T1 cells. Representative traces of respiration (**E**) and H_2O_2 production rate (**F**) measurement (vehicle—green (**E**) and light green (**F**) lines; compound 6—red (**E**) and purple (**F**) lines). CI—complex, I; CII—complex II; LEAK—substrate dependent respiration rate; OXPHOS—oxidative phosphorylation dependent state; P—pyruvate; M—malate; ADP—saturating ADP; G—glutamate; S—succinate; Rot—rotenone, AmA—antimycin A. OXPHOS coupling efficiency corresponds to 1-Respiratory Control Ratio^{-1}. Flux Control Factor indicates on the input of each substrate and/or pathway to the electron transfer system performance. Values are shown as mean ± S.D. (n = 3–4 experiments). Significant difference (*- $p < 0.05$) compared with control.

metabolite levels induced by isoselenazolium salts. Thus, it is more likely that fused isoselenazolium salts alter NAD^+ homeostasis by acting on NAD^+-dependent pathways (e.g. SIRT and PARP family enzymes, Preiss-Handler pathway) or on the energy metabolism processes, rather than on NAD^+ biosynthesis. The mechanisms of action could be partly related to the inhibition of pyruvate metabolism, as breast cancer cell proliferation relies heavily on pyruvate metabolism[40]. The inhibition of pyruvate metabolism by a blockade of the mitochondrial pyruvate transporter was recently shown to decrease the uptake of extracellular lactate, thus inhibiting lactate-driven metabolic symbiosis between cancer cells[41]. These metabolic changes resulted in sensitization of cancer cells to oxidative stress and inhibition of cell growth. Isoselenazolium salts block pyruvate-dependent mitochondrial respiration without affecting complex I, leading to the selective disruption of cancer cell metabolism and dramatically increased ROS production. Thus, isoselenazolium salts exhibit dual activity: they both inhibit pyruvate-dependent metabolism and simultaneously induce oxidative stress that results in the inhibition of cell division and causes cytotoxic effects.

The isoselenazolium salt-stimulated pyruvate metabolism-driven ROS production could be explained by several mechanisms[42]: (a) effect on electron transfer system; (b) effect on tricarboxylic acid cycle (TCA); (c) effect on pyruvate metabolism pathway. The main sites of ROS production in electron transfer system are complexes I and III[43]. Since there is no change in ROS production in the presence of rotenone, i.e. in the conditions when

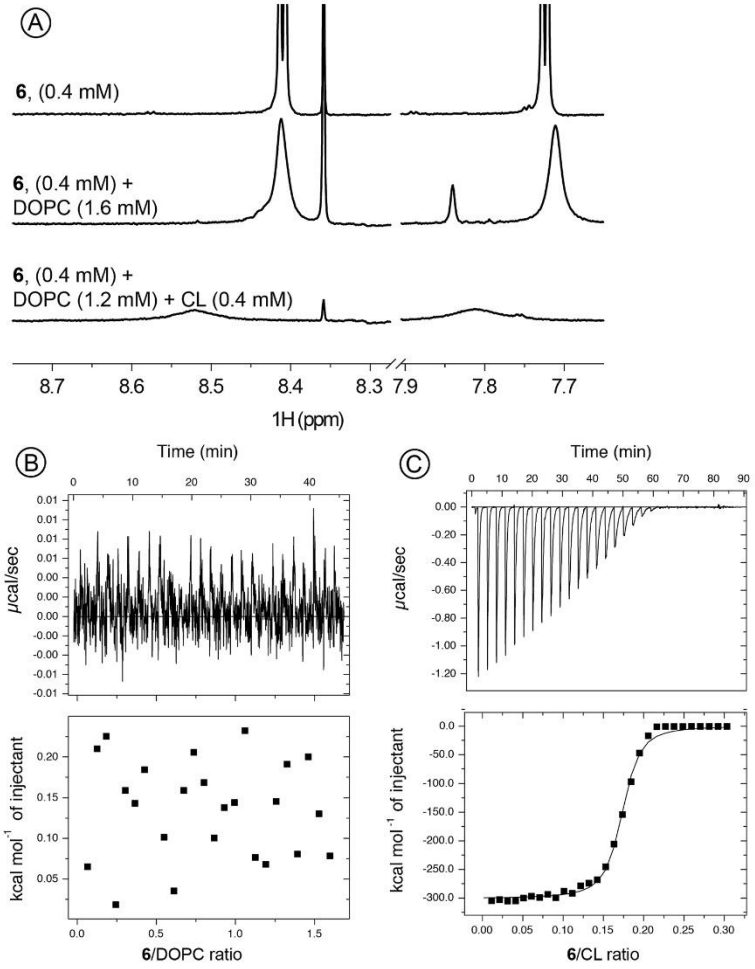

Figure 5. (**A**) 600 MHz ^{1}H NMR spectra of 0.4 mM **6** (top), 0.4 mM **6** and 1.6 mM DOPC (middle) and 0.4 mM **6** and 1.2 mM DOPC with 0.4 mM CL (bottom) in 90% H_2O/10% D_2O. (The zoomed aromatic region is shown. Full spectra presented in SI); (**B**) and (**C**) Binding isotherms and calorimetric curves at 25 °C for titration of DOPC and CL/DOPC (1:3) containing vesicles with serial injections of compound **6**.

complex I is inhibited, we can conclude that isoselenazolium salts do not affect complex III. Another option is that isoselenazolium salt-induced ROS production could be linked to the reverse electron transport via complex I. However, titration experiments with compound 6 at complex I-linked oxidative phosphorylation-dependent state showed that there is a significant difference in ROS production between complex I substrates used (pyruvate or glutamate), indicating that it is more likely that isoselenazolium salt-stimulated ROS production is not related to the induction of reverse electron transport process. Another source of increased pyruvate-driven ROS production could be 2-oxoglutarate dehydrogenase in TCA cycle[44]. The substrate flux through 2-oxoglutarate dehydrogenase is supported by both pyruvate and glutamate metabolism, thus, in the case of inhibition of 2-oxoglutarate dehydrogenase isoselenazolium salts would affect metabolism with both substrates. Our data showed that isoselenazolium salts do not inhibit glutamate metabolism; moreover, we observed the stimulation of glutamate metabolism in the presence of pyruvate after addition of tested compounds, as indicated by increased flux control factor (ESI, Fig. S1). Thus, the involvement of 2-oxoglutarate dehydrogenase in the isoselenazolium salt-induced ROS production could be excluded. Other proposed mechanism of action is the inhibition of pyruvate metabolism by either inhibiting pyruvate transport or pyruvate dehydrogenase complex (PDC). Since

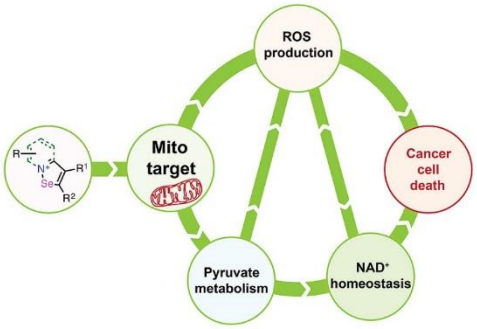

Figure 6. Proposed cytotoxicity-inducing mechanism of action of isoselenazolium salts.

compounds at tested concentrations did not affect the pyruvate dehydrogenase activity (ESI Fig. S2), it is more likely that isoselenazolium salts alter pyruvate transport; however, the involvement of PDC inhibition cannot be fully excluded.

Since the mitochondrial membrane potential ($\Delta\psi_m$) in cancer cells is at least 60 mV higher than that of normal cell mitochondria[45], positively charged molecules could be a useful approach for selectively targeting cancer cell mitochondria. Moreover, the accumulation of lipophilic cations inside the membrane is dependent on the membrane potential and increases by ten-fold for every 61.5 mV[45–47]. NMR and ITC experiments confirmed that fused isoselenazolium salt **6** selectively interacts with CL, a component of the inner mitochondrial membrane. Obviously, such selective binding takes place between a positively charged isoselenazolium core and negatively charged CL phosphate moieties. The ability of the isoselenazolium salt to bind to CL could explain the observed inhibition of pyruvate-dependent metabolism and the induction of ROS production, particularly because a similar mechanism of action was described for doxorubicin, an anthracycline antibiotic widely used as an anticancer agent[48]. However, unlike doxorubicin, at the studied concentrations, isoselenazolium salts do not inhibit electron transfer but specifically affect pyruvate-dependent metabolism, indicating they may have less pronounced cardiotoxic side effects. Taking into account doxorubicin-induced cardiotoxicity, further studies will be focused on the cardiac safety of the presented isoselenazolium compounds for the further development of novel isoselenazolium derivatives with improved cytotoxic selectivity to cancer cells compared with normal cells, particularly cardiomyocytes.

Methods

Tested compounds. Isoselenazolium salts were synthesized, purified and characterized by spectroscopy and elemental analysis as described before[22]:

3-bromo-2-(2-hydroxy-2-methylethyl)-[1,2]selenazolo[2,3-*a*]pyridinium chloride (**1**).
3-bromo-2-(hydroxydiphenylmethyl)-[1,2]selenazolo[2,3-*a*]pyridin-8-ium (**2**).
3-bromo-2-(1-hydroxycyclohexyl)-[1,2]selenazolo[2,3-*a*]pyridinium chloride (**3**).
3-bromo-2-(1-hydroxycyclohexyl)-5-methyl-[1,2]selenazolo[2,3-*a*]pyridin-8-ium (**4**).
3-Bromo-2-(1-hydroxycycloheptyl)-[1,2]selenazolo[2,3-*a*]pyridinium bromide (**5**).
3-bromo-2-(1-hydroxycyclohexyl)[1,2]selenazolo[2,3-*b*]thiazolium chloride (**6**).
3-bromo-*N*-methyl-2-(1-hydroxycyclohexyl)[1,2]selenazolo[2,3-*b*]imidazolium bromide (**7**).
Sodium selenite, Na_2SeO_3, a simple and toxic selenium compound, was used as a reference.

Cell culture. MCF-7 (human breast adenocarcinoma, estrogen-positive) and 4T1 (mouse carcinoma), as breast cancer cell lines, and H9C2 (rat cardiomyoblasts), NIH 3T3 (mouse fibroblasts), HEKa (primary human epidermal keratinocytes), MDCK (Madin-Darby Canine Kidney) cells, and A7r5 (rat vascular smooth muscle cells), as normal cell lines, were obtained from the American Type Culture Collection [ATCC] collection for use in the current study. All cell lines were cultured in Dulbecco's modified Eagle's medium (DMEM) containing 10% fetal bovine serum (FBS) and 4 mM L-glutamine at 37 °C and 5% CO_2.

Cytotoxicity assay[49]. Cell viability was assessed by the addition of 3-(4,5-dimethylthiazol-2-yl)-2,5-diphenyltetrazolinium bromide (MTT). Briefly, cells were seeded ($2–6\times10^4$ cells/ml) in 96-well plates and allowed to attach for 24 h. Solutions of test compounds were prepared and serially diluted to obtain the appropriate concentrations. The cells were treated with the test compounds at different concentrations (0.032–100 μM) and incubated for 48 h at 37 °C and 5% CO_2. Then, the culture medium was removed, and medium containing 0.2 mg/ml MTT was added. After 3 h (37 °C, 5% CO_2), the MTT-containing medium was removed, and 200 μl of dimethyl sulfoxide (DMSO) was immediately added to each sample. The absorbance was assessed at 540 nm using a Tecan multiplate reader Infinite 1000 (Austria). The half-maximal inhibitory concentration (IC_{50}) of each compound was calculated using Graph Pad Prism 3.0.

Measurement of NMN, NAD⁺ and NADH levels. For fluorometric measurements of NMN, a previously described method was used, with minor modifications[50]. Briefly, MCF-7 cells (1×10^5 cells per well) were seeded in a 24-well plate. After 24 h, cells were treated with 3 selected compounds (2 µM) for 10 min. The cells were washed with PBS and then lysed by adding 200 µl of 1 M $HClO_4$ to each well and incubating at 4 °C for 20 min. The cells were harvested by scraping and transferred to a tube. The extracts were neutralized with 100 µl of 2 M KOH for 5 min at room temperature and 50 µl of 0.1 M bicine (pH 7.4) was added. The samples were centrifuged at 14 000 × g for 10 min at 4 °C, and the supernatant was collected for further analysis. The protein concentration in each sample was determined using a Bio-Rad protein assay kit. Twenty-five microliters of sample or standard solution (0.3 to 20 µM NMN) was transferred into a flat-bottom 96-well black plate and mixed with 10 µl of 2 M KOH and 10 µl of ice-cold 20% acetophenone. The reaction was incubated for 2 min at 4 °C, after which 45 µl of 88% formic acid was added, and the samples were incubated for another 10 min at 37 °C on a shaker. The fluorescence was measured using a Tecan multiplate reader Infinite 1000 (Austria) with excitation at 382 nm and emission at 420 nm.

The NAD^+/NADH ratio in the MCF-7 cells exposed to the test compounds (2 µM) for 10 min was measured using an NAD^+/NADH assay kit (Abcam, ab65348) according to the manufacturer's instructions.

NAMPT activity assay. MCF-7 cells (5×10^6 cells per well) were grown in a 6-well plate and then incubated with the test compounds (2 µM) for 4 h. The cells were harvested by scraping, washed with PBS and lysed with 50 mM Tris–HCl (pH 7.5), 150 mM NaCl, 1 mM DTT, 1 mM PMSF, 0.002 mg/ml leupeptin and pepstatin (2×10^6 cells in 100 µl buffer solution). After three freeze–thaw cycles at -80 °C, the cell extract was centrifuged at 15 000 × g for 30 min at 4 °C. The supernatant was collected, and the protein concentrations were determined using a Bio-Rad protein assay kit. The NAMPT enzyme reaction was performed as described previously[51]. The enzymatic reaction mixture contained 50 mM Tris–HCl buffer (pH 7.5), 12 mM $MgCl_2$, 2 mM DTT, 0.02% BSA, 2.5 mM ATP, 0.8 mM PRPP, and 50 µM nicotinamide. To initiate the reaction, 25 µl of cell extract was added to the reaction mixture, and the samples were incubated for 1.5 h at 37 °C. The enzymatic reaction was stopped by incubation at 95 °C for 1 min, and then samples were cooled and centrifuged at 10 000 × g for 5 min. The concentrations of the NAMPT reaction product, nicotinamide mononucleotide (NMN), in the samples were determined using a described method[52]. Twenty microliters of each reaction mixture was transferred to a 96-well black plate, and then 10 µl of 2 M KOH and 10 µl of 20% acetophenone in DMSO were added to the wells. After incubation on ice for 2 min, 45 µl of 88% formic acid was added. The fluorescence was measured using a Tecan multiplate reader Infinite 1000 (Austria) with excitation at 382 nm and emission at 445 nm. The NMN concentrations in the reaction mixtures were determined by comparison with NMN standards in the range of 0.16–20 µM. The NAMPT activity in the cell lysates is expressed as the concentration of NMN in µmol per mg protein per hour based on standard NMN readings.

High-resolution fluorespirometry[53]. High-resolution fluorespirometry was performed using an Oxygraph-2 k system (OROBOROS INSTRUMENTS, Austria). All experiments were performed at 37 °C in MiR05 medium (110 mM sucrose, 60 mM K-lactobionate, 0.5 mM EGTA, 3 mM $MgCl_2$, 20 mM taurine, 10 mM KH_2PO_4, 20 mM HEPES, pH 7.1 at 30 °C, and 0.1% BSA essentially fatty acid free). The medium was reoxygenated when the oxygen concentration dropped to 80 µM. H_2O_2 flux was simultaneously measured with respirometry in the O2k-Fluorometer using the H_2O_2-sensitive probe Ampliflu Red (AmR) as described[53]. The H_2O_2/O flux ratio [%] was calculated as the H_2O_2 flux/(0.5 O_2 flux).

In permeabilized 4T1 cells, pyruvate + malate (5 and 2 mM) or glutamate + malate (10 and 2 mM) were used to determine complex I (CI)-linked LEAK (L) respiration. ADP was added to a concentration of 5 mM to determine the oxidative phosphorylation-dependent respiration (OXPHOS state). Succinate (10 mM, complex II (CII) substrate) was then added to reconstitute convergent CI&II-linked respiration. Rotenone (0.5 µM, an inhibitor of complex I) and antimycin A (2.5 µM, an inhibitor of complex III) were added to determine the CII-linked OXPHOS capacity and residual oxygen consumption (ROX), respectively. Compound **6** was added to permeabilized cells after the addition of the respective substrates in the OXPHOS state (titration experiment) or in the LEAK state. In addition, compounds **3**, **6** and **7** were tested at 1 µM in the OXPHOS coupling protocol in the LEAK state. The OXPHOS coupling efficiency was calculated as:

$$1 - \frac{Resp.rate\ LEAK\ state}{Resp.rate\ OXPHOS\ state}$$

The substrate-dependent flux control factor was calculated as:

$$1 - \frac{Resp.rate\ before\ addition\ of\ respective\ substrate}{Resp.rate\ after\ addition\ of\ respective\ substrate}$$

Nuclear magnetic resonance studies. Cardiolipin (CL) liposomes for NMR analysis were prepared by the thin-film method followed by sonication and extrusion. The desired amount of CL stock solution (5 mg/ml, in ethanol, Avanti Polar Lipids, Inc.) and 1,2-dioleoyl-sn-glycero-3-phosphocholine (DOPC) stock solution (25 mg/ml, $CHCl_3$, Avanti Polar Lipids) were added to a round-bottom flask, and the organic solvents were removed using a rotary evaporator. The obtained lipid thin film was dried *in vacuo* overnight. Then, the dry lipid film was rehydrated in D18 HEPES buffer (20 mM, pH 7.4, 10% D_2O) and gently vortexed, and the samples were sonicated for 30 min in a bath-type sonicator. The obtained sample of liposomes was extruded 21 times

through a 100-nm pore polycarbonate filter (Nucleopore Corp., CA). Similarly, liposomes from DOPC only were prepared.

To study the interactions of compound **6** with CL and DOPC liposomes, a stock solution of **6** (2 mM) in D18 HEPES buffer (20 mM, pH 7.4, 10% D_2O) was added to CL/DOPC or DOPC liposome dispersions to reach 400:1200:400 μM CL/DOPC/**6** solution or 1600:400 μM DOPC/**6** solution followed by gentle vortexing for 30 s.

NMR spectra were acquired on a 600-MHz Bruker Avance NEO spectrometer equipped with a 5 mm QCI-F quadruple resonance pulsed-field-gradient cryoprobe. The temperature was calibrated against methanol and set to 25 °C. Chemical shifts were referenced to the water resonance at 4.77 ppm with respect to 4,4-dimethyl-4-silapentane-1-sulfonic acid (DSS). The samples contained 0.8 mM **6** in 90% H_2O and 10% D_2O with and without DOPC or CL/DOPC liposomes. The NMR data were processed and analyzed using MestReNova software.

Isothermal titration calorimetry studies[54,55]. Liposomes for isothermal titration calorimetry (ITC) studies were prepared by the thin-film method: the desired volume of DOPC (25 mg/ml, $CHCl_3$, Avanti Polar Lipids) and CL (5 mg/ml, EtOH, Avanti Polar Lipids) stock solutions were concentrated to dryness under reduced pressure, and the lipid films were resuspended in HEPES buffer (20 mM, pH 7.4) to prepare 50:150 μM CL/DOPC or 200 μM DOPC liposome dispersions. The obtained large multilamellar liposomes were sonicated in a bath-type sonicator (Cole Parmer Ultrasonic Cleaner 8891CPX (USA)) at room temperature for 30 min and then extruded (LiposoFast-Basic, Avestin) through a 100 nm polycarbonate filter 21 times. The quality of the resulting small unilamellar vesicles was determined by dynamic light scattering (DLS) (Zetasizer Nano ZSP, Malvern Panalytical Ltd., UK).

The experiments were carried out using an isothermal titration calorimeter (MicroCal iTC200, Malvern Panalytical Ltd., UK). To carry out the titration, the injection syringe was filled with a solution of compound **6** (100 μM), and the reaction cell was filled with liposome dispersion (200 μM of total lipid). The experiments were performed at 25 and 37 °C with a stirring speed of 750 rpm. The titration was conducted with thirty 1-μl injections with 180 s intervals between injections to ensure complete equilibration. The data consisted of a series of heat flows as a function of time, which were collected automatically and analyzed by Origin 7 software (OriginLab Corporation, Northampton, USA, www.originlab.com, 2002). The changes in enthalpy (ΔH) due to the interactions between **6** and the liposome dispersions were recorded, and then stoichiometry (N), the association constant (K_A), the dissociation constant (K_D), entropy (ΔS) and the Gibbs free energy (ΔG) were calculated. The obtained sigmoidal titration curves were evaluated assuming independent saturable binding sites in the outer vesicle interface. The integration of the enthalpograms was carried out using the one-site binding model (1:1).

Statistical analysis. All in vitro experiments were repeated at least three times. Data are presented as the mean ± standard deviation (S.D.). Statistically significant differences in the mean values were evaluated using one-way ANOVA. If ANOVA provided $p < 0.05$, Dunnett's test was performed. The differences were considered significant when $p < 0.05$. The data were analyzed using Graph Pad Prism software (Graph Pad Inc., La Jolla, USA).

Conclusions

Isoselenazolium salts with electrophilic selenium are a promising heterocyclic system for further elaboration as antitumor drug candidates. Our data confirm that isoselenazolium salts bind to the mitochondrial membrane-specific lipid CL, indicating the possible direct mitochondria-targeting ability of these salts. Furthermore, these compounds suppress cancer cell growth by modulating tumor cell energy metabolism and inducing marked ROS production. Our future studies will be focused on the development of novel derivatives containing isoselenazolium moieties with improved selective uptake by cancer cells compared with normal cells, especially cardiomyocytes.

Received: 22 February 2020; Accepted: 26 November 2020
Published online: 09 December 2020

References

1. Siegel, R. L., Miller, K. D. & Jemal, A. Cancer statistics, 2019 (US statistics). *CA. Cancer J. Clin.* **69**, 7–34 (2019).
2. DeSantis, C. E. *et al.* Breast cancer statistics, 2019. *CA. Cancer J. Clin.* **69**, 438–451. https://doi.org/10.3322/caac.21583 (2019).
3. Housman, G. *et al.* Drug resistance in cancer: an overview. *Cancers (Basel).* **6**, 1769–1792 (2014).
4. Roth, K. G., Mambetsariev, I., Kulkarni, P. & Salgia, R. The mitochondrion as an emerging therapeutic target in cancer. *Trends Mol. Med.* **26**, 1–15. https://doi.org/10.1016/j.molmed.2019.06.009 (2019).
5. Myers, R. A., Wirth, S., Williams, S. & Kiel, P. J. Enasidenib: an oral IDH2 inhibitor for the treatment of acute myeloid leukemia. *J. Adv. Pract. Oncol.* **9**, 435–440 (2018).
6. Cannino, G., Ciscato, F., Masgras, I., Sánchez-Martín, C. & Rasola, A. Metabolic plasticity of tumor cell mitochondria. *Front. Oncol.* **8**, 33 (2018).
7. Dias, A. S., Almeida, C. R., Helguero, L. A. & Duarte, I. F. Metabolic crosstalk in the breast cancer microenvironment. *Eur. J. Cancer* **121**, 154–171 (2019).
8. Kalyanaraman, B. *et al.* A review of the basics of mitochondrial bioenergetics, metabolism, and related signaling pathways in cancer cells: Therapeutic targeting of tumor mitochondria with lipophilic cationic compounds. *Redox Biol.* **14**, 316–327 (2018).
9. Cai, X. *et al.* Selenium exposure and cancer risk: an updated meta-analysis and meta-regression. *Sci. Rep.* **6**, 1–18 (2016).
10. Abdulah, R., Kobayashi, K., Yamazaki, C. & Koyama, H. Molecular targets of selenium in prostate cancer prevention (Review). *Int. J. Oncol.* **39**, 301–309 (2011).
11. Vinceti, M. *et al.* Selenium for preventing cancer (Cochrane Review). *Cochrane Database Syst. Rev.* https://doi.org/10.1002/14651858.CD005195 (2018).

12. He, X. *et al.* Enhanced bioreduction-responsive diselenide-based dimeric prodrug nanoparticles for triple negative breast cancer therapy. *Theranostics* **8**, 4884–4897 (2018).
13. Behroozi, F. *et al.* Engineering folate-targeting diselenide-containing triblock copolymer as a redox-responsive shell-sheddable micelle for antitumor therapy in vivo. *Acta Biomater.* **76**, 239–256 (2018).
14. Fan, C. D. *et al.* Selenocysteine induces apoptosis in human glioma cells: evidence for TrxR1-targeted inhibition and signaling crosstalk. *Sci. Rep.* **7**, 1–11 (2017).
15. Hatfield, D. L., Tsuji, P. A., Carlson, B. A. & Gladyshev, V. N. Selenium and selenocysteine: roles in cancer, health and development. *Trends Biochem. Sci.* **39**, 112–120 (2014).
16. Soares, A. T. G. *et al.* Organoselenotriazoles attenuate oxidative damage induced by mitochondrial dysfunction in mev-1 Caenorhabditis elegans mutants. *J. Trace Elem. Med. Biol.* **53**, 34–40 (2019).
17. Luo, J. *et al.* Rational design and optimization of selenophenes with basic side chains as novel potent selective estrogen receptor modulators (SERMs) for breast cancer therapy. *Medchemcomm* **8**, 1485–1497 (2017).
18. Yang, Y. N. *et al.* Enhancement of non-homologous end joining DNA repair capacity confers cancer cells resistance to the novel selenophene compound, D-501036. *Cancer Lett.* **309**, 110–118 (2011).
19. Shiah, H. S. *et al.* Mitochondria-mediated and p53-associated apoptosis induced in human cancer cells by a novel selenophene derivative, D-501036. *Biochem. Pharmacol.* **73**, 610–619 (2007).
20. Arsenyan, P., Vasiljeva, J., Domracheva, I., Kanepe-Lapsa, I. & Gulbe, A. Selenopheno[2,3-f]coumarins: a novel scaffold with antimetastatic activity against melanoma and breast cancer. *New J. Chem.* **43**, 11851–11864 (2019).
21. Azad, G. K. & Tomar, R. S. Ebselen, a promising antioxidant drug: Mechanisms of action and targets of biological pathways. *Mol. Biol. Rep.* **41**, 4865–4879 (2014).
22. Arsenyan, P., Vasiljeva, J., Belyakov, S., Liepinsh, E. & Petrova, M. Fused selenazolinium salt derivatives with a Se-N$^+$ bond: preparation and properties. *Eur. J. Org. Chem.* **2015**, 5842–5855 (2015).
23. Arsenyan, P. & Vasiljeva, J. Selenazolium salts as catalysts in oxidation reactions. *Mendeleev Commun.* **27**, 621–622 (2017).
24. Witek, K. *et al.* Selenazolinium salts as "small molecule catalysts" with high potency against ESKAPE bacterial pathogens. *Molecules* **22**, 1–16 (2017).
25. Rendekova, J. *et al.* The selenium-nitrogen bond as basis for reactive selenium species with pronounced antimicrobial activity. *Curr. Org. Synth.* **14**, 1082–1090 (2017).
26. El Khoury, M. *et al.* Targeting bacterial cardiolipin enriched microdomains: an antimicrobial strategy used by amphiphilic aminoglycoside antibiotics. *Sci. Rep.* **7**, 1–12 (2017).
27. Szeto, H. H. First-in-class cardiolipin-protective compound as a therapeutic agent to restore mitochondrial bioenergetics. *Br. J. Pharmacol.* **171**, 2029–2050 (2014).
28. Cenini, G. & Voos, W. Mitochondria as potential targets in Alzheimer disease therapy: an update. *Front. Pharmacol.* **10**, 1–20 (2019).
29. Zhang, J. *et al.* Cardiolipins are biomarkers of mitochondria-rich thyroid oncocytic tumors. *Cancer Res.* **76**, 6588–6597 (2016).
30. Sapandowski, A. *et al.* Cardiolipin composition correlates with prostate cancer cell proliferation. *Mol. Cell. Biochem.* **410**, 175–185 (2015).
31. Larrouy-Maumus, G. Lipids as biomarkers of cancer and bacterial infections. *Curr. Med. Chem.* **26**, 1924–1932 (2018).
32. Houtkooper, R. H., Cantó, C., Wanders, R. J. & Auwerx, J. The secret life of NAD+: an old metabolite controlling new metabolic signaling pathways. *Endocr. Rev.* **31**, 194–223 (2010).
33. Poljsak, B. NAD+ in cancer prevention and treatment: pros and cons. *J. Clin. Exp. Oncol.* **5**, 1–15 (2016).
34. Zhu, Y., Liu, J., Park, J., Rai, P. & Zhai, R. G. Subcellular compartmentalization of NAD+ and its role in cancer: a sereNADe of metabolic melodies. *Pharmacol. Ther.* **200**, 27–41 (2019).
35. Katsyuba, E., Romani, M., Hofer, D. & Auwerx, J. NAD+ homeostasis in health and disease. *Nat. Metab.* **2**, 9–31 (2020).
36. Stacpoole, P. W. Therapeutic targeting of the pyruvate dehydrogenase complex/pyruvate dehydrogenase kinase (PDC/PDK) axis in cancer. *J. Natl. Cancer Inst.* **109**, 1–14 (2017).
37. Martinez-Outschoorn, U. E., Peiris-Pagés, M., Pestell, R. G., Sotgia, F. & Lisanti, M. P. Cancer metabolism: a therapeutic perspective. *Nat. Rev. Clin. Oncol.* **14**, 11–31 (2017).
38. Dickerson, T., Jauregui, C. E. & Teng, Y. Friend or foe? Mitochondria as a pharmacological target in cancer treatment. *Future Med. Chem.* **9**, 2197–2210 (2017).
39. Lin, S. J. & Guarente, L. Nicotinamide adenine dinucleotide, a metabolic regulator of transcription, longevity and disease. *Curr. Opin. Cell Biol.* **15**, 241–246 (2003).
40. Diers, A. R., Broniowska, K. A., Chang, C., Hogg, N. & Program, R. B. Pyruvate fuels mitochondrial resiration and proliferation of breast cancer cells. *Biochem. J.* **444**, 561–571 (2016).
41. Corbet, C. *et al.* Interruption of lactate uptake by inhibiting mitochondrial pyruvate transport unravels direct antitumor and radiosensitizing effects. *Nat. Commun.* **9**, 1–11 (2018).
42. Quinlan, C. L., Perevoshchikova, I. V., Hey-Mogensen, M., Orr, A. L. & Brand, M. D. Sites of reactive oxygen species generation by mitochondria oxidizing different substrates. *Redox Biol.* **1**, 304–312 (2013).
43. Zhao, R. Z., Jiang, S., Zhang, L. & Yu, Z. B. Mitochondrial electron transport chain, ROS generation and uncoupling (review). *Int. J. Mol. Med.* **44**, 3–15 (2019).
44. Fernandez, E. & Bolaños, J. P. α-Ketoglutarate dehydrogenase complex moonlighting: ROS signalling added to the list. *J. Neurochem.* **139**, 689–690 (2016).
45. Esma, U. *et al.* Selectivity in photodynamic action: higher activity of mitochondria targeting photosensitizers in cancer cells. *ChemPhotoChem* **3**, 129–132 (2019).
46. Murphy, M. P. Selective targeting of bioactive compounds to mitochondria. *Trends Biotechnol.* **15**, 326–330 (1997).
47. Sharma, A. *et al.* Overcoming drug resistance by targeting cancer bioenergetics with an Activatable Prodrug. *Chem* **4**, 2370–2383 (2018).
48. Drahansky, M. *et al.* We are IntechOpen, the world's leading publisher of Open Access books Built by scientists, for scientists TOP 1 %. *Intech* **i**, 13 (2016).
49. Mosmann, T. Rapid colorimetric assay for cellular growth and survival: application to proliferation and cytotoxicity assays. *J. Immunological Methods* **65**, 55–63 (1983).
50. Formentini, L., Moroni, F. & Chiarugi, A. Detection and pharmacological modulation of nicotinamide mononucleotide (NMN) in vitro and in vivo. *Biochem. Pharmacol.* **77**, 1612–1620 (2009).
51. Zamporlini, F. *et al.* Novel assay for simultaneous measurement of pyridine mononucleotides synthesizing activities allows dissection of the NAD + biosynthetic machinery in mammalian cells. *FEBS J.* **281**, 5104–5119 (2014).
52. Zhang, R. Y. *et al.* A fluorometric assay for high-throughput screening targeting nicotinamide phosphoribosyltransferase. *Anal. Biochem.* **412**, 18–25 (2011).
53. Makrecka-Kuka, M., Krumschnabel, G. & Gnaiger, E. High-resolution respirometry for simultaneous measurement of oxygen and hydrogen peroxide fluxes in permeabilized cells, tissue homogenate and isolated mitochondria. *Biomolecules* **5**, 1319–1338 (2015).
54. Su, H. & Xu, Y. Application of ITC-based characterization of thermodynamic and kinetic association of ligands with proteins in drug design. *Front. Pharmacol.* **9**, 1–7 (2018).

55. Leavitt, S. & Freire, E. Direct measurement of protein binding energetics by isothermal titration calorimetry. *Curr. Opin. Struct. Biol.* **11**, 560–566 (2001).

Acknowledgements
This work was supported by Latvian Institute of Organic Synthesis internal grant (IG-2020-01 for Pavels Dimitrijevs) and SAM project Nr. 1.1.1.1/19/A/016. Authors would like to thank J. Vasiljeva for re-synthesis of isoselenazolium salts and I. Kanepe-Lapsa for assistance.

Author contributions
P.A., M.M.K. and M.D. designed the research. P.D. performed preparation of liposomal models and ITC studies, I.D. studied cytotoxicity and NAD + homeostasis, K.J. performed and analyzed NMR experiments, M.M.K. studied and analyzed effects of isoselenazolium salts on mitochondria functions. P.A. wrote the manuscript with contributions from all authors.

Competing interests
The authors declare no competing interests.

Additional information
Supplementary Information The online version contains supplementary material available at https://doi.org/10.1038/s41598-020-78620-8.

Correspondence and requests for materials should be addressed to P.A.

Reprints and permissions information is available at www.nature.com/reprints.

Publisher's note Springer Nature remains neutral with regard to jurisdictional claims in published maps and institutional affiliations.

Third Publication

Sensors & Actuators: B. Chemical 346 (2021) 130537

Contents lists available at ScienceDirect

Sensors and Actuators: B. Chemical

journal homepage: www.elsevier.com/locate/snb

Cardiolipin in the spotlight: Quantitative analysis and fluorescence-based competitive binding assay

Pavels Dimitrijevs [a,b], Pavel Arsenyan [a,*]

[a] Latvian Institute of Organic Synthesis, Aizkraukles 21, LV-1006, Riga, Latvia
[b] Riga Stradins University, Dzirciema 16, Riga, LV-1007, Latvia

ARTICLE INFO

Keywords:
Cardiolipin
Fluorescent probe
Quantitative analysis
Competitive binding

ABSTRACT

Cardiolipin (CL) is a key phospholipid responsible for mitochondrial function and cristae integrity. The CL level is associated with various diseases characterized by mitochondrial dysfunction, including ischemic heart diseases and cancer. CL is an attractive target for mitochondria-specific drugs, but unnecessary interaction with CL might lead to detrimental side effects such as heart failure and kidney dysfunction. Thus, a simple and robust method for CL quantification and a reliable assay for the determination of drug affinity for CL are desired. We report a new fluorescent CL-specific probe with impressive photophysical properties that allows CL quantification in mitochondrial fractions isolated from cell and tissue homogenates and enables estimates of drug affinity for CL in the first fluorescence-based competitive binding assay. It was found that CL concentration is elevated in mitochondrial fractions isolated from cancer cells and cells with high proliferation rate (up to 108.5 ± 16.0 nmol/mg prot in mouse colon carcinoma cells, CT-26). CL concentration in mitochondria from brain tissue (66.11 ± 5.78 nmol/mg prot) is circa twice higher than in heart and kidney mitochondria (37.49 ± 8.69 and 33.95 ± 5.32 nmol/mg prot, respectively.) Generally, positively charged substances bind with CL, but their affinity is highly variable with EC_{50} values ranging from sub-micromolar to millimolar concentration.

1. Introduction

Cardiolipin (CL) is a signature phospholipid of the inner mitochondrial membrane (IMM) in eukaryotes and the cytoplasmic membrane in prokaryotes. [1] CL has two structural features – two negatively charged phosphodiester moieties and a conical shape that promotes negative curvature of the membrane [2]. The latter is crucial for inward folding of the IMM and cristae formation [3,4]. Additionally, CL directly interacts with electron transport chain complexes, promoting supercomplex formation [5], and is required for optimal activity of the respiratory chain. [6] Similarly, anaerobic respiratory complexes in bacteria are stabilized by CL [7]. Therefore, CL is essential for maintaining mitochondrial morphology and function. Distinctive structural properties and specific localization make CL an attractive pharmacological target for mitochondria-specific therapies [8,9], antimicrobial therapies [10,11] and drug delivery strategies [12]. Moreover, the mitochondrial toxicity of some drugs, e.g., anthracyclines and aminoglycosides, is in part attributed to their ability to interact with CL, leading to serious side effects such as heart failure [13] and kidney damage [14,15]. Consequently, exploring the binding with CL is crucial for screening new mitochondria-targeted drugs and antibiotics, as well as for evaluating the potential of drugs to cause mitochondrial toxicity by interacting with CL.

Previously, binding with CL was detected by time-consuming ^{1}H and ^{13}C NMR experiments, [16,17] which are semiquantitative and require large amounts of materials. Other methods are based on a compound`s intrinsic properties [18,19] and do not imply a unified approach for screening. Earlier, 10-*N*-nonyl acridine orange (NAO) was used as a fluorescent probe for the evaluation of 3′,6-dinonyl neamine binding to anionic phospholipids, [20] although NAO has significant drawbacks and, therefore, limited use as a probe for competition assays: the emission intensity is relatively low and unstable due to low solubility in aqueous media. Therefore, there is great demand for a robust method that would allow rapid compound screening for CL targeting as well as quantitative characterization of binding affinity.

Notably, the level of CL also has clinical significance, as CL depletion is a hallmark of ischemic diseases, [21] cardiac failure [21], diabetes [22], neurodegenerative disorders [23], and aging [24], and abnormally high CL levels and remodeling are identified as a novel molecular signature of thyroid oncocytic [25] and prostate tumors [26].

* Corresponding author.
E-mail address: pavel@osi.lv (P. Arsenyan).

https://doi.org/10.1016/j.snb.2021.130537
Received 27 April 2021; Received in revised form 13 July 2021; Accepted 29 July 2021
Available online 4 August 2021

Quantitative analysis of CL in biological samples by TLC, HPLC or MS is challenging and requires lipid extraction from the material and lipid separation during which some amount of CL may be lost [27]. There is one commercially available CL-specific fluorescent probe, TTAPE-Me [28], that forms a fluorescent complex with CL, but its fluorescence intensity is very low (Supplementary Fig. 1); hence, a large amount of both sample and probe is necessary for obtaining qualitative results. Therefore, a simple and robust method for CL quantification is still desired.

Herein, we report our discovery of a novel NAO analog with significantly improved photophysical properties for the quantitative analysis of CL and the development of an assay for evaluating binding affinity for CL.

2. Materials and methods

2.1. Synthesis of NAO analogs

NAO analogs were synthesized as shown in the Scheme 1. The procedure for the preparation of the NAO analogs and their structural characterizations are deliberated in the Supporting Information.

2.2. Preparation of liposomes

Liposomes for CL and other phospholipid binding studies were prepared by thin film method described previously [29]. Detailed description of the procedure can be found in the Supporting Information.

2.3. Cardiolipin quantitative analysis

A 10 mM stock solution of **10** in ethanol was made and diluted to 40 μM with buffer containing 10 mM KCl and 10 mM Tris, pH 6.7. TTAPE-Me stock solution (500 μM) was prepared using buffer. Prior to measuring the CL concentration in the mitochondrial fraction, liposomes titration with **10** and TTAPE-Me was performed in triplicate to obtain a calibration curve. In a 96-well plate, a solution of **10** (10 μM) or TTAPE-Me (125 μM) in buffer containing 10 mM KCl and 10 mM Tris, pH 6.7, was titrated with diluted mitochondrial fraction and incubated for 15 min at 37 °C. Then, the fluorescence intensity was measured at 529 nm (λexc = 497 nm). The CL concentration in the sample well was calculated by interpolation of the calibration curve, and the total mitochondrial CL concentration was calculated using Eq. 1:

$$C_{CL} = \frac{n \times D \times 1000}{V \times P}; nmol \Big/ mgprot \quad (1)$$

where

n is the amount of CL in the sample well, nmol;
D is the sample dilution factor;
V is the sample volume added into the reaction well, μL;
P is the mitochondrial protein concentration of the sample, mg/mL.

2.4. Competitive binding studies

A 10 mM stock solution of **10** in ethanol was made and diluted to 50 μM with 20 mM HEPES buffer, pH 6.8, 7.4 or 7.8. A 20 μM stock solution of CL containing lipid vesicles and a stock solution of a ligand were prepared in the same buffer. In a 96-well microplate, a solution of lipid vesicles containing CL (CL final concentration 2.5 μM) was titrated in triplicate with a ligand and mixed gently with a micropipette by sucking the solution up and down. Additionally, CLs containing lipid vesicles without a ligand were prepared in triplicate (vehicle). Next, a 96-well plate was incubated in a plate shaker with a thermostat for 10/30/60 min (500 RPM, 25 or 37 °C). Then, an appropriate amount of **10** stock solution was added to the wells (the final concentration of **10** was 5 μM) and mixed gently with a micropipette. Next, the 96-well plate was incubated for 15 min in a plate shaker with a thermostat (500 RPM, 37 °C), and the fluorescence intensity was measured using a Tecan Infinite 1000 microplate reader (Tecan Austria GmbH, Salzburg, Austria) at excitation and emission wavelengths of 497 and 529 nm, respectively. The obtained data were analyzed with GraphPad Prism® 8.0 (GraphPad, Inc., La Jolla, USA). The fluorescence intensity was normalized by setting CL vesicles with **10** without a ligand (vehicle) as 0% and the maximal effect of the ligand as 100 %. Normalized fluorescence intensity was plotted against the concentration of the ligand on a logarithmic scale and fit with a suitable fitting model (4 Pl or biphasic) to calculate EC_{50} values. Before carrying out a competitive binding experiment on isolated mitoplasts, **10** was titrated with mitoplasts from each batch to determine the optimal volume of mitoplast solution to saturate a 5 μM probe solution. In other aspects, competitive binding was performed similarly to that in CL vesicles.

2.5. Statistical analysis

Data are presented as the mean ± SD. Unpaired Student's *t*-test was used to compare data obtained by using **10** and TTAPE-Me. The differences were considered significant when $p < 0.05$. The data were analyzed using GraphPad Prism® 8.0 (GraphPad, Inc., La Jolla, USA) and Microsoft Excel 2016 (Microsoft corp. Redmond, U.S).

3. Results and discussion

3.1. Design of improved nonyl acridine orange analogs

NAO has many disadvantages as a fluorescence probe: it is poorly soluble in physiological media and exhibits low photoluminescence quantum yield (Φ) and small fluorescence intensity differences between the CL-bound and unbound states. Accordingly, NAO would have a low CL detection limit along with a narrow scale and low precision for competitive binding studies. Moreover, the fluorescence of NAO in HEPES buffer decreased by 15.7 % in 30 min (Supplementary Figure 2). To obtain appropriate fluorescent probes for competitive binding studies, these problems must be solved.

Recently, [29] we showed that replacing the nonyl group with a 3-(trimethylsilyl)propyl substituent improves AO analog solubility and stability in aqueous medium but increases fluorescence intensity by a

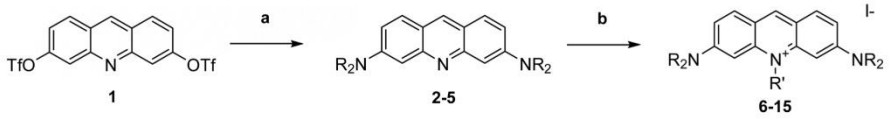

Scheme 1. Synthesis of acridinium salts **6-15.** Reaction conditions: a) cyclic amine (3 equiv.), $Pd(OAc)_2$ (25 mol-%), BINAP (30 mol-%), Cs_2CO_3 (4 equiv.), xylene, reflux, 16 h; b) R`-I, $Na_2CO_3$, dichlorobenzene or toluene, reflux, 10-40 min. **2** ($NR_2$ = azetidinyl, 69 %), **3** ($NR_2$ = pyrrolidyl, 54 %), **4** ($NR_2$ = piperidyl, 65 %), **5** ($NR_2$ = morpholyl, 67 %), **6** ($NR_2$ = $N(CH_3)_2$, R` = C_9H_{19}, 77 %), **7** (NR_2 = $N(CH_3)_2$, R` = $Me_3Si(CH_2)_3$, 97 %), **8** ($NR_2$ = azetidinyl, R` = CH_3, 75 %), **9** (NR_2 = azetidinyl, R` = $CD_3$, 89 %), **10** ($NR_2$ = azetidinyl, R` = $Me_3Si(CH_2)_3$, 61 %), **11** (NR_2 = azetidinyl, R` = $C_9H_{19}$, 76 %), **12** ($NR_2$ = azetidinyl, R` = $C_{12}H_{25}$, 54 %), **13** (NR_2 = pyrrolidyl, R` = $Me_3Si(CH_2)_3$, 98 %), **14** ($NR_2$ = piperidyl, R` = $Me_3Si(CH_2)_3$, 59 %), **15** (NR_2 = morpholyl, R` = $Me_3Si(CH_2)_3$, 63 %).

modest 30 %. We hypothesized that the introduction of cyclic amino groups in the acridinium salt structure at positions 3 and 6 could lead to an increase in Φ without loss of CL specificity. Based on published reports [30], an azetidinyl substituent markedly improves Φ, presumably by hindering twisting of the C_{aryl}–N bond and disfavoring the formation of a twisted internal charge transfer state. To confirm this hypothesis, compounds **2**-**5** were first synthesized using palladium-catalyzed cross-coupling of **1** with cyclic amines [30] and then alkylated with the corresponding alkyl iodide in the presence of sodium carbonate [29] to obtain acridinium iodides **6**-**15** (Scheme 1).

The molecular structures of derivatives **8**-**10** and **14** (**8**, CCDC 2,025,824; **9**, CCDC 2,025,825; **10**, CCDC 2,025,823; **14**, CCDC 025822, Supplementary Figure 3) were unambiguously confirmed by X-ray analysis.

As expected, azetidinyl AO analogs **8–10** exhibit a 4-fold higher Φ (≈60 %) than NAO (Table 1). Pyrrolidyl-substituted acridinium salt **13** displays moderate Φ (40 %), but piperidyl and morpholyl analogs **14** and **15** exhibit very low Φ, 2.7 % and 6.8 %, respectively. The Φ of azetidinyl-substituted analogs decreases with elongation of the alkyl chain at position 10; however, compounds bearing methyl and 3-(trimethylsilyl)propyl groups display the highest Φ, while extending the alkyl chain to dodecyl groups led to a drop in Φ to 16.1 %. Therefore, azetidinyl-substituted acridinium iodides **8** and **10** were selected for further studies.

3.2. Binding of the novel fluorescent probes to cardiolipin and other phospholipids

The binding of the selected acridinium salts with CL was evaluated and compared with that of NAO using 1,2-dioleoyl-*sn*-glycero-3-phosphocholine (DOPC) and CL liposomes (75:25 mol%). NAO binds to CL at a 2 to 1 M ratio, [29] and its binding is accompanied by a decrease in fluorescence intensity (FI) at 529 nm (λ_{exc} = 497 nm). *N*-methyl-substituted diazetidinyl acridinium **8** lacks a hydrophobic alkyl chain and does not form a stable complex with CL, which is confirmed by an increase in fluorescence intensity of 13 % after 10 min (Supplementary Figure 4). In turn, 3-(trimethylsilyl)propyl substituted derivative **10** interacted with CL similarly to NAO with a 2 to 1 saturating ratio (Supplementary Figure 5) and with a substantially larger difference (in a.u.) between CL-bound and unbound states (Supplementary Figure 6). Notably, the fluorescence of **10** and its complex with CL was stable in buffer for at least 30 min, in contrast to NAO (Supplementary Figure 7), which can be explained by approx. 5-fold higher solubility of **10** (0.188 mg/ml versus 0.041 mg/mL). It is important to note that **10** retains the same specificity toward CL as NAO (Fig. 1B). Notably, in this experiment, phospholipids – phosphatidylethanolamine, phosphatidylinositol, phosphatidic acid and phosphatidylserine were taken at equal concentrations (8 μM the lipid of interest, 24 μM DOPC), but in the IMM, the total amount of negatively charged phospholipids is significantly lower than the amount of CL. [31] Moreover, use of the simple CL/DOPC liposomal model yielded similar decrease of FI to the more complex IMM membrane model consisting of the 4 main IMM phospholipids (10 PI, 25 % CL, 30 % PE, 35 % DOPC). Therefore, the introduction of azetidynil and 3-(trimethylsilyl)propyl groups overcame the shortcomings of NAO – poor fluorescent properties, solubility and stability in aqueous medium – and preserved the specificity toward CL. Consequently, **10** was chosen as a fluorescent probe for the quantitative analysis of CL and for the development of an assay for measuring the binding affinity of biologically active substances for CL.

Table 1
Photoluminescence properties of NAO analogues (20 mM HEPES buffer, pH = 7.4).

Comp.	R	R'	Φ, %	$\lambda_{abs}/\lambda_{em}$, nm
6	Me_2N	C_9H_{19}	15.5	497/529
7	Me_2N	$Me_3Si(CH_2)_3$	18.7	491/529
8		CH_3	59.9	498/529
9		CD_3	61.5	498/529
10		$Me_3Si(CH_2)_3$	60.7	497/529
11		C_9H_{19}	47.9	498/529
12		$C_{12}H_{25}$	16.1	496/529
13		$Me_3Si(CH_2)_3$	40.0	511/529
14		$Me_3Si(CH_2)_3$	2.7	484/547
15		$Me_3Si(CH_2)_3$	6.8	488/547

3.3. Cardiolipin quantitative analysis

Quantitative analysis of CL was performed on a CL/DOPC liposomal model: **10** was titrated with CL in the 0.05–8 μM range, and a linear regression curve (R^2 = 0.9930) was obtained (Fig. 1A) with a greater linear slope of the titration curve (-6403 ± 135) than that of NAO (-1223 ± 27). As **10** binds with CL at a 2:1 ratio, the maximal CL concentration that can be measured is half the concentration of the probe. Next, since CL is almost exclusively located in mitochondria, the CL amount was measured in mitochondrial fractions from lysates of different cell lines using calibration curves obtained with liposomal CL solutions. The lysate of human erythrocytes was taken as a negative control because human erythrocytes have no mitochondria [32] and hence no CL. In parallel, CL concentration was measured with TTAPE-Me and compared with the results obtained with **10** using Student`s *t*-test (Fig. 1C and Supplementary Table 1). In all studied cell lines, no statistically significant difference ($p > 0.37$, Student`s *t*-test) in the determined CL concentration was found using **10** or TTAPE-Me. Moreover, in erythrocytes, no CL was detected, thus confirming the selectivity of **10** for CL. Cardiomyocytes are considered rich in mitochondria [33] and contain a relatively large amount of CL. For example, 26.6 ± 3.7 nmol of CL per mg of mitochondrial protein was found in rat cardiomyocytes (H9C2). Notably, cancer cell lines and cell lines with high proliferation rates (NIH/3T3, mouse Swiss albino embryo fibroblasts, and CHO-K1, Chinese hamster ovary cells) contain comparable or even higher amounts of CL. The highest CL concentration among the studied cell lines, 108.5 ± 16.0 nmol/mg prot, was found in mouse colon carcinoma cell (CT-26) mitochondria, which is consistent with published data on elevated CL levels in colon cancer [34]. To check the reproducibility of the obtained results, the CL concentration was measured in mitochondrial fractions from 3 different subcultures of H9C2, Jurkat, 4T1 and MCF-7 cells (Supplementary Table 2), and no significant deviations between subcultures were found.

The greatest advantage of **10** as a fluorescent probe is that the procedure is simple (as lipid extraction and separation are not necessary), and fast: only 15 min of incubation and a single point emission measurement are required, producing a clear and stable response.

The next step was to confirm whether it is possible to measure CL concentration in mitochondrial fractions isolated from tissue. For example, this would allow the study of CL levels in different pathological conditions or exploration of the influence of drug treatment on CL levels by analyzing samples from experiments *in vivo*. Mitochondrial fractions were isolated from healthy C57Bl/6 J mouse heart, kidney and brain tissue homogenates, and CL content was analyzed by the same method as previously described. No statistically significant difference between CL concentrations obtained by **10** or TTAPE-Me was found ($p > 0.44$, Student`s *t*-test). Mouse heart and kidney mitochondria contained similar amounts of CL, 37.49 ± 8.69 and 33.95 ± 5.32 nmol/mg prot, respectively (Fig. 1D). Previously reported CL concentrations of 15–20 nmol/mg protein for mouse heart mitochondria [33,35] might be underestimated because of potential CL loss during lipid extraction and separation procedures. Interestingly, the CL concentration in mouse brain mitochondria was almost twice as high as that in the heart and kidney (66.11 ± 5.78 nmol/mg prot). The obtained value was slightly higher than the previously reported value (52.7 ± 4.5 nmol/mg prot),

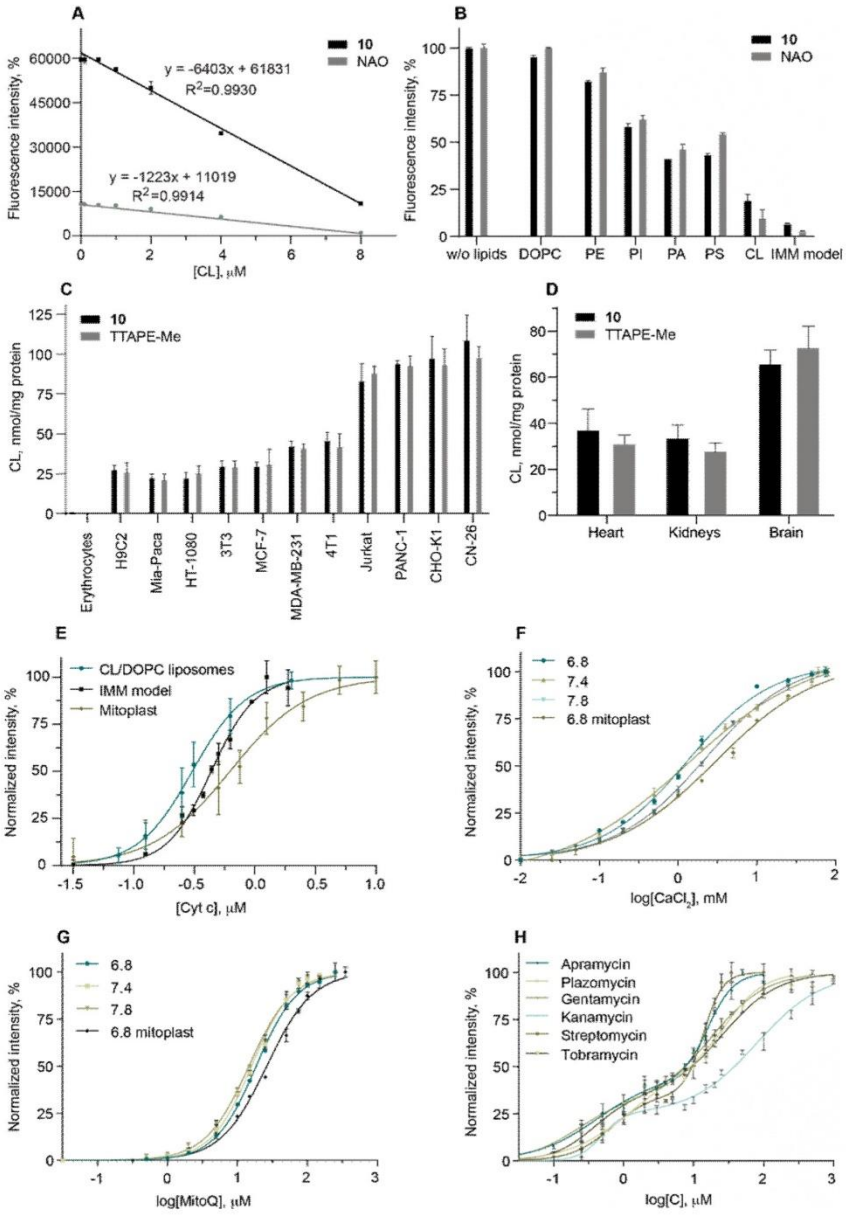

Fig. 1. A) **10** and NAO (16 μM) titration with CL/DOPC liposomes in 20 mM HEPES, pH 7.4 at 37 °C. B) Interaction of **10** and NAO with phospholipids. Columns represent relative fluorescence intensity (FI) - the lower intensity indicates higher specificity toward a particular phospholipid. Phospholipids were taken at 8 μM with 24 μM of DOPC (32 μM of DOPC, when DOPC was taken alone) in 20 mM HEPES, pH 7.4, FI measured at 37 °C after 15 min of incubation. C) CL amount in mitochondrial fractions from cell lysates, nmol/mg total protein, measured using **10** and TTAPE-Me, n = 3-5. In all cases, $p > 0.05$, Student`s *t*-test. D) CL amount in mitochondrial fractions from C57Bl/6 J mice tissue homogenates, nmol/mg total protein, measured using **10** and TTAPE-Me, n = 3-5. In all cases, $p > 0.05$, Student`s *t*-test. E) Cyt *c* binding with CL in CL/DOPC liposomes, IMM model (10 PI, 25 % CL, 30 % PE, 35 % DOPC) in 20 mM HEPES, pH 7.4 and mitoplast in 20 mM HEPES, pH 6.8 at 37 °C. Representative binding curves of $CaCl_2$ (F) and mitoQ (G) binding with CL in CL/DOPC liposomes in 20 mM HEPES at pH 6.8, 7.4 and 7.8 and isolated mitoplasts in 20 mM HEPES, pH 6.8 at 37 °C. H) Aminoglycosides` binding with CL in CL/DOPC liposomes in 20 mM HEPES, pH 7.4. PE – phosphatidylethanolamine, PI – phosphatidylinositol, PA – phosphatidic acid, PS – phosphatidylserine.

[36,37] which could also be explained by the lipid extraction step before CL quantification or CL level fluctuations between different mouse strains. In summary, the developed fluorescent dye **10** is suitable for the fast and straightforward measurement of CL concentrations in mitochondrial fractions from cultured cell lysates and animal tissue homogenates. Considering that loss of CL content is a characteristic attribute of mitochondrial dysfunctions, e.g., Barth syndrome, [38] ischemic heart diseases [21], neurodegenerative diseases [23] and aging [39], this practical tool will be indispensable in studying the role of CL levels in these pathological conditions. Although the developed assay allows the quantification of total CL, its limitation is the inability to distinguish between CL species with different alkyl chain compositions.

3.4. An assay for measuring the binding affinity of biologically active compounds for cardiolipin

Endogenous CL ligand – cytochrome *c* (cyt *c*) [40] and CL/DOPC liposomes (25:75 mol%) were selected as an IMM model for developing and optimizing the experimental procedure. The incubation time was varied from 10 to 60 min at 25 or 37 °C. Based on the obtained data, 10 min of incubation at 37 °C was sufficient for the complete saturation of CL with cyt *c*. The most pronounced response was observed at 5.0 μM **10** and 2.5 μM CL. Nonlinear regression analysis of the normalized fluorescence intensity versus log[cyt *c*] plot allowed the determination of EC_{50} values. Next, the ability of cyt *c* to bind CL was evaluated at different pH values representing the mitochondrial intermembrane space (6.8), cytosol (7.4), and mitochondrial matrix (7.8). [41] The results confirmed that the affinity of cyt *c* toward CL is not pH-dependent (EC_{50} = 0.26–0.33 μM) (Supplementary Figure 8). A similar EC_{50} value (0.44 ± 0.02 μM) was obtained in experiments with a more complex model of the IMM consisting of 4 main phospholipids (phosphatidylinositol, CL, phosphatidylethanolamine and DOPC, 10:25:30:35 mol%) (Fig. 1E). Therefore, simple CL/DOPC liposomes are suitable for competitive binding studies as an artificial membrane model. A natural lipid membrane, mitoplasts isolated from a rat heart, can also be applied. In this case, cyt *c* had a twofold higher EC_{50} value (0.78 ± 0.15 μM, value obtained from 3 separately isolated mitochondrial fractions, n = 9, Fig. 1E), probably because of CL interaction with other IMM proteins or cyt *c* interference with other mitoplast components.

The developed method allowed fast and convenient determination of cyt *c* binding affinity for CL in both artificial and natural membrane models at different pH values (titration of 1 compound in triplicate takes approx. 1 h). Considering the strong and pH-independent binding of cyt *c* as well as its commercial availability, cyt *c* can be proposed as a reference compound. To validate the method, different ligands were studied (Table 2).

Since CL has two negative charges, inorganic salts were chosen as the first compound group. $Ca^{2+}$and Mg^{2+} as well as monovalent cations [42] are known to interact with CL; furthermore, Ca^{2+} at high concentrations even prevents cyt *c* – CL electrostatic interactions. [43] In this assay, both Ca^{2+} (Fig. 1F), Mg^{2+} (Supplementary Figure 9) and Zn^{2+} (Supplementary Figure 10) bind with CL, but in contrast to cyt *c*, their EC_{50} values lie in the mM range. NH_4^+ cations have a lower affinity for CL and show a two-site binding pattern (Supplementary Figure 11), in turn, Na^+ cations fail to reach saturation even at 300 mM concentration. Notably, Hg^{2+} ions quench the fluorescence of the probe due to the formation of a complex with **10**.

The second group included compounds that affect mitochondrial functions: triphenylphosphonium (TPP) salts; lipophilic cations for drug delivery into mitochondria [12] (nonyl TPP bromide and MitoQ – the TPP cation conjugated to ubiquinone); metformin, which inhibits mitochondrial respiratory complex I; [44] thimerosal, which causes depolarization of mitochondrial membrane potential [45]; acyclovir and abacavir, which inhibit mitochondrial DNA polymerase γ [44]; antimycin A, which inhibits mitochondrial respiratory complex III [44]; and carbonyl cyanide *m*-chlorophenylhydrazone (CCCP), a protonophore used to uncouple mitochondrial respiration. [46] The obtained results show that compounds containing TPP cations readily bind to CL with EC_{50} values in the 15÷37 μM range (Fig. 1G and Supplementary Fig. 12). In turn, metformin, thimerosal, acyclovir and abacavir did not show any signs of displacement of **10** at the tested concentrations. It was not possible to assess antimycin A and CCCP binding to CL due to quenching of the fluorescent probe.

The third compound group was antibiotics, represented by vancomycin, which inhibits mitochondrial respiratory complex I; [47] rifampicin and ampicillin, which induce overproduction of reactive oxygen species (ROS) and mitochondrial dysfunction [48,49]; dodecyl trimethylammonium chloride, a membrane permeabilizing agent [50]; and various aminoglycosides which not only cause mitochondrial damage [51] but might include CL as one of the molecular targets accounting for their antimicrobial activity [10]. Considering CL as a potential target for antimicrobial activity, experiments conducted at pH 7.4 are more relevant because this value is close to the pH in the

Table 2
EC_{50} values of the studied compounds, μM*.

	pH = 6.8	pH = 7.4	pH = 7.8	pH = 6.8, mitoplast
Inorganic salts				
$MgCl_2$	1141 ± 122	1102 ± 66	1300 ± 94	1576 ± 190
Zn gluconate	683 ± 111	736 ± 37	344 ± 32	792 ± 125
$CaCl_2$	1285 ± 129	1334 ± 101	1701 ± 154	2703 ± 246
NH_4Cl	14,849 ± 2002	14,270 ± 165	9170 ± 149	4930 ± 107
	88,827 ± 3392	45,130 ± 153	82,020 ± 130	68,290 ± 810
NaCl	>100,000	>100,000	>100,000	>100,000
$HgCl_2$	q	q	q	q
Compounds that affect mitochondrial function				
Cytochrome c	0.26 ± 0.02	0.32 ± 0.06	0.33 ± 0.06	0.78 ± 0.15
Nonyl TPP bromide	36.65 ± 2.93	19.76 ± 0.75	28.82 ± 1.02	43.31 ± 3.87
MitoQ	19.55 ± 1.67	15.92 ± 0.87	17.06 ± 0.17	30.67 ± 5.14
Metformin	>500	>500	>500	n.t.
Thimerosal	>500	>500	>500	n.t.
Acyclovir	>500	>500	>500	n.t.
Abacavir	>500	>500	>500	n.t.
Antimycin A	q	q	q	n.t.
CCCP	q	q	q	n.t.
Antibiotics				
Vancomycin	796 ± 47.04	433.7 ± 62.11	346.1 ± 21.17	1732.33 ± 28.99
Rifampicin	q	q	q	n.t.
Ampicillin Na	>500	>500	>500	n.t.
Dodecyl trimethyl-ammonium chloride	74.41 ± 8.47	30.71 ± 2.75	23.16 ± 2.74	69.20 ± 3.67
Apramycin	0.85 ± 0.04; 102.45 ± 1.50	0.63 ± 0.21; 14.54 ± 0.59	0.58 ± 0.04; 27.87 ± 2.70	2.79 ± 0.31; 592.6 ± 76.25
Gentamycin	1.04 ± 0.09; 383.93 ± 17.82	0.22 ± 0.03; 19.19 ± 1.44	0.38 ± 0.05; 24.15 ± 3.90	1.83 ± 0.69; 297.95 ± 54.96
Streptomycin	1.22 ± 0.20; 87.51 ± 6.22	0.60 ± 0.15; 14.15 ± 2.17	0.89 ± 0.12; 16.28 ± 2.83	2.33 ± 0.05; 155.04 ± 69.07
Tobramycin	n.t.	0.40 ± 0.16; 26.16 + 2.79	n.t.	n.t.
Kanamycin	n.t.	0.44 ± 0.10; 80.12 ± 13.45	n.t.	n.t.
Plazomicin	n.t.	1.13 ± 0.46; 29.36 ± 4.16	n.t.	n.t.

* All experiments were done at least in triplicate, n≥9 for cyt c, n.b. – no binding, n.t. – not tested, q- fluorescence of **10** is quenched by a studied compound.

periplasm of Gram-negative bacteria, e.g., *E. coli* [52]. Vancomycin affinity for CL was low, with EC_{50} values the in sub-millimolar range in the artificial membrane, and reached ≈1.7 mM when mitoplasts were used as the membrane model (Supplementary Figure 13). Our results are in good agreement with data published by Domenech et al. [11] who showed that a high concentration (600 nM) of vancomycin is required to induce only slight permeabilization of CL-containing lipid vesicles. Rifampicin quenches the fluorescence of **10**, which can be explained by the fact that the tetrahydroxynaphthalene moiety in rifampicin molecule exhibits a pKa of 1.7 related to the 4-hydroxy group. [53] Under physiological conditions at pH 6.8–7.8, rifampicin may interact with a molecule of dye **10** both electrostatically and by π-π stacking, depleting the photoluminescence of **10**. Ampicillin does not interact with CL at the tested concentrations, which supports the observation that the bactericidal effect of ampicillin is not influenced by the reduced amount of anionic lipids in *E. coli*. [54] The affinity of dodecyl trimethylammonium chloride for CL is close to that of the lipophilic phosphonium cation and is clearly pH-dependent: a 3-fold decrease in EC_{50} values was observed when the pH was raised from 6.8 to 7.8 (Supplementary Figure 14).

Aminoglycosides show a two-site binding pattern and exhibit high affinity for CL with EC_{50Hi} values ≤1 μM (Fig. 1H and Supplementary Figures 15–17). It has been shown that at high concentrations aminoglycosides cause destabilization and disruption of the negatively charged membranes. [55–58] We hypothesize that the first part of the binding curve with low EC_{50} value describes electrostatic binding of positively charged aminoglycosides with negatively charged phosphate groups of CL in the external surface of a bilayer membrane, and the second part of the binding curve with high EC_{50} value is a consequence of the apparent destabilization or disruption of the membrane that renders more free phosphate groups that can bind with aminoglycosides from otherwise inaccessible inside of the lipid bilayer. Gentamycin had the highest affinity for CL among the studied drugs, and its EC_{50Hi} values were almost equal to that of cyt *c* at pH 7.4–7.8. In total, the assay was validated by testing 26 substances of different natures – inorganic salts, peptide (cyt *c*), glycopeptide (vancomycin), polycationic sugars (aminoglycosides), phosphonium and ammonium lipophilic cations, guanine (abacavir, acyclovir) and guanidine (metformin) containing drugs, and others. The developed assay does not require special equipment other than a fluorimeter and is time-efficient, which makes it suitable for screening a large number of compounds. In general, positively charged substances bind with CL, but their affinity varies markedly; the EC50 values lie in the sub-micromolar to millimolar range. The interaction of the fluorescent probe with the studied compounds, e.g., heavy metal ions, is a limitation of the assay; therefore, a blank titration without CL must always be performed to avoid misinterpretation of the results.

4. Conclusions

We report that simple modification of the NAO structure – the replacement of dimethylamino groups with azetidinyl moieties at positions 3 and 6, as well as the replacement of the nonyl group with a 3-(trimethylsilyl)propyl group, significantly improves the photochemical properties in buffer solutions at physiological pH. The improved quantum yield and fluorescence stability of **10** in buffer allowed its application in further developments. The use of azetidinyl-substituted **10** as a CL-specific fluorescent probe facilitates the quantitative analysis of CL in mitochondrial fractions. Mitochondrial fractions obtained from cultured cells or tissue homogenates can be used; thus, samples from *in vitro* and *in vivo* experiments can be analyzed.

Most importantly, the same fluorescent probe **10** can be used in competitive binding studies to measure and compare the affinities of various substances for CL. The new screening technique allows to evaluate CL as a potential molecular target for therapies designed to protect or damage the mitochondrial membrane, for antimicrobial therapy, or as a landmark for targeted drug delivery into mitochondria. Additionally, this method might help to predict interactions of drugs with the mitochondrial membrane and, perhaps, to warn about possible side effects related to mitochondrial dysfunction.

Author contributions

P.A. was responsible for conceptualization, data curation, supervision, visualization; P.D. developed methodology and made synthetic work, P.D. developed binding assay and made all studies. The manuscript was written through contributions of both authors. All authors have given approval to the final version of the manuscript.

Declaration of Competing Interest

Pavels Dimitrijevs and Pavel Arsenyan have filed patent applications on the novel NAO- analogs, their use in CL quantitative analysis and competitive binding method, whose value may be affected by this publication.

Acknowledgement

This work was supported by Latvian Institute of Organic Synthesis internal grant (IG-2020-01 for Pavels Dimitrijevs) and SAM project Nr. 1.1.1.1/19/A/016. Cardiac, kidney and brain tissue samples of healthy C57Bl/6 J mice and cardiac tissue from healthy Sprague Dawley rats were kindly provided by LIOS Laboratory of Pharmaceutical Pharmacology. Authors would like to sincerely thank Dr. S. Belyakov for X-ray analysis, K. Leduskrasts for photo-physical experiments and I. Domracheva for culturing the cells.

Appendix A. Supplementary data

Supplementary material related to this article can be found, in the online version, at doi:https://doi.org/10.1016/j.snb.2021.130537.

References

[1] E. Mileykovskaya, W. Dowhan, Cardiolipin membrane domains in prokaryotes and eukaryotes, Biochim. Biophys. Acta Biomembr. 1788 (2009) 2084–2091, https://doi.org/10.1016/j.bbamem.2009.04.003.
[2] E. Beltrán-Heredia, F.C. Tsai, S. Salinas-Almaguer, F.J. Cao, P. Bassereau, F. Monroy, Membrane curvature induces cardiolipin sorting, Commun. Biol. 2 (2019) 1–7, https://doi.org/10.1038/s42003-019-0471-x.
[3] R. Kojima, Y. Kakimoto, S. Furuta, K. Itoh, H. Sesaki, T. Endo, Y. Tamura, Maintenance of Cardiolipin and crista structure requires cooperative functions of mitochondrial dynamics and Phospholipid Transport, Cell Rep. 26 (2019) 518–528, https://doi.org/10.1016/j.celrep.2018.12.070.
[4] N. Ikon, R.O. Ryan, Cardiolipin and mitochondrial cristae organization, Biochim. Biophys. Acta Biomembr. 1859 (2017) 1156–1163, https://doi.org/10.1016/j.bbamem.2017.03.013.
[5] M. Zhang, E. Mileykovskaya, W. Dowhan, Cardiolipin is essential for organization of complexes III and IV into a supercomplex in intact yeast mitochondria, J. Biol. Chem. 280 (2005) 29403–29408, https://doi.org/10.1074/jbc.M504955200.
[6] G. Paradies, V. Paradies, F.M. Ruggiero, G. Petrosillo, Role of Cardiolipin in mitochondrial function and dynamics in health and disease: molecular and pharmacological aspects, Cells 8 (2019) 728, https://doi.org/10.3390/cells8070728.
[7] R. Arias-Cartin, S. Grimaldi, P. Arnoux, B. Guigliarelli, A. Magalon, Cardiolipin binding in bacterial respiratory complexes: structural and functional implications, Biochim. Biophys. Acta - Bioenerg. 1817 (2012) 1937–1949, https://doi.org/10.1016/j.bbabio.2012.04.005.
[8] A.D. Tate, P.J. Antonelli, K.R. Hannabass, C.O. Dirain, Mitochondria-targeted antioxidant mitoquinone reduces cisplatin induced ototoxicity in guinea pigs, Otolaryngol. Head and Neck Surg. (United States). 156 (2017) 543–548, https://doi.org/10.1177/0194599816678381.
[9] A.V. Birk, S. Liu, Y. Soong, W. Mills, P. Singh, J.D. Warren, S.V. Seshan, J. D. Pardee, H.H. Szeto, The mitochondrial-targeted compound SS-31 re-energizes ischemic mitochondria by interacting with cardiolipin, J. Am. Soc. Nephrol. 24 (2013) 1250–1261, https://doi.org/10.1681/ASN.2012121216.
[10] M. El Khoury, J. Swain, G. Sautrey, L. Zimmermann, P. Van Der Smissen, J. L. Décout, M.P. Mingeot-Leclercq, Targeting bacterial cardiolipin enriched microdomains: an antimicrobial strategy used by amphiphilic aminoglycoside antibiotics, Sci. Rep. 7 (2017) 1–12, https://doi.org/10.1038/s41598-017-10543-3.
[11] O. Domenech, G. Francius, P.M. Tulkens, F. Van Bambeke, Y. Dufrêne, M. P. Mingeot-Leclercq, Interactions of oritavancin, a new lipoglycopeptide derived

from vancomycin, with phospholipid bilayers: effect on membrane permeability and nanoscale lipid membrane organization, Biochim. Biophys. Acta Biomembr. 1788 (2009) 1832–1840, https://doi.org/10.1016/j.bbamem.2009.05.003.
[12] J. Zielonka, J. Joseph, A. Sikora, M. Hardy, O. Ouari, J. Vasquez-Vivar, G. Cheng, M. Lopez, B. Kalyanaraman, Mitochondria-targeted triphenylphosphonium-based compounds: syntheses, mechanisms of action, and therapeutic and diagnostic applications, Chem. Rev. 117 (2017) 10043–10120, https://doi.org/10.1021/acs.chemrev.7b00042.
[13] N. Koleini, B.E. Nickel, A.L. Edel, R.R. Fandrich, A. Ravandi, E. Kardami, Oxidized phospholipids in doxorubicin-induced cardiotoxicity, Chem. Biol. Interact. 303 (2019) 35–39, https://doi.org/10.1016/j.cbi.2019.01.032.
[14] E. Kovács, T. Savopol, M.M. Iordache, L. Săplăcan, I. Sobaru, C. Istrate, M. P. Mingeot-Leclercq, M.G. Moisescu, Interaction of gentamicin polycation with model and cell membranes, Bioelectrochemistry 87 (2012) 230–235, https://doi.org/10.1016/j.bioelechem.2012.03.001.
[15] N.A.G. Santos, C.S. Catão, N.M. Martins, C. Curti, M.L.P. Bianchi, A.C. Santos, Cisplatin-induced nephrotoxicity is associated with oxidative stress, redox state unbalance, impairment of energetic metabolism and apoptosis in rat kidney mitochondria, Arch. Toxicol. 81 (2007) 495–504, https://doi.org/10.1007/s00204-006-0173-2.
[16] M.A. Parker, V. King, K.P. Howard, Nuclear magnetic resonance study of doxorubicin binding to cardiolipin containing magnetically oriented phospholipid bilayers, Biochim. Biophys. Acta Biomembr. 1514 (2001) 206–216, https://doi.org/10.1016/S0005-2736(01)00371-6.
[17] J.A. Bassam Soussi, Ann Christin Bylund Fellenius, Tore Schersten, ^{1}H n.m.r. Evaluation of the ferricytochrome c-cardiolipin interaction, Biochem. J. 265 (1990) 227–232.
[18] F. Sinibaldi, L. Fiorucci, A. Patriarca, R. Lauceri, T. Ferri, M. Coletta, R. Santucci, Insights into cytochrome c-cardiolipin interaction. Role played by ionic strength, Biochem 47 (2008) 6928–6935, https://doi.org/10.1021/bi800048v.
[19] K. Nicolay, R.J.M. Timmers, E. Spoelstra, R. Van Der Neut, J.J. Fok, Y.M. Huigen, A.J. Verkleij, B. De Kruijff, The interaction of adriamycin with cardiolipin in model and rat liver mitochondrial membranes, BBA - Biomembr. 778 (1984) 359–371, https://doi.org/10.1016/0005-2736(84)90380-8.
[20] G. Sautrey, M. El Khoury, A. Giro Dos Santos, L. Zimmermann, M. Deleu, L. Lins, J. L. Décout, M.P. Mingeot-Leclercq, Negatively charged lipids as a potential target for new amphiphilic aminoglycoside antibiotics: a biophysical study, J. Biol. Chem. 291 (2016) 13864–13874, https://doi.org/10.1074/jbc.M115.665364.
[21] G. Paradies, V. Paradies, F.M. Ruggiero, G. Petrosillo, Cardiolipin and mitochondrial function in health and disease, Antioxidants Redox Signal. 20 (2014) 1925–1953, https://doi.org/10.1089/ars.2013.5280.
[22] X. Han, J. Yang, K. Yang, Z. Zhongdan, D.R. Abendschein, R.W. Gross, Alterations in myocardial cardiolipin content and composition occur at the very earliest stages of diabetes: a shotgun lipidomics study, Biochem 46 (2007) 6417–6428, https://doi.org/10.1021/bi7004015.
[23] C.B. Pointer, A. Klegeris, Cardiolipin in central nervous system physiology and pathology, Cell. Mol. Neurobiol. 37 (2017) 1161–1172, https://doi.org/10.1007/s10571-016-0458-9.
[24] G. Petrosillo, M. Matera, G. Casanova, F.M. Ruggiero, G. Paradies, Mitochondrial dysfunction in rat brain with aging. Involvement of complex I, reactive oxygen species and cardiolipin, Neurochem. Int. 53 (2008) 126–131, https://doi.org/10.1016/j.neuint.2008.07.001.
[25] J. Zhang, W. Yu, S. Ryu, J. Lin, G. Buentello, R. Tibshirani, J. Suliburk, L.S. Eberlin, Cardiolipins are biomarkers of mitochondria-rich thyroid oncocytic tumors, Cancer Res. 76 (2016) 6588–6597, https://doi.org/10.1158/0008-5472.CAN-16-1545.
[26] A. Sapandowski, M. Stope, K. Evert, M. Evert, U. Zimmermann, D. Peter, I. Päge, M. Burchardt, L. Schild, Cardiolipin composition correlates with prostate cancer cell proliferation, Mol. Cell. Biochem. 410 (2015) 175–185, https://doi.org/10.1007/s11010-015-2549-1.
[27] M. Schlame, Methods in Cell Biology, Elsevier Inc., 2007, pp. 223–240, https://doi.org/10.1016/S0091-679X(06)80011-7.
[28] Z. Chen, L. Tan, L. Hu, Y. Luan, Superior fluorescent probe for detection of potassium ion, Talanta 144 (2015) 247–251, https://doi.org/10.1016/j.talanta.2015.06.015.
[29] P. Dimitrijevs, I. Domracheva, P. Arsenyan, Improved method for the preparation of nonyl acridine orange analogues and utilization in detection of cardiolipin, New J. Chem. 44 (2020) 9626–9633, https://doi.org/10.1039/d0nj02116d.
[30] J.B. Grimm, B.P. English, J. Chen, J.P. Slaughter, Z. Zhang, A. Revyakin, R. Patel, J. J. Macklin, D. Normanno, R.H. Singer, T. Lionnet, L.D. Lavis, A general method to improve fluorophores for live-cell and single-molecule microscopy, Nat. Methods 12 (2015) 244–250, https://doi.org/10.1038/nmeth.3256.
[31] S.E. Horvath, G. Daum, Lipids of mitochondria, Prog. Lipid Res. 52 (2013) 590–614, https://doi.org/10.1016/j.plipres.2013.07.002.
[32] Z.W. Zhang, J. Cheng, F. Xu, Y.E. Chen, J.B. Du, M. Yuan, F. Zhu, X.C. Xu, S. Yuan, Red blood cell extrudes nucleus and mitochondria against oxidative stress, IUBMB Life 63 (2011) 560–565, https://doi.org/10.1002/iub.490.
[33] E.R. Pennington, K. Funai, D.A. Brown, S.R. Shaikh, The role of cardiolipin concentration and acyl chain composition on mitochondrial inner membrane molecular organization and function, Biochim. Biophys. Acta - Mol. Cell Biol. Lipids. 1864 (2019) 1039–1052, https://doi.org/10.1016/j.bbalip.2019.03.012.
[34] S. Ben Zichri, S. Kolusheva, A.I. Shames, E.A. Schneiderman, J.L. Poggio, D. E. Stein, E. Doubijensky, D. Levy, Z. Orynbayeva, R. Jelinek, Mitochondria membrane transformations in colon and prostate cancer and their biological implications, Biochim. Biophys. Acta Biomembr. 1863 (2021) 183471, https://doi.org/10.1016/j.bbamem.2020.183471.
[35] T.J. Grevengoed, S.A. Martin, L. Katunga, D.E. Cooper, E.J. Anderson, R. C. Murphy, R.A. Coleman, Acyl-CoA synthetase 1 deficiency alters cardiolipin species and impairs mitochondrial function, J. Lipid Res. 56 (2015) 1572–1582, https://doi.org/10.1194/jlr.M059717.
[36] M.A. Kiebish, X. Han, H. Cheng, J.H. Chuang, T.N. Seyfried, Cardiolipin and electron transport chain abnormalities in mouse brain tumor mitochondria: lipidomic evidence supporting the Warburg theory of cancer, J. Lipid Res. 49 (2008) 2545–2556, https://doi.org/10.1194/jlr.M800319-JLR200.
[37] M.A. Kiebish, X. Han, H. Cheng, T.N. Seyfried, In vitro growth environment produces lipidomic and electron transport chain abnormalities in mitochondria from non-tumorigenic astrocytes and brain tumours, ASN Neuro 1 (2009) 125–138, https://doi.org/10.1042/AN20090011.
[38] F. Valianpour, R.J.A. Wanders, H. Overmars, F.M. Vaz, P.G. Barth, A.H. Van Gennip, Linoleic acid supplemention of Barth syndrome fibroblasts restores cardiolipin levels: implications for treatment, J. Lipid Res. 44 (2003) 560–566, https://doi.org/10.1194/jlr.M200217-JLR200.
[39] A.J. Chicco, G.C. Sparagna, Role of cardiolipin alterations in mitochondrial dysfunction and disease, Am. J. Physiol. - Cell Physiol. 292 (2007), https://doi.org/10.1152/ajpcell.00243.2006.
[40] Y.A. Vladimirov, E.V. Proskurnina, A.V. Alekseev, Molecular mechanisms of apoptosis. Structure of cytochrome c-cardiolipin complex, Biochem 78 (2013) 1086–1097, https://doi.org/10.1134/S0006297913100027.
[41] J. Santo-Domingo, N. Demaurex, The renaissance of mitochondrial pH, J. Gen. Physiol. 139 (2012) 415–423, https://doi.org/10.1085/jgp.201110767.
[42] T.E. Merchant, T. Glonek, 31P NMR of tissue phospholipids: competition for Mg^{2+}, Ca^{2+}, Na^{+} and K^{+} cations, Lipids. 27 (1992) 551–559, https://doi.org/10.1007/BF02536139.
[43] Y. Huang, L. Liu, C. Shi, J. Huang, G. Li, Electrochemical analysis of the effect of Ca^{2+} on cardiolipin-cytochrome c interaction, Biochim. Biophys. Acta - Gen. Subj. 1760 (2006) 1827–1830, https://doi.org/10.1016/j.bbagen.2006.08.013.
[44] K. Chan, D. Truong, N. Shangari, P.J.O. Brien, Drug-induced mitochondrial toxicity, expert Opin, Drug Metab. Toxicol. 1 (2005) 655–669.
[45] L. Yel, L.E. Brown, K. Su, S. Gollapudi, S. Gupta, Thimerosal induces neuronal cell apoptosis by causing cytochrome c and apoptosis inducing factor release from mitochondria, Int. J. Mol. Med. 16 (2005) 971–977, https://doi.org/10.3892/ijmm.16.6.971.
[46] C.E. Ganote, S.C. Armstrong, Effects of CCCP-induced mitochondrial uncoupling and cyclosporin A on cell volume, cell injury and preconditioning protection of isolated rabbit cardiomyocytes, J. Mol. Cell. Cardiol. 35 (2003) 749–759, https://doi.org/10.1016/S0022-2828(03)00114-7.
[47] Y. Arimura, T. Yano, M. Hirano, Y. Sakamoto, N. Egashira, R. Oishi, Mitochondrial superoxide production contributes to vancomycin-induced renal tubular cell apoptosis, Free Radic. Biol. Med. 52 (2012) 1865–1873, https://doi.org/10.1016/j.freeradbiomed.2012.02.038.
[48] S. Kalghatgi, C.S. Spina, J.C. Costello, M. Liesa, J.R. Morones-Ramirez, S. Slomovic, A. Molina, O.S. Shirihai, J.J. Collins, Bactericidal antibiotics induce mitochondrial dysfunction and oxidative damage in mammalian cells, Sci. Transl. Med. 5 (2013), https://doi.org/10.1126/scitranslmed.3006055.
[49] A. Chowdhury, A. Santra, K. Bhattacharjee, S. Ghatak, D.R. Saha, G.K. Dhali, Mitochondrial oxidative stress and permeability transition in Isoniazid and Rifampicin induced liver injury in mice, J. Hepatol. 45 (2006) 117–126, https://doi.org/10.1016/j.jhep.2006.01.027.
[50] S. Wessels, H. Ingmer, Modes of action of three disinfectant active substances: a review, Regul. Toxicol. Pharmacol. 67 (2013) 456–467, https://doi.org/10.1016/j.yrtph.2013.09.006.
[51] R. Esterberg, T. Linbo, S.B. Pickett, P. Wu, H.C. Ou, E.W. Rubel, D.W. Raible, Mitochondrial calcium uptake underlies ROS generation during aminoglycoside-induced hair cell death, J. Clin. Invest. 126 (2016) 3556–3566, https://doi.org/10.1172/JCI84939.
[52] J.C. Wilks, J.L. Slonczewski, pH of the cytoplasm and periplasm of Escherichia coli: rapid measurement by green fluorescent protein fluorimetry, J. Bacteriol. 189 (2007) 5601–5607, https://doi.org/10.1128/JB.00615-07.
[53] M.J. O'Neil, The Merck Index - an Encyclopedia of Chemicals, Drugs, and Biologicals, 13th ed., Whitehouse Station, NJ: Merck and Co., Inc, 2001.
[54] D.G. Rodionov, E.E. Ishiguro, Ampicillin induced bacteriolysis of Escherichia coli is not affected by reduction in levels of anionic phospholipids, FEMS Microbiol. Lett. 156 (1997) 85–89, https://doi.org/10.1016/S0378-1097(97)00406-0.
[55] R. Brasseur, G. Laurent, J.M. Ruysschaert, P. Tulkens, Interactions of aminoglycoside antibiotics with negatively charged lipid layers. Biochemical and conformational studies, Biochem. Pharmacol. 33 (1984) 629–637, https://doi.org/10.1016/0006-2952(84)90319-8.
[56] T. Joshi, Z.X. Voo, B. Graham, L. Spiccia, L.L. Martin, Real time examination of aminoglycoside activity towards bacterial mimetic membranes using Quartz Crystal Microbalance with Dissipation monitoring (QCM-D), Biochim. Biophys. Acta Biomembr. 1848 (2015) 385–391, https://doi.org/10.1016/j.bbamem.2014.10.019.
[57] A.M. Alexander, I. Gonda, E.S. Harpur, J.B. Kayes, Interaction of aminoglycoside antibiotics with phospholipid liposomes studied by microelectrophoresis, J. Antibiot. 32 (1979) 504–510, https://doi.org/10.7164/antibiotics.32.504.
[58] A. Forge, G. Zajic, S. Davies, N. Weiner, J. Schacht, Gentamicin alters membrane structure as shown by freeze fracture of liposomes, Hear. Res. 37 (1989) 129–140, https://doi.org/10.1016/0378-5955(89)90035-X.

Pavels Dimitrijevs was born in 1995 in Daugavpils, Latvija. He graduated from Riga Stradins University Faculty of Pharmacy in 2019 and started his doctoral studies in pharmacy ibid. Currently, he is an assistant at Latvian Institute of Organic synthesis. His

research interests include chemistry of selenium containing compounds, fluorescent probes and lipid nanoparticles.

Pavel Arsenyan was born in 1975 in Liepaja, Latvia. He is head of Pharmacomodulator's synthesis group in Latvian Institute of Organic synthesis since 2005. He obtained his PhD in 2001 in the University of Latvia. Research interests include chemistry of selenium and tellurium containing compounds and their antitumor activity investigations, development of new methods in heterocyclic chemistry, organometallic chemistry, elaboration of eco-friendly synthetic methods, OLEDs and fluorescent dyes.

Fourth Publication

European Journal of Medicinal Chemistry 257 (2023) 115504

Contents lists available at ScienceDirect

European Journal of Medicinal Chemistry

journal homepage: www.elsevier.com/locate/ejmech

Research paper

Development of isoselenazolium chlorides as selective pyruvate kinase isoform M2 inhibitors

Pavels Dimitrijevs [a], Marina Makrecka-Kuka [a], Agnieszka Bogucka [b], Marko Hyvönen [b], Teodors Pantelejevs [a], Pavel Arsenyan [a,*]

[a] Latvian Institute of Organic Synthesis, Aizkraukles 21, LV1006, Riga, Latvia
[b] Department of Biochemistry, University of Cambridge, Sanger Building, 80 Tennis Ct Rd, Cambridge, CB2 1GA, UK

ARTICLE INFO

Keywords:
Cancer
Metabolic reprogramming
Pyruvate kinase M2
Selenium

ABSTRACT

Alterations in cancer metabolic pathways open up an opportunity for targeted and effective elimination of tumor cells. Pyruvate kinase M2 (PKM2) is predominantly expressed in proliferating cells and plays an essential role in directing glucose metabolism in cancer. Here, we report the design of novel class of selective PKM2 inhibitors as anti-cancer agents and their mechanism of action. Compound **5c** being the most active with $IC_{50} = 0.35 \pm 0.07$ μM, also downregulates PKM2 mRNA expression, modulates mitochondrial functionality, induces oxidative burst and is cytotoxic for various cancer types. Isoselenazolium chlorides have an unusual mechanism of PKM2 inhibition, inducing a functionally deficient tetrameric assembly, while exhibiting a competitive inhibitor character. The discovery of robust PKM2 inhibitors not only offers candidates for anticancer therapy but is also crucial for studying the role of PKM2 in cancer.

1. Introduction

Cancer is a disease caused by the accumulation of genetic mutations and dysregulated gene expression, leading to uncontrolled cell proliferation. In order to support growth, cancer cells must meet a high energy demand, maintain a reduction-oxidation balance and produce building blocks for biomass generation. This is achieved through so called metabolic reprogramming that includes upregulation of glucose transport and key glycolytic enzymes, promoting aerobic glycolysis (Warburg effect) [1]. This concept has recently been challenged by many studies demonstrating that mitochondrial metabolism is equally important for ATP production and tumorigenesis [2–5]. Remarkably, many cancer types express a particular isoform of pyruvate kinase, PKM2, that catalyzes conversion of phosphoenolpyruvate to pyruvate in the final step of glycolysis. This is a critical point where the flux of glucose-derived carbons is determined, either towards tricarboxylic acid cycle in mitochondria for ATP production and lactate production by lactate dehydrogenase for cytosolic NADH oxidation or pentose phosphate pathway and serine biosynthesis for nucleotide and fatty acid production [6]. PKM2 can be switched between highly enzymatically active tetramer and a relatively inactive dimer by allosteric activators and inhibitors to adapt to varying environmental conditions [7]. Moreover, PKM2 is involved in the regulation of mitochondrial respiration, mitochondrial-dependent apoptosis and reduces oxidative damage to mitochondria [8]. As an essential regulation node that is characteristic for cancer cells, PKM2 opens a perfect opportunity for therapeutic intervention.

Up to date, a few classes of PKM2 inhibitors were described, including amino acids phenylalanine, alanine and tryptophan [9] and natural flavonoids such as apigenin [10], however, the most studied PKM2 inhibitors are naphthoquinones shikonin and its second-generation analogue, compound 3 k. Nevertheless, their inhibitory activity is relatively low (*in vitro* $IC_{50} = 8.82 \pm 2.62$ μM and 2.95 ± 0.53 μM for shikonin and 3 k, respectively) [11], and the mechanism of inhibition has not been elucidated [12].

Recently, we developed heterocyclic molecules with a Se–N^+ bond – isoselenazolium salts, that inhibited pyruvate-dependent mitochondrial respiration [13]. In this work, we proceeded with structural modification and surprisingly, found potent and selective PKM2 inhibitors. Herein, we describe synthesis of the novel compounds, their cytotoxicity on various cancer cell lines, impact on mitochondrial respiration and ROS production, inhibition of pyruvate kinase isoforms, modulation of PKM2 mRNA expression, and propose the inhibitory mechanism based on NMR, size-exclusion chromatography (SEC), mass photometry,

* Corresponding author.
E-mail address: pavel@osi.lv (P. Arsenyan).

https://doi.org/10.1016/j.ejmech.2023.115504
Received 16 April 2023; Received in revised form 12 May 2023; Accepted 16 May 2023
Available online 18 May 2023

differential scanning fluorimetry (DSF), isothermal titration calorimetry (ITC) and enzyme kinetics studies.

2. Results

2.1. Synthesis

The initial idea was to introduce nicotinamide moiety in isoselenazolopyridinium core to resemble to some extent a part of NAD^+ structure, and to study the impact of the amide group and its position on cytotoxicity. We set out to prepare isoselenazolopyridinium chlorides bearing amide and similar functional groups - carboxylic acid and methyl ester substituents in all possible positions of the pyridine ring (Scheme 1). The treatment of pyridine bromides **1a-c** with ethynyl cyclohexanol in the presence of palladium catalyst let us to produce ethynyl substituted derivatives **2a-c** in high yields. The corresponding carboxylic acids were obtained by hydrolysis of ester group with NaOH (**3a-c**) and amides **4a-c** were synthesized in the reaction of **2a-c** with saturated methanolic solution of NH_3. Methyl-d3 2-((1-hydroxycyclohexyl)ethynyl)isonicotinate (**2d**) was prepared by the treatment of a suspension of **3c** and CD_3OD with HOBt hydrate and EDC•HCl in DMF. Having all ethynyl pyridines in hand we moved to the creation of isoselenazolium ring based on a previously established procedure [14]. Ethynyl pyridines **2a-d**, **3a-c** and **4a-c** were treated with *in situ* prepared $SeBr_4$ by dissolving selenium(IV) oxide in concentrated hydrobromic acid in dioxane/water. After consumption of a substrate, the crude material was dissolved in the mixture of EtOH/water and eluted through ion-exchange resins (IRA-401) pretreated with hydrochloric acid yielding isoselenazolopyridinium chlorides **5a-d**, **6a-c** and **7a-c**. However, the treatment of 2-((1-hydroxycyclohexyl)ethynyl)nicotinic acid and its amide and methyl ester derivatives with $SeBr_4$ was unsuccessful and resulted in only traces of the desired products.

Based on the preliminary SAR data, cyclohexyl substituent at position 2 was replaced by cyclobutyl, cyclopentyl, adamantlyl, tridecyl, and difluorocyclohexyl groups. Isoselenazolopyridinium chlorides **5f-k**, **7d-f** were synthesized in the similar manner (Table 2, Scheme 2).

Methyl- and fluoro-substituted pyridine bromides were used as a starting material to obtain compounds **5j** and **5k**. In general, the conversion of the reaction was high in all cases, the yields varied due to different methods of isolation and purification of desired compounds bearing Se–N^+ bond. Molecular structures of **5a** (CCDC2178481), **5e** (CCDC 2179108), **6b** (CCDC 2178824), and **7e** (CCDC 2178826) were confirmed by X-ray diffraction. Depending on pH of the media, isoselenazolium chlorides can exist in chloride and zwitterion forms [14]. The exact form can be detected by X-ray and ^{77}Se NMR spectra. Selenium signal lies in 1200–1300 ppm region in the case of isoselenazolium chlorides and around 1100 ppm in zwitterions such as **5e** and **5f**.

Also, it should be noted that the distance between selenium and oxygen of the hydroxy group is shorter in zwitterions forming an additional bond (Se–O = 2.006 Å; Se–N^+ = 2.131 Å in the crystal structure of **5e**). We speculate that the formation of this additional bond stabilizes isoselenazolium cycle in aqueous media at higher pH. We evaluated the stability of the isoselenazolium salt **5c** by ^{77}Se NMR (Supplementary materials spectra section) at pH ranging from 6.0 to 10.0, which confirms the heterocycle stability throughout the physiological pH range.

2.2. Cytotoxicity of isoselenazolium salts

The cytotoxicity of new isoselenazolium salts was studied in human and mouse breast cancer (MCF-7, HCC1937, MDA-MB-231, 4T1), T cell leukemia (Jurkat) and human lung adenocarcinoma (A549) cells, and the data are summarized in Table 1. As we expected the new compounds to modulate mitochondrial function, rat cardiomyoblasts (H9C2) were selected as a normal cell line control because they contain a large number of mitochondria [15] and are widely used to assess mitochondrial toxicity *in vitro* [16]. First, the influence of the carboxyl, methoxy carbonyl, and amide group position of the pyridinium ring was studied. Carboxyl group in any position reduced cytotoxicity and selectivity towards cancer cells, probably, because of the poor solubility and low cell permeability. Compounds **5a** and **6a** were excluded from the study due

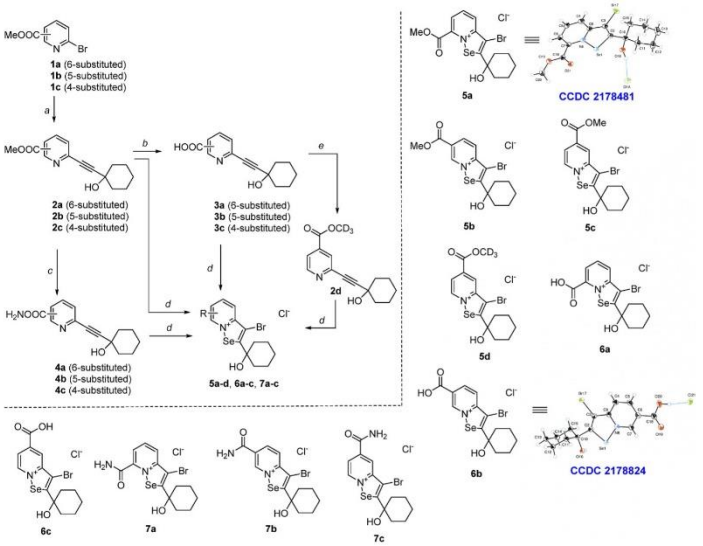

Scheme 1. Synthesis of isoselenazolopyridinium chlorides **5a-e**, **6a-c** and **7a-c**. *Reaction conditions: a*: terminal acetylene (1.4 equiv.), CuI (0.01–0.05 equiv.), $(Ph_3P)_2PdCl_2$ (0.01–0.05 equiv.), DMF/iPr_2NH or Et_3N, 50 or 80 °C, 2–5 h; *b*: 1. NaOH (5 equiv.), 2. HCl, MeOH/H_2O, rt, overnight; *c*: NH_3, MeOH, rt, overnight; *d*: $SeBr_4$, dioxane, rt; *e*: CD_3OD, EDC × HCl, HOBt × H_2O, DMF, rt, 2 h.

Table 1
Cytotoxic activity of **5b-7f** against cardiomyoblasts and cancer cell lines. Values are shown as the means ± S.D. from 3 to 5 independent experiments.

Compound	Cytotoxicity, IC_{50}, μM						
	H9C2	Jurkat	MCF7	HCC1937	A549	MDA-MB-231	4T1
Doxorubicin	3.90 ± 0.60	0.32 ± 0.08	0.47 ± 0.14	1.08 ± 0.10	0.23 ± 0.07	0.41 ± 0.08	0.065 ± 0.008
5b	0.89 ± 0.27	0.25 ± 0.06	0.87 ± 0.29	0.31 ± 0.11	1.31 ± 0.20	0.43 ± 0.14	0.70 ± 0.18
5c	2.46 ± 0.60	0.44 ± 0.25	1.16 ± 0.09	0.33 ± 0.03	1.30 ± 0.23	0.51 ± 0.15	0.32 ± 0.03
5d	0.64 ± 0.28	0.49 ± 0.06	0.38 ± 0.09	0.54 ± 0.02	1.20 ± 0.46	0.40 ± 0.11	1.11 ± 0.04
5e	2.97 ± 0.22	3.24 ± 0.49	2.80 ± 0.75	3.03 ± 0.40	9.12 ± 1.42	6.51 ± 0.67	>10
5f	0.77 ± 0.14	0.48 ± 0.22	0.36 ± 0.13	0.41 ± 0.13	8.70 ± 1.43	1.66 ± 0.35	2.04 ± 0.60
5g	1.06 ± 0.03	0.48 ± 0.27	0.28 ± 0.13	0.24 ± 0.10	1.16 ± 0.25	0.48 ± 0.13	1.48 ± 0.44
5h	4.76 ± 0.18	6.18 ± 0.16	6.87 ± 0.75	2.89 ± 0.37	nt	nt	nt
5i	3.63 ± 0.38	3.38 ± 0.30	3.79 ± 0.57	2.45 ± 0.43	nt	nt	nt
5j	1.68 ± 0.36	1.16 ± 0.19	1.08 ± 0.02	1.19 ± 0.27	2.93 ± 0.47	1.38 ± 0.40	2.34 ± 0.51
5k	0.90 ± 0.24	0.45 ± 0.11	0.30 ± 0.18	0.34 ± 0.05	1.12 ± 0.26	0.37 ± 0.14	0.96 ± 0.14
6b	3.55 ± 0.18	3.26 ± 0.54	>10 μM	3.85 ± 0.61	nt	nt	nt
6c	7.82 ± 0.19	6.61 ± 2.15	>10 μM	5.82 ± 0.72	7.03 ± 0.10	6.12 ± 0.47	6.81 ± 0.33
7a	2.63 ± 0.44	1.88 ± 0.42	3.85 ± 0.41	1.33 ± 0.30	nt	nt	nt
7b	1.27 ± 0.13	0.60 ± 0.25	2.30 ± 0.87	1.50 ± 0.34	nt	nt	nt
7c	1.41 ± 0.17	1.00 ± 0.15	2.22 ± 0.57	0.60 ± 0.25	2.81 ± 0.58	1.15 ± 0.20	1.41 ± 0.28
7d	1.41 ± 0.26	1.43 ± 0.36	1.00 ± 0.08	0.60 ± 0.25	3.17 ± 0.23	1.36 ± 0.18	1.25 ± 0.08
7e	0.91 ± 0.25	0.91 ± 0.29	0.61 ± 0.04	0.74 ± 0.26	2.21 ± 0.36	0.65 ± 0.21	0.56 ± 0.02
7f	1.91 ± 0.55	2.00 ± 0.25	1.01 ± 0.08	0.91 ± 0.10	3.72 ± 0.40	2.42 ± 0.18	4.32 ± 0.73

nt = not tested.

Table 2
IC_{50} values of isoselenazolium chlorides for PKM2 inhibition and their inhibitory activity on PKM1, PKR and LDH at 1 μM concentration. PKM2, pyruvate kinase M2 isoform; PKM1, pyruvate kinase M1 isoform; PKR, pyruvate kinase R isoform; LDH, L-lactate dehydrogenase from rabbit muscle; FBP, fructose-1,6-bisphosphate; Se-Py, 3-bromo-2-(1-hydroxycyclohexyl)- [1,2]selenazolo[2,3-a] pyridinium chloride, nt – not tested.

Compound	IC_{50}, μM		Inhibition at 1 μM, %		
	PKM2	PKM2 with FBP (250 μM)	PKM1	PKR	LDH
Apigenin	>20	>20	nt	nt	nt
Comp. 3k [29]	>20	>20	nt	nt	nt
Se-Py [13,14]	2.924 ± 0.356	2.731 ± 0.277	nt	nt	nt
5b	0.545 ± 0.059	0.303 ± 0.081	16	39	10
5c	0.350 ± 0.068	0.477 ± 0.104	13	21	10
5d	0.478 ± 0.143	0.610 ± 0.022	10	16	13
5e	0.854 ± 0.263	0.603 ± 0.023	26	20	7
5f	0.380 ± 0.138	0.517 ± 0.036	20	42	6
5g	0.637 ± 0.137	0.572 ± 0.021	11	29	2
5h	>1	nt	nt	nt	nt
5i	>1	nt	nt	nt	nt
5j	0.897 ± 0.385	nt	29	15	7
5k	1.355 ± 0.295	nt	10	28	7
6b	>1	nt	nt	nt	nt
6c	1.064 ± 0.266	nt	4	5	9
7a	>1	nt	nt	nt	nt
7b	>1	nt	nt	nt	nt
7c	0.420 ± 0.097	0.572 ± 0.103	15	37	6
7d	0.362 ± 0.038	0.542 ± 0.030	26	40	13
7e	1.010 ± 0.264	nt	21	11	6
7f	0.901 ± 0.173	nt	23	29	9

to low solubility in aqueous medium. In turn, derivatives with methoxy carbonyl or amide group in position 5 and 6 exhibited high cytotoxicity toward a wide range of malignant cell lines. In particular, **5c** with the methoxy carbonyl group at position 5 stood out with a favorable cytotoxicity profile. In turn, introduction of fluorine atom in position 6 or methyl group in position 7 ruined selectivity toward cancer cells. Then, we proceeded with modification of the structure in position 2 and concluded that bulky (adamantyl) or lipophilic (2-hydroxypentadecan-2-yl) substituents at this position reduce cytotoxicity and/or selectivity toward cancer cells. However, it was found that optimal substituent is 1-hydroxycyclohexanyl group, and cytotoxicity for most of the cell lines decreased with smaller carbon atom number in hydroxycycloalkane ring.

While some analogues, such as **5g** and **5f**, are worth mentioning, **5c** was the most selective and exhibited the highest cytotoxic activity in a broader spectrum of cancer cell lines. Hence, we proceeded to study its mechanism of action.

*2.3. Compound **5c** modulates pyruvate-dependent respiration, induces mitochondrial H_2O_2 production rate and dyscoupling of electron transport system*

The impact of **5c** on mitochondrial respiration was studied in HCC1937, MCF-7, 4T1 and Jurkat cells by high-resolution fluorespirometry (Fig. 1). These cell lines showed significant differences in mitochondrial metabolic activity and their maximal oxygen consumption rate (OCR) was in the following descending order: MCF-7>4T1>HCC1937>Jurkat (Fig. 1A–D). Surprisingly, **5c** significantly increased OCR in all cell lines in the presence of pyruvate and malate in either LEAK, OXPHOS or both states. However, **5c** abruptly interrupted OXPHOS coupling in the presence CI substrates (pyruvate and malate) in MCF-7 (Fig. 1E), HCC1937(Fig. 1G) and Jurkat (Fig. 1H), but not in 4T1 cells (Fig. 1F). Compound **5c** does not seem to have a direct impact on CI because rotenone effect was almost identical in the treatment and control groups, except for HCC1937, where rotenone effect was reduced. In addition, there were no substantial changes in mitochondrial function in the CII-linked OXPHOS state.

Elevated OCR might be explained by the increase in ROS production (Fig. 2A–D). Immediately after addition of **5c** there was a massive increase in the rate of H_2O_2 production in all cell lines. The most pronounced H_2O_2 production spikes were in the presence of CI substrates. Higher H_2O_2/O ratios (Fig. 2E–H) indicate that more oxygen is shifted toward ROS production rather than participating in electron transfer

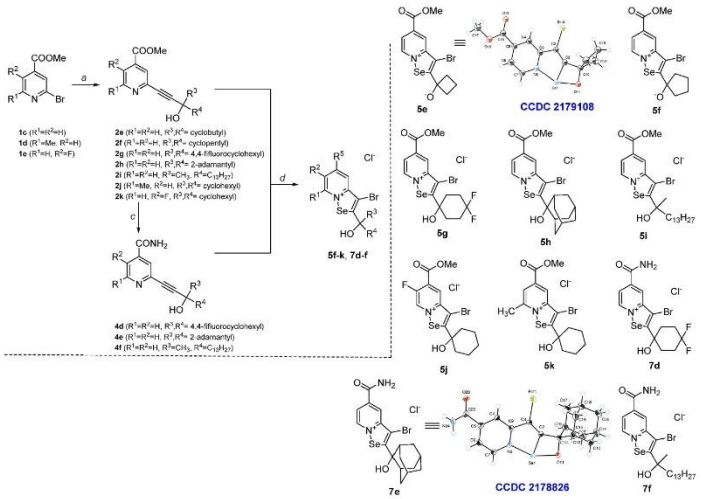

Scheme 2. Synthesis of isoselenazolopyridinium chlorides **5f-l** and **7d-f**. *Reaction conditions: a*: terminal acetylene (1.4 equiv.), CuI (0.01–0.05 equiv.), $(Ph_3P)_2PdCl_2$ (0.01–0.05 equiv.), DMF/iPr_2NH or Et_3N, 50 or 80 °C, 2–5 h; *b*: NH_3, MeOH, rt, overnight; *c*: $SeBr_4$, dioxane/water, rt.

system. Some studies also report that an increase in ROS level causes an increase in proton leak [17,18], and this phenomenon might explain the observed reduction in coupling efficiency.

The observed increase in mitochondrial ROS production may arise from CI or complex III (CIII) produced superoxide anion. However, $O_2^{\bullet-}$ production by CIII is low and it is unlikely to be associated with such significant effects [19]. In turn, CI can produce extensive amount of $O_2^{\bullet-}$ and H_2O_2 during both, forward (NADH-oxidizing) and reverse (NAD^+-reducing) electron transport. The latter can be ruled out, because H_2O_2 production is not abolished by rotenone, confirming that electrons do not enter into CI through the CoQ-binding site(s) in the reverse direction [20]. Another way to induce mitochondrial ROS production is by decreasing NAD^+/NADH ratio [20]. However, **5c** did not decrease NAD^+/NADH ratio in 4T1 cells, but increased it (Fig. 3C). Notably, **5c** significantly reduced NAD^+ and NADH intracellular pools by 42.8% and 57.4%, respectively (Fig. 3A). In contrast, no effect on NAD^+ and NADH pools or NAD^+/NADH ratio was found in a parallel experiment with H9C2 cells (Fig. 3B). We hypothesized that NAD^+ could be consumed by PARP1, that becomes overactivated by ROS [21–23]. To our surprise, we found that **5c** exhibited moderate PARP1 inhibitory activity with IC_{50} = 0.250 ± 0.08 μM, and, therefore, NAD^+ pool depletion cannot be Previously, we showed that isoselenazolium salts bind mitochondria-specific phospholipid cardiolipin (CL) using isothermal titration calorimetry (ITC) [13]. To determine whether the interaction with CL-rich mitochondrial membrane domains might lead to the observed proton leak, we used a fluorescence-based competitive binding assay to study relative affinity of **5c** toward CL in isolated mitoplasts from rat liver (Fig. 2H) [24]. Although **5c** binds to CL (EC_{50} = 3490 ± 298 μM), the affinity is approximately 100 times lower compared to classic mitotargeting moiety nonyl triphenylphosphium bromide (EC_{50} = 32.22 ± 2.64 μM) and approx. 5000 times lower compared to cytochrome *c* (EC_{50} = 0.70 ± 0.14 μM), an endogenous CL ligand. Therefore, it is unlikely that the interaction of **5c** with CL induces proton leak and decreases coupling efficiency, especially, bearing in mind that the majority of basal proton conductance is regulated through the inner mitochondrial membrane proteins, and the lipid bilayer of the inner membrane accounts for only 5% of the proton leak [25,26]. Hence, we proceeded to look at other molecular targets that might be associated with mitochondrial metabolism.

2.4. Isoselenazolium salts selectively inhibit pyruvate kinase M2 isoform

Compound **5c** at a concentration of 1 μM was tested on a metabolic enzyme panel as well as on Bcls and Mcl-1 (Supplementary Tables 1 and 2, respectively), and it was found that it selectively inhibited pyruvate kinase M2 (PKM2), one of the four isoforms of pyruvate kinase that is predominantly expressed in cancer tissues [27,28].

Motivated by this observation, we determined PKM2 IC_{50} values for the isoselenazolium series by a LDH-coupled assay (Table 2) [29]. Isoselenazolium salts did not inhibit LDH and, therefore, did not interfere with the used assay. We found that compounds **5b-7f** selectively inhibit PKM2, and compound **5c** as well as its amide analogue **7c** stand out with 0.350 ± 0.068 and 0.420 ± 0.097 μM IC_{50} values, respectively. Surprisingly, we found that previously described PKM2 inhibitors apigenin and compound 3 k did not inhibit PKM2 at concentrations up to 20 μM in used conditions [29,30]. The studied isoselenazolium salts are more selective toward PKM2, as no compound reached 50% inhibition of either PKM1 or PKR at 1 μM concentration. Notably, addition of fructose-1,6-bisphosphate (FBP), the natural allosteric activator of PKM2, did not significantly impact the inhibitory activity of the studied compounds.

Importantly, ester or amide group in isoselenazolopyridinium ring is essential for PKM2 inhibition, as the previously published unsubstituted 3-bromo-2-(1-hydroxycyclohexyl)- [1,2]selenazolo[2,3-a]pyridinium chloride (Se-Py) is approximately 8 times less potent than **5c** and **7c** [13]. Also, the structure-activity relationship (SAR) pattern found here (Fig. 4A) corresponds well to that of cytotoxicity. In order to elucidate binding and inhibition mechanisms of isoselenazolium salts, we proceeded with biochemical and biophysical studies of the most potent inhibitors **5c** and **7c**.

2.5. Isoselenazolium salts act as competitive, reversible inhibitors of PKM2

Steady-state kinetic parameters for PKM2 were determined in the presence of **5c** in order to characterize the mechanism of inhibition. By plotting the initial reaction velocity as a function of phosphoenolpyruvate (PEP) or ADP at varying concentrations of **5c** (Fig. 4B and C), a classic competitive inhibitor pattern can be distinguished in the case of

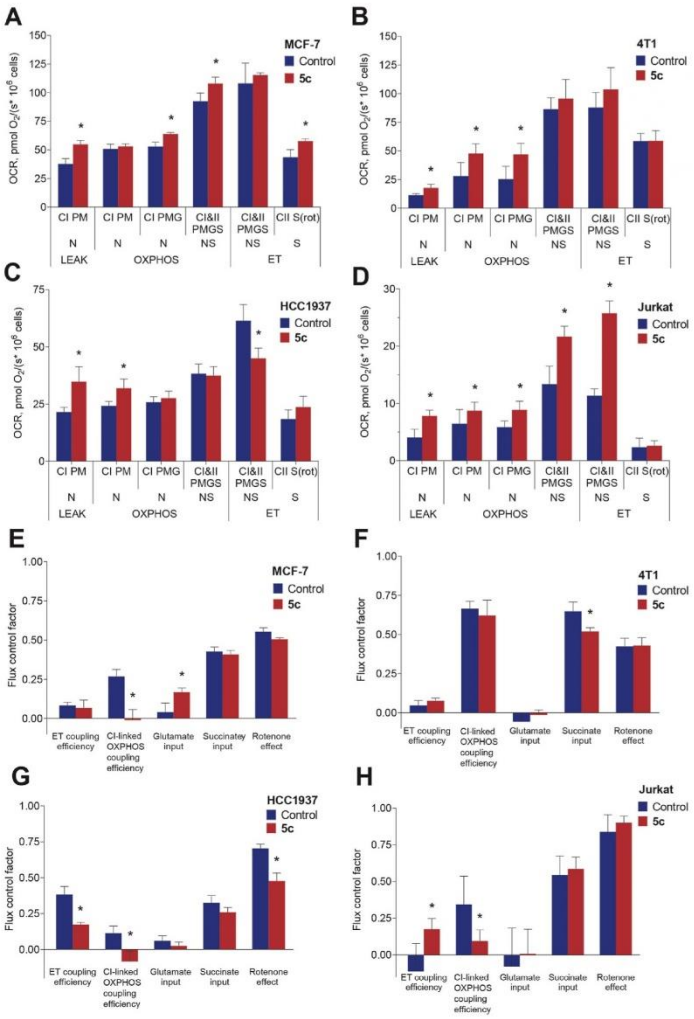

Fig. 1. The effect of **5c** at 1 μM concentration on mitochondrial respiration rate. Respiratory parameters in permeabilized (**A**) MCF-7, (**B**) 4T1, (**C**) HCC1937, (**D**) Jurkat cells. Flux control factors in permeabilized (**E**) MCF-7, (**F**) 4T1, (**G**) HCC1937, (**H**) Jurkat cells. OCR—oxygen consumption rate, CI—complex, I; CII—complex II; LEAK—substrate dependent respiration rate; OXPHOS—oxidative phosphorylation dependent state; ET—electron transfer, uncoupled state; P—pyruvate; M—malate; G—glutamate; S—succinate; N—NADH-generating substrates; NS—NADH-generating substrates and succinate; rot—rotenone. Flux control factors indicate the input of each substrate and/or pathway to the electron transfer system performance. Rotenone effect corresponds to 1-OCR after the addition of rot/OCR before the addition of rot. Values are shown as mean ± S.D. (n = 3–5 experiments). Statistically significant difference (*) was considered when $p < 0.05$ (Students *t*-test) compared to the control group (vehicle-DMSO).

both substrates - the value of V_{max}^{App} is constant, while the K_M^{App} increased at higher inhibitor concentrations (Supplementary Tables 3 and 4). Selenium atom in the isoselenazolium moiety has electrophilic nature and may potentially react covalently with the nucleophilic cysteine or lysine sidechains on the surface of PKM2. The reversibility of **7c** binding was tested using ligand-observed one-dimensional ^{1}H NMR. WaterLOGSY experiments detect the transfer of magnetization from water protons to the ligand or, in the case of ligand association and dissociation occurring at the timescale of the NMR measurement, the transfer of magnetization from water to the protein and then to the ligand. Protons of free **7c** were observed with negative peak intensities, resulting from the cross relaxation via the nuclear Overhauser effect (NOE) (Fig. 5A, bottom). The addition of PKM2 to **7c** caused an inversion of the peak intensity, i.e., negative NOE, suggesting that a reversible, noncovalent binding of the ligand to PKM2 has occurred, and the molecule has dissociated during the mixing time of the WaterLOGSY sequence (Fig. 5A, top).

2.6. Isoselenazolium salts reduce the dimer/tetramer ratio of PKM2

PKM2 is regulated by a range of metabolites that affect its quaternary assembly by promoting or inhibiting the more active tetrameric state, or by inducing interprotomer movements that result in altered activity [31–34]. To evaluate the effect of isoselenazolium salts on the oligomeric assembly of PKM2, we performed analytical size-exclusion chromatography (SEC) measurements. Under the experimental conditions tested, PKM2 elutes from the column primarily as tetrameric species, corresponding to the first peak in the chromatogram, followed by a dimer/monomer peak of a smaller magnitude (Fig. 5B). As expected, the ratio of tetramer to dimer/monomer increased at higher protein concentrations (Fig. 5B). Incubation of 5 μM PKM2 with **5c** or **7c** resulted in

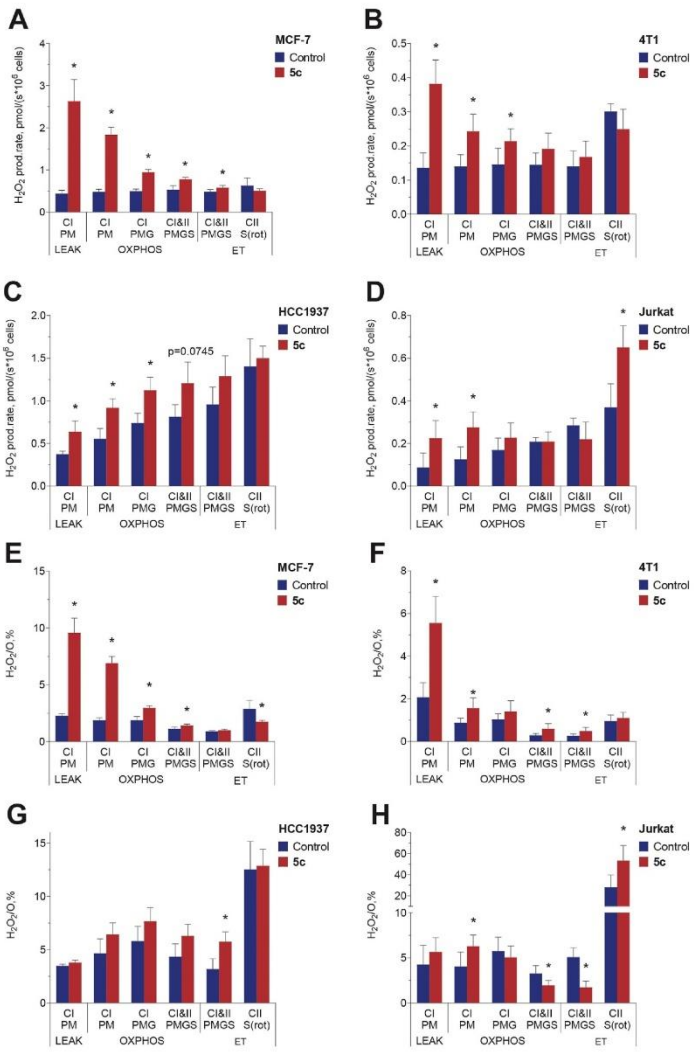

Fig. 2. Effect of 1 μM **5c** on H_2O_2 production rate in permeabilized (**A**) MCF-7, (**B**) 4T1, (**C**) HCC1937 and (**D**) Jurkat cells. H_2O_2/O ratio in in permeabilized (**E**) MCF-7, (**F**) 4T1, (**G**) HCC1937 and (**H**) Jurkat cells. CI—complex, I; CII—complex II; LEAK—substrate dependent respiration rate; OXPHOS—oxidative phosphorylation dependent state; ET— electron transfer, uncoupled state; P—pyruvate; M—malate; G—glutamate; S—succinate; rot—rotenone. Values are shown as mean ± S.D. (n = 3–5 experiments). Statistically significant difference (*) was considered when $p < 0.05$ (Students *t*-test) compared to the control group (vehicle-DMSO).

a dose-dependent increase in the tetramer ratio, with a concurrent reduction in the dimer/monomer peak (Fig. 5C). However, due to the sensitivity limitations of the method, SEC requires micromolar concentration of a protein, and the observed PKM2 dimer/tetramer ratio might not be physiologically relevant, taking in mind that it is highly dependent on the concentration. Therefore, we decided to apply single-molecule mass photometry to explore oligomeric state of PKM2 at 100 times lower concentration (50 nM). At this concentration (Fig. 5D) PKM2 is mostly in the dimeric state (69.1 ± 1.9% of total oligomers), while monomers and tetramers are less prevalent (11.1 ± 3.0% and 19.8 ± 4.3%, respectively). As in the SEC experiment, the addition of **7c** led to a decrease in the dimer population in a dose-dependent manner, and at 5 μM two-fold reduction was observed (69.1 ± 1.9% vs 35.8 ± 4,0%, $p < 0.0001$). At the same time, monomer percentage was increased only at 5 μM (up to 38.0 ± 3.8%, $p = 0.0002$). Interestingly, formation of trimeric species, that could not be distinguished by the SEC, with molecular mass of approx. 180 kDa can be clearly observed (Supplementary Fig. 1). As expected, addition of FBP (100 μM) increased the amount of tetramer and trimer at the expense of the dimer (Fig. 5G). When both FBP and **7c** were added, the changes in oligomer populations became more complex, however, at 5 μM concentration, there was also almost two-fold reduction in the amount of dimer (43.2 ± 2.5% vs 23.7 ± 1.8%, $p < 0.0001$), but in this case there was an increase in the proportion of tetrameric enzyme (36.6 ± 1.5% vs 52.6 ± 3.7%, $p = 0.0004$). Both SEC and mass photometry results are in stark contrast to previously published observations that natural activators of PKM2, such as FBP and serine, promote the formation of tetramers, while PKM2 inhibitors increase the proportion of dimeric/monomeric species [32].

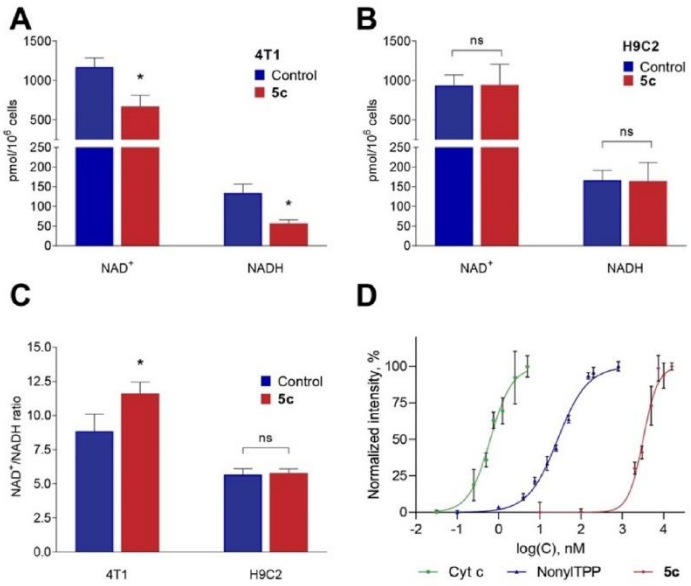

Fig. 3. NAD^+ and NADH concentrations in **(A)** 4T1 and **(B)** H9C2 cells after treatment with 1 μM **5c**. **(C)** NAD^+/NADH ratio in 4T1 and H9C2 cells after treatment with 1 μM **5c**. **(D)** Cardiolipin binding curves of cytochrome *c* (cyt *c*), nonyltriphenyphosphonium bromide (NonylTPP) and **5c** in mitoplasts isolated from rat liver. Values are shown as mean ± S.D. (n = 3–5 experiments). Statistically significant difference (*) was considered when $p < 0.05$ (Students *t*-test) compared to the control group (vehicle-DMSO).

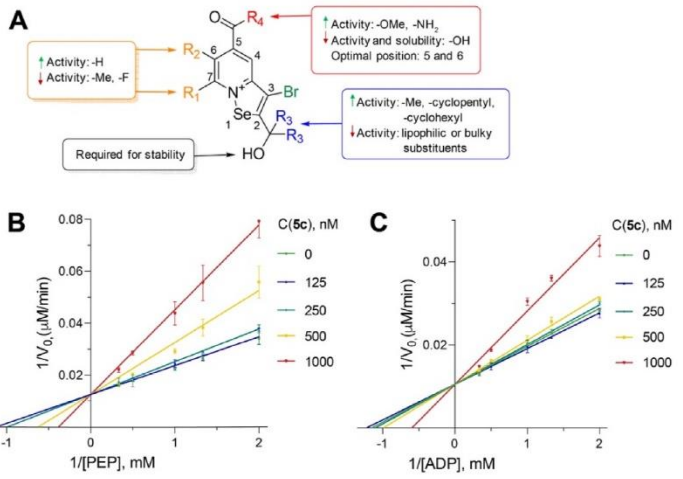

Fig. 4. (A) Structure-activity relationship for PKM2 inhibitory activity of isoselenazolopyridinium salts. (B) PKM2 initial reaction rate (V_0) with respect to PEP concentration at constant ADP concentration (2 mM) in the absence or in the presence of **5c** at different concentrations. (C) PKM2 initial reaction rate (V_0) with respect to ADP concentration at constant PEP concentration (2 mM) in the absence or in the presence of **5c** at different concentrations.

2.7. PKM2 is thermally destabilized by isoselenazolium salts

Melting temperature (T_m) of PKM2 was examined using a SYPRO Orange-based differential scanning fluorimetry (DSF) assay. PKM2 melting curves displayed a multi-modal character (Fig. 5H). Decrease in PKM2 concentration from 5 to 2.5 μM led to an increase of the low-stability species. For 2.5 μM PKM2, three distinct transitions were observed: the first in 20–40 °C range, followed by 40–50 °C, and finally a dominant transition at 60 °C. These data suggest that a mixture of species of different stabilities exist that, presumably, represent distinct oligomeric states. Alternatively, the observed species may represent different conformational states in the oligomeric assembly, such as the previously reported T- or R-states [34].

FBP has been shown to stabilize PKM2 against thermal denaturation, and our data is in a good agreement with previously published report and consistent with our mass photometry measurements [34]. FBP

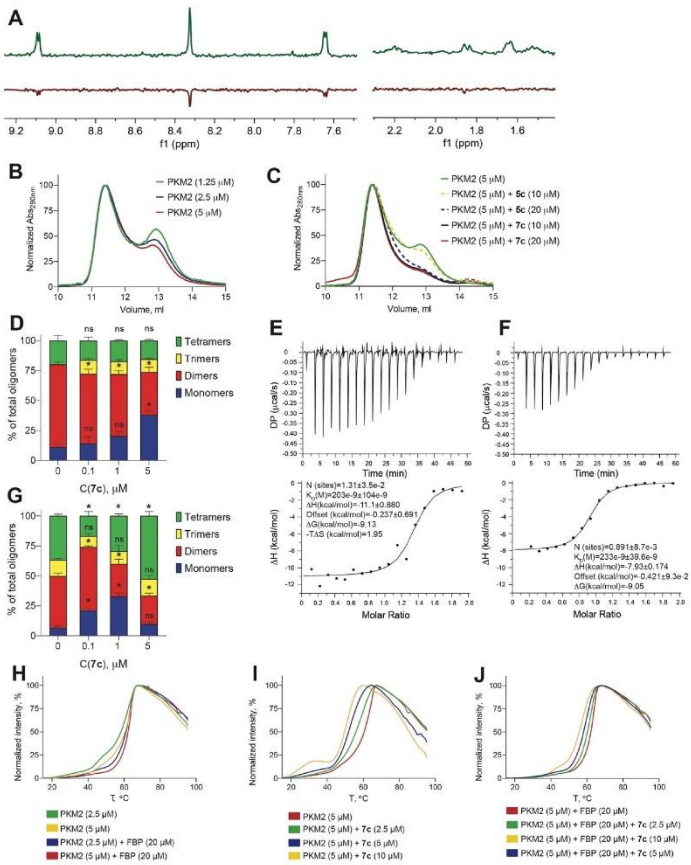

Fig. 5. (A) WaterLOGSY spectra of 250 μM **7c** alone (bottom, red) or in the presence of 12.5 μM PKM2 (top, green). (B) SEC of PKM2 at various concentrations. (C) SEC of 5 μM PKM2 preincubated with **5c** or **7c** at either 10 μM or 20 μM concentration. (D) Oligomeric state of PKM2 (50 nM) in the presence of **7c** at different concentrations revealed by mass photometry (n = 3). (E) Isotherm of PKM2 (20 μM) titration with FBP (200 μM). (F) Isotherm of PKM2 (20 μM) titration with FBP (200 μM) after pre-incubation with **7c** (40 μM). (G) Oligomeric state of PKM2 (50 nM) in the presence of FBP (100 μM) and **7c** at different concentrations revealed by mass photometry (n = 3). (H) DSF thermal melt data for PKM2 alone or in the presence of FBP. (I) DSF thermal melt data for PKM2 (5 μM) in the presence of **7c** at various concentrations. (J) DSF thermal melt data for PKM2 (5 μM) in the presence of FBP (20 μM) and **7c** at various concentrations. DSF curves are presented as a mean value of 3 independent experiments. Statistically significant difference (*) was considered when $p < 0.05$ (one-way ANOVA) compared to the control group.

decreased the population of low-stability species (Fig. 5H) but did not change the temperature at which maximum fluorescence is obtained, suggesting that FBP induced the formation of high-stability species but did not significantly stabilize the tertiary fold.

Compound **7c** destabilized PKM2 in a dose-dependent manner (Fig. 5I). Destabilization may arise as a result of a change in the oligomeric assembly or as a result of changes in the tertiary fold. At saturating concentration (10 μM), **7c** induced the formation of a significantly destabilized population which melts at 20–40 °C, that is only marginally present for PKM2 alone. In turn, FBP decreased the magnitude of destabilization induced by **7c** (Fig. 5J). Because FBP does not appear to stabilize the tertiary, but rather the quaternary structure, it is possible that **7c** and FBP induce competing conformational changes in the PKM2 oligomer. This suggestion is in line with the ITC data, which showed that FBP had a high affinity for PKM2 in the absence (Fig. 5E) and in the presence of **7c** (Fig. 5F) but had a substantially lower enthalpy of binding in the latter case, suggesting that the local interactions of FBP with the enzyme are maintained, while its effect on the quaternary structure is perturbed.

2.8. Compound 5c affects mRNA expression of PKM2 and not that of PKM1 in HCC1937 and 4T1 cells

Another way to modulate enzyme activity is to reduce its expression. The expression of PKM1 and PKM2 mRNA was evaluated by qPCR, and compound 3 k was used as a positive control [35]. Treatment of 4T1 cells with 0.25 and 0.5 μM **5c** for 24 h resulted in an approximately three-fold decrease in the expression of PKM2 mRNA with respect to untreated cells ($p < 0.001$), while the expression of PKM1 was not significantly altered (Fig. 6A and B, respectively). In case of HCC1937, treatment with 0.25 and 0.5 μM **5c** decreased the expression of PKM2 by 4 times and 20 times, respectively (Fig. 6C). At the same time, PKM1 expression was not statistically significantly reduced by **5c** (Fig. 6D), however, compound 3 k induced a three-fold decrease in PKM1 mRNA levels ($p = 0.0021$). Therefore, **5c** modulates the expression of PKM2 mRNA more effectively and selectively than compound 3 k in both studied cell lines.

3. Discussion

Here, we describe novel isoselenazolium derivatives that selectively inhibit PKM2 and exhibit a high cytotoxic effect against several cancer cell lines. The proposed mechanism of action is schematically shown in

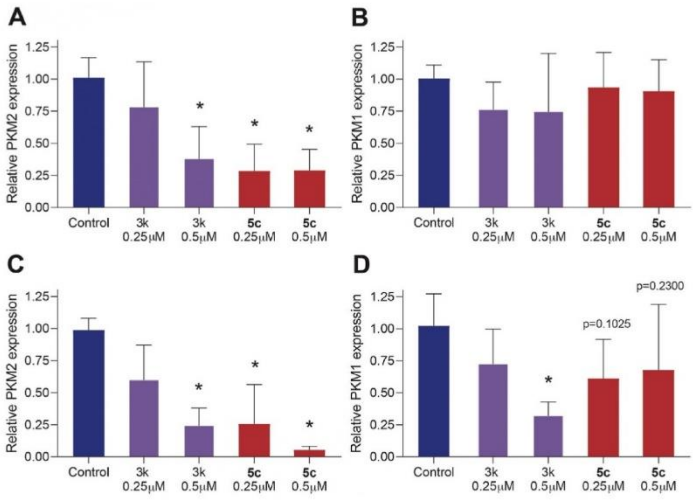

Fig. 6. Relative PKM2 mRNA expression in 4T1(A) and HCC1937 (C) cells and relative PKM1 mRNA expression in 4T1(B) and HCC1937 (D) cells obtained by qPCR after 24 h treatment with compound 3 k or **5c** at 0.25 and 0.5 μM concentrations (n = 5–7). Statistically significant difference (*) was considered when $p < 0.05$ (one-way ANOVA) compared to the control group (vehicle).

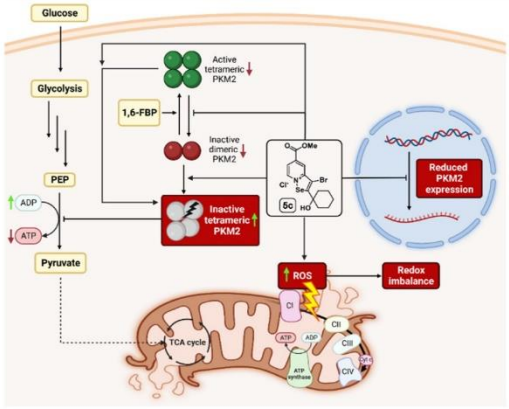

Fig. 7. Proposed mechanism of action. Compound **5c** reduces dimer/tetramer ratio of PKM2 and induces inactive conformation of both dimeric and tetrameric PKM2, thus inhibiting the production of pyruvate and ATP. **5c** causes uncoupling of complex I and OXPHOS by promoting ROS production, leading to redox imbalance. In parallel, **5c** reduces PKM2 gene expression.

Fig. 7. As PKM2 is the only enzyme producing ATP in the energy payoff phase of glycolysis, inhibition of PKM2 makes the main ATP production pathway in cancer cells unprofitable. At the same time, compound **5c** disrupts complex I and OXPHOS coupling, presumably by a drastic increase in ROS production, that should furthermore exacerbate the cellular energy crisis. Although it has been shown that PKM2 in its inactive dimeric state stimulates ROS detoxification by increasing glucose-6-phosphate flux into the pentose phosphate pathway, which provides NADPH for glutathione reductase [36], and inhibits ROS-induced apoptosis by phosphorylating and stabilizing Bcl2 [37], it does not cope with isoselenazolium induced oxidative burst. Moreover, we found that **5c** significantly decreased NAD^+ and NADH pools in 4T1 cells and had no effect on H9C2 cells. Whether it is a consequence of inhibition of PKM2 or an off-target effect remains to be discovered.

Knowing the molecular mechanism of the interaction of a ligand with a target protein can be beneficial for hit to lead optimization of a drug. Atomic-level structural methods, such as protein X-ray crystallography, provide the most detailed insight for target-based drug design, however, our attempts to obtain PKM2 co-crystals were unsuccessful. Therefore, we relied on other biochemical and biophysical methods to explore the binding mechanism of our compound series. Although isoselenazolium salts have a kinetic signature of a competitive inhibitor, it does not necessarily mean that they unequivocally bind to the active site of the enzyme. An inhibitor and a substrate could bind to different sites that negatively interfere with one another, that is, through allosteric interactions driven by inhibitor-induced conformational changes [38]. To the best of our knowledge, such competitive allosteric inhibition has been reported only a few times [39–41]. On the basis of the DSF, SEC and mass photometry data, we suggest that isoselenazolium salts inhibit PKM2 in a noncanonical fashion, inducing an unstable, functionally deficient tetrameric conformation.

Under hypoxic conditions or upon stimulation, e.g. EGFR activation, the dimeric form of PKM2 can translocate into the nucleus where it acts as a regulator for such transcription factors as HIF-1α and β-catenin, that are essential for tumorigenesis and provoke further cancer specific metabolic reprogramming [42,43]. Additionally, once in the nucleus, PKM2 functions as a protein kinase and phosphorylates STAT3, Histone H3 and Bub3, which promote proliferation and survival of cancer cells [44,45]. Reducing the amount of dimeric species may therefore be a desired feature of a PKM2 inhibitor. It has been reported that among numerous post-translational modifications PKM2 can undergo PARylation in a nucleus by PARP1. PARylation enhances nuclear retention of PKM2 and is required for proto-oncogene c-Myc and glycolysis-related GLUT and LDHA genes induction [46]. Furthermore, synergy between the PKM2 inhibitor shikonin and PARP1 inhibitor olaparib was recently shown in ovarian cancer models both *in vitro* and *in vivo* [47]. Considering the dual inhibitory activity on both PKM2 and PARP1, future research should certainly further test what impact isoselenazolium salts

have on the nuclear functions of PKM2.

4. Conclusions

We have discovered a novel series of potent and isoform-selective PKM2 inhibitors bearing a carbonyl- [1,2]isoselenazolo[2,3-*a*]pyridinium moiety. We found that unlike other PKM2 inhibitors, isoselenazolium derivatives reduce the proportion of dimeric PKM2 species and induce an unstable PKM2 conformation that results in impaired enzymatic function. Moreover, PKM2 is inhibited both at the protein and transcript level, as was shown by the reduction in PKM2 mRNA. This inhibitory activity leads to intracellular redox imbalance and, consequently, to cell death. In conclusion, these findings provide a basis for the novel class of drug candidates with a unique molecular mechanism and reveal specific structural features of PKM2. Furthermore, a potent and stable inhibitor would be an integral part of the future studies focusing on the metabolic role of PKM2 in oncogenesis.

5. Experimental section

5.1. Chemistry

5.1.1. General information

Unless otherwise stated, all reagents were purchased from commercial suppliers and used without further purification. Ultrapure water was obtained from a Milli-Q system (18.2 MΩ cm). Thin layer chromatography (TLC) was performed using MERCK Silica gel 60 F254 plates and visualized by UV (254 nm) fluorescence. ZEOCHEM silica gel (ZEOprep 60/35–70 μm – SI23501) was used for column chromatography. ^{1}H spectra were recorded on Bruker 300 or Bruker 400 spectrometer at 400 MHz, ^{13}C spectra were recorded on a Bruker 400 spectrometer at 101.3 MHz at 298 K in $CDCl_3$, CD_3OD or the mixture of thereof. The ^{1}H chemical shifts are given relatively to residual $CHCl_3$ signal (7.26 ppm) or CD_3OD (3.31 ppm), ^{13}C – relatively to $CDCl_3$ (77.16 ppm) or CD_3OD (49.0 ppm). The melting points were determined on "Optimelt", and the results are given without correction. Single crystals of 5a (CCDC 2178481), 6 b (CCDC 2178824), 5e (CCDC 2179108), and 7e (CCDC 2178826) were investigated on a Rigaku XtaLAB Synergy, Dualflex, HyPix diffractometer. 3-bromo-2-(1-hydroxycyclohexyl)- [1,2]selenazolo[2,3-a]pyridinium chloride (Se-Py) [13], 3,6-di(azetidin-1-yl)-10-(3-(trimethylsilyl)propyl)acridin-10-ium iodide (MitoCLue) [24], as well as nonyltriphenyphosphonium bromide [24] were prepared according to literature procedures. All compounds are >95% pure by HPLC analysis.

5.1.2. General procedure for the synthesis of 2a–k

Copper (I) iodide (0.05 equiv.), $(Ph_3P)_2PdCl_2$ (0.05 equiv.) and bromopyridine **1** (1 equiv.) were dissolved in DMF (10 ml for 5 mmol of **1**) and dry diisopropylamine (4 ml for 5 mmol of **1**) and flushed with Ar for 10 min. Then, solution of terminal acetylene (1.4 equiv.) in DMF (5 ml for 6.5 mmol of terminal acetylene) was added in one portion. The reaction mixture was flushed with Ar for additional 10 min and stirred at 80 °C for 5 h. Then the reaction mixture was cooled, 250 ml of EtOAc were added and precipitates were filtered off. Organic layer washed with 1% aqueous solution of ammonia (2 × 100ml), saturated NH_4Cl solution in water and saturated NaCl solution in water (both 2 × 100ml). Organic layer was collected, dried over Na_2SO_4 for 4 h filtered and evaporated under reduced pressure.

5.1.2.1. Methyl 6-((1-hydroxycyclohexyl)ethynyl)picolinate (2a). Compound **2a** (790 mg, 65%) was obtained from 1 g of methyl 6-bromopicolinate (**1a**) by re-crystallization from petroleum ether/EtOAc as white-yellow solid. ^{1}H NMR (400 MHz, $CDCl_3$) δ 8.06 (dd, *J* = 7.8, 1.1 Hz, 1H), 7.6–8.00 (m, 1H), 7.60 (dd, *J* = 7.8, 1.1 Hz, 1H), 4.00 (s, 3H), 2.08–1.98 (m, 2H), 1.93–1.46 (m, 7H), 1.39–1.24 (m, 1H). ^{13}C NMR (101 MHz, $CDCl_3$) δ 165.4, 148.4, 143.6, 137.3, 130.7, 124.3, 94.4, 83.4, 69.00, 53.2, 39.7, 25.3, 23.2. HRMS: calcd. for $C_{15}H_{18}NO_3$ $[M+H]^+$ 260.1287, found 260.1296.

5.1.2.2. Methyl 6-((1-hydroxycyclohexyl)ethynyl)nicotinate (2b). **2b** was isolated after purification of crude material by flash chromatography on silica gel (eluent: DCM/EtOAc 0–50%) as white-yellow solid (450 mg, 94%, from 400 mg of methyl 6-bromonicotinate (**1b**)). ^{1}H NMR (400 MHz, $CDCl_3$) δ 9.15 (dd, *J* = 2.2, 0.9 Hz, 1H), 8.24 (dd, *J* = 8.2, 2.2 Hz, 1H), 7.49 (dd, *J* = 8.2, 0.9 Hz, 1H), 3.95 (s, 3H), 2.10–1.98 (m, 2H), 1.82–1.51 (m, 7H), 1.37–1.19 (m, 1H). ^{13}C NMR (101 MHz, $CDCl_3$) δ 165.4, 151.1, 146.8, 137.4, 126.8, 124.9, 96.5, 83.1, 69.0, 52.7, 39.7, 25.2, 23.3. HRMS: calcd. for $C_{15}H_{18}NO_3$ $[M+H]^+$ 260.1287, found 260.1284.

5.1.2.3. Methyl 2-((1-hydroxycyclohexyl)ethynyl)isonicotinate (2c). Derivative **2c** (1.23 g, quant., from 1 g of methyl 2-bromoisonicotinate (**1c**)) was obtained by recrystallization from Et_2O/petroleum ether as white-yellow solid. ^{1}H NMR (400 MHz, $CDCl_3$) δ 8.72 (dd, *J* = 5.1, 0.9 Hz, 1H), 7.97 (dd, *J* = 1.6, 0.9 Hz, 1H), 7.77 (dd, *J* = 5.1, 1.6 Hz, 1H), 3.97 (s, 3H), 2.38–2.14 (m, 2H), 2.13–1.98 (m, 2H), 1.84–1.46 (m, 5H), 1.39–1.18 (m, 1H). ^{13}C NMR (101 MHz, $CDCl_3$) δ 165.1, 150.7, 144.1, 138.0, 126.6, 122.1, 94.8, 83.0, 69.1, 53.1, 39.8, 25.2, 23.3. HRMS: calcd. for $C_{15}H_{18}NO_3$ $[M+H]^+$ 260.1287, found 260.1291.

5.1.2.4. Methyl 2-((1-hydroxycyclobutyl)ethynyl)isonicotinate (2e). Prepared from **1c**. Crude material was purified by flash chromatography on silica gel using the mixture of petroleum ether/EtOAc (2:1) as eluent. Yield: 139 mg (33%). ^{1}H NMR (400 MHz, $CDCl_3$) δ 8.70 (dd, *J* = 5.1, 0.9 Hz, 1H), 7.95 (dd, *J* = 1.6, 0.9 Hz, 1H), 7.75 (dd, *J* = 5.1, 1.6 Hz, 1H), 3.95 (s, 3H), 3.36 (s, 1H), 2.62–2.52 (m, 2H), 2.42–2.31 (m, 2H), 1.99–1.78 (m, 2H). ^{13}C NMR (101 MHz, $CDCl_3$) δ 165.1, 150.8, 144.1, 137.9, 126.5, 122.1, 94.4, 82.2, 68.0, 53.0, 38.4, 13.1. HRMS: calcd. for $C_{13}H_{14}NO_3$ $[M+H]^+$ 232.0974, found 232.0991.

5.1.2.5. Methyl 2-((1-hydroxycyclopentyl)ethynyl)isonicotinate (2f). Prepared from **1c**. Crude material was purified by flash chromatography on silica gel using the mixture of DCM/EtOAc (10:1 → 4:1) as eluent. Yield: 350 mg (61%). ^{1}H NMR (400 MHz, $CDCl_3$) **δ** 8.69 (dd, *J* = 5.1, 0.9 Hz, 1H), 7.93 (dd, *J* = 1.6, 0.9 Hz, 1H), 7.74 (dd, *J* = 5.1, 1.6 Hz, 1H), 3.94 (s, 3H), 2.78 (s, 1H), 2.16–2.00 (m, 4H), 1.95–1.71 (m, 4H). ^{13}C NMR (101 MHz, $CDCl_3$) δ 165.1, 150.7, 144.2, 137.8, 126.4, 122.0, 94.8, 81.9, 74.6, 53.0, 42.5, 23.7.

5.1.2.6. Methyl 2-((4,4-difluoro-1-hydroxycyclohexyl)ethynyl)isonicotinate (2g). Prepared from **1c**. Crude material was purified by flash chromatography on silica gel using the mixture of petroleum ether/EtOAc (1:1) as eluent. Yield: 472 mg (69%). ^{1}H NMR (400 MHz, $CDCl_3$) **δ** 8.72 (d, *J* = 5.1 Hz, 1H), 7.95 (s, 1H), 7.80 (d, *J* = 4.3 Hz, 1H), 3.96 (s, 3H), 2.23 (s, 8H). ^{13}C NMR (101 MHz, $CDCl_3$) δ 164.88, 150.75, 143.44, 138.17, 129.15, 128.34, 126.72, 122.61, 122.54, 93.16, 82.92, 66.42, 53.11, 35.74 (t, *J* = 5.1 Hz), 30.33 (t, *J* = 24.9 Hz). HRMS: calcd. for $C_{15}H_{16}NO_3$ $[M+H]^+$ 296.1098, found 296.1103.

5.1.2.7. Methyl 2-(((1R,2S,5S)-2-hydroxyadamantan-2-yl)ethynyl)isonicotinate (2h). Prepared from **1c**. Crude material was purified by flash chromatography on silica gel using the mixture of DCM/EtOAc (8:1 → 3:1) as eluent. Yield: 454 mg (63%). ^{1}H NMR (400 MHz, $CDCl_3$) **δ** 8.71 (dd, *J* = 5.1, 0.9 Hz, 1H), 7.94 (dd, *J* = 1.6, 0.9 Hz, 1H), 7.74 (dd, *J* = 5.1, 1.6 Hz, 1H), 3.95 (s, 3H), 2.61–2.48 (m, 1H), 2.30–2.17 (m, 4H), 2.16–2.05 (m, 2H), 1.92–1.77 (m, 4H), 1.75–1.66 (m, 2H), 1.64–1.53 (m, 2H). ^{13}C NMR (101 MHz, $CDCl_3$) δ 165.2, 150.8, 144.3, 137.8, 126.5, 121.9, 95.4, 83.8, 72.9, 53.0, 38.8, 37.6, 35.7, 31.7, 27.0, 26.9. HRMS: calcd. for $C_{19}H_{22}NO_3$ $[M+H]^+$ 312.1600, found 312.1613.

5.1.2.8. Methyl 2-(3-hydroxy-3-methylhexadec-1-yn-1-yl)isonicotinate (2i). Prepared from **1c**. Crude material was re-crystallized from the mixture petroleum ether/EtOAc and kept at −20 ∘C overnight. Precipitates were collected and dried under reduced pressure. Yield: 847 mg (95%). ^{1}H NMR (400 MHz, $CDCl_3$) δ 8.72 (d, J = 5.2 Hz, 1H), 7.96 (s, 1H), 7.77 (dd, J = 5.2, 1.7 Hz, 1H), 3.96 (s, 3H), 1.82–1.73 (m, 2H), 1.60 (s, 3H), 1.60–1.50 (m, 3H), 1.41–1.17 (m, 19H), 0.87 (t, J = 6.98 Hz, 3H). ^{13}C NMR (101 MHz, $CDCl_3$) δ 165.1, 150.7, 144.1, 138.0, 126.6, 122.1, 94.9, 82.1, 68.7, 53.1, 43.6, 32.1, 29.9–29.7 (m, 8C), 29.5, 24.8, 22.8, 14.3. HRMS: calcd. for $C_{24}H_{38}NO_3$ $[M+H]^+$ 388.2852, found 388.2864.

5.1.2.9. Methyl 5-fluoro-2-((1-hydroxycyclohexyl)ethynyl)isonicotinate (2j). Prepared from methyl 2-bromo-5-fluoroisonicotinate (**1e**). Crude material was purified by flash chromatography on silica gel using the mixture of DCM/EtOAc (1:0 → 10:1) as eluent. Yield: 175 mg (59%). ^{1}H NMR (400 MHz, CD_3OD) δ 8.57 (dd, J = 2.5, 0.6 Hz, 1H), 7.88 (dd, J = 5.7, 0.5 Hz, 1H), 3.96 (s, 3H), 2.08–1.93 (m, 2H), 1.91–1.48 (m, 9H), 1.42–1.21 (m, 1H). ^{13}C NMR (101 MHz, CD_3OD) δ 163.7 (d, J = 3.3 Hz), 158.9, 156.2, 141.6 (d, J = 27.1 Hz), 140.9 (d, J = 5.8 Hz), 129.2, 127.5 (d, J = 9.7 Hz), 95.7, 82.5, 69.2, 53.6, 40.5, 26.3, 24.2. ^{19}F NMR (376 MHz, CD_3OD) δ −126.3 (d, J = 5.2 Hz). HRMS: calcd. for $C_{15}H_{17}NO_3F$ $[M+H]^+$ 278.1192, found 278.1201.

5.1.2.10. Methyl 2-((1-hydroxycyclohexyl)ethynyl)-6-methylisonicotinate (2k). Prepared from methyl 2-bromo-6-methylisonicotinate (**1f**). Crude material was purified by flash chromatography on silica gel using the mixture of DCM/EtOAc (1:0 → 1:1) as eluent. Yield: 280 mg (47%). ^{1}H NMR (400 MHz, CD_3OD) δ 7.78–7.75 (m, 1H), 7.75–7.72 (m, 1H), 3.95 (d, J = 0.8 Hz, 3H), 2.58 (s, 3H), 2.11–1.93 (m, 2H), 1.86–1.54 (m, 8H), 1.43–1.24 (m, 1H). ^{13}C NMR (101 MHz, CD_3OD) δ 166.2, 161.4, 144.3, 140.1, 124.7, 123.2, 96.0, 83.3, 69.2, 53.4, 40.6, 26.3, 24.2, 23.9. HRMS: calcd. for $C_{16}H_{20}NO_3$ $[M + H]^+$ 274.1443, found 274.1452.

5.1.3. General procedure for the synthesis of 3a–d

The solution of **2a-d** (200 mg, 0.769 mmol) in 10 ml of MeOH was treated with NaOH (153 mg, 3.844 mmol, 5 equiv.) in 5 ml of water and stirred at room temperature overnight. Then the reaction mixture was acidified by 2 N HCl to pH 2 and extracted with EtOAc (3 × 50ml). Organic layers were combined, dried over Na_2SO_4, filtered, and evaporated under reduced pressure to yield pure **3a-d**.

5.1.3.1. 6-((1-hydroxycyclohexyl)ethynyl)picolinic acid (3a). Prepared from **2a**. White solid (165 mg, 87%). ^{1}H NMR (400 MHz, CD_3OD) δ 8.09 (dd, J = 7.8, 1.1 Hz, 1H), 8.00 (dd, J = 7.8 Hz, 7.8 Hz, 1H), 7.71 (dd, J = 7.8, 1.1 Hz, 1H), 2.08–1.93 (m, 2H), 1.80–1.52 (m, 7H), 1.40–1.25 (m, 1H). ^{13}C NMR (101 MHz, CD_3OD) δ 166.8, 149.3, 144.1, 139.8, 131.8, 125.3, 96.7, 82.9, 69.2, 40.5, 26.3, 24.1. HRMS: calcd. for $C_{14}H_{16}NO_3$ $[M + H]^+$ 246.1130, found 246.1125.

5.1.3.2. 6-((1-hydroxycyclohexyl)ethynyl)nicotinic acid (3b). Prepared from **2b**. White solid (170 mg, 90%). ^{1}H NMR (400 MHz, CD_3OD) δ 9.05 (dd, J = 2.2, 0.9 Hz, 1H), 8.35 (dd, J = 8.1, 2.2 Hz, 1H), 7.61 (dd, J = 8.1, 0.9 Hz, 1H), 2.08–1.95 (m, 2H), 1.84–1.54 (m, 7H), 1.40–1.25 (m, 1H). ^{13}C NMR (101 MHz, CD_3OD) δ 167.3, 151.6, 147.4, 139.3, 128.2, 127.3, 98.2, 83.4, 69.3, 40.5, 26.3, 24.2. HRMS: calcd. for $C_{14}H_{16}NO_3$ $[M + H]^+$ 246.1130, found 246.1136.

5.1.3.3. 2-((1-hydroxycyclohexyl)ethynyl)isonicotinic acid (3c). Prepared from **2c**. White solid (165 mg, 87%). ^{1}H NMR (400 MHz, CD_3OD) δ 8.67 (dd, J = 5.1, 0.9 Hz, 1H), 7.97 (dd, J = 1.6, 0.9 Hz, 1H), 7.87 (dd, J = 5.1, 1.6 Hz, 1H), 2.03–1.98 (m, 2H), 1.82–1.56 (m, 7H), 1.41–1.28 (m, 1H). ^{13}C NMR (101 MHz, CD_3OD) δ 166.9, 151.5, 145.0, 140.9, 127.8, 123.7, 96.4, 83.3, 61.5, 40.6, 26.3, 24.2. HRMS: calcd. for $C_{14}H_{16}NO_3$ $[M + H]^+$ 246.1130, found 246.1134.

5.1.4. Synthesis of methyl-d3 2-((1-hydroxycyclohexyl)ethynyl) isonicotinate (2d)

To a suspension of **3c** (0.2 g, 0.816 mmol), HOBt hydrate (0.124 g, 0.816 mmol), CD_3OD (0.5 ml) in 3 ml of DMF EDC•HCl (0.156 g, 0.816 mmol) was added in one portion. Resulting mixture was stirred for 2 h at room temperature. Then it was poured in 50 ml of ethyl acetate and organic layer washed with saturated solution of NaCl in water (5 × 30 ml). Next, organic layer was filtered through celite pad and evaporated under reduced pressure yielding 0.15 g (70%) of **2d**. ^{1}H NMR (400 MHz, CD_3OD) δ 8.68 (dd, J = 5.1, 0.9 Hz, 1H), 7.96 (dd, J = 1.6, 0.9 Hz, 1H), 7.85 (dd, J = 5.1, 1.6 Hz, 1H), 2.08–1.94 (m, 2H), 1.91–1.48 (m, 8H), 1.44–1.23 (m, 1H). ^{13}C NMR (101 MHz, CD_3OD) δ 166.0, 151.7, 145.1, 139.9, 127.5, 123.4, 96.5, 83.2, 69.2, 40.6, 26.3, 24.2. HRMS: calcd. for $C_{15}H_{15}D_3NO_3$ $[M+H]^+$ 263.1475, found 263.1479.

5.1.5. General procedure for the preparation of 4a–g

5 ml of saturated NH_3 solution in MeOH were added to the solution of ester 2 (1 mmol) in MeOH and stirred at room temperature overnight. The reaction was monitored by LC-MS, and after full conversion solvent was removed under reduced pressure. The residue was several times dissolved in MeOH and evaporated under reduced pressure to remove excess of NH_3.

5.1.5.1. 6-((1-hydroxycyclohexyl)ethynyl)picolinamide (4a). Prepared from **2a**. Analytically pure **4a** was obtained as a white solid (242 mg, quant.). ^{1}H NMR (400 MHz, CD_3OD) δ 8.06 (dd, J = 7.8, 1.1 Hz, 1H), 7.94 (t, J = 7.8 Hz, 1H), 7.65 (dd, J = 7.8, 1.1 Hz, 1H), 2.06–1.95 (m, 2H), 1.83–1.54 (m, 7H), 1.34 (m, J = 15.1, 8.9, 5.1 Hz, 1H). ^{13}C NMR (101 MHz, CD_3OD) δ 168.5, 151.4, 143.6, 139.2, 131.0, 122.5, 95.3, 83.6, 69.3, 40.6, 26.3, 24.2. HRMS: calcd. for $C_{14}H_{17}N_2O_2$ $[M+H]^+$ 245.1290, found 245.1296.

5.1.5.2. 6-((1-hydroxycyclohexyl)ethynyl)nicotinamide (4b). Prepared from **2b**. Saturated $NaHCO_3$ solution in water was added to crude material and extracted with EtOAc (3 × 50 ml), organic layers were combined, dried over Na_2SO_4, filtered and evaporated under reduced pressure to yield pure **4b** as a white solid (200 mg, 82%). ^{1}H NMR (400 MHz, CD_3OD) δ 8.96 (dd, J = 2.3, 0.9 Hz, 1H), 8.25 (dd, J = 8.2, 2.3 Hz, 1H), 7.60 (dd, J = 8.2, 0.9 Hz, 1H), 2.05–1.94 (m, 2H), 1.82–1.55 (m, 7H), 1.39–1.26 (m, 1H). ^{13}C NMR (101 MHz, CD_3OD) δ 169.2, 149.9, 146.6, 137.6, 130.1, 128.1, 97.7, 83.3, 69.3, 40.5, 26.3, 24.2. HRMS: calcd. for $C_{14}H_{17}N_2O_2$ $[M+H]^+$ 245.1290, found 245.1296.

5.1.5.3. 2-((1-hydroxycyclohexyl)ethynyl)isonicotinamide (4c). **4c** was obtained as a white solid (154 mg, 56%, from 290 mg of 2c). ^{1}H NMR (400 MHz, CD_3OD) δ 8.63 (dd, J = 5.2, 0.9 Hz, 1H), 7.91 (dd, J = 1.7, 0.9 Hz, 1H), 7.75 (dd, J = 5.2, 1.7 Hz, 1H), 2.07–1.95 (m, 2H), 1.82–1.52 (m, 7H), 1.40–1.26 (m, 1H). ^{13}C NMR (101 MHz, CD_3OD) δ 169.0, 151.4, 144.9, 143.8, 126.3, 122.2, 96.3, 83.3, 69.3, 40.6, 26.3, 24.2. HRMS: calcd. for $C_{14}H_{17}N_2O_2$ $[M+H]^+$ 245.1290, found 245.1296.

5.1.5.4. 2-((1-hydroxy(4,4-difluoro)cyclohexyl)ethynyl)isonicotinamide (4d). Prepared from **2h**. **4e** was obtained as a white solid (160 mg, quant.). ^{1}H NMR (400 MHz, CD_3OD) δ 8.65 (dd, J = 5.2, 0.9 Hz, 1H), 7.93 (dd, J = 1.7, 0.9 Hz, 1H), 7.77 (dd, J = 5.2, 1.7 Hz, 1H), 2.22–1.97 (m, 8H). ^{13}C NMR (101 MHz, CD_3OD) δ 168.9, 151.5, 144.4, 143.8, 126.4, 122.4, 36.6 (t, J = 5.2 Hz), 31.2 (t, J = 25.0 Hz). HRMS: calcd. for $C_{14}H_{15}N_2O_2F_2$ $[M+H]^+$ 281.1102, found 281.1104.

5.1.5.5. 2-(((1R,2S,5S)-2-hydroxyadamantan-2-yl)ethynyl)isonicotinamide (4e). Prepared from **2f**. **4f** was obtained as a white solid (145 mg, 145 mg, 99%). ^{1}H NMR (400 MHz, CD_3OD) δ 8.61 (dd, J = 5.2, 0.9 Hz, 1H), 7.90 (dd, J = 1.7, 0.9 Hz, 1H), 7.73 (dd, J = 5.2, 1.7 Hz, 1H), 2.33–2.21 (m, 4H), 2.10–2.01 (m, 2H), 1.91–1.82 (m, 3H), 1.81–1.73 (m, 3H), 1.67–1.55 (m, 2H). ^{13}C NMR (101 MHz, CD_3OD) δ

168.8, 151.0, 144.9, 143.5, 126.2, 121.9, 97.2, 83.8, 73.1, 39.4, 38.6, 36.3, 32.4, 28.1, 28.0. HRMS: calcd. for $C_{18}H_{21}N_2O_2$ $[M+H]^+$ 297.1603, found 297.1616.

5.1.5.6. 2-(3-hydroxy-3-methylhexadec-1-yn-1-yl)isonicotinamide (4f). Prepared from **2i**. **4g** was obtained as a white solid (158 mg, 99%). ^{1}H NMR (400 MHz, $CDCl_3$) δ 8.57 (dd, J = 5.2, 0.9 Hz, 1H), 7.77 (dd, J = 1.8, 0.9 Hz, 1H), 7.61 (dd, J = 5.2, 1.7 Hz, 1H), 1.76–1.63 (m, 2H), 1.57–1.40 (m, 2H), 1.51 (s, 3H), 1.33–1.14 (m, 20H), 0.88–0.75 (m, 3H). ^{13}C NMR (101 MHz, $CDCl_3$) δ 167.2, 150.2, 143.8, 141.6, 125.0, 120.7, 95.6, 81.3, 67.9, 43.4, 32.0, 29.9, 29.7 (m, 5H), 29.6, 29.4, 29.1, 24.7, 22.7, 14.1. HRMS: calcd. for $C_{23}H_{37}N_2O_2$ $[M+H]^+$ 373.2855, found 373.2870.

5.1.6. General procedure for the synthesis of 5–7

To a solution of SeO_2 (4 equiv.) in 48% HBr (16 equiv.), 2, 3, or 4 (1 equiv.) in 1,4-dioxane (5 mL for 1 equiv. of 2, 3, or 4) was added and the mixture was stirred at room temperature overnight. After the consumption of a substrate (LC-MS), ether (50 ml) was added and precipitates were filtered off, dissolved in the mixture of EtOH/water (1:1) and eluted through ion-exchange resins (IRA-401) pretreated with hydrochloric acid and evaporated under reduced pressure.

5.1.6.1. 3-bromo-2-(1-hydroxycyclohexyl)-7-(methoxycarbonyl)-[1,2]selenazolo[2,3-a]pyridin-8-ium chloride (5a). **5a** was obtained by re-crystallization from MeCN (291 mg, 84%, prepared from **2a**). Melting point: 174–176 °C. ^{1}H NMR (400 MHz, CD_3OD) δ 8.68 (dd, J = 8.2, 1.7 Hz, 1H), 8.63–8.53 (m, 2H), 4.23 (s, 3H), 2.55–2.42 (m, 2H), 2.07–1.97 (m, 2H), 1.86–1.74 (m, 6H), 1.52–1.37 (m, 1H). ^{13}C NMR (101 MHz, CD_3OD) δ 180.11, 164.11, 159.46, 141.49, 139.69, 130.31, 125.20, 95.67, 79.53, 55.62, 34.77, 25.66, 21.84. ^{77}Se NMR (76 MHz, CD_3OD) δ 1247.0. HRMS: calcd. for $C_{14}H_{17}BrNO_3Se$ $[M]^+$ 417.9557, found 417.9547. HPLC: 95.9% (RT = 8.14 min, Apollo C18-13 5 μm (4.6 mm × 150 mm), mobile phase 5–95% acetonitrile + 0.1% H_3PO_4, 1 mL min^{-1}, 40 °C).

5.1.6.2. 3-bromo-2-(1-hydroxycyclohexyl)-6-(methoxycarbonyl)-[1,2]selenazolo[2,3-a]pyridin-8-ium chloride (5b). Crude product was purified by reverse phase chromatography (KP-C18-HS column, 30 g, H_2O (pH = 3)/MeCN 5–85%, the product came out at 20%) to yield **5b** (25 mg, 7%, prepared from **2b**). Melting point: 208–210 °C (decomp.). ^{1}H NMR (400 MHz, CD_3OD) δ 10.13 (dd, J = 1.6, 0.8 Hz, 1H), 8.79 (dd, J = 9.0, 1.6 Hz, 1H), 8.40 (dd, J = 9.0, 0.8 Hz, 1H), 4.05 (s, 3H), 2.51–2.39 (m, 2H), 2.06–1.97 (m, 2H), 1.89–1.65 (m, 5H), 1.51–1.38 (m, 1H). ^{13}C NMR (101 MHz, CD_3OD) δ 181.9, 164.0, 160.6, 145.6, 140.6, 126.2, 125.8, 94.9, 79.5, 53.9, 34.6, 25.6, 21.9. ^{77}Se NMR (76 MHz, CD_3OD) δ 1332.0. HRMS: calcd. for $C_{15}H_{17}NO_3BrSe$ $[M]^+$ 417.9557, found 417.9555. HPLC: 98.7% (RT = 7.61 min, Adamas C18-2 (4.6 mm × 150 mm), mobile phase 5–95% acetonitrile + 0.1% H_3PO_4, 1 mL min^{-1}, 40 °C).

5.1.6.3. 3-bromo-2-(1-hydroxycyclohexyl)-5-(methoxycarbonyl)-[1,2]selenazolo[2,3-a]pyridin-8-ium chloride (5c). **5c** was obtained by re-crystallization from MeCN (0.208 g, 60%, prepared from **2c**). Melting point: 182–184 °C (decomp.). ^{1}H NMR (400 MHz, CD_3OD) δ 9.61 (dd, J = 6.7, 0.8 Hz, 1H), 8.69 (dd, J = 1.9, 0.8 Hz, 1H), 8.09 (dd, J = 6.7, 1.8 Hz, 1H), 4.07 (s, 3H), 2.52–2.39 (m, 2H), 2.10–1.95 (m, 2H), 1.87–1.68 (m, 5H), 1.51–1.37 (m, 1H). ^{13}C NMR (101 MHz, CD_3OD) δ 180.0, 164.4, 159.4, 144.3, 141.7, 126.1, 121.2, 95.5, 79.3, 54.3, 34.7, 25.6, 21.9. ^{77}Se NMR (76 MHz, CD_3OD) δ 1212.5. HRMS: calcd. for $C_{15}H_{17}NO_3BrSe$ $[M]^+$ 417.9557, found 417.9565. HPLC: 97.4% (RT = 7.80 min, Adamas C18-2 (4.6 mm × 150 mm), mobile phase 5–95% acetonitrile + 0.1% H_3PO_4, 1 mL min^{-1}, 40 °C).

5.1.6.4. 3-bromo-2-(1-hydroxycyclohexyl)-5-((methoxy-d3)carbonyl)-[1,2]selenazolo[2,3-a]pyridin-8-ium chloride (5d). **5d** was obtained by re-crystallization from EtOAc (117 mg, 43%, prepared from **2d**). ^{1}H NMR (400 MHz, CD_3OD) δ 9.64 (dd, J = 6.7, 0.8 Hz, 1H), 8.69 (dd, J = 1.8, 0.8 Hz, 1H), 8.09 (dd, J = 6.7, 1.8 Hz, 1H), 2.51–2.40 (m, 2H), 2.02 (d, J = 14.4 Hz, 2H), 1.85–1.72 (m, 5H), 1.50–1.38 (m, 1H). ^{13}C NMR (101 MHz, CD_3OD) δ 180.0, 164.4, 159.4, 144.3, 141.7, 126.1, 121.2, 95.5, 79.3, 34.7, 25.6, 21.9. ^{77}Se NMR (76 MHz, CD_3OD) δ 1217.1. HRMS: calcd. for $C_{15}H_{14}D_3BrNO_3Se$ $[M]^+$ 420.9745, found 420.9750. HPLC: 96.1% at 210 nm, 98.4 at 254 nm (RT = 8.09 min, Apollo C18-13 5 μm (4.6 mm × 150 mm), mobile phase 5–95% acetonitrile + 0.1% H_3PO_4, 1 mL min^{-1}, 40 °C).

5.1.6.5. 1-(3-bromo-5-(methoxycarbonyl)-[1,2]selenazolo[2,3-a]pyridin-8-ium-2-yl)cyclobutan-1-olate (5e). The residue was purified by flash chromatography on Al_2O_3 using the mixture of DCM/MeOH (97:3) yielding 15 mg (5%) of **5e** (prepared from **2e**). Melting point: 75–76 °C (decomp.). ^{1}H NMR (400 MHz, CD_3OD) δ 9.10 (dd, J = 6.1, 0.9 Hz, 1H), 8.46 (dd, J = 1.7, 0.9 Hz, 1H), 7.79 (dd, J = 6.1, 1.7 Hz, 1H), 4.03 (s, 3H), 2.96–2.86 (m, 2H), 2.56–2.46 (m, 2H), 2.39–2.25 (m, 1H), 2.03–1.91 (m, 1H). ^{13}C NMR (101 MHz, CD_3OD) δ 183.1, 165.4, 158.4, 143.5, 139.9, 124.3, 119.0, 88.2, 84.1, 53.8, 36.9, 12.6. ^{77}Se NMR (76 MHz, CD_3OD) δ 1119.6. HRMS: calcd. for $C_{13}H_{13}BrNO_3Se$ $[M]^+$ 389.9239, found 389.9252. HPLC: 96.4% (RT = 7.35 min, Adamas C18-2 (4.6 mm × 150 mm), mobile phase 5–95% acetonitrile + 0.1% H_3PO_4, 1 mL min^{-1}, 40 °C).

5.1.6.6. 1-(3-bromo-5-(methoxycarbonyl)-[1,2]selenazolo[2,3-a]pyridin-8-ium-2-yl)cyclopentan-1-olate (5f). The residue was purified by flash chromatography on Al_2O_3 using the mixture of DCM/MeOH (97:3) followed by re-crystallization from MeCN. Yield: 78 mg (29%) of **5f** (prepared from **2f**). Melting point: 162–164 °C (decomp.). ^{1}H NMR (400 MHz, CD_3OD) δ 9.04 (dd, J = 6.1, 0.9 Hz, 1H), 8.37 (dd, J = 1.7, 0.9 Hz, 1H), 7.74 (dd, J = 6.1, 1.7 Hz, 1H), 4.02 (s, 1H), 2.43-2.34 (m, 2H), 2.03-1.85 (m, 6H). ^{13}C NMR (101 MHz, CD_3OD) δ 182.0, 165.3, 157.9, 143.5, 139.5, 124.0, 118.7, 91.0, 87.5, 53.8, 39.8, 25.4. ^{77}Se NMR (76 MHz, CD_3OD) δ 1117.5. HRMS: calcd. for $C_{14}H_{15}BrNO_3Se$ $[M]^+$ 403.9395, found 403.9537. HPLC: 99.4% (RT = 7.67 min, Adamas C18-2 (4.6 mm × 150 mm), mobile phase 5–95% acetonitrile + 0.1% H_3PO_4, 1 mL min^{-1}, 40 °C).

5.1.6.7. 3-bromo-2-(4,4-difluoro-1-hydroxycyclohexyl)-5-(methoxycarbonyl)-[1,2]selenazolo [2,3-a]pyridin-8-ium chloride (5g). **5g** was obtained by re-crystallization from EtOAc/MeCN (62 mg, 25%, prepared from **2g**). Melting point: 195–198 °C (decomp.). ^{1}H NMR (400 MHz, CD_3OD) δ 9.70 (dd, J = 6.7, 0.8 Hz, 1H), 8.71 (dd, J = 1.8, 0.8 Hz, 1H), 8.13 (dd, J = 6.7, 1.9 Hz, 1H), 4.07 (s, 3H). ^{13}C NMR (101 MHz, CD_3OD) δ 177.8 (d, J = 3.0 Hz), 164.3, 159.3, 144.5, 141.9, 126.2, 121.5, 96.3, 77.1, 77.1, 54.3, 31.7 (d, J = 10.1 Hz), 29.83 (t, J = 25.3 Hz). ^{19}F NMR (376 MHz, CD_3OD) δ −94.5 (d, J = 239.8 Hz), −105.1 to −106.4 (m). ^{77}Se NMR (76 MHz, CD_3OD) δ 1226.0. HRMS: calcd. for $C_{15}H_{15}BrF_2NO_3Se$ $[M]^+$ 453.9369, found 453.9389. HPLC: 99.3% (RT = 7.73 min, Adamas C18-2 (4.6 mm × 150 mm), mobile phase 5–95% acetonitrile + 0.1% H_3PO_4, 1 mL min^{-1}, 40 °C).

5.1.6.8. 3-bromo-2-((1R,2S,5S)-2-hydroxyadamantan-2-yl)-5-(methoxycarbonyl)-[1,2]selenazolo[2,3-a]pyridin-8-ium chloride (5h). Obtained by re-crystallization from EtOAc/MeCN followed by re-crystallization from MeCN/MeOH (16 mg, 11%, prepared from **2h**). ^{1}H NMR (400 MHz, $CD_3OD/CDCl_3$) δ 9.89 (d, J = 6.4 Hz, 1H), 8.89 (d, J = 1.5 Hz, 1H), 8.18–8.08 (m, 1H), 4.08 (s, 3H), 2.61–2.56 (m, 2H), 2.47–2.34 (m, 4H), 2.04–1.97 (m, 3H), 1.95–1.89 (m, 1H), 1.86–1.82 (m, 2H), 1.76–1.71 (m, 2H). ^{13}C NMR (101 MHz, $CD_3OD/CDCl_3$) δ 176.1, 163.7, 157.9, 143.7, 141.4, 127.1, 121.7, 98.9, 83.4, 54.3, 42.7, 40.2, 38.2, 35.4, 34.0, 27.8, 27.4. ^{77}Se NMR (76 MHz, $CD_3OD/CDCl_3$) δ 1246.2. HRMS: calcd. for $C_{19}H_{21}BrNO_3Se$ $[M]^+$ 469.9870, found 469.9880. HPLC: 95.1% (RT = 8.75 min, Apollo C18-15 5 μm (4.6 mm × 150 mm), mobile phase

5–95% acetonitrile + 0.1% H_3PO_4, 1 mL min^{-1}, 40 °C).

5.1.6.9. 3-bromo-2-(2-hydroxypentadecan-2-yl)-5-(methoxycarbonyl)-[1,2]selenazolo[2,3-a]pyridin-8-ium chloride (5i). The residue was purified by flash chromatography on silica gel using the mixture of DCM/EtOAc (1:1) followed by DCM/MeOH mixture (95:5). Yield: 115 mg (70%) of **5i** (prepared from **2i**). ^{1}H NMR (400 MHz, CD_3OD) δ 9.69 (dd, J = 6.7, 0.8 Hz, 1H), 8.69 (dd, J = 1.8, 0.8 Hz, 1H), 8.09 (dd, J = 6.7, 1.8 Hz, 1H), 4.07 (s, 3H), 2.41–2.29 (m, 1H), 2.03–1.92 (m, 1H), 1.83 (s, 3H), 1.71–1.56 (m, 1H), 1.42–1.21 (m, 21H), 0.93–0.84 (m, 3H). ^{13}C NMR (101 MHz, CD_3OD) δ 178.2, 164.4, 158.7, 144.5, 141.7, 126.0, 121.1, 95.8, 80.0, 54.2, 40.3, 33.1, 30.8, 30.7, 30.7, 30.61, 30.5, 30. 5, 26.4, 24.6, 23.7, 14.4. ^{77}Se NMR (76 MHz, CD_3OD) δ 1235.6. HRMS: calcd. for $C_{24}H_{37}BrNO_3Se$ $[M]^+$ 546.1117, found 546.1111. HPLC: 99.8% at 374 nm (RT = 11.06 min, Adamas C18-1 (4.6 × 150 mm), mobile phase 5–95% acetonitrile + 0.1% H_3PO_4, 1 mL min^{-1}, 40 °C).

5.1.6.10. 3-bromo-6-fluoro-2-(1-hydroxycyclohexyl)-5-(methoxycarbonyl)-[1,2]selenazolo[2,3-a]pyridin-8-ium chloride (5j). Obtained by re-crystallization from EtOAc (123 mg, 25%, prepared from **2j**). ^{1}H NMR (400 MHz, CD_3OD) δ 9.86 (dd, J = 4.6, 0.6 Hz, 1H), 8.68–8.56 (m, 1H), 4.07 (s, 3H), 2.50–2.35 (m, 2H), 2.05 (s, 2H), 1.85–1.70 (m, 5H), 1.52–1.35 (m, 1H). ^{13}C NMR (101 MHz, CD_3OD) δ 179.0 (d, J = 3.4 Hz), 162.3 (d, J = 3.8 Hz), 156.4 (d, J = 3.0 Hz), 134.3 (d, J = 41.6 Hz), 127.7, 94.5, 79.6, 54.4, 34.6, 25.6, 21.9. ^{19}F NMR (376 MHz, CD_3OD) δ −128.06 to −128.15 (m). ^{77}Se NMR (76 MHz, CD_3OD) δ 1243.9. HRMS: calcd. for $C_{15}H_{16}BrFNO_3Se$ $[M]^+$ 435.9463, found 435.9460. HPLC: 97.2% at 210 nm, 96.5% at 254 nm (RT = 2.25 min, Adamas C18-2 5 μm (4.6 × 150 mm), mobile phase 40–95% acetonitrile + 0.1% H_3PO_4, 1 mL min^{-1}, 40 °C).

5.1.6.11. 3-bromo-2-(1-hydroxycyclohexyl)-5-(methoxycarbonyl)-7-methyl-[1,2]selenazolo[2,3-a]pyridin-8-ium chloride (5k). Crude product was stirred with 20 ml of EtOAc for 1 h, then precipitates were filtered off yielding **5k** (276 mg, 59%, prepared from **2k**). ^{1}H NMR (400 MHz, CD_3OD) δ 8.63 (dd, J = 1.7, 0.7 Hz, 1H), 8.19–8.11 (m, 1H), 4.07 (s, 3H), 2.98 (t, J = 0.7 Hz, 3H), 2.51–2.43 (m, 2H), 2.09–1.98 (m, 2H), 1.85–1.72 (m, 5H), 1.53–1.39 (m, 1H). ^{13}C NMR (101 MHz, CD_3OD) δ 178.6, 164.6, 158.6, 154.8, 142.3, 123.8, 121.2, 96.6, 79.1, 54.2, 34.7, 25.6, 22.6, 22.0. ^{77}Se NMR (76 MHz, CD_3OD) δ 1160.1. HRMS: calcd. for $C_{16}H_{19}BrNO_3Se$ $[M]^+$ 431.9714, found 431.9719. HPLC: 96.5% at 223 nm, 97.6 at 254 nm (RT = 8.84 min, Adamas C18-2 (4.6 mm × 150 mm), mobile phase 5–95% acetonitrile + 0.1% H_3PO_4, 1 mL min^{-1}, 40 °C).

5.1.6.12. 3-bromo-7-carboxy-2-(1-hydroxycyclohexyl)-[1,2]selenazolo[2,3-a]pyridin-8-ium chloride (6a). Obtained by re-crystallization from EtOAc/EtOH mixture (55 mg, 19%, prepared from **3a**). Melting point: 230–232 °C (decomp.).^{1}H NMR (400 MHz, $CDCl_3/CD_3OD$) δ 8.54–8.44 (m, 3H), 2.44–2.32 (m, 2H), 2.01–1.92 (m, 2H), 1.83–1.65 (m, 5H), 1.44–1.30 (m, 1H). ^{13}C NMR (101 MHz, $CDCl_3/CD_3OD$) δ 180.5, 163.7, 157.7, 140.7, 140.5, 128.7, 123.9, 94.6, 78.7, 34.1, 24.9, 21.0. ^{77}Se NMR (76 MHz, $CDCl_3/CD_3OD$) δ 1253.5. HRMS: calcd. for $C_{14}H_{15}NO_3BrSe$ $[M]^+$ 403.9401, found 403.9401. HPLC: 98.3% (RT = 8.84 min, Adamas C18-2 (4.6 mm × 150 mm), mobile phase 5–95% acetonitrile + 0.1% H_3PO_4, 1 mL min^{-1}, 40 °C).

5.1.6.13. 3-bromo-6-carboxy-2-(1-hydroxycyclohexyl)-[1,2]selenazolo[2,3-a]pyridin-8-ium chloride (6b). The residue was purified by reverse phase chromatography (KP-C18-HS column, 30 g, H_2O (pH = 3)/MeCN 5–85%, the product came out at 21%) to yield **6b** (16 mg, 18%, prepared from **3b**). Melting point: 210–212 °C (decomp.). ^{1}H NMR (400 MHz, CD_3OD) δ 10.13 (dd, J = 1.5, 0.8 Hz, 1H), 8.79 (dd, J = 8.9, 1.5 Hz, 1H), 8.39 (dd, J = 8.9, 0.8 Hz, 1H), 2.52–2.39 (m, 2H), 2.07–1.97 (m, 2H), 1.91–1.69 (m, 5H), 1.51–1.34 (m, 1H). ^{13}C NMR (101 MHz, CD_3OD) δ 181.5, 164.6, 160.5, 145.8, 141.0, 126.7, 126.1, 94.8, 79.4, 34.6, 25.6, 21.9. ^{77}Se NMR (76 MHz, CD_3OD) δ 1222.40. HRMS: calcd. for $C_{14}H_{15}NO_3BrSe$ $[M]^+$ 403.9401, found 403.9391. HPLC: 99.5% (RT = 7.31 min, Adamas C18-2 (4.6 mm × 150 mm), mobile phase 5–95% acetonitrile + 0.1% H_3PO_4, 1 mL min^{-1}, 40 °C).

5.1.6.14. 3-bromo-5-carboxy-2-(1-hydroxycyclohexyl)-[1,2]selenazolo[2,3-a]pyridin-8-ium chloride (6c). Obtained by re-crystallization from MeCN (40 mg, 12%, prepared from **3c**). Melting point: 210–212 °C (decomp.). ^{1}H NMR (400 MHz, CD_3OD) δ 9.64 (dd, J = 6.7, 0.8 Hz, 1H), 8.70 (dd, J = 1.9, 0.8 Hz, 1H), 8.09 (dd, J = 6.7, 1.8 Hz, 1H), 2.52–2.39 (m, 2H), 2.07–1.97 (m, 2H), 1.86–1.67 (m, 5H), 1.52–1.34 (m, 1H). ^{13}C NMR (101 MHz, CD_3OD) δ 179.7, 165.0, 159.3, 144.2, 142.9, 126.2, 121.5, 95.4, 79.2, 34.7, 25.6, 21.9. ^{77}Se NMR (76 MHz, CD_3OD) δ 1215.2. HRMS: calcd. for $C_{14}H_{15}NO_3BrSe$ $[M]^+$ 403.9401, found 403.9409. HPLC: 97.9% at 210 nm, 98.1% at 254 nm (RT = 7.23 min, Apollo C18-13 5 μm (4.6 × 150 mm), mobile phase 5–95% acetonitrile + 0.1% H_3PO_4, 1 mL min^{-1}, 40 °C).

5.1.6.15. 3-bromo-7-carbamoyl-2-(1-hydroxycyclohexyl)-[1,2]selenazolo[2,3-a]pyridin-8-ium chloride (7a). **7a** was obtained by re-crystallization from MeCN (125 mg, 29%, prepared from **4a**). Melting point: 220–222 °C (decomp.). ^{1}H NMR (400 MHz, CD_3OD) δ 8.62 (dd, J = 8.4, 1.7 Hz, 1H), 8.57 (dd, J = 8.4, 7.2 Hz, 1H), 8.51 (dd, J = 7.2, 1.7 Hz, 1H), 2.55–2.42 (m, 2H), 1.88–1.68 (m, 7H), 1.52–1.36 (m, 1H). ^{13}C NMR (101 MHz, CD_3OD) δ 180.6, 164.6, 159.1, 141.2, 140.9, 129.1, 121.9, 95.4, 79.3, 34.8, 25.7, 21.8. ^{77}Se NMR (76 MHz, CD_3OD) δ 1242.8. HRMS: calcd. for $C_{14}H_{16}N_2O_2BrSe$ $[M]^+$ 402.9560, found 402.9551. HPLC: 99.4% (RT = 7.67 min, Adamas C18-2 (4.6 mm × 150 mm), mobile phase 5–95% acetonitrile + 0.1% H_3PO_4, 1 mL min^{-1}, 40 °C).

5.1.6.16. 3-bromo-6-carbamoyl-2-(1-hydroxycyclohexyl)-[1,2]selenazolo[2,3-a]pyridin-8-ium chloride (7b). The residue was purified by reverse phase chromatography (KP-C18-HS column, 30 g, H_2O (pH = 3)/MeCN 5–85%, the product came out at 17%) to yield **7b** (48 mg, 27%, prepared from 4 b). ^{1}H NMR (400 MHz, CD_3OD) δ 9.98 (dd, J = 1.6, 0.7 Hz, 1H), 8.73 (dd, J = 8.9, 1.7 Hz, 1H), 8.38 (dd, J = 8.9, 0.8 Hz, 1H), 2.51–2.39 (m, 2H), 2.07–1.97 (m, 2H), 1.86–1.67 (m, 6H), 1.51–1.36 (m, 1H). ^{13}C NMR (101 MHz, CD_3OD) δ 180.6, 166.0, 159.8, 144.3, 139.4, 129.5, 125.9, 94.6, 79.4, 34.6, 25.6, 21.9. ^{77}Se NMR (76 MHz, CD_3OD) δ 1222.3. HRMS: calcd. for $C_{14}H_{16}N_2O_2BrSe$ $[M]^+$ 402.9560, found 402.9559. Melting point: 208–210 °C (decomp.). HPLC: 97.7% (RT = 6.60 min, Adamas C18-2 (4.6 mm × 150 mm), mobile phase 5–95% acetonitrile + 0.1% H_3PO_4, 1 mL min^{-1}, 40 °C).

5.1.6.17. 3-bromo-5-carbamoyl-2-(1-hydroxycyclohexyl)-[1,2]selenazolo[2,3-a]pyridin-8-ium chloride (7c). Obtained by re-crystallization from MeCN (58 mg, 19%, prepared from **4c**). Melting point: 205–207 °C (decomp.). ^{1}H NMR (400 MHz, CD_3OD) δ 9.59 (dd, 0H), 8.68 (dd, J = 1.9, 0.8 Hz, 1H), 8.02 (dd, J = 6.7, 1.9 Hz, 1H), 2.57–2.34 (m, 2H), 2.14–1.98 (m, 2H), 1.87–1.67 (m, 6H), 1.56–1.32 (m, 1H). ^{13}C NMR (101 MHz, CD_3OD) δ 179.4, 166.7, 159.3, 145.8, 144.0, 124.6, 120.6, 95.3, 79.3, 34.7, 25.6, 22.0. ^{77}Se NMR (76 MHz, CD_3OD) δ 1213.0. HRMS: calcd. for $C_{14}H_{16}N_2O_2BrSe$ $[M]^+$ 402.9560, found 402.9564. HPLC: 99.5% (RT = 6.34 min, Adamas C18-2 (4.6 mm × 150 mm), mobile phase 5–95% acetonitrile + 0.1% H_3PO_4, 1 mL min^{-1}, 40 °C).

5.1.6.18. 3-bromo-5-carbamoyl-2-(4,4-difluoro-1-hydroxycyclohexyl)-[1,2]selenazolo[2,3-a]pyridin-8-ium chloride (7d). **7d** was obtained by re-crystallization from MeCN (63 mg, 24%, prepared from **4d**). Melting point: 192–195 °C (decomp.). ^{1}H NMR (400 MHz, CD_3OD) δ 9.63 (dd, J = 6.8, 0.8 Hz, 1H), 8.71 (dd, J = 1.9, 0.8 Hz, 1H), 8.06 (dd, J = 6.7, 1.9 Hz, 1H), 2.87–2.72 (m, 2H), 2.31-2.14 (s, 6H). ^{13}C NMR (101 MHz, CD_3OD) δ 177.2, 166.5, 159.2, 146.0, 144.2, 124.8, 120.9, 96.1, 77.1, 31.7 (d, J = 10.2 Hz), 29.8 (t, J = 25.3 Hz). ^{19}F NMR (376 MHz, CD_3OD)

δ −94.48 (d, J = 239.5 Hz), −105.40 to −106.2 (two m). ^{77}Se NMR (76 MHz, CD_3OD) δ 1222.2. HRMS: calcd. for $C_{14}H_{14}BrF_2N_2O_2Se$ $[M]^+$ 438.9372, found 438.9371. HPLC: 95.4% (RT = 6.59 min, Apollo C18-15 5 μm (4.6 mm × 150 mm), mobile phase 5–95% acetonitrile + 0.1% H_3PO_4, 1 mL min^{-1}, 40 °C).

5.1.6.19. 3-bromo-5-carbamoyl-2-((1R,2S,5S)-2-hydroxyadamantan-2-yl)-[1,2]selenazolo[2,3-a]pyridin-8-ium chloride (7e). Obtained by re-crystallization from MeCN/EtOAc (124 mg, 53%, prepared from **4e**). ^{1}H NMR (400 MHz, CD_3OD) δ 9.57 (dd, J = 6.7, 0.8 Hz, 1H), 8.82 (dd, J = 2.0, 0.8 Hz, 1H), 8.05 (dd, J = 6.8, 2.0 Hz, 1H), 2.69–2.62 (s, 2H), 2.43–2.42 (m, 2H), 2.14–1.73 (m, 10H). ^{13}C NMR (101 MHz, CD_3OD) δ 184.1, 168.7, 157.7, 143.5, 141.8, 123.8, 118.2, 92.1, 89.2, 41.0, 39.6, 39.6, 35.5, 35.4, 28.3, 28.1. ^{77}Se NMR (76 MHz, CD_3OD) δ 1283.4. HRMS: calcd. for $C_{18}H_{20}BrN_2O_2Se$ $[M]^+$ 454.9868, found 454.9890. HPLC: 95.8% (RT = 7.36 min, Apollo C18-15 5 μm (4.6 mm × 150 mm), mobile phase 5–95% acetonitrile + 0.1% H_3PO_4, 1 mL min^{-1}, 40 °C).

5.1.6.20. 3-bromo-5-carbamoyl-2-(2-hydroxypentadecan-2-yl)-[1,2]selenazolo[2,3-a]pyridin-8-ium chloride (7f). Obtained by re-crystallization from MeCN/EtOAc (75 mg, 33%, prepared from **4f**). Melting point: 128–130 °C. ^{1}H NMR (400 MHz, CD_3OD) δ 9.64 (dd, J = 6.7, 0.8 Hz, 1H), 8.73–8.65 (m, 1H), 8.03 (dd, J = 6.7, 1.9 Hz, 1H), 2.42–2.30 (m, 1H), 2.03–1.91 (m, 1H), 1.83 (s, 3H), 1.70–1.57 (m, 1H), 1.41–1.21 (m, 21H), 0.94–0.84 (m, 3H). ^{13}C NMR (101 MHz, CD_3OD) δ 177.4, 166.6, 158.6, 145.8, 144.1, 124.6, 120.6, 95.8, 79.9, 40.3, 33.1, 30.8, 30.7, 30.7, 30.6, 30.5, 30.5, 26.4, 24.6, 23.7, 14.4. ^{77}Se NMR (76 MHz, CD_3OD) δ 1234.4. HRMS: calcd. for $C_{23}H_{36}BrN_2O_2Se$ $[M]^+$ 531.1120, found 531.1136. HPLC: 95.06% at 221 nm, 96.5% at 365 nm (RT = 8.66 min, Adamas C18-1 (4.6 mm × 150 mm), mobile phase 5–95% acetonitrile + 0.1% H_3PO_4, 1 mL min^{-1}, 40 °C).

5.2. Cell culture

MCF-7 (human breast adenocarcinoma), HCC1937 (human breast carcinoma), MDA-MB-231 (human breast adenocarcinoma), 4T1 (mouse carcinoma), A549 (human lung adenocarcinoma), Jurkat (human leukemic T cells) and H9C2 (rat cardiomyoblasts) were obtained from the American Type Culture Collection [ATCC] collection for use in the current study. Cell lines were cultured at 37 °C and 5% CO_2 in Dulbecco's modified Eagle's medium (DMEM) or Roswell Park Memorial Institute (RMPI-1640) in Jurkat case, containing 10% fetal bovine serum (FBS) and 1% Pen/Strep according to recommendations.

5.3. Cytotoxicity assay

Cell viability was assessed by the addition of 3-(4,5-dimethylthiazol-2-yl)-2,5-diphenyltetrazolinium bromide (MTT). Briefly, cells were seeded (5 × 10^3 cells per well) in 96-well plates and allowed to attach for 24 h. Solutions of test compounds were prepared and serially diluted to obtain the appropriate concentrations. The cells were treated with test compounds at different concentrations (0.041–100 μM) and incubated for 48 h at 37 °C and 5% CO_2. Then, the culture medium was removed, and medium containing 1 mg/ml MTT was added. After 1 h (37 °C, 5% CO_2), the MTT-containing medium was removed, and 100 μL of isopropanol was immediately added to each sample. The optical density was assessed at 570/650 nm (Hidex Sense microplate reader, Hidex Finland). Jurkat cells were seeded at density 10 × 10^3 cells per well and were treated with the test compounds 2 h after seeding. To assess cell viability, Jurkat cells were further incubated with alamarBlue® (Bio-Rad Laboratories, Hercules, California, USA). After 2 h, fluorescence (Ex 544 nm/Em 590 nm) was measured using Hidex Sense microplate reader (Hidex, Finland). The half-maximal inhibitory concentration (IC_{50}) of each compound was calculated using GraphPad Prism® 8.0 (GraphPad, Inc., La Jolla, USA).

5.4. High-resolution fluorespirometry

High-resolution respirometry was performed using Oxygraph-2k system (OROBOROS INSTRUMENTS, Austria). All experiments were performed at 37 °C in MiR05 medium (110 mM sucrose, 60 mM K-lactobionate, 0.5 mM EGTA, 3 mM $MgCl_2$, 20 mM taurine, 0.1% BSA essentially fatty acid free, 10 mM KH_2PO_4, 20 mM HEPES, pH 7.1). The medium was reoxygenated when the oxygen concentration dropped to 80 μM. First, cells (5 × 10^5/ml or 7.5 × 10^5/ml) were placed in a chamber and permeabilized with saponin (50 μg/ml) for 10 min. Then, pyruvate (5 mM) and malate (2 mM) were used to determine complex I (CI)-linked LEAK respiration. Compound **5c** (1 μM) was added to permeabilized cells in the LEAK state after the addition of pyruvate and malate. After that, ADP (5 mM) was added to determine the oxidative phosphorylation-dependent respiration (OXPHOS state). Then glutamate (10 mM) was added to support CI-dependent respiration. Succinate (10 mM, complex II (CII) substrate) was added sequentially to reconstitute convergent CI&II-linked respiration. To determine electron transfer (ET) capacity, an uncoupler, carbonyl cyanide-p-trifluoromethoxyphenylhydrazone (CCCP), was titrated in 0.5 μM steps until the maximal respiration rate was reached. Then, rotenone (0.5 μM, an inhibitor of CI) and antimycin A (2.5 μM, an inhibitor of complex III) were added to determine CII-linked ET capacity and residual oxygen consumption (ROX), respectively. Flux control factors were calculated as described by Gnaiger et al. [3] H_2O_2 flux was simultaneously measured by the O2k-Fluorometer module using the H_2O_2-sensitive probe Amplex Red (AmR) as previously described [4]. Briefly, generation of the superoxide anion $O2^{\bullet-}$ was estimated as the release of H_2O_2 monitored fluorometrically by the Amplex Red/-horseradish peroxidase system, whereby Amplex Red (non-fluorescent) becomes oxidized to Resorufin (fluorescent). The assay medium was supplemented with Amplex Red (5 μM), horseradish peroxidase (2 U/ml) and Cu,Zn-superoxide dismutase (2 U/ml) for quantitative conversion of released $O2^{\bullet-}$ into H_2O_2. Resorufin fluorescence was monitored at 590 nm (λ_{Exc} = 560 nm). The system was calibrated by additions of known quantities of H_2O_2.

5.5. Measurement of NAD^+ and NADH concentrations

4T1 or H9C2 cells (2 × 10^5 cells per well) were seeded in a 24-well plate. After 24 h, cells were treated with **5c** (1 μM) for 20 min in triplicate. Then, the cells were washed with PBS, counted (trypan blue, using LUNA-FL™ dual fluorescence cell counter Logos biosystems, South Korea), detached with trypsin and transferred into Eppendorf tubes. After that, the cells were centrifuged at 1000 *g* for 5 min at 4 °C, washed with PBS and centrifuged again. Then the cells were resuspended in 400 μL of extraction buffer provided in NAD+/NADH Quantitation Kit (Sigma-Aldrich, cat. # MAK037) and homogenized by sonication on ice (30% amplitude, 5 s pulse, 15 s pause, 5 cycles). Obtained samples were vortexed for 10 s and centrifuged at 13000 *g* for 10 min at 4 °C with 10 kDa cut-off spin filter. 50 μL of a sample were used in the assay for total NAD^+ detection according to the kit manufacturer's protocol. 125 μL of the sample were transferred to an Eppendorf and heated to 70 °C on a water bath for 30 min to decompose NAD^+. Then, the samples were cooled on ice and 50 μL were used for NADH detection according to kit manufacturer's protocol. The measurements were done in duplicate for every sample. NAD^+ concentration was calculated as NAD_{total} – NADH. The ratio of NAD^+/NADH in a sample was determined by the following equation: $NAD^+/NADH = (NAD_{total} - NADH)/NADH$. Statistically significant differences in the mean values were evaluated using unpaired Student's *t*-test. The differences were considered significant when $p < 0.05$. Statistical analysis was carried out using GraphPad Prism 8.0 (GraphPad, Inc., La Jolla, USA).

5.6. Cardiolipin competitive binding studies

Competitive binding experiment was carried out as previously described [2]. Briefly, a liver of a healthy Sprague Dawley rat was homogenized on ice in 1:10 (w/v) medium containing 180 mM KCl, 10 mM Tris and 1 mM EGTA (pH 7.7 at 4 °C) using Teflon glass homogenizer. Mitoplasts were isolated from rat liver homogenates by differential centrifugation as described elsewhere and were frozen until the analysis. 10 mM stock solution of 3,6-di(azetidin-1-yl)-10-(3-(trimethylsilyl)propyl)acridin-10-ium iodide (MitoCLue) was made in DMSO and diluted to 50 μM with 20 mM HEPES buffer, pH = 6.8. Before carrying out a competitive binding experiment on isolated mitoplasts, MitoCLue was titrated with mitoplasts from each batch to determine the optimal volume of mitoplast solution to saturate 5 μM probe solution. The assay was carried out in a black 96-well microplate in 20 mM HEPES buffer, pH = 6.8. A mitoplasts solution was titrated in triplicate with a ligand and mixed gently with a micropipette. Additionally, mitoplasts without a ligand were also placed in triplicate (vehicle). Cytochrome *c* (Sigma-Aldrich, Cytochrome *c* from equine heart, cat. #C7752) and nonyltriphenyphosphonium bromide were used as positive controls. Next, a 96-well plate was incubated in a plate shaker with a thermostat for 10 min (500 RPM, 37 °C). Then, an appropriate amount of MitoCLue 50 μM stock solution was added to the wells (the final concentration of MitoCLue was 5 μM) and mixed gently with a micropipette. Next, the plate was additionally incubated for 15 min in a plate shaker with a thermostat (500 RPM, 37 °C), and the fluorescence intensity was measured using a Tecan Infinite 1000 microplate reader (Tecan Austria GmbH, Salzburg, Austria) at excitation and emission wavelengths of 497 and 529 nm, respectively. The obtained data were analyzed with GraphPad Prism® 8.0 (GraphPad, Inc., La Jolla, USA). The fluorescence intensity was normalized by setting mitoplasts with MitoCLue (vehicle) as 0% and the maximal effect of the ligand as 100%. Normalized fluorescence intensity was plotted against the concentration of the ligand on a logarithmic scale and fit with a 4 PL model to calculate EC_{50} values.

5.7. Screening on metabolic enzyme panel and bcls

Screening was performed by BPS Bioscience (San Diego, USA) according to the standard biochemical assay procedures with relevant reference controls.

5.8. Pyruvate kinase activity assay

Pyruvate kinase (PK) activity was measured by a coupled enzyme system with lactate dehydrogenase (LDH) in which the pyruvate produced by PK was reduced to lactate with the concomitant oxidation of NADH to NAD. The test was conducted at room temperature (approx. 22 °C) in a solution containing 50 mM Tris (pH 7.4), 10 mM $MgCl_2$, 100 mM KCl, 2 mM ADP, 5 units of lactate dehydrogenase (LDH, Sigma-Aldrich, cat. # 427217-M), 0.4 mM NADH, 1.75 nM PK (PKM2, BPS Bioscience, cat. #50295, PKM1, BPS Bioscience, cat. #40502, PKR, BPS Bioscience, cat. #40500) and the test compounds at different concentrations (0–10 μM). After 10 min incubation, the reaction was initiated with 1 mM PEP (the final reaction volume was 200 μl). The reaction progress was monitored by the decrease in the absorbance at 340 nm at 37 °C for 20 min (Hidex Sense microplate reader, Hidex Finland). Negative control experiments contained no PK. For additional experiments, where PKM2 activation was desired, 250 μM FBP (Sigma-Aldrich, cat. #F0752) was added. The half-maximal inhibitory concentration (IC_{50}) of each compound was calculated by plotting inhibition % against the concentration of the ligand on a logarithmic scale and fitting with a 4 PL model using GraphPad Prism® 8.0 (GraphPad, Inc., La Jolla, USA).

5.9. Measurement of PKM2 steady-state kinetics

Steady-state kinetic measurements of PKM2 were performed using a Hidex Sense microplate reader (Hidex Finland). Initial velocities for the forward reaction were measured using a coupled reaction with lactate dehydrogenase as described above. First, calibration curve for NADH (0–0.5 mM) was obtained in the reaction buffer in the absence of PKM2. Initial reaction velocity versus substrate concentrations were measured by the decrease in absorbance at 340 nm at 37 °C in the absence or in the presence of 5c, in a reaction buffer containing 50 mM Tris (pH 7.4), 10 mM $MgCl_2$, 100 mM KCl, 1.75 nM PKM2, 0.4 mM NADH, 2 mM ADP and 5 units of LDH. Reactions were initiated by adding PEP at a desired concentration (0–3 mM) in a total reaction volume of 200 μL per well. Analogues experiment was carried out with respect to ADP, when PEP concentration was kept constant (1 mM), and ADP concentration was varied from 0 to 3 mM. The experiments were carried out in triplicate. Kinetic constants were determined by fitting initial velocity curves to Michaelis-Menten steady-state kinetic model using GraphPad Prism® 8.0 (GraphPad, Inc., La Jolla, USA).

5.10. LDH activity assay

LDH activity assay was performed in a solution containing 50 mM Tris (pH 7.4), 100 mM KCl, 10 mM $MgCl_2$, 0.5 mM NADH, 5 units of LDH and 1 μM of the tested compounds. After 10 min incubation at room temperature, the reaction was initiated by the addition of pyruvate (5 mM final concentration) and the reaction progress was monitored by the decrease in the absorbance at 340 nm at 37 °C for 10 min (Hidex Sense microplate reader, Hidex Finland).

5.11. PARP1 activity assay

PARP1 activity was evaluated using PARP1 chemiluminescent assay kit (BPS Bioscience, cat. # 80551) according to the manufacturer's instructions.

5.12. Protein expression and purification

The PKM2 synthetic gene fragment was prepared by Twist Bioscience (California, US) using the canonical PKM2 protein sequence (Uniprot P14618-1) as template for DNA codon-optimization for expression in *E. coli*. The synthetic gene was cloned into a pEXP-GB1 expression vector (Addgene #112565) containing an N-terminal His 8-tag fused to a GB1 solubility enhancing tag, followed by a TEV protease cleavage site. The expression plasmid was transformed into chemi-competent *E. coli* strain T7Express (New England Biolabs, #C2566H) and the cells were used to inoculate 4 L of 2xYT medium supplemented with 100 μg/ml ampicillin. Cells were grown at 37 °C with shaking at 200 RPM until an OD_{600} = 0.7–1.0, after which they were cooled down to 18 °C and overnight expression was induced with 500 μM IPTG. Next day, cells were collected by centrifugation, resuspended in lysis buffer (50 mM Tris pH 8.0, 500 mM NaCl, 10% glycerol, 20 mM Imidazole) and lysed by sonication. The lysate was applied on a HisTrap HP 5 ml column (Cytiva) pre-equilibrated with IMAC buffer A (50 mM Tris pH 8.0, 500 mM NaCl, 10% glycerol, 20 mM Imidazole). The column was then washed with 8 CV IMAC buffer A, and the protein was eluted with IMAC buffer B (50 mM Tris pH 8.0, 500 mM NaCl, 200 mM Imidazole). Protein-containing fractions were pooled and concentrated on an Amicon 10 kDa MWCO spin concentrator (Merck Millipore), after which the protein was applied on a Superdex 200 16/600 size exclusion column (Cytiva) pre-equilibrated with SEC buffer (20 mM HEPES pH 7.5, 300 mM NaCl). PKM2 eluted at 60–70 ml volume and peak fractions were collected, concentrated to ~20 mg/ml and flash-frozen for long-term storage.

5.13. Analytical size-exclusion chromatography (SEC)

PKM2 was buffer-exchanged into analytical size-exclusion chromatography (SEC) buffer (50 mM Tris pH 8.0, 150 mM KCl, 10 mM $MgCl_2$) on a NAP-5 desalting column (Cytiva). A Superdex 200 10/300 SEC

column was equilibrated with the same buffer. PKM2 was diluted to the desired final concentration and incubated with **5c**, **7c** or DMSO control. Final DMSO concentration was 1% in all measurements. 300 μL of each sample was applied on the SEC column and eluted at 0.7 ml min^{-1} flow rate. The absorbance values (mAU) at 280 nm were normalized against the early-eluting, highest peak corresponding to the tetrameric species.

5.14. Differential scanning fluorimetry

DSF reactions were set up in DSF buffer (50 mM Tris pH 8.0, 150 mM KCl, 10 mM $MgCl_2$), containing 10 μM protein, 10x SYPRO orange dye (ThermoFisher). 25 μL reactions were set up in in triplicates, in a 96-well PCR plate (Sarstedt #72.1979.202). Additionally, FBP and/or **7c** were included in the reactions. Thermal denaturation was measured over a 15–95.3 °C temperature range, with a 2% per min gradient, on a Prism 7500 real-time PCR system (Applied Biosystems) using the ROX filter set. Melt curves were fitted with a web implementation of the MTSA software [5], using a Sigmoid-5 model with T_m value at the mid-point. Normalized fluorescence values were plotted with GraphPad Prism 8.0 (GraphPad, Inc., La Jolla, USA).

5.15. WaterLOGSY experiment

NMR samples were prepared in 18 mM Tris pH 8.0, 90 mM KCl, 9 mM $MgCl_2$, 10% D_2O, 0.25% DMSO-d_6. **7c** was analyzed either alone at 250 μM or pre-incubated with 10 μM PKM2. NMR experiments were performed at 298 K on a 600 MHz Bruker Avance Neo 600 spectrometer equipped with an HCN triple-resonance pulsed-field-gradient cryoprobe. Water-LOGSY experiments were collected in 256 scans using a mixing time of 2 s, a 20 ms trim pulse to suppress protein signals, and water suppression using excitation sculpting with gradients.

5.16. Single-molecule mass photometry

The mass photometry experiments were carried out on TwoMP instrument (Refeyn, UK) at room temperature, i.e. approx. 21 °C. Microscope coverslips (High Precision 24 × 50 mm, Marienfeld Superior) were prepared by rinsing them successively with isopropanol and Milli-Q water and drying under a stream of clean nitrogen. The high concentration protein stocks were buffer exchanged on PD Sephadex SpinTrap G-25 column (Sigma) to fresh and degassed PBS buffer.

Standard protein solutions of Bovine serum albumin (BSA), Immunoglobulin G (IgG), and triglobulin protein (Tg) were used to generate the mass calibration of the contrast intensity to mass values. Mass photometry data was acquired with 10.9 μm × 4.3 μm instrument field of view and collected for 60 s at a 50 Hz frame rate on a 46.3 $μm^2$ detection area. At least 5×10^3 particles were detected in each acquisition. A series of solutions containing PKM2 and **7c** (0.1, 1, and 5 μM) in the absence or presence of 100 μM FBP were incubated for approximately 10 min before being loaded into the well on the coverslip. PKM2 and **7c** solution was mixed with the PBS buffer in 1:1 drop ratio to obtain samples of 50 nM total protein concentration. The PBS buffer was supplemented with appropriate concentration of **7c** and FBP to prevent additives dilution during the measurement.

The resulting video data was analyzed using DiscoverMP software provided by the instrument manufacturer (Refeyn, UK). Raw contrast values were converted to molecular mass using the standard mass calibration, and binding events combined in 5.8 kDa bin width. Quantification of oligomer populations was achieved by integrating the peaks around the assumed size of the respective oligomer species and by calculation according to the total binding events or PKM2 population. Statistics were obtained from triplicate measurements of counts obtained for each oligomer population. Statistically significant differences in the mean values were evaluated using one-way ANOVA followed by Dunnett's test. The differences were considered significant when $p < 0.05$. Statistical analysis was carried out using GraphPad Prism 8.0 (GraphPad, Inc., La Jolla, USA).

5.17. Isothermal titration calorimetry (ITC)

Purified PKM2 was buffer-exchanged into ITC buffer (20 mM HEPES pH 7.4, 150 mM KCl, 10 mM $MgCl_2$) on a NAP-5 desalting column (Cytiva) and diluted in the same buffer to 40 μM. **7c** was diluted in DMSO to a concentration of 10 mM and then further diluted in ITC buffer to 80 μM. For preparing cell solution, equal volumes of PKM2 and **7c** solutions were then mixed, resulting in final concentrations of 40 μM and 20 μM for **7c** and PKM2, respectively. Alternatively, ligand-free cell solution was prepared by mixing PKM2 solution with ITC buffer supplemented with 0.8% DMSO. Syringe solution was prepared by diluting FBP to 200 μM in ITC buffer supplemented with 0.4% DMSO. All solutions were degassed by applying low vacuum and then kept on ice prior measurement. The same syringe solution was used for both measurements to minimize stoichiometry differences due to pipetting error. Titrations were performed on a PEAQ ITC instrument (Malvern Pananalytical, UK) using the following settings: 25 °C, DP = 5 μcal/s, 750 rpm stirring speed 18 × 2 μl injections. Thermograms were integrated and isotherms fitted using the ITC analysis software provided by the manufacturer (Malvern Pananalytical, UK).

5.18. Quantitative PCR

The effect of compound **5c** on PKM1 and PKM2 mRNA expression in 4T1 and HCC1937 cells was determined using quantitative PCR (qPCR) analysis. 4T1 and HCC1937 cells were seeded in a 24-well plate at a density of 1×10^5 cells per well and incubated with compound 3 k (BLDpharm, cat. #94164-88-2) or compound **5c** (0.25 μM and 0.5 μM final concentration) for 24 h. Total RNA from cells was isolated using Ambion PureLink RNA Mini Kit according to the manufacturer's protocol. First-strand cDNA synthesis was performed using the High-Capacity cDNA Reverse Transcription Kit (Applied BiosystemsTM, Foster City, CA, USA) following the manufacturer's instructions. The qPCR analysis of gene expression was performed using SYBR Green Master Mix (Applied BiosystemsTM) on a Bio-Molecular Systems MIC qPCR Cycler according to the manufacturer's protocol and using the following conditions: 95.0 °C for 10 min, [95.0 °C for 15 s, 60 °C for 60 s] (60 cycles), 95.0 °C for 60 s, followed by melt curve analysis from 72.0 to 95.0 °C, 0.3 °C/s. The relative expression levels for PKM1 and PKM2 genes were calculated using ΔΔCt method and normalized to the expression of the β-actin gene. Data are presented as the mean ± SD. Shapiro-Wilk normality test of the data was performed and statistically significant differences in the mean values were evaluated using one-way ANOVA followed by Dunnett's test. The differences were considered significant when $p < 0.05$. Statistical analysis was carried out using GraphPad Prism 8.0 (GraphPad, Inc., La Jolla, USA). Primers were designed using Primer-BLAST tool. The primers were as follows:

Gene	Forward primer sequence	Reverse primer sequence
h-PKM1	CGAGCCTCAAGTCACTCCAC	GTGAGCAGACCTGCCGACT
h-PKM2	ATTATTTGAGGAACTCCGCCGCCT	ATTCCGGGTCACAGCAATGATGG
h-β-actin	GCCGTTCCGAAAGTTGCC	ATCATCATCCATGGTGAGCTGG
m-PKM1	CGAGCCTCCAGTCACTCCAC	GTGAGCACTCCTGCCAGACT
m-PKM2	GCTATTCGAGGAACTCCGCCGCCT	ATTTCGAGTCACGGCAATGATAG
m-β-actin	CCTCTATGCCAACACAGTGC	CATCGTACTCCTGCTTGCTG

Author Contributions

P. A. led the project, P.A., P. D., M.M.K., T.P. designed the research. P.A. and P.D. synthesized isoselenazolium derivatives. P.D. and M.M.K. guided cytotoxicity studies and performed high resolution fluorespirometry. P.D. made NAD+/NADH measurements and cardiolipin binding studies. M.M.K and P.D performed isoselenazolium enzymatic screening. P.D. determined steady-state-kinetic parameters for PKM2. T.

P. performed size-exclusion chromatography of PKM2, WaterLOGSY experiments, differential scanning fluorimetry of PKM2, and isothermal titration calorimetry. mRNA expression studies were designed by P.D. A. B. and M.H. performed mass photometry studies. P.A., P.D. and T.P. wrote the manuscript with support and contributions from all authors.

Declaration of competing interest

The authors declare the following financial interests/personal relationships which may be considered as potential competing interests: Pavel Arsenyan, Pavels Dimitrijevs, Marina Makrecka-Kuka has patent pending to The rights belongs to Latvian Institute of Organic Synthesis.

Data availability

Data will be made available on request.

Acknowledgement

This work was supported by ERDF project Nr.1.1.1.1/19/A/016. Dr. Teodors Pantelejevs was supported by ERDF project Nr. 1.1.1.5/21/A/002. Liver tissue samples of healthy Sprague Dawley rats were kindly provided by LIOS Laboratory of Pharmaceutical Pharmacology (Prof. M. Dambrova). Authors would like to sincerely thank Dr. S. Belyakov for X-ray analysis and LIOS Laboratory of Biotechnology (Prof. E. Parisini) for the permission to use equipment to produce PKM2 enzyme. Graphical abstract and Fig. 7 were created with BioRender.com.

Appendix A. Supplementary data

Supplementary data to this article can be found online at https://doi.org/10.1016/j.ejmech.2023.115504.

References

[1] M. Upadhyay, J. Samal, M. Kandpal, O.V. Singh, P. Vivekanandan, The Warburg effect: insights from the past decade, Pharmacol. Ther. 137 (2013) 318–330, https://doi.org/10.1016/j.pharmthera.2012.11.003.
[2] J. Fan, J.J. Kamphorst, R. Mathew, M.K. Chung, E. White, T. Shlomi, J. D. Rabinowitz, Glutamine driven oxidative phosphorylation is a major ATP source in transformed mammalian cells in both normoxia and hypoxia, Mol. Syst. Biol. 9 (2013) 1–11, https://doi.org/10.1038/msb.2013.65.
[3] S.E. Weinberg, N.S. Chandel, Targeting mitochondria metabolism for cancer therapy, Nat. Chem. Biol. 11 (2015) 9–15, https://doi.org/10.1038/nchembio.1712.
[4] F. Weinberg, R. Hamanaka, W.W. Wheaton, S. Weinberg, J. Joseph, M. Lopez, B. Kalyanaraman, G.M. Mutlu, G.R.S. Budinger, N.S. Chandel, Mitochondrial metabolism and ROS generation are essential for Kras-mediated tumorigenicity, Proc. Natl. Acad. Sci. U.S.A. 107 (2010) 8788–8793, https://doi.org/10.1073/pnas.1003428107.
[5] X.L. Zu, M. Guppy, Cancer metabolism: facts, fantasy, and fiction, Biochem. Biophys. Res. Commun. 313 (2004) 459–465, https://doi.org/10.1016/j.bbrc.2003.11.136.
[6] T. Li, J. Han, L. Jia, X. Hu, L. Chen, Y. Wang, PKM2 coordinates glycolysis with mitochondrial fusion and oxidative phosphorylation, Protein and Cell 10 (2019) 583–594, https://doi.org/10.1007/s13238-019-0618-z.
[7] D.Y. Gui, C.A. Lewis, M.G. Vander Heiden, Allosteric regulation of PKM2 allows cellular adaptation to different physiological states, Sci. Signal. 6 (2013) 1–5, https://doi.org/10.1126/scisignal.2003925.
[8] J. Gao, Y. Zhao, T. Li, X. Gan, H. Yu, The role of PKM2 in the regulation of mitochondrial function: focus on mitochondrial metabolism, oxidative stress, dynamic, and apoptosis, Oxid. Med. Cell. Longev. 2022 (2022).
[9] B. Rathod, S. Chak, S. Patel, A. Shard, Tumor pyruvate kinase M2 modulators: a comprehensive account of activators and inhibitors as anticancer agents, RSC Med. Chem. 12 (2021) 1121–1141, https://doi.org/10.1039/D1MD00045D.
[10] E. Aslan, S. Adem, In vitro effects of some flavones on human pyruvate kinase isoenzyme M2: the effects of flavones on PKM2, J. Biochem. Mol. Toxicol. 29 (2015) 109–113, https://doi.org/10.1002/jbt.21673.
[11] X. Ning, H. Qi, R. Li, Y. Jin, M.A. McNutt, Y. Yin, Synthesis and antitumor activity of novel 2, 3-didithiocarbamate substituted naphthoquinones as inhibitors of pyruvate kinase M2 isoform, J. Enzym. Inhib. Med. Chem. 33 (2018) 126–129, https://doi.org/10.1080/14756366.2017.1404591.
[12] S. Arora, G. Joshi, A. Chaturvedi, M. Heuser, S. Patil, R. Kumar, A perspective on medicinal chemistry approaches for targeting pyruvate kinase M2, J. Med. Chem. 65 (2022) 1171–1205, https://doi.org/10.1021/acs.jmedchem.1c00981.
[13] M. Makrecka-Kuka, P. Dimitrijevs, I. Domracheva, K. Jaudzems, M. Dambrova, P. Arsenyan, Fused isoselenazolium salts suppress breast cancer cell growth by dramatic increase in pyruvate-dependent mitochondrial ROS production, Sci. Rep. 10 (2020) 1–12, https://doi.org/10.1038/s41598-020-78620-8.
[14] P. Arsenyan, J. Vasiljeva, S. Belyakov, E. Liepinsh, M. Petrova, Fused selenazolinium salt derivatives with a Se-N$^+$ bond: preparation and properties, Eur. J. Org Chem. 2015 (2015) 5842–5855, https://doi.org/10.1002/ejoc.201500582.
[15] A.V. Kuznetsov, S. Javadov, S. Sickinger, S. Frotschnig, M. Grimm, H9c2 and HL 1 cells demonstrate distinct features of energy metabolism, mitochondrial function and sensitivity to hypoxia-reoxygenation, Biochim. Biophys. Acta, Mol. Cell Res. 1853 (2015) 276–284, https://doi.org/10.1016/j.bbamcr.2014.11.015.
[16] C.W. Kim, K.C. Choi, Effects of anticancer drugs on the cardiac mitochondrial toxicity and their underlying mechanisms for novel cardiac protective strategies, Life Sci. 277 (2021), 119607, https://doi.org/10.1016/j.lfs.2021.119607.
[17] P.S. Brookes, Mitochondrial H+ leak and ROS generation: an odd couple, Free Radic. Biol. Med. 38 (2005) 12–23, https://doi.org/10.1016/j.freeradbiomed.2004.10.016.
[18] K.S. Echtay, D. Roussel, J. St-Pierre, M.B. Jekabsons, S. Cadenas, J.A. Stuart, J. A. Harper, S.J. Roebuck, A. Morrison, S. Pickering, J.C. Clapham, M.D. Brand, Superoxide activates mitochondrial uncoupling proteins, Nature 415 (2002) 96–99, https://doi.org/10.1038/415096a.
[19] H.J. Forman, A. Azzi, On the virtual existence of superoxide anions in mitochondria: thoughts regarding its role in pathophysiology, Faseb. J. 11 (1997) 374–375, https://doi.org/10.1096/fasebj.11.5.9141504.
[20] M.P. Murphy, How mitochondria produce reactive oxygen species, Biochem. J. 417 (2009) 1–13, https://doi.org/10.1042/BJ20081386.
[21] P.A. Konstantinopoulos, U.A. Matulonis, PARP Inhibitors in ovarian cancer: a trailblazing and transformative journey, Clin. Cancer Res. 24 (2018) 4062–4065, https://doi.org/10.1158/1078-0432.CCR-18-1314.
[22] F. Zhang, R. Xie, F.M. Munoz, S.S. Lau, T.J. Monks, PARP-1 hyperactivation and reciprocal elevations in intracellular Ca 2 + during ROS-induced nonapoptotic cell death, Toxicol. Sci. 140 (2014) 118–134, https://doi.org/10.1093/toxsci/kfu073.
[23] Y. Du, H. Yamaguchi, Y. Wei, J.L. Hsu, H. Wang, Y. Hsu, W. Lin, W. Yu, P. G. Leonard, G.R.L. Iv, M. Chen, K. Nakai, M. Hsu, C. Chen, Y. Sun, Y. Wu, W. Chang, W. Huang, C. Liu, Y. Chang, C. Chen, M. Park, P. Jones, G. N. Hortobagyi, M. Hung, Blocking c-Met – mediated PARP1 phosphorylation enhances anti-tumor effects of PARP inhibitors, Nat. Med. 22 (2016), https://doi.org/10.1038/nm.4032.
[24] P. Dimitrijevs, P. Arsenyan, Cardiolipin in the spotlight: quantitative analysis and fluorescence-based competitive binding assay, Sensor. Actuator. B Chem. 346 (2021), 130537, https://doi.org/10.1016/j.snb.2021.130537.
[25] J. Cheng, G. Nanayakkara, Y. Shao, R. Cueto, L. Wang, W.Y. Yang, Y. Tian, H. Wang, X. Yang, Mitochondrial proton leak plays a critical role in pathogenesis of cardiovascular diseases, Adv. Exp. Med. Biol. 982 (2017) 359–370, https://doi.org/10.1007/978-3-319-55330-6_20.
[26] M.D. Brand, J.L. Pakay, A. Ocloo, J. Kokoszka, D.C. Wallace, P.S. Brookes, E. J. Cornwall, The basal proton conductance of mitochondria depends on adenine nucleotide translocase content, Biochem. J. 392 (2005) 353–362, https://doi.org/10.1042/BJ20050890.
[27] W.R. Liu, M.X. Tian, L.X. Yang, Y.L. Lin, L. Jin, Z. Bin Ding, Y.H. Shen, Y.F. Peng, D. M. Gao, J. Zhou, S.J. Qiu, Z. Dai, R. He, J. Fan, Y.H. Shi, PKM2 promotes metastasis by recruiting myeloid-derived suppressor cells and indicates poor prognosis for hepatocellular carcinoma, Oncotarget 6 (2015) 846–861, https://doi.org/10.18632/oncotarget.2749.
[28] W.J. Israelsen, T.L. Dayton, S.M. Davidson, B.P. Fiske, A.M. Hosios, G. Bellinger, J. Li, Y. Yu, M. Sasaki, J.W. Horner, L.N. Burga, J. Xie, M.J. Jurczak, R.A. Depinho, C.B. Clish, T. Jacks, R.G. Kibbey, G.M. Wulf, D. Di Vizio, G.B. Mills, L.C. Cantley, M. G. Vander Heiden, PKM2 isoform-specific deletion reveals a differential requirement for pyruvate kinase in tumor cells, Cell 155 (2013) 397, https://doi.org/10.1016/j.cell.2013.09.025.
[29] X. Ning, H. Qi, R. Li, Y. Li, Y. Jin, Discovery of novel naphthoquinone derivatives as inhibitors of the tumor cell specific M2 isoform of pyruvate kinase, Eur. J. Med. Chem. 138 (2017) 343–352, https://doi.org/10.1016/j.ejmech.2017.06.064.
[30] S. Shan, J. Shi, P. Yang, B. Jia, H. Wu, X. Zhang, Z. Li, Apigenin restrains colon cancer cell proliferation via targeted blocking of pyruvate kinase M2-dependent glycolysis, J. Agric. Food Chem. 65 (2017) 8136–8144, https://doi.org/10.1021/acs.jafc.7b02757.
[31] D. Srivastava, S. Nandi, M. Dey, Mechanistic and structural insights into cysteine-mediated inhibition of pyruvate kinase muscle isoform 2, Biochemistry 58 (2019) 3669–3682, https://doi.org/10.1021/acs.biochem.9b00349.
[32] S. Nandi, M. Dey, Biochemical and structural insights into how amino acids regulate pyruvate kinase muscle isoform 2, J. Biol. Chem. 295 (2020) 5390–5403, https://doi.org/10.1074/jbc.RA120.013030.
[33] J.A. Macpherson, A. Theisen, L. Masino, L. Fets, P.C. Driscoll, V. Encheva, A. P. Snijders, S.R. Martin, J. Kleinjung, P.E. Barran, F. Fraternali, D. Anastasiou, Functional cross-talk between allosteric effects of activating and inhibiting ligands underlies PKM2 regulation, Elife 8 (2019) 1–36, https://doi.org/10.7554/eLife.45068.
[34] P. Wang, C. Sun, T. Zhu, Y. Xu, Structural insight into mechanisms for dynamic regulation of PKM2, Protein and Cell 6 (2015) 275–287, https://doi.org/10.1007/s13238-015-0132-x.
[35] J.H. Park, A. Kundu, S.H. Lee, C. Jiang, S.H. Lee, Y.S. Kim, S.Y. Kyung, S.H. Park, H.S. Kim, Specific pyruvate kinase m2 inhibitor, compound 3k, induces autophagic cell death through disruption of the glycolysis pathway in ovarian cancer cells, Int. J. Biol. Sci. 17 (2021) 1895–1908, https://doi.org/10.7150/ijbs.59855.

[36] D. Anastasiou, G. Poulogiannis, J.M. Asara, M.B. Boxer, J. Jiang, M. Shen, G. Bellinger, A.T. Sasaki, J.W. Locasale, D.S. Auld, C.J. Thomas, M.G. Vander Heiden, C. Lewis, Inhibition of pyruvate kinase M2 by reactive oxygen species contributes to cellular antioxidant responses, Science 334 (2011) 1278–1283, https://doi.org/10.1126/science.1211485.Inhibition.

[37] J. Liang, R. Cao, X. Wang, Y. Zhang, P. Wang, H. Gao, C. Li, Mitochondrial PKM2 regulates oxidative stress induced apoptosis by stabilizing Bcl2, Cell Res. 27 (2017) 329–351, https://doi.org/10.1038/cr.2016.159.

[38] A. Robert, Copeland, Evaluation of Enzyme Inhibitors in Drug Discovery: A Guide for Medicinal Chemists and Pharmacologists, second ed., John Wiley & Sons, Inc., 2013 https://doi.org/10.1002/9781118540398.

[39] L. Luo, C.A. Parrish, N. Nevins, D.E. McNulty, A.M. Chaudhari, J.D. Carson, V. Sudakin, A.N. Shaw, R. Lehr, H. Zhao, S. Sweitzer, L. Lad, K.W. Wood, R. Sakowicz, R.S. Annan, P.S. Huang, J.R. Jackson, D. Dhanak, R.A. Copeland, K. R. Auger, ATP-competitive inhibitors of the mitotic kinesin KSP that function via an allosteric mechanism, Nat. Chem. Biol. 3 (2007) 722–726, https://doi.org/10.1038/nchembio.2007.34.

[40] M.S. Alphey, L. Pirrie, L.S. Torrie, W.A. Boulkeroua, M. Gardiner, A. Sarkar, M. Maringer, W. Oehlmann, R. Brenk, M.S. Scherman, M. Mcneil, M. Rejzek, R. A. Field, M. Singh, D. Gray, N.J. Westwood, J.H. Naismith, Allosteric competitive inhibitors of the glucose-1-phosphate thymidylyltransferase (RmlA) from Pseudomonas aeruginosa, ACS Chem. Biol. 8 (2013) 387–397.

[41] H.C. Feldman, M. Tong, L. Wang, R. Meza acevedo, T. Gobillot, I. Lebedev, S. B. Hari, M.J. Gliedt, K. Arinjay, B.J. Backes, F.R. Papa, M.A. Seeliger, D.J. Maly, Structural and functional analysis of the allosteric inhibition of IRE1α with ATP competitive kinase ligands structural and functional analysis of the allosteric inhibition of IRE1α with ATP-competitive ligands, ACS Chem. Biol. 11 (2016) 2195–2205, https://doi.org/10.1021/acschembio.5b00940.

[42] W. Yang, Y. Xia, H. Ji, Y. Zheng, J. Liang, W. Huang, K. Aldape, X. Gao, Z. Lu, Nuclear PKM2 regulates β-catenin transactivation upon EGFR activation, Nature 480 (2011) 118–122, https://doi.org/10.1038/nature10598.

[43] N. Azoitei, A. Becher, K. Steinestel, A. Rouhi, K. Diepold, F. Genze, T. Simmet, T. Seufferlein, PKM2 promotes tumor angiogenesis by regulating HIF 1aα through NF-κB activation, Mol. Cancer 15 (2016) 1–15, https://doi.org/10.1186/s12943-015-0490-2.

[44] S. Zhu, Y. Guo, X. Zhang, H. Liu, M. Yin, X. Chen, C. Peng, Pyruvate kinase M2 (PKM2) in cancer and cancer therapeutics, Cancer Lett. 503 (2021) 240–248, https://doi.org/10.1016/j.canlet.2020.11.018.

[45] Q. Li, D. Zhang, X. Chen, L. He, T. Li, X. Xu, M. Li, Nuclear PKM2 contributes to gefitinib resistance via upregulation of STAT3 activation in colorectal cancer, Sci. Rep. 5 (2015) 1–12, https://doi.org/10.1038/srep16082.

[46] N. Li, L. Feng, H. Liu, J. Wang, M. Kasembeli, M.K. Tran, J. Tweardy, S.H. Lin, J. Chen, PARP inhibition suppresses growth of EGFR-mutant cancers by targeting nuclear PKM2, Cell Res. 15 (2017) 843–856, https://doi.org/10.1016/j.celrep.2016.03.070.PARP.

[47] S. Zhou, D. Li, D. Xiao, T. Wu, X. Hu, Y. Zhang, J. Deng, J. Long, S. Xu, J. Wu, G. Li, M. Peng, X. Yang, Inhibition of PKM2 enhances sensitivity of olaparib to ovarian cancer cells and induces DNA damage, Int. J. Biol. Sci. 18 (2022) 1555–1568, https://doi.org/10.7150/ijbs.62947.